Theoretical investigation of optical fibre surface plasmon resonance palladium-based hydrogen sensors

Fionn Downes

A thesis submitted for the degree of Doctor of Philosophy in Physics

Institute of Technology Sligo

Supervised by Dr. C. M. Taylor

Submitted to the Institute of Technology Sligo, June 2018

i. Declaration

The work described is entirely my own, except for assistance mentioned in the acknowledgements and noted in the list of publications.

Fionn Downes

_____

ii. Abstract

This thesis is an investigation into the operation and optimization of a series of optical fibre surface plasmon resonance (OFSPR) based hydrogen sensors. All devices we investigate are based on a multimode optical fibre that employs a multilayer stack sensing structure coated on the core of the cladding-stripped fibre.

For the first time, we investigate the use of a PdY alloy as the H_2 sensitive layer in an OFSPR sensor. The alloying of Pd with Y significantly improves durability and permeability. We show that the sensor operates at a level comparable to a pure Pd sensor. We investigate the influence that the thickness of each multilayer component has on sensor performance, and demonstrate a series of optimal sensing configurations that maximize sensor performance for a range of incident light wavelengths.

Next, we investigate the operation of a nanocomposite based multilayer structure consisting of Pd nanoparticles embedded in a SiO_2 dielectric matrix. We investigate the influence that multilayer component thicknesses, and nanocomposite volume fraction have on performance, and compare operation to an individual multilayer based device.

We investigated the operation of a dual-channel sensor by including additional channels along the fibre core. We determined the influence that the thickness of each multilayer component has on the performance of both channels, propose a specific optimal sensor, and demonstrate the operation of additional multi-channel configurations.

Lastly, we demonstrate the first evidence of surface plasmon and waveguide mode resonance stimulated at equal wavelengths, using a single multilayer sensing configuration. We characterized the origin of each resonance mode. We demonstrate a drastic improvement in sensor figure of merit compared to that determined using the widely referenced optimal OFSPR sensing configuration. This improvement is attributed to the co-operation between the SPR & TE resonance modes.

iii. Acknowledgements

I wish to express my sincere gratitude to my supervisor Dr. Cian M. Taylor for his advice and guidance throughout my career, without which, this research would not be possible.

For financial assistance, I would like to acknowledge the Institute of Technology Sligo Round 5 President's Bursary.

I wish to thank all of the staff at the Institute of Technology Sligo, for providing a healthy work environment that promotes high quality research.

Finally, I wish to thank my parents Louise and Willie for their love and support, and my siblings Darragh, Fearghus, and Bláithín.

iv. Contents

v. List of Figures

1 Chapter 1: Theory

1.1 Introduction

1.1.1 History of Surface Plasmon Resonance

In 1902 Robert Williams Wood made an observation while working on a Rowland dividing-engine at the John Hopkins University. Upon observing the radiation illuminated from a reflecting surface accompanied by a diffraction grating, a pattern of bright and dark fringes "uneven distribution of light", was observed (Wood 1902). The theory of diffraction at the time was inadequate to explain this observation and Wood attempted to find out if possible modifications must be introduced. Following the work of Quincke, Rayleigh, Rowland, and Wien & Rubens; Wood realised that polarisation could describe the unusual behaviour. He found that the anomalies appeared only when the direction of vibration was at right angles with the ruling, however the reason for this occurrence was still unclear.

A B

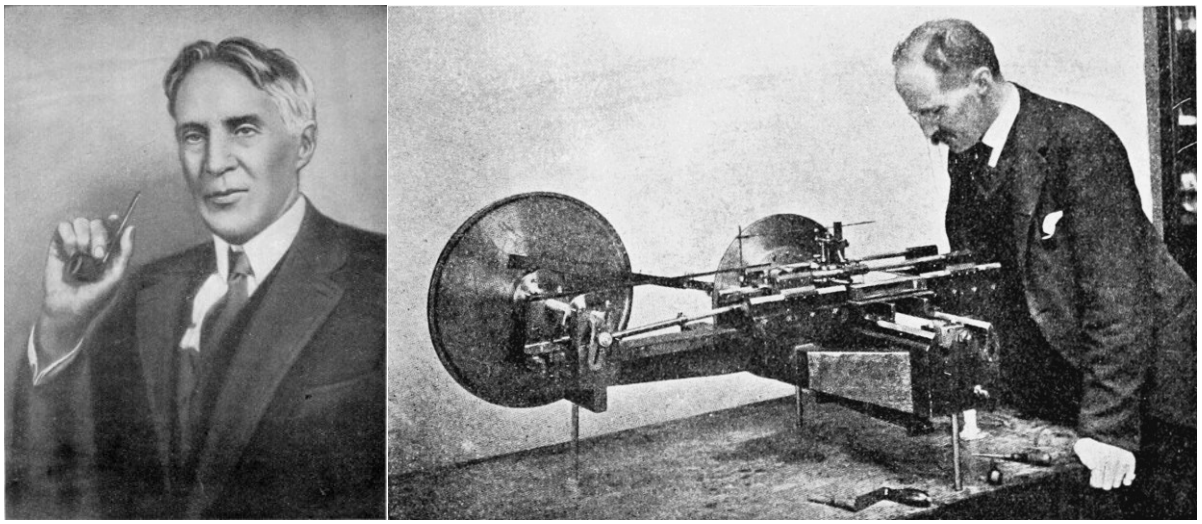

Figure 1-1 – (A) Portrait of R. W. Wood taken in 1910. (B) Prof. Rowland's Dividing Engine which was used in the experiment by Woods during his experiment that lead to the discovery of surface plasmon resonance.

In 1907 Rayleigh attempted to explain this occurrence, suggesting that the higher order of the wavelength emerges outside of the grating (Rayleigh 1907b; Rayleigh 1907a), however he could not explain the enhanced reflection that occurred under certain cases by Wood. The same year, while studying the propagation of plane electromagnetic waves along a conductor, a special surface wave solution to Maxwell's equations was derived by Zenneck (Zenneck 1907),

demonstrating theoretically that surface electromagnetic waves occur at the boundary between a metal and a loss free medium. He stated that the lossy part of the dielectric function is responsible for binding the electromagnetic waves to the boundary interface. Two years later Sommerfeld theorized in a very in depth paper that the surface waves decayed exponentially perpendicular to the interface (Sommerfeld 1909). Additionally the amplitudes of these surface waves varied as a function of the inverse of the square root of the horizontal distance from the source dipole. Oscillations in ionized gases were studied by (Tonks and Langmuir 1929), where the term plasma electron oscillations was coined.

Fano in 1941 revisited "Sommerfeld Waves" in an attempt to visualise their physical meaning. Fano theoretically validated that the observations made by Wood were due to the excitation of surface plasmon waves on the surface of the diffraction grating interface (Fano 1941). Pines and Bohm designed a physical picture of the representation of collective electrons in a dense electron cloud (Pines and Bohm 1952), and discovered that in an electron gas, if an electron moves with greater velocity than the thermal speed, then it excites collective oscillations in the form of a wake trailing the particle. They proceeded to calculate the collective oscillation frequency, as well as the energy emitted by the particles. Later in 1957, while investigating the popular topic of the characteristic energy losses by fast electrons, Ritchie hypothesised that surface plasmon oscillations was the reason for this missing energy. Soon after, Turbadar was experimentally investigating the reflectance of s- & p- polarised light from a thin film of Al deposited onto glass (Turbadar 1959). He observed that the reflectance from p- polarised light increases to a maximum near the critical angle, but for certain thickness of Al, the reflectance increase is closely followed by a sharp dip. Unfortunately, Turbadar did not link this phenomenon to SPR at the time of publication.

Stern and Ferrell went on to demonstrate Ritchie's predictions by exciting surface plasmons at both an aluminium and magnesium surface (Stern and Ferrell 1960). They demonstrated that surface waves give a natural explanation of the low lying characteristic energy losses, thus proving Ritchie's theory. That same year Powell and Swan (Powell and Swan 1960) reported on the measurements made by Stern and Ferrell by observing the loss spectra of Al and Mg during oxidation. A brief note in the paper indicates their gratitude towards Stern and Ferrell during this time, as Powell and Swan's paper was submitted in October 1959, and long before Stern and Ferrell's submission in March 1960: *"The authors are indebted to Dr. Stern for communicating some of the theoretical results prior to their publication" (Powell and Swan 1960).*

8 year later, a physicist by the name of Andreas Otto devised a method of stimulating SPR while working at the University of Munich (Otto 1968). If p-polarised light shone through a glass prism at an acute incident angle such that frustrated total internal reflection could occur, this results in the generation of an evanescent wave at the outer prism/air interface. Otto realised that if the flat surface of a suitable metallic material was brought near, but not in contact with the location where this evanescent wave occurs in a vacuum, some of the energy would appear to be lost as seen from the sudden drop in reflectivity. The drop in reflectivity was very sensitive to minute changes in air gap thickness, incident angle, and materials employed. This observation was very like that observed by Turbadar. These experimental results were then compared with the *"theory of metal optics"* (Fresnel equations). Otto found that no information on surface roughness was necessary to compare the theory with experiment, "thus eliminating the possibility of his results occurring due to physical abnormalities on the metallic surface such as grating effects". While this method is sound; 50 years ago, it was difficult to maintain a thin finite air gap between metallic materials and glass prism.

Later that year, two researchers working at the University of Hamburg by the names Kretschmann and Raether extended upon Otto's configuration by considering the fact that provided the metallic layer is thinner than the amplitude of the evanescent wave generated at the prism surface, the metallic layer could be placed in direct contact with the prism, and the generated EV wave could stimulate SPR at the metallic/air interface (Kretschm.E and Raether 1968). Similarly, this results in a sharp dip in the reflectance of incident light, at a specific angle. The ease of construction and operation of the Kretschmann configuration over Otto's similar set-up resulted in Kretschmann's method being replicated by thousands of researchers over the years for the purpose of studying SPR. In addition, it is noted that Kretschmann and Raether's paper was published in English, while Otto's paper was originally published in German, which at the time may have been an influential factor rate at which scientific knowledge is shared around the world. Replicating the Otto and Kretschmann structures were part of the foundational steps in our modelling of OFSPR for hydrogen sensing applications.

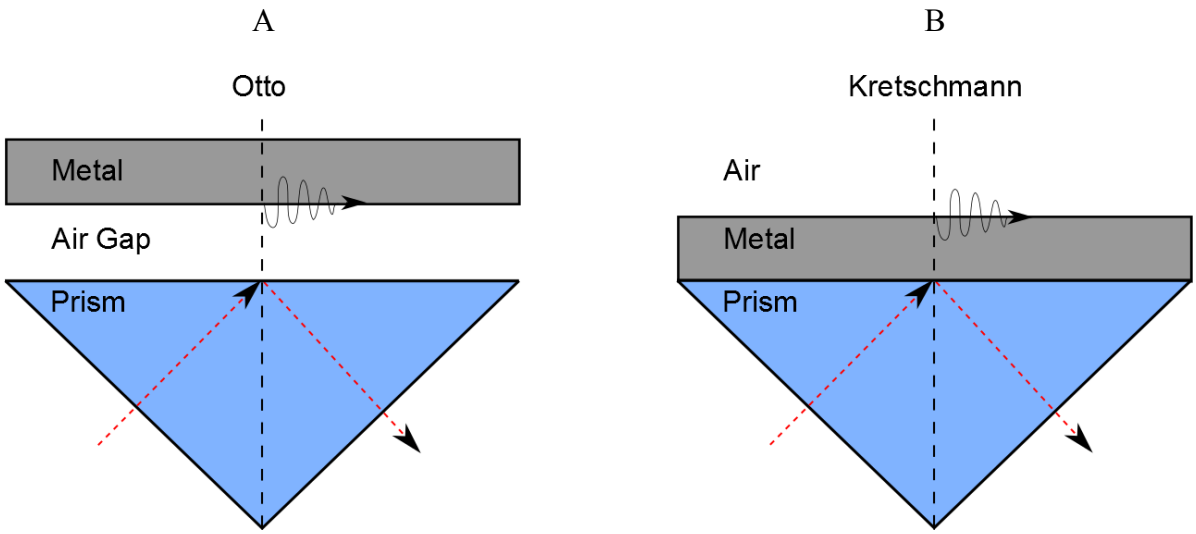

Figure 1-2 – (A) Schematic representation of the Otto configuration; this consisted of a glass prism in near proximity to a continuous metallic film, separated by air. (B) Kretschmann configuration; the metallic film is exceptionally thin, and in direct contact with the glass prism. Depending on the angle, wavelength, and polarization of incident radiation, it is possible to stimulate surface plasmon resonance using both of the configurations illustrated.

Schematic representations of the Otto and Kretschmann configurations are illustrated in Fig. 1-2. The direct detection of hydrogen through absorbance-based optical methods is not possible because hydrogen is non-adsorbing in the UV, visible spectrum, and IR. Hydrogen detection can be achieved however by considering the change in optical properties of certain materials upon exposure. Soon after the publication of Kretschmann and Raether's paper, Pd was used for the first time for hydrogen sensing (Lewis 1967). This material proved to be highly sensitive and selective towards H_2 gas, and in addition, the (Pd + H_2) reaction was reversible. Around the same time, Pt-WO_3 was used as an alternative H_2 sensitive material (Shaver 1967), as it also demonstrated high performance. Since then, both materials have been at the forefront of hydrogen sensing (Huebert *et al.* 2011).

Soon after, the principle of SPR was employed in biological applications (Gordon Ii and Swalen 1977), as it became possible to determine the optical constants of organic monolayers on gold, using a structure similar to the Kretschmann configuration. Thereafter, the principle of SPR was used in many other biological and medical applications, but for this report, we will focus on chemical based sensing of H_2 gas.

While there were many electronic based hydrogen detection devices established in the field that make use of the strong, selective Pd permittivity (Lundström *et al.* 1975; D'Amico *et al.* 1982), the first ever optical fibre based hydrogen sensor employing Pd was first developed in

1984 (Butler 1984). This consisted of a Pd coated wire, which expanded under exposure to H_2, and thus changed the effective optical path length of the fibre. This configuration demonstrated good sensitivity, a wide dynamic range, and reversible reactions. Soon after, this opened up the gateway for a multitude of researchers to carry out work utilizing optical fibre Pd based sensors for H_2 detection. Butler continued research in this area in subsequent years, he described the operation of a micro-mirror OF hydrogen sensor (Butler 1991; Butler 1994). The change in reflectivity of Pd was in proportion to the hydrogen concentration present.

In 1993, SPR was successfully achieved using OF technology (Jorgenson and Yee 1993). This is achieved by removing a small section of the optical fibre cladding, and replacing with Ag. Changes in parameters such as metallic film thickness, bulk refractive index, and metallic dielectric permittivity could be demonstrated by observing changes in the spectral intensity distribution. For example, it was observed that upon introducing a higher real-index high-fructose corn syrup solution into the flow cell; the resonance wavelength of the surface plasmon would shift towards the red end of the spectrum.

The same year, Chadwick and Gal developed the first ever surface plasmon resonance Pd based hydrogen sensing device (Chadwick and Gal 1993). The motive behind this device was to overcome the difficulty in optically determining H_2 concentrations that disallow the applications of common analytical techniques such as IR and UV-visible absorption spectroscopies. This operated using the Kretschmann configuration consisting of glass accompanied with a (20nm) thick Pd film, which was stimulated using p- polarised light of wavelength (λ=600nm). The Pd continuous film was exposed to 5% H_2 concentrations in a N_2 environment. They reported up to 90% relative intensity change, with a response time of ($\approx$ 30s). They continued to develop this sensor and reported improved performance the following year (Chadwick *et al.* 1994). Further advances in optical fibre SPR Pd based hydrogen sensors were realised with the inclusion of waveguide techniques (Tobiška *et al.* 2001).

Alternative optical based SPR H_2 sensors utilising Pd have been developed structures such as grating (Lin *et al.* 2008) that do not make use of an optical fibre. However, OF technology is advantageous in allowing for the possibility of remote deployment and multipoint sensing. SPR necessitates a metallic component, specifically a material whose dielectric properties are of the form ($\varepsilon = \varepsilon_{re} + i\varepsilon_{im}$); where ($\varepsilon_{re} < 0$), and ($\varepsilon_{im} > 0$). Historically, both gold (Au) and silver (Ag) have been used excite SPR (A. K. Sharma and B. D. Gupta 2005; Lee and El-Sayed 2006; Gwon and Lee 2010; Chen *et al.* 2011; Choi *et al.* 2011; Oates *et al.* 2011; Perrotton *et al.*

2011b; Ciprian and Hlubina 2013b). Ag has the advantage of producing a sharp resonance dip (small linewidth of the SPR curve) leading to high detection accuracy (Gupta and Sharma 2005; Chen and Jiang 2010; Perrotton *et al.* 2011b; X.G. Wang *et al.* 2013a). This is due to the relatively large real component of the Ag dielectric permittivity. We will talk about this in more detail in subsequent chapters. Using Au as a component in the SPR transducer layer leads to a large shift in resonance angle relative to the change in the refractive index of the sensing layer (Chen and Jiang 2010). Au is chemically stable whereas Ag is easily oxidised when exposed to the environment. Good performance in an optical fibre based SPR device necessitates high detection accuracy as well as sensitivity. We will discuss this further in subsequent sections.

Employing the results obtained from her previous work on calculating the Casimir force between a sphere and a plane, by determining the energy from their interaction with surface plasmons (Noguez and Román-Velázquez 2004), it has been demonstrated that the inclusion of nanoparticle sensing films in waveguide structures can improve sensor performance (Noguez 2007).

Finally, in the last 10 years there has been much research carried out in OFSPR H_2 sensing, much of which we will compare and discuss in relation to our own work presented in this thesis. The most influential regarding this research was the development of the first OFSPR Pd based H_2 sensor operating in wavelength modulation (Perrotton *et al.* 2011b). This consisted of an optical fibre structure, with a transducer layer overlaying a (1cm) long gap of the cladding. The transducer layer consisted of multiple individual continuous film layers: ($Ag/SiO_2/Pd$). Observation of the spectral resonance shifts allowed Perrotton *et al*. to determine the hydrogen concentration surrounding the transducer layer.

For this study, we focused on the development of an optical fibre based surface plasmon resonance hydrogen sensor using palladium as a hydrogen sensitive source. As palladium or a palladium alloy absorbs hydrogen, the dielectric permittivity of the metal changes, which can be measured accurately by optical means. Table 1-1 provides a quick summary of important contributions made to the field of OFSPR H_2 sensing.

Year	Author/s	Contribution
1902	Woods	First experimental observation of SPR.
1907	Rayleigh	Attempted to explain Woods findings.
1907	Zenneck	Derived solution to Maxwell's equations that SPR waves occur at the boundary between metal and loss free medium.
1909	Sommerfeld	Surface waves decay exponentially at right angles to the metallic \ loss free interface.
1929	Tonks & Langmuir	Developed theory of electronic oscillations in ionised gas, defined plasma.
1941	Fano	Validated that the observations made by Wood was due to SPR.
1952	Pines & Bohm	Calculated collective oscillation frequency of electrons in a gas.
1957	Ritchie	Predicted SP oscillations was the reason for excessive energy losses in fast electrons.
1959	Turbadar	Observed SPR using metallic film and glass; did not link findings to any of the aforementioned papers.
1960	Stern & Ferrell	Developed theory that validates Ritchie's predictions.
1960	Powel & Swan	Experimentally validated Stern & Ferrell's findings.
1967	Lewis	Pd is highly sensitive to hydrogen gas.
1967	Shaver	Pt-WO_3 is also highly sensitive to hydrogen gas.
1968	Otto	Developed Otto configuration, prism metallic structure that can generate SPR. Applied theory to Fresnel equations.
1968	Kretschmann & Raether	Developed Kretschmann configuration; similar to Otto's method except the metallic film is placed directly onto the dielectric prism.
1977	Gordon & Swalen	Application of SPR to organic materials.
1984	Butler	First OF Pd based H_2 sensor.
1993	Chadwick & Gal	First SPR H_2 sensing device.
1993	Jorgenson & Yee	First OFSPR sensing device.
2001	Tobiska	First OFSPR Pd H_2 sensor employing waveguide techniques.
2011	Perrotton	First OFSPR Pd H_2 sensor operating in wavelength modulation.

Table 1-1 – Short summary of important discoveries in the history of surface plasmon resonance, hydrogen sensing, and optical fibre based devices.

1.1.2 Basic Theory of Surface Plasmon Resonance

Next, we will introduce the theory and formulae relating to SPR. A surface plasmon is an electron density wave propagating transversely along a metallic interface. Longitudinal charge density or "plasma" oscillations propagate through the metal with a given plasma frequency ω_p given by.

$$\omega_p = \sqrt{\frac{4\pi n e^2}{m_0}} \qquad (1\text{-}1)$$

Where e is the charge of a single electron, m_0 is the mass of an electron, and n is the density of free electrons. If these oscillations occur on the metallic surface, propagating along the boundary between the metallic layer and air, they are known as surface plasmons. As these waves are transverse in nature, they can only be stimulated by p- polarised (TM) light. Figure (3) displays a schematic representation of a TM light wave coupling with a SPW at the metal-air interface.

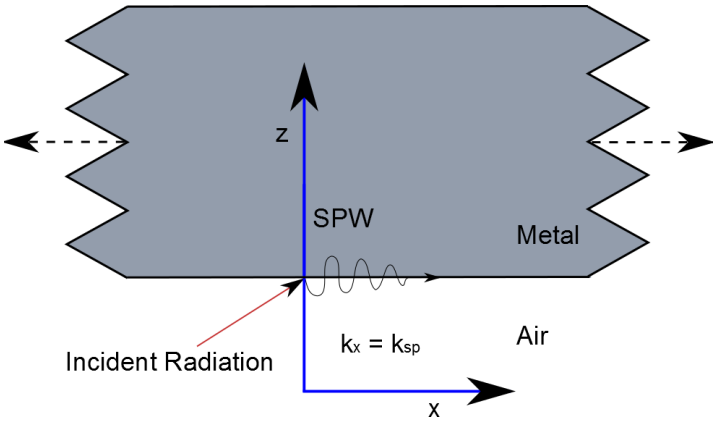

Figure 1-3 – Schematic representation of incident p- polarized radiation coupling with a surface plasmon wave, on the surface of an infinitely long metallic slab, adjacent to an infinite layer of air.

It is useful to imagine a layer of metal in contact with a dielectric as shown above. We consider a surface plasmon wave traveling through the metal along the x-axis with the z-axis acting as the normal through the interface between the two layers, then the electromagnetic field associated with the surface plasmon wave is given by (Raether 1986)

$$E = E_0 \exp[i(k_x x \pm k_z z - \omega t)] \qquad (1\text{-}2)$$

Where E_0 is the electromagnetic field, k_x and k_z are the x and z wavectors respectively. These are complex in nature and make for an exponential decay of the electromagnetic field. The + and – represent $z \geq 0$ and $z \leq 0$ respectively. The wavevector k_x is given by the equation:

$$k_x = \frac{2\pi}{\lambda_p} \tag{1-3}$$

λ_p is the plasma wavelength. The dispersion relationship for the SPW can be described as:

$$k_{sp} = k_x = \frac{\omega}{c}\left(\frac{\varepsilon_m \varepsilon_d}{\varepsilon_m + \varepsilon_d}\right)^{1/2} \tag{1-4}$$

$$\omega = \frac{2\pi c}{\lambda} \tag{1-5}$$

ω is the frequency, c is the speed of light in a vacuum, ε_m is the dielectric constant of the metal, ε_d is the dielectric constant of the dielectric material. The SPW undergoes an exponential decay in both the metal and the dielectric material. Similarly, the evanescent wave generated in both the Otto and Kretschmann structures, resulting from incident TM radiation propagating through the prism at an incident angle greater than the critical, can be represented by k_{ev}:

$$k_{ev} = \frac{\omega}{c}\sqrt{\varepsilon_p} Sin\theta \tag{1-6}$$

Where ε_p is the dielectric permittivity of the glass prism. In the case of Ag, the plasma wavelength is $1.4541\ x\ 10^{-7}$ (Sharma and Mohr 2008a; Sharma and Mohr 2008b; Sharma 2012). Therefore, we find that equation (1-3) becomes

$$k_x = \frac{2\pi}{\lambda_p} = \frac{2\pi}{1.4541\ x\ 10^{-7}} = 4.3210\ x\ 10^7 m^{-1}$$

The wavevector of the SPW can be described in terms of its real and imaginary components (Raether 1986):

$$k_{sp} = k_x' + ik_x'' \tag{1-7}$$

$$k_x' = \frac{\omega}{c}\left(\frac{\varepsilon_m{}'\varepsilon_d}{\varepsilon_m{}' + \varepsilon_d}\right)^{\frac{1}{2}} \tag{1-8}$$

$$k_x'' = \frac{\omega}{c}\left(\frac{\varepsilon_m{}'\varepsilon_d}{\varepsilon_m{}' + \varepsilon_d}\right)^{\frac{3}{2}} \frac{\varepsilon_m{}''}{2(\varepsilon_m{}')^2} \tag{1-9}$$

To take an example, we determine the real and imaginary wavevector components for a SPW stimulated using Ag.

$$k_x' = \frac{2\pi}{\lambda}\left(\frac{\varepsilon_m'\varepsilon_d}{\varepsilon_m' + \varepsilon_d}\right)^{\frac{1}{2}} = 1.566\ x\ 10^7 m^{-1}$$

$$k_x'' = \frac{2\pi}{\lambda}\left(\frac{\varepsilon_m'\varepsilon_d}{\varepsilon_m' + \varepsilon_d}\right)\frac{\varepsilon_m''}{2(\varepsilon_m')^2} = 1.111\ x\ 10^5 m^{-1}$$

The imaginary component of the wavevector allows us to calculate the decay length l_d of the SPW, the normalized output power of which decreases as $e^{\frac{-1}{-2k_x''}}$ (Raether 1986).

$$l_d = (2k_x'')^{-1} \qquad (1\text{-}10)$$

$$l_d = (2k_x'')^{-1} = \frac{c}{\omega}\left(\frac{\varepsilon_m'\varepsilon_d}{\varepsilon_m' + \varepsilon_d}\right)^{-3/2}\frac{\varepsilon_m'^{\,2}}{\varepsilon_m''} = 4.501\ x\ 10^{-6} m$$

We will explain briefly why this configuration permits the stimulation of SPR by light. Resonance occurs between the incident light, and the surface plasmon wave when the wavevector of incoming radiation match that of the most loosely bound electrons in the metal. Consider an infinite slab of a metallic surface alongside air. A surface plasmon can be generated by light if the k-vector and the frequency of the light wave match that of the surface plasmon. For example, say you want to excite a surface plasmon on Ag using light of wavelength 633nm in air, the wavevector for the light wave is defined as:

$$k = \frac{2\pi}{\lambda} = \frac{2\pi}{633nm} = 9.926\ x\ 10^6 m^{-1}$$

The dielectric permittivity of the Ag layer according to the Brendel-Bormann model is $\varepsilon_{Ag,\lambda} = -14.4686 + i1.1940$ when illuminated by light of the same wavelength. We investigate the dielectric permittivity of various materials in subsequent chapters. The wavevector for the SPW that occurs at the boundary between the metal and the dielectric is defined by equation (1-8)

$$9.926\ x\ 10^6\ x\left(\frac{(-14.4686\ +\ 1.1940i)\times 1}{-14.4686\ +\ 1.1940i + 1}\right)^{1/2} = 1.028\ x\ 10^7\ +\ 3.128i\ x\ 10^4 m^{-1}$$

It can be seen that the wavevector of the light wave is smaller than the real part of the surface plasmon wave wavevector: $k_x' = 1.566\ x\ 10^7 m^{-1}$. Therefore, this light wave cannot stimulate a SPW. In order for resonance to occur between the two waves, the real part of the wavevectors much match. One way to get over this mismatch is to send light through a material of a higher

refractive index, for example glass at $n = 1.5$. Now we find for light of the same wavelength the wavevector is:

$$k = \frac{2\pi}{\lambda} = \frac{2n\pi}{633nm} = 1.489\ x\ 10^{7} m^{-1}$$

Now the wavevector is too large. What we want is that the real component of the k-vector of the light to match that of the SP:

$$k'_{sp} = k'_{x} \qquad (1\text{-}11)$$

We can achieve this by-passing light through a glass prism at a specific angle of incidence. The incident angle can be chosen such that real component of the incident light wavevector matches that of the surface plasmon wave:

$$k'_{sp} = k'_{x} = k' sin\theta \qquad (1\text{-}12)$$

$$1.0288\ x\ 10^{7} = 1.489\ x\ 10^{7} sin\theta$$

$$\theta = 43.7°$$

Therefore, by sending light of wavelength 633nm through Ag coated glass prism at an angle of (θ=43.7˚) a SP will be excited via resonance with the light. This method of excitation is known as surface plasmon resonance. Fig. 1-4 displays the amount of light reflected across a range of incident angles for glass prism structure coated with thin layer Ag. The reflectance is lowest at an incident angle of (θ=43.7˚). As we will discuss in subsequent chapters, the thickness of the thin film metallic layer also plays a small part in determining the resonance angle.

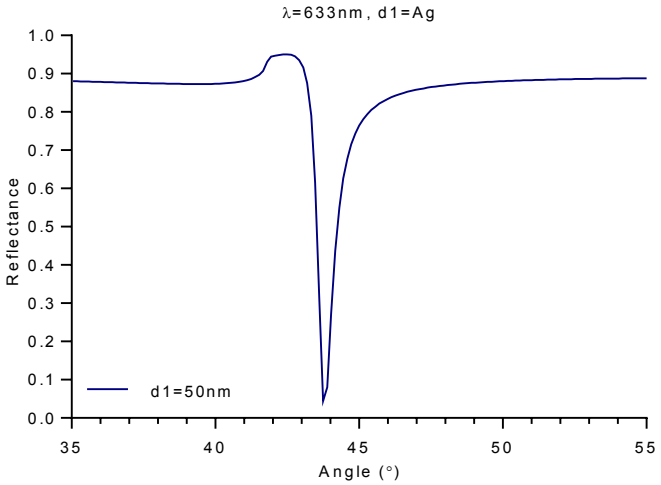

Figure 1-4 – Plot showing reflectance of p- polarized light (λ=633nm), when shone onto a Kretschmann configuration with (Ag=50nm).

1.1.3 Interaction of light with a multi-layer structure

Our sensor employs a multilayer sensing stack structure consisting of multiple independent materials on an unclad section of an optical fibre core. d_j is the thickness of the first layer covering the fibre core, and dj is the thickness of the final layer in direct contact with the analyte region "air" or "hydrogen". Fig. 1-5 indicates the behaviour of light interacting with multilayer stack structure, where j is the number of layers. And d_j is the thickness of the j^{th} layer.

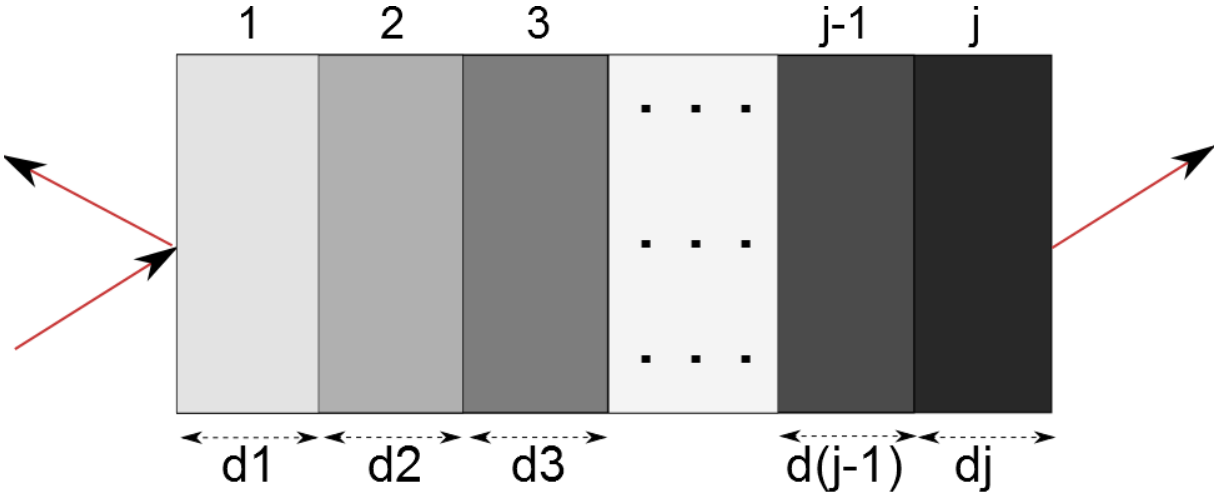

Figure 1-5 – Schematic representation of light interacting with a multi-layer sensing structure, where dj is the thickness of the j^{th} layer in the multi-layer structure.

Fresnel theory can be used to determine the interaction that occurs when light comes into contact with the interface between two media. However, when more than one interface is

present, the partial reflection of waves can themselves be partially transmitted. Thus, the net reflection from the multilayer structure is a sum of these reflections. Depending on the distance between successive layers and the wavelength of the light source, these series of reflections can interfere both constructively and destructively.

There are continuity conditions for the electric field across the boundaries from one medium to the next. Thus, the resultant field through a multilayer stack structure can be determined using a simple matrix operation involving the initial field, dielectric function of each medium, and respective distance between media. A stack of layers can then be represented as a system matrix, which is the product of the individual layer matrices. Finally, the system matrix is converted back into reflection and transmission coefficients. This known as the characteristic transfer matrix method.

Although only TM polarised radiation can stimulate SPR, the influence from TE oscillations need to be considered when calculating photon normalized output power through the optical fibre, as in reality; it is very unlikely that a only a single oscillation mode is permitted along a cylindrical multimode optical fibre.

The dielectric permittivity $\varepsilon_{j,\lambda}$ of any layer j can be described by the real and imaginary components of the refractive indices. The j^{th} layer has a complex refractive index n_j.

$$\varepsilon_{j,\lambda} = \left(n'_{j,\lambda} + in''_{j,\lambda}\right)^2 \tag{1-13}$$

The reflectance for s- and p- polarizations were calculated independently using the characteristic matrix M of the combined N-layer structure given by:

$$M = \prod_{j=1}^{N} M_j \tag{1-14}$$

$$M_j = \begin{bmatrix} cos\beta_j & -i/q_j \, sin\beta_j \\ -iq_j sin\beta_j & cos\beta_j \end{bmatrix} \tag{1-15}$$

M_j is the transition matrix for layer j, and M is the characteristic matrix of the multilayer system. Using this formulation, the propagation of both s- & p- polarized light can be determined. The term q_j differs depending on the oscillation of propagation, where $q_j = q_{j(s)}$ for s- polarised light, and $q_j = q_{j(p)}$ for p-polarized light, while β_j is the same for both.

$$q_{j(s)} = \sqrt{\varepsilon_j - {n_1}^2 sin^2\theta} \tag{1-16}$$

$$q_{j(p)} = \sqrt{\varepsilon_j - \frac{{n_1}^2 sin^2\theta}{\varepsilon_j}} \quad (1\text{-}17)$$

$$\beta_j = \frac{2\pi}{\lambda} d_j \sqrt{\varepsilon_j - {n_1}^2 sin^2\theta} \quad (1\text{-}18)$$

In this series of equations, ε_j is the dielectric permittivity of layer j. θ is the input angle of light of wavelength λ. n_j is the complex refractive index for layer j which has a thickness of d_j. The reflection coefficients of each mode of oscillation through the film were calculated by determining the Fresnel coefficients $r_{s,p}$.

$$r_{s,p} = \frac{q_1(M(1,1) + M(1,2)q_N) - (M(2,1) + M(2,2)q_N)}{q_1(M(1,1) + M(1,2)q_N) + (M(2,1) + M(2,2)q_N)} \quad (1\text{-}19)$$

The reflectance R of each mode of vibration from light of wavelength λ at angle θ through the fibre is simply the square of the corresponding reflection coefficient.

$$R_{s,p} = |r_{s,p}|^2 \quad (1\text{-}20)$$

In order to extend this model to allow for optical fibre applications, several other parameters need to be considered. The number of reflections N_{ref} that occur through the fibre at input angle θ can be calculated from the length of the fibre L and the diameter of the core D.

$$N_{ref} = \frac{L}{Dtan(\theta)} \quad (1\text{-}21)$$

Similar to the dielectric permittivity, the critical angle θ_c for a particular fibre is spectrally dependent via its relationship to n_{core} and n_{clad} which are the refractive indices of the core and cladding respectively.

$$\theta_c = arcsin\left(\frac{n_{clad}}{n_{core}}\right) \quad (1\text{-}22)$$

Finally, n_{core} and n_{clad} are related by the following equation (1-23), where NA is the fibre numerical aperture.

$$n_{clad} = \sqrt{{n_{core}}^2 - NA^2} \quad (1\text{-}23)$$

The normalised output power through the fibre at a specific wavelength λ can then be calculated by summing the reflectance coefficients across all angles between the critical angle and 90°. We used Gauss-Legendre in numerical integration; see Appendix A. Perrotton *et al*. presented a good representation of the normalised intensity output through a fibre that includes both TM and TE contributions (Perrotton *et al.* 2011b).

$$P_{Out,\lambda} = {}^{1}/_{2} \int_{\theta_c}^{90} |r_p(\theta)|^{2N} I_{0,\lambda}(\theta_{in})\, d\theta + {}^{1}/_{2} \int_{\theta_c}^{90} |r_s(\theta)|^{2N} I_{0,\lambda}(\theta_{in}) d\theta \quad (1\text{-}24)$$

While this model gives a reasonably accurate representation of the output power through a fibre, an extension to this model that accounts for the intensity distribution between the range of guided modes dP, and is defined by:

$$P_{nor} = \frac{{}^{1}/_{2} \int_{\theta_c}^{\pi/2} (|r_s(\theta)|^{2N_{ref}} + |r_p(\theta)|^{2N_{ref}}) dP d\theta}{\int_{\theta_c}^{\pi/2} dP d\theta} \quad (1\text{-}25)$$

$$dP \approx \frac{{n_1}^2 sin\theta cos\theta}{(1 - {n_1}^2 cos^2\theta)^2} d\theta \quad (1\text{-}26)$$

A

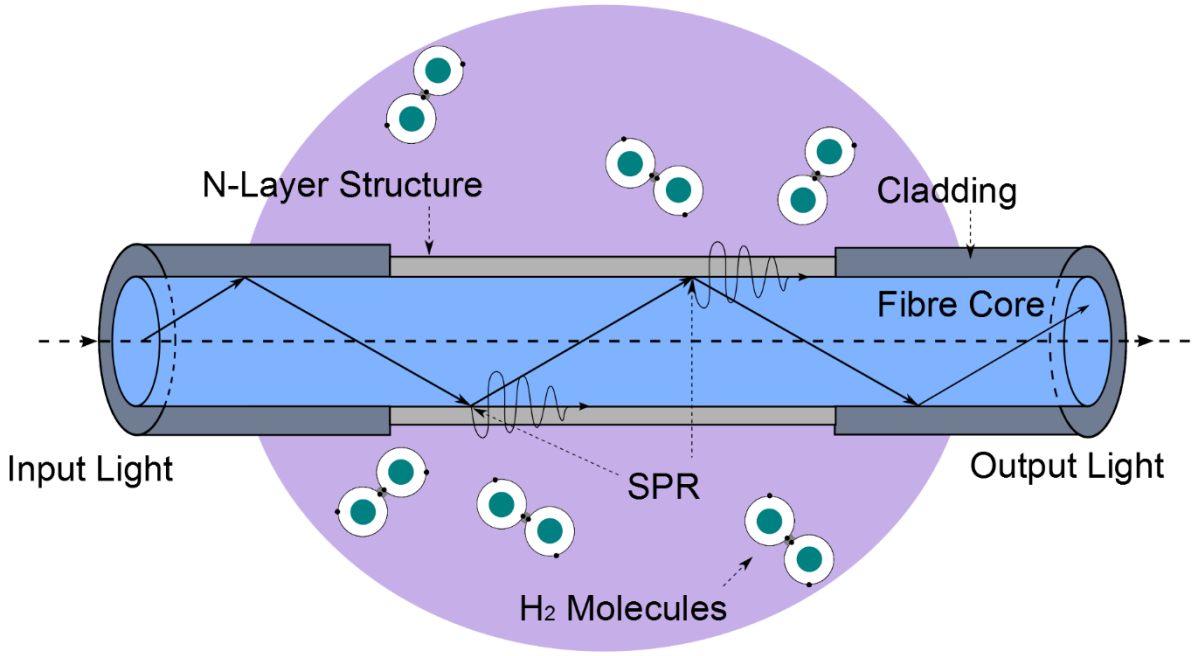

B

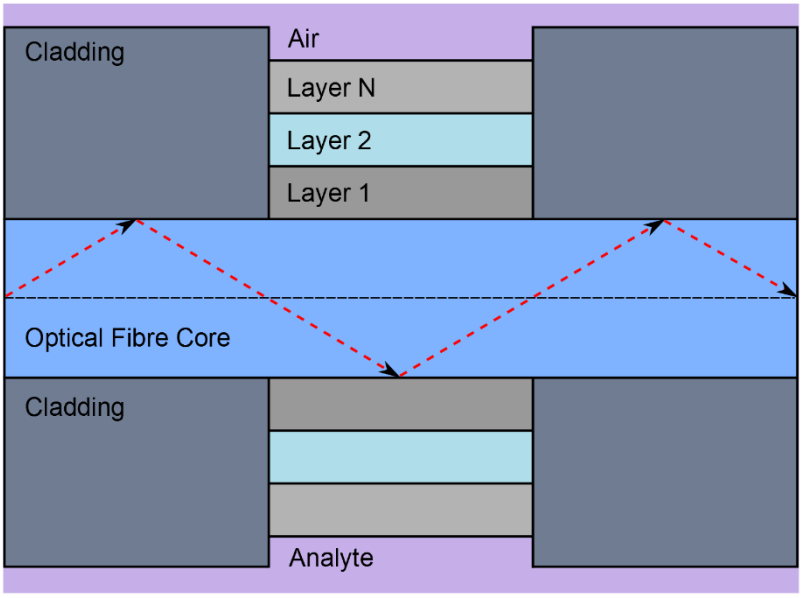

Figure 1-6 – (A) Schematic representation of an optical fibre surface plasmon resonance hydrogen sensor. Light propagates along the fibre core by total internal reflection. Once light of a specific wavelength comes into contact with the transducer layer at a suitable angle, it is absorbed by surface electrons in the multilayer sensing structure through surface plasmon resonance. (B) Close up schematic representation of the multilayer sensing structure (transducer layer) within the optical fibre sensing configuration.

Fig. 1-6(A) displays a schematic representation of an optical fibre surface plasmon resonance hydrogen sensing device. Light propagates along the fibre core by total internal reflection. Once TM polarised light of a specific wavelength comes into contact with layer 1 at a specific angle, resonance occurs resulting in the absorption of a fraction of the radiation, which can be seen as a decrease in the power output through the fibre. Fig. 1-6(B) demonstrates a close up view of the multilayer sensing structure surrounding the fibre core. The dielectric permittivity of layer N changes in the presence of hydrogen gas, and thus results in the surface plasmon resonance angle, and thus the resonance wavelength. This change can be measured accurately using the optical fibre; this fact is the basis for our sensor.

1.1.4 Modelling Sensor Performance

There has been some inconsistency between researchers with definitions of a sensor figure of merit. This primarily comes from the different methods of determining a sensor's sensitivity and detection accuracy, which depends on the type of instrument you're using and method of analysis.

For example, Perrotton and Sharma have defined signal to noise ratio as the change in resonance wavelength with respect to the full width half maximum $\mathrm{SNR} = \frac{\Delta\lambda_{\mathrm{res}}}{\Delta\mathrm{FWHM}}$ (A. K. Sharma and B. D. Gupta 2005; Sharma and Mohr 2008b; Perrotton *et al.* 2011b). They did not discuss a figure of merit. Sharma also mentions determining the signal to noise ratio by considering the shift in resonance wavelength relative to the spectral width at some reference output power value $\mathrm{SNR} = \frac{\Delta\lambda_{\mathrm{res}}}{\Delta\lambda_{\mathrm{SW}}}$ (Sharma and Mohr 2008a), where $\Delta\lambda_{\mathrm{SW}}$ is the spectral width of the response curve at this reference output power. If we are using the angular interrogation method, then the sensitivity and signal to noise ratio would be defined depending on the sensor type, for example sensitivity $\mathrm{Sn} = \frac{\Delta\theta_{\mathrm{res}}}{\Delta\mathrm{n}}$ where and θ_{res} is the resonance angle and n is the refractive index of the sensing layers, and $\mathrm{SNR} = \frac{\Delta\mathrm{R}}{\Delta\theta_{\mathrm{res}}}$ where R is the reflectivity (Sharma *et al.* 2007). Ciprian and Hlubina had an interesting method of determining the performance of their device, where sensitivity was measured as the shift in resonance wavelength vs the change in ethanol concentration present in their analyte region, $Sn = \frac{\Delta\lambda_{\mathrm{res}}}{\Delta\mathrm{C}}$ (Ciprian and Hlubina 2013b). They did not determine a signal to noise ratio. Instead they measured the detection accuracy; a measure of the spectral width of the resonance condition. $\mathrm{DA}_{10} = \frac{1}{\Delta\lambda_{10}}$, where $\Delta\lambda_{10}$

is the width of the resonance condition at output power: $P_{out} = 1.1 \times P_{min}$, where P_{min} is the output power at resonance. These two measurements clearly distinguished between the sensitivity of a sensor, and the actual width of the resonance condition. In addition, they provide a metric by which the resonance linewidth can be determined even if it does not fall below a previously specified number at resonance. Finally they combined the two parameters in the form of a figure if merit $\mathrm{FOM} = \frac{\Delta\lambda_{\mathrm{res}}}{\Delta C_{E_{th}} \Delta\lambda_{10}}$, which allowed for an overall performance metric of a series of devices to be determined. As this figure of merit allows one to determine the performance of a wide range of structures of varying resonance depths, we choose to employ this method of determining sensor performance.

The sensitivity (Sn) of a gas sensor is a measure of how much it's unique sensing property changes relative to a change in surrounding gaseous concentration. OFSPR sensors determine surrounding gaseous concentration by measuring differences in the spectral resonance. Sensitivity is defined as the shift in resonant wavelength $\Delta\lambda_{res}$ with respect to the overall change in surrounding gaseous hydrogen concentration ΔC_{H_2} (Sharma and Gupta 2004; A. K. Sharma and B. D. Gupta 2005; Sharma and Mohr 2008a; Perrotton *et al.* 2011b; Ciprian and Hlubina 2013b).

$$Sn = \frac{\Delta\lambda_{res}}{\Delta C_{H_2}} \qquad (1\text{-}27)$$

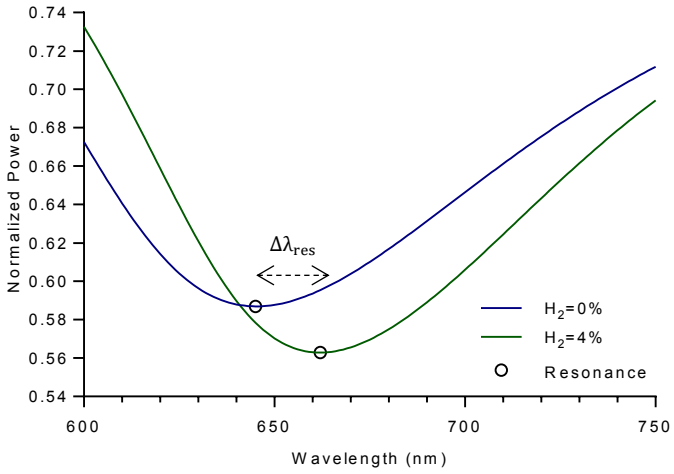

Figure 1-7 – Plot showing normalized output power across the spectral domain of a multilayer sandwich structure OFSPR sensor in the presence of 0 & 4% H_2. Image demonstrates the method of determining the sensor's sensitivity.

Fig. 1-7 displays the normalized output power for an OF structure. The blue curve represents a hydrogen free environment. In the presence of 4% hydrogen gas, the resonance curve shifts towards longer wavelengths as indicated by the green curve. The resonant wavelengths of both the hydrogen free and hydride environments are indicated below. The spectral difference between the resonance wavelengths of both curves is indicated as $\Delta\lambda_{res}$. The main observation to be made here is that the spectral location of the lowest point in Fig. 1-7 (resonance wavelength) undergoes a shift towards higher wavelengths in the presence of H_2. This spectral shift allows the sensor's sensitivity to be determined.

In order to maximise sensor sensitivity, the shift in the resonance wavelength $\Delta\lambda_{res}$ should be at a maximum relative to the change in surrounding hydrogen concentration ΔC_{H_2}. Another method of measuring sensor performance involves measuring the spectral width of the resonance condition generated upon H_2 exposure. Normally this spectral width is measured at the full width half maximum, (50%) normalized output power (Sharma and Gupta 2004; Perrotton *et al.* 2011b). However in some configurations, normalized output power does not drop this low at the resonance wavelength. Specifically, in our research, both s- and p- oscillations contribute to the output power, and since s- polarized radiation cannot stimulate a SPP, the resultant depth resonance condition observed in the output power spectrum will be reduced. In order to ensure we can accurately determine the resonance linewidth we measure the spectral difference between two points 10% above the minimum normalized output power on the hydrogen curve $\Delta\lambda_{10}$. (Sharma and Mohr 2008a; Ciprian and Hlubina 2013b). The inverse of this value is known as the sensors detection accuracy (DA). The two points $\lambda_{10\rightarrow}$ and $\lambda_{10\leftarrow}$ indicating the longer and shorter λ_{10} positions are shown in Fig. 1-8.

$$DA = \frac{1}{\Delta\lambda_{10}} \qquad (1\text{-}28)$$

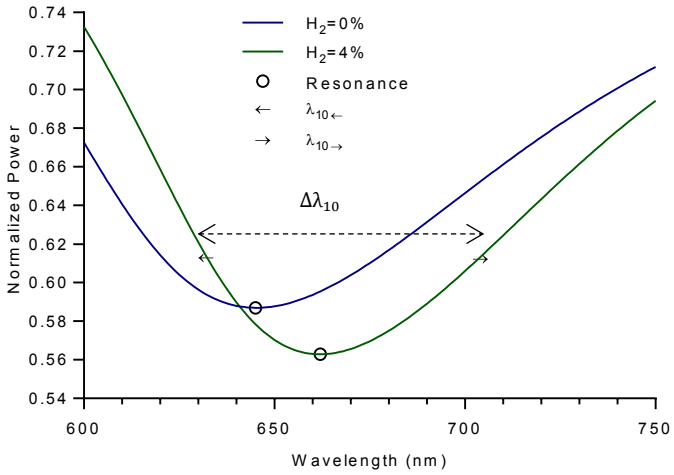

Figure 1-8 – Plot showing normalized output power / intensity across the spectral domain of a multilayer sandwich structure OFSPR sensor in the presence of 0 & 4% H_2. Image demonstrates the method of determining the sensor's detection accuracy.

Finally we employed a method of measuring figure of merit FOM which takes into account both sensitivity and detection accuracy measurements as determined using equations (1-27 & -28) respectively.

$$FOM = \frac{\Delta\lambda_{res}}{\Delta C_{H_2}\Delta\lambda_{10}} \qquad (1\text{-}29)$$

In this section, we gave an introduction into the discovery of surface plasmon resonance, and a brief history of optical fibre SPR based hydrogen sensing devices. We presented the core models that are used in determining the behaviour of light as it interacts with a structure consisting of multiple layer of different media relating to the Kretschmann configuration, as well as the optical fibre structure. These core models will be employed throughout this thesis.

1.2 Modelling the Interaction of Light with Matter

1.2.1 Metals

In this section, we investigate several materials for use in our sensing device, as well as detail the methods involved in modelling their respective optical properties. The dielectric permittivity describes how an electric field interacts with a medium. This quantify is a function of incident wavelength. Several different methods exist that model this behaviour. We begin by considering metallic materials that are relevant to our research. We then proceed to discuss various other materials that make up our optical fibre multilayer sensing configuration.

1.2.1.1 Drude model

The dielectric permittivity of a metallic compound is complex in nature "comprised of real ε'_m and imaginary components ε''_m", thus the dielectric permittivity can be described using equation (1-30).

$$\varepsilon_{m,\lambda} = \varepsilon'_m + i\varepsilon''_m \tag{1-30}$$

These dielectric properties have been studied and measured by many researchers over the years. The Drude model is a famous early approximation that describes the dielectric permittivity of various metals (Drude 1900b; Drude 1900a). This model solely employs contributions from harmonic oscillation of free electrons that make up the metallic structure, and can be determined using equation (1-31).

$$\varepsilon_{m,\lambda} = \varepsilon'_m + i\varepsilon''_m = 1 - \frac{\lambda^2 \lambda_c}{{\lambda_p}^2(\lambda_c + i\lambda)} \tag{1-31}$$

$$\lambda_p = \left(\frac{Ne^2}{4\pi^2 c^2 m\varepsilon_0}\right)^{-\frac{1}{2}} \tag{1-32}$$

$$\lambda_c = \frac{2\pi c R_{bulk}}{v_f} \tag{1-33}$$

λ_c denotes the collision wavelength. This accounts for the damping of electron density due to collisions between electrons. The plasma wavelength λ_p is defined by the frequency of the oscillations of electron density. R_{bulk} is the mean free path of the conduction electrons and v_f is the Fermi velocity (velocity of electrons at the Fermi energy). The equation format and input parameters for several metals are shown below in Table 1-2, which were taken from: (Sharma and Mohr 2008b; Sharma and Mohr 2008a; Sharma 2012).

Quantity	Ag	Au	Al	Cu
$\lambda_p\ (m)$	1.4541×10^{-7}	1.6826×10^{-7}	1.0657×10^{-7}	1.3617×10^{-7}
$\lambda_c\ (m)$	1.7614×10^{-5}	8.9342×10^{-6}	2.4511×10^{-5}	4.0852×10^{-5}

Table 1-2 – Table showing the plasma and collision wavelengths for the Drude model approximation of the complex dielectric permittivity of Ag, Au, Al, Au.

1.2.1.2 Lorentz-Drude Model

Five years after the publication of Drude's model, Hendrik Lorentz undertook research to improve this approximation by also considering the harmonic contributions from bound electronic within the metallic structure (Lorentz 1905). This model is described in equation (1-34).

$$\varepsilon_{\Omega} = 1 - \frac{{\omega_p}^2}{\omega^2 + i\omega\gamma_{fe}} + \chi_{\infty} + \sum \frac{S_{IB}{\omega_{IB}}^2}{({\omega_{IB}}^2 - \Omega^2 - i\Omega\gamma_{IB})} \quad (1\text{-}34)$$

Where S_{IB} is the harmonic oscillator (HO) strength, ω_{IB} is the frequency of HO, γ_{IB} is the damping constant of the, ω_p is the plasma frequency, and γ_{fe} is the damping constant of free electron contribution. The formatting of the equation was taken from (Quinten 2011).

1.2.1.3 Brendel-Bormann model

Many years later, Sommerfeld expanded upon this model further by combining it with Fermi Dirac statistics to give us the Drude-Sommerfeld model (Sommerfeld 1928), and since then many improvements have been made to the theory that give a more accurate representation of the dielectric permittivity of certain media. Kim *et al.* have demonstrated the broadening function that describes certain metals and their oxides is closer to the Gaussian lineshape than the Lorentzian (Kim *et al.* 1992). One such model that employs a Gaussian lineshape in determining the bound electron contributions to the dielectric permittivity of metallic substances is the Brendel-Bormann model (Brendel and Bormann 1992). Rakic *et al.* have determined the optical functions of numerous metallic substances using the Brendel-Bormann model (Rakic *et al.* 1998). Under this formulation, the dielectric permittivity ε can be understood as arising from the combined effects of free and bound electrons as follows:

$$\varepsilon_{m,\lambda} = \varepsilon_{f,\lambda} + \sum \varepsilon_{b,\lambda} \quad (1\text{-}35)$$

$$\varepsilon_{f,\lambda} = 1 - \frac{{\Omega_p}^2}{\Omega(\Omega - i\gamma_0)} \quad (1\text{-}36)$$

$$\Omega_p = \sqrt{f_0} w_p \quad (1\text{-}37)$$

$$\Omega = \frac{2\pi c}{\lambda} \tag{1-38}$$

$$\varepsilon_{b,\lambda} = \frac{i\sqrt{\pi} f {w_p}^2}{2\sqrt{2}a\sigma}\left[cef\left(\frac{a+w}{\sqrt{2}\sigma}\right) + cef\left(\frac{a-w}{\sqrt{2}\sigma}\right)\right] \tag{1-39}$$

$$a = \sqrt{\Omega^2 + i\Omega\gamma} \tag{1-40}$$

$$cef = e^{-z^2} erfc(-iz) \tag{1-41}$$

$$erfc(z) = \frac{2}{\sqrt{\pi}}\int_x^{+\infty} e^{-t^2} dt \tag{1-42}$$

Ω_p is the plasma frequency associated with intraband transitions, f_0 oscillator strength, w_p plasma frequency, $erfc(z)$ is the complementary error function. The parameters for Ag, Au and Pd for the Brendel-Bormann model are shown in Table 1-3, and were taken from (Rakic *et al.* 1998).

Quantity	Ag	Au	Pd
$\mathrm{w_p}(s^{-1}) = \frac{q}{\hbar} \times$	9.01	9.03	9.72
$\mathrm{f_0}\ (s) =$	0.821	0.77	0.33
$\gamma_0(s^{-1}) = \frac{q}{\hbar} \times$	0.049	0.5	0.009
$f =$	0.05 0.133 0.051 0.467 4	0.0540 0.0500 0.3120 0.7190 1.6480	0.7690 0.0930 0.3090 0.4090
$\gamma = \frac{q}{\hbar} \times$	0.189 0.067 0.019 0.117 0.052	0.0740 0.0350 0.0830 0.1250 0.1790	2.3430 0.4970 2.0220 0.1190
$w = \frac{q}{\hbar} \times$	2.025 5.185 4.343 9.809 18.56	0.2180 2.8850 4.0690 6.1370 27.9700	0.0660 0.5020 2.4320 5.9870
$\sigma\ (s^{-1}) = \frac{q}{\hbar} \times$	1.894 0.665 0.189 1.17 0.516	0.7420 0.3490 0.8300 1.2460 1.7950	0.6940 0.0270 1.1670 1.3310

Table 1-3 – Table showing the plasma and collision wavelengths for the Brendel-Bormann model approximation of the complex dielectric permittivity of Ag, Au, Pd.

In summary, Drude model provides a good first approximation of the optical function that describes metallic substances, by considering harmonic contributions made by free electrons. This approximation can be improved by including the additional Lorentz-Drude terms that

describe the influence of bound electrons within the metallic structure. Specifically, when modelling surface plasmon resonance, the Brendel-Bormann model improves on Lorentz-Drude representation, by employing a Gaussian lineshape in determining the bound electron contributions, which is a closer representation of the surface plasmon lineshape.

We determined the dielectric permittivity in Fig. 1-9 of a series of metals in order to observe any discrepancy between the between the Drude, and Brendel-Bormann representation of the optical functions.

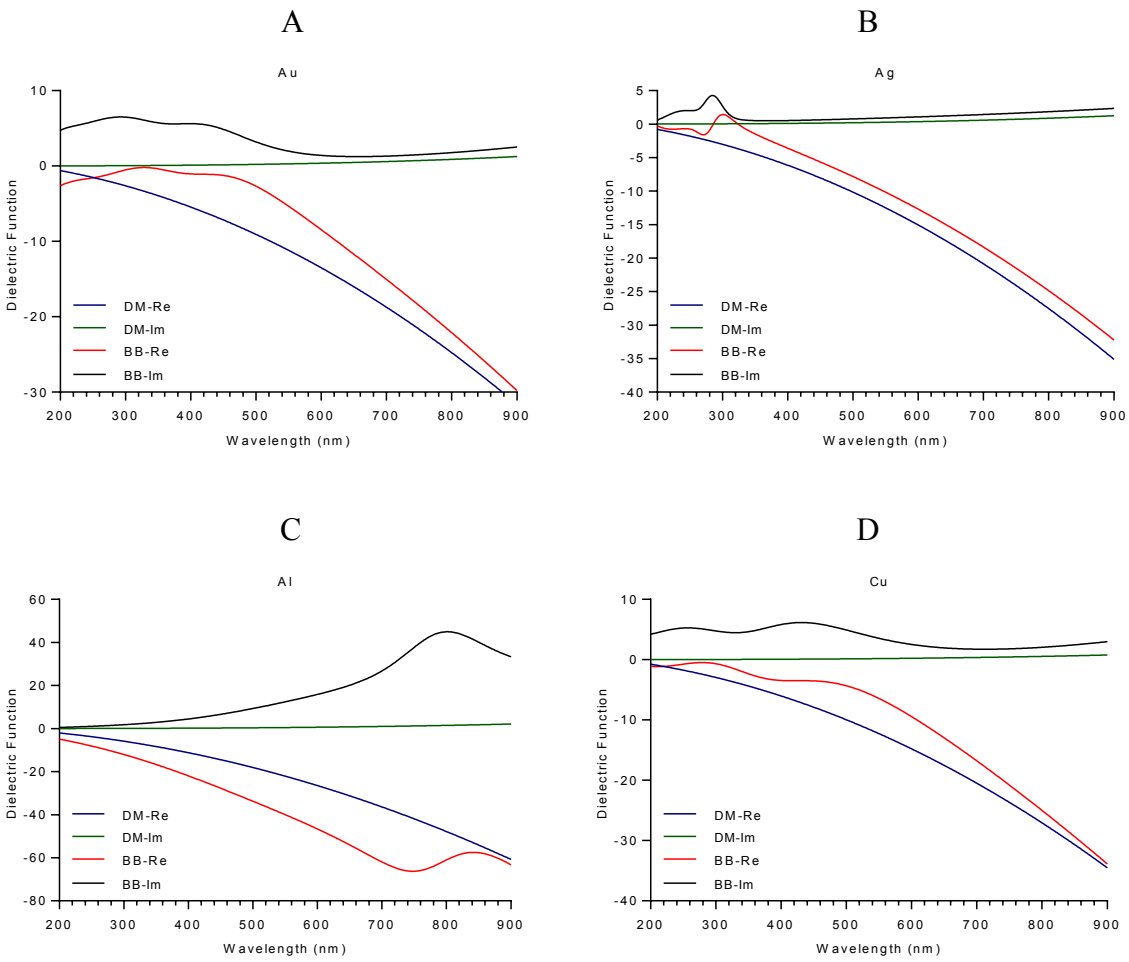

Figure 1-9 – Plot displays the variation of the real and imaginary components of the complex dielectric permittivity with incident wavelength using both the Drude model and the Brendel Bormann model for (a) Ag, (b) Au, (c) Al, (d) Cu.

In Fig. 1-9, each plot displays the variation in both the real and imaginary parts of the complex dielectric permittivity using the Drude model: DM_{Re}, DM_{Im}, and the Brendel-Bormann model: BB_{Re}, BB_{Im}, for different metals Ag, Au, Al, Cu. The dielectric permittivity of each metal follows the same general trend when modelled using the Drude or BB model. However, it can

be seen that the Brendel-Bormann representation model indicates harmonic oscillations caused by bound electrons that the Drude model does not. This can be seen in Fig. 1-9(A), for both the real and imaginary Ag permittivity models, at the lower end of the observed wavelength spectrum, and can be observed in Fig. 1-9(B, C, D) at various other wavelengths. Table 1-4 displays the dielectric permittivity for each metal when observed using a wavelength of 900nm. There exists a notable difference between the results generated by both models.

Dielectric Permittivity	Drude Model	Brendel-Bormann Model
ε_{Ag}	$-37.2088 + 1.9523\mathrm{i}$	$-32.2185 + 2.3528\mathrm{i}$
ε_{Au}	$-27.3229 + 2.8531\mathrm{i}$	$-29.7950 + 2.52139\mathrm{i}$
ε_{Al}	$-70.224 + 2.6152\mathrm{i}$	$-63.2569 + 33.3936\mathrm{i}$
ε_{Cu}	$-33.8815 + 2.9922\mathrm{i}$	$-42.6627 + 0.9619\mathrm{i}$

Table 1-4 – Table comparing the dielectric permittivity of Ag, Au, Al, Cu, as calculated using the Drude and Brendel-Bormann models.

subsequent modelling of the optical properties of metallic substances employs the Brendel-Bormann model (Brendel and Bormann 1992), and relevant parameters were taken from (Rakic *et al.* 1998).

1.2.1.4 Choice of Metal Layer

As stated previously, in order to stimulate resonance, a substance incorporating both a negative real component as well as a positive imaginary component to its complex dielectric permittivity is necessary. For this reason, metals are an ideal material from which to stimulate SPR. We have previously described the spectral behaviour of the dielectric permittivity of various metals. Next, we will investigate the influence that the choice of metallic substance has on the SPR resonance condition. Once we have determined a suitable metal that facilitates SPR, we can decide upon an optimal metallic thickness. In order to achieve this, we employ the Kretschmann configuration depicted in Fig. 1-10 (Kretschm.E and Raether 1968).

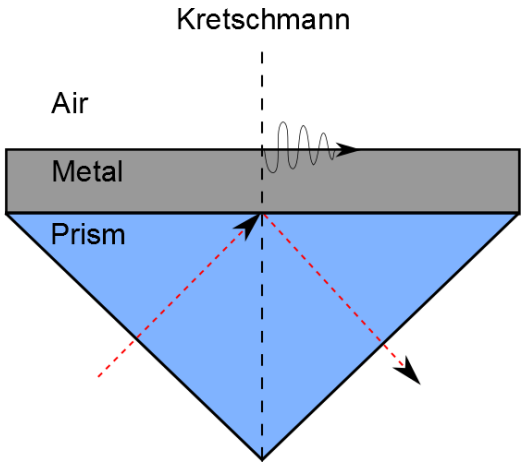

Figure 1-10 – Schematic representation of the Kretschmann configuration consisting of a dielectric prism coated with a metallic substance.

In Fig. 1-10, polychromatic p- polarized light enters a glass prism, and propagates towards a metallic film. At the glass-metal interface, most of the light undergoes total internal reflection, and propagates away from the metallic film through the glass prism, as illustrated by the direction of the red line in Fig. 1-10. Interestingly, at a specific angle of incidence, the wavevector of the incident p- polarized light matches that of a surface plasmon polarization. Consequently, some of the total incident radiation is absorbed by the surface electrons in the metal. This energy stimulates a surface plasmon, which proceeds to propagate along the boundary between the metal layer and the air with decreasing amplitude. The specific optical properties of the metallic film (metallic dielectric permittivity) are responsible for the SP resonance angle, resonance wavelength, penetration depth, wavevector, linewidth; and the dielectric permittivity of the metallic film is unique to each metallic material. These parameters can be used to define the performance of a SPR sensor.

For our research, in order to determine the most suitable metal to employ in our sensor, we need to take into account sensitivity, robustness, and detection accuracy. The ideal sensor should be both highly sensitive to analyte changes and produce a sharp SPR dip (high detection accuracy), but also ensure that it maintains these attributes during repeated operations, when exposed to a variety of external environmental influences. Common metals used to stimulate SPR include Au and Ag (Anuj K. Sharma and B. D. Gupta 2005; Lee and El-Sayed 2006; Chen and Jiang 2010; Gwon and Lee 2010; Choi *et al.* 2011; Oates *et al.* 2011; Ciprian and Hlubina

2013b; Perrotton *et al.* 2013). When considering the wavelength interrogation method, both Au and Ag permits the stimulation of resonance conditions, which undergo a spectral shift if the refractive index of the analyte region around the metallic film changes. It should be noted that the spectral shift of the resonance condition stimulated using Ag is of a larger magnitude than that using Au; under conditions of equal film thicknesses, and equal change in analyte index. Thus, the sensitivity of Ag is greater than Au for wavelength interrogation based SPR sensing applications (A. K. Sharma and B. D. Gupta 2005; Ciprian and Hlubina 2013b).

As we've seen, depending on the instrument and method of detection, sensitivity can also be defined as the shift in resonance angle relative to the change in the refractive index of the sensing layer (angular interrogation method). Using this measurement method, the angular location of a SPR condition generated by both Au & Ag undergoes a shift due to changes in the analyte refractive index. Contrary to the wavelength interrogation method, the resonance shift in of resonance condition stimulated using Au is greater than that of Ag, and consequently, Au has larger sensitivity than Ag (Chen and Jiang 2010). In our research, we employ an optical fibre configuration that uses polychromatic light for sensing applications. All incident rays are launched simultaneously along the fibre core; thus, the wavelength interrogation method is employed by, and a Ag based sensor operates with higher sensitivity than Au.

In terms of robustness, Au is a highly stable element (A. K. Sharma and B. D. Gupta 2005; Ciprian and Hlubina 2013b), and the robust nature of this metal makes it an ideal for SPR sensing applications in harsh environments. It is well known that Ag is highly susceptible to oxidation (Choi *et al.* 2011; Ciprian and Hlubina 2013b), therefore a Ag sensing layer undergoes rapid degradation during operation. Some researchers have suggested that Ag cannot be utilized for SPR due to its highly reactive nature (Gwon and Lee 2010), however this hazardous reaction can be mitigated by employing a protective overlayer coating, such as SiO_2 (Perrotton *et al.* 2013), on the Ag. In addition, SiO_2 has been shown to be highly permeable to H_2 (Fishbein *et al.* 1987; Mrstik *et al.* 1993), which is essential for a hydrogen sensing composite structure.

Finally, when considering the detection accuracy of the sensing device, it has been stated that Ag produces a much sharper SPR dip than Au, in both the angular and wavelength interrogation methods. (Chen and Jiang 2010; Choi *et al.* 2011). We investigate this by modelling the p-polarized reflectance from two structures containing different metallic films (Au & Ag) of

equal metallic thickness using the Kretschmann configuration and the angular interrogation method in Fig. 1-11.

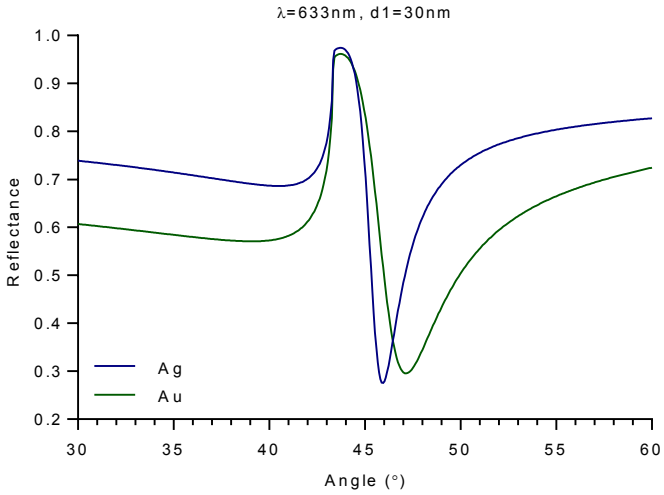

Figure 1-11 – Plot showing reflectance against incident angle of p- polarized radiation for an Au/Ag coated glass prism; (λ=633nm), (Au/Ag=30nm).

We observe in Fig. 1-11 that both metals stimulate SPR, however the linewidth of the resonance condition produced using Ag is sharper than Au. We investigated this concept in order to understand the influence that film thickness, has on each resonance condition. Thus, Fig. 1-12 (A & B) depict the reflectance from similar structures to Fig. 1-11, where the metallic film thicknesses have been increased to (40 & 50nm).

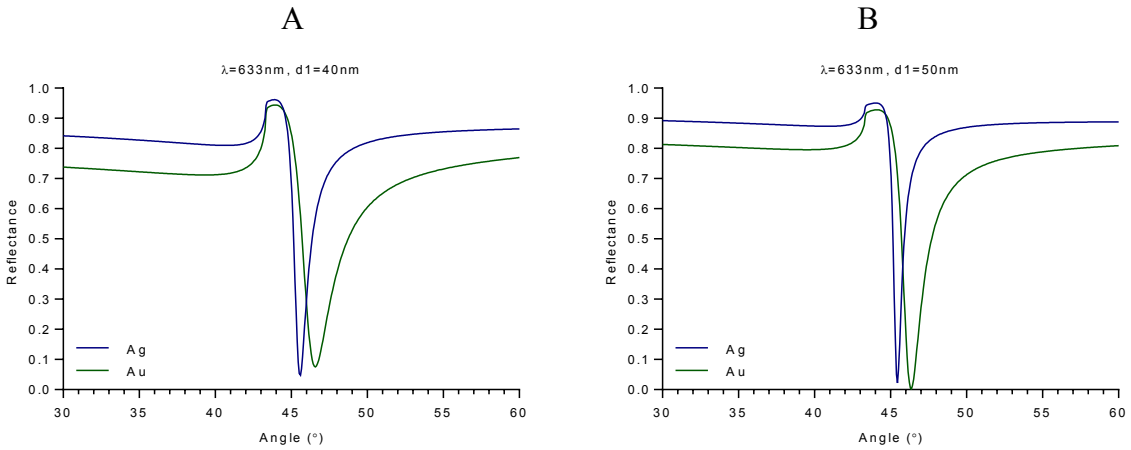

Figure 1-12 – (A) Plot showing reflectance against incident angle of p- polarized radiation for an Au/Ag coated glass prism; (λ=633nm), (Au/Ag=40nm). (B) (Au/Ag=50nm).

In Fig. 1-11 & 12, we observe that the width of the resonance conditions generated using Ag are consistently narrower than that produced by Au at the same thickness and incident wavelength. The reason that Ag produces a sharper SPR dip than Au can therefore de understood by considering the difference in the dielectric permittivity between the two metals. At a wavelength of 633nm, the dielectric permittivity of Au is -10.587 + 1.273i, and Ag is -14.469 + 1.194i, as calculated using the Brendel-Bormann model. As we can see, there is a difference in both the real and imaginary dielectric permittivity components between Au and Ag. In order to understand the influence that each permittivity component has on the SPR condition, we generated reflectance data from a number of artificial materials, where we controlled the individual components that make constitute the metallic dielectric permittivity. Fig. 1-13 demonstrates the influence that the imaginary component ε_{Im} of the metallic permittivity has on the resonance condition, where the real component was kept constant at the value determined for Ag at (λ=633nm).

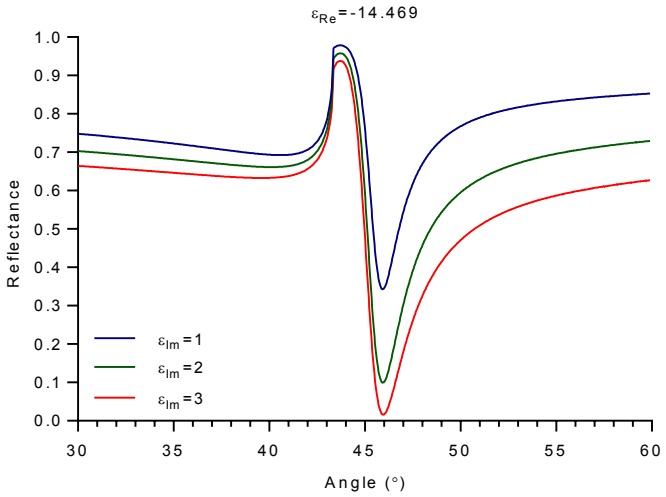

Figure 1-13 – Plot showing the influence that the imaginary component of the complex dielectric permittivity has on the SPR curve.

It can be seen that increasing the magnitude of the positive imaginary component results in a deeper resonance dip. both Au and Ag have similar imaginary components; $\varepsilon''_{Au} = 1.273$ and $\varepsilon''_{Ag} = 1.194$, and as we've seen in Fig. 1-11 & 12, the depths of the resonance conditions stimulated using Au and Ag are similar. Their respective optical functions differ most when considering the real components; $\varepsilon'_{Au} = -10.587$ and $\varepsilon'_{Ag} = -14.469$. Fig 14 demonstrates

the influence that the real component of the metallic dielectric permittivity on the resonance condition.

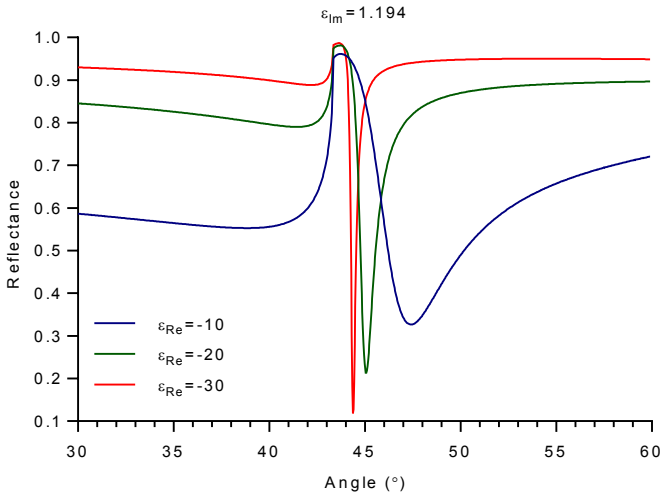

Figure 1-14 – Plot showing the influence that the real component of the complex dielectric permittivity has on the SPR curve.

It can be seen in Fig. 1-14, that the sharpness of the resonance dip depends strongly on the magnitude of the real component of the dielectric permittivity. This sheds light on the reason why Ag produces a sharper dip than Au at most observable wavelengths since the negative real component of the complex permittivity of Ag is of a larger magnitude than Au at the same wavelength.

In summary, Au may prove to be more stable as a component of our transducer layer, however in order ensure high sensitivity and detection accuracy in our optical fibre sensing configuration, we choose to employ Ag. In addition, the durability of Ag can be improved by employing a dielectric overlayer. Next, we investigate the influence that metallic thickness has on the resonance condition.

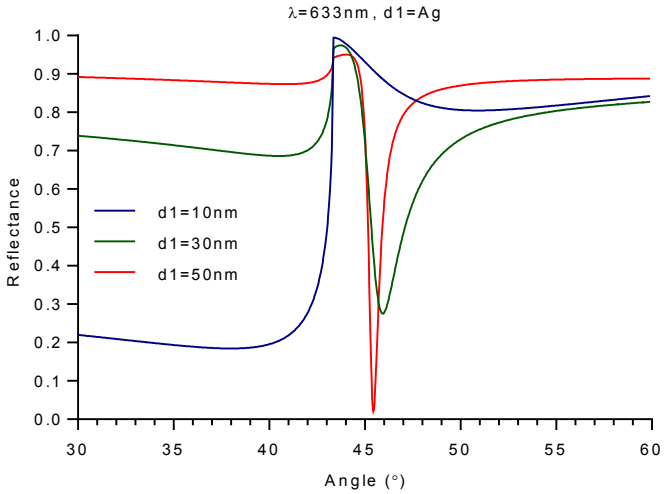

Figure 1-15 – Plot showing reflectance against incident angle for p- polarized radiation of a Ag coated glass prism; (λ=633nm), (Ag=10,30,50nm).

Fig. 1-15 demonstrates the influence that the thickness of the continuous metallic Ag film has on the resonance condition. There is a nonlinear relationship between the thickness of the Ag layer, and the magnitude of the change in reflectance at resonance as well as the minimum reflectance value. Ideally, the resonance dip should be as low as possible. This can be achieved when the two main forms of energy loss (internal Γ_i & radiative damping Γ_r) are equivalent (Raether 1986). We explain this relationship by considering the similarity between surface plasmon resonance and the Lorentzian model for a driven harmonic oscillator. If we consider a linear harmonic oscillator with a resonance frequency ω_{res} the response of this oscillator to a driving frequency ω_d can be described by a Lorentzian function:

$$I_\omega = \frac{\left(\frac{\Gamma}{2}\right)^2}{(\omega - \omega_{res})^2 + \left(\frac{\Gamma}{2}\right)^2} \qquad (1\text{-}43)$$

I_ω represents the normalized output power response of the oscillator to a driving frequency of ω, and Γ is the linewidth of the resonance dip. We can model reflectance of light R_ω by considering the inverse of the plot produced by a Lorentzian function:

$$R_\omega = 1 - \frac{\left(\frac{\Gamma}{2}\right)^2}{(\omega - \omega_{res})^2 + \left(\frac{\Gamma}{2}\right)^2} \quad (1\text{-}44)$$

There are two types of damping that occur during surface plasmon resonance, namely internal and radiative damping. Internal damping Γ_i is the name given to energy loss that occurs along the surface of the metal (Raether 1986). This form of energy loss is specific to the choice of film material and is difficult to adjust without modifying the shape of the continuous film.

$$\Gamma_i = k_{x''} = \frac{\omega}{c}\left(\frac{\varepsilon_m{}'\varepsilon_d}{\varepsilon_m' + \varepsilon_d}\right)^{\frac{3}{2}} \frac{\varepsilon_m''}{2(\varepsilon_m')^2} \quad (1\text{-}45)$$

Another method of damping occurs by the emission of EM radiation (radiative damping Γ_r). Radiative damping occurs when the SP re-radiates light back into the prism, arising from an overlap between the evanescent SP field, and the interface between the metal and the prism, and strongly depends of the thickness of the metal. The expression below describes the reflectance of a SP in terms of the surface plasmon propagation constant β_0, and the propagation constant as contributed by the prism β_R (Raether 1986):

$$R = 1 - \frac{4\beta_0''\beta_R''}{(k_x - \beta_{SP}')^2 + (\beta_0'' + \beta_R'')^2} \quad (1\text{-}46)$$

We can say that $\beta_0'' = \Gamma_i$ internal damping, and β_R'' = Γ_r radiative damping. Substituting both terms, we now have the following relationship (Raether 1986):

$$R = 1 - \frac{4\Gamma_i\Gamma_r}{(k_x - \beta_{SP}')^2 + (\Gamma_i + \Gamma_r)^2} \quad (1\text{-}47)$$

In order to minimize the reflectance condition, the following relationship must occur; $k_x - \beta_{SP}{}' = 0$, the wavevector the incident light ray matches the real part of the propagation constant of the surface plasmon. As a final point, we consider the minimum SPR dip $k_x = \beta_{SP}'$:

$$R_{min} = 1 - \frac{4\Gamma_i\Gamma_r}{(\Gamma_i + \Gamma_r)^2} \quad (1\text{-}48)$$

From equation (1-48) it is clear that $R_{min} = 0$ provided $\Gamma_i = \Gamma_r$. This insight is very important. We know that the magnitude of the radiative damping Γ_r depends on the thickness of the metal

layer; therefore, by carefully choosing the thickness of the metal such that $\Gamma_i \approx \Gamma_r$; we can achieve near maximum absorbance of incident radiation by the SP.

Although this low dip is desirable, what's more important is the sensitivity, detection accuracy of the sensor, and the response time of our sensor. Therefore, these are the factors on which we focus on during the optimisation process. It is clear that the metallic layer is the key driver of the resonance. By measuring sensor performance for several different thicknesses of Ag, we can determine the optimal thickness for our sensor.

1.2.2 Dielectrics

We mentioned previously that a dielectric overlayer can be used to improve the durability of the metallic film component. More importantly, the dielectric overlayer is employed in order to modulate the SPR angle. Fig. 1-16(A) shows a schematic representation the previously described Kretschmann configuration consisting of a Ag film deposited onto a silica prism. Fig. 1-16(B) illustrates the inclusion of a SiO_2 dielectric overlayer.

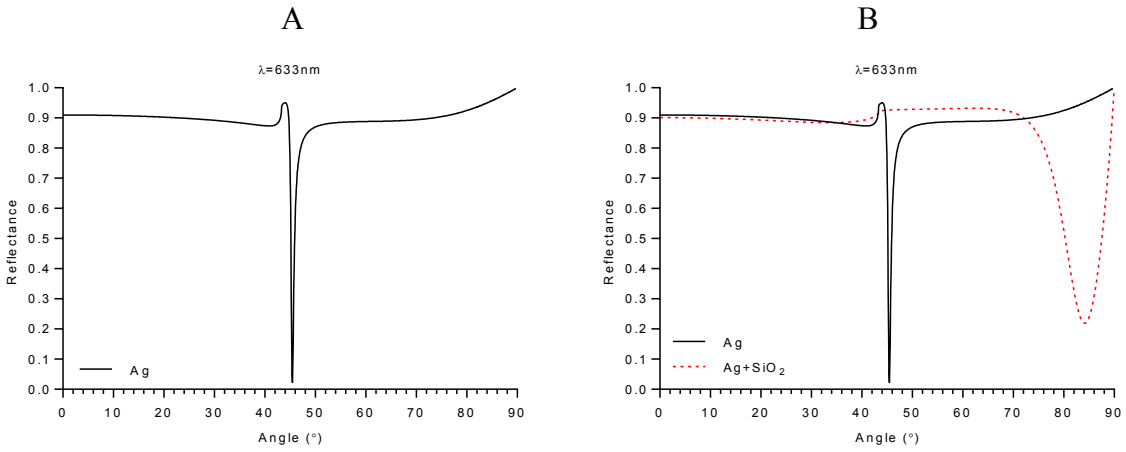

Figure 1-16 – (A) Plot showing reflectance against incident angle for p- polarized radiation of a Ag coated glass prism; (λ=633nm), (d1=50nm). (B) Inclusion of a SiO_2 dielectric overlayer (d2=120nm).

In Fig. 1-16(A), while it is clear that surface plasmon resonance is permitted, resonance occurs at (θ_R=45.46˚). Using a silica based optical fibre, with a numerical aperture of 0.22, operating in the visible range according to equations (1-22 & -23), the critical angle will be ($\theta_C \approx$81.5˚). Thus, by including a dielectric material such as SiO_2 of (d2=120nm) onto the surface of the Ag film, it can be seen in Fig. 1-16(B) that the resonance angle shifts to (θ_R=84.17˚), which is

greater than the optical fibre critical angle. Therefore, this configuration permits the stimulation of surface plasmon resonance using an optical fibre configuration.

A very useful method of modelling the refractive index of a dielectric material was derived by Wilhelm Sellmeier (Sellmeier 1871).

$$n_\lambda{}^2 = 1 + \frac{a_1\lambda^2}{\lambda^2 - b_1} + \frac{a_2\lambda^2}{\lambda^2 - b_2} + \cdots + \frac{a_i\lambda^2}{\lambda^2 - b_i} \quad (1\text{-}49)$$

n_λ is the refractive index of the dielectric material observed with light of wavelength λ. a_i and b_i are experimentally determined coefficients and differ for each dielectric material. Over time several different values have been calculated relating to the constants a_i and b_i in the dispersion formula in order to model the spectral dependant refractive index of various dielectric materials. When modelling the Otto and Kretschmann configurations, their set-up included a glass prism. The refractive index of this dielectric material can be described by the following Sellmeier dispersion relationship for Schott BK7 glass:

$$n_{BK7} = \sqrt{1 + \frac{a_1\lambda^2}{\lambda^2 - b_1} + \frac{a_2\lambda^2}{\lambda^2 - b_2} + \frac{a_3\lambda^2}{\lambda^2 - b_2}} \quad (1\text{-}50)$$

$a_1 = 1.03961212$, $a_2 = 0.231792344$, $a_3 = 1.0146945$, $b_1 = 6.0006987 \times 10^{-3} m^2$, $b_2 = 2.00179144 \times 10^{-2} m^2$, $b_3 = 1.013560653 \times 10^{2} m^2$, λ in μm (PM-Optics 2014; Refractiveindex.info 2015).

An OF structure typical contains a core made of silica, which has been heated thereby altering its crystal lattice structure. Since there are various different methods of manufacturing this fused silica material, varying in reaction temperature, oxidation time and cycles etc.; it is safe to assume that there are several different calculated constants relating to the Sellmeier Dispersion equation for fused silica. Thus, we investigated several of these formulae by comparing their refractive indices in order to determine the most suitable for our fibre core.

$$n_{SiO_2-M-1965} = \sqrt{1 + \frac{a_1\lambda^2}{\lambda^2 - b_1} + \frac{a_2\lambda^2}{\lambda^2 - b_2} + \frac{a_3\lambda^2}{\lambda^2 - b_2}} \quad (1\text{-}51)$$

$a_1 = 0.6961663$, $a_2 = 0.4079426$, $a_3 = 0.8974794$, $b_1 = 0.0684043m^2$, $b_2 = 0.1162414m^2$, $b_3 = 9.896161m^2$, λ in μm (Malitson 1965; Kitamura *et al.* 2007; Chen *et al.* 2011; Sharma 2012; Ciprian and Hlubina 2013b):

$$n_{SiO_2-GT-1998} = \sqrt{1 + \frac{A_1\lambda^2}{\lambda^2 - {B_1}^2} + \frac{A_2\lambda^2}{\lambda^2 - {B_2}^2} + \frac{A_3\lambda^2}{\lambda^2 - {B_3}^2}} \quad (1\text{-}52)$$

$A_1 = 0.6961663$, $A_2 = 0.4079426$, $A_3 = 0.8974794$, $B_1 = 0.004679148m$, $B_2 = 0.01351206m$, $B_3 = 97.93400m$, λ in μm (Ghatak and Thyagarajan 1998; Sharma *et al.* 2007; Sharma and Mohr 2008b).

$$n_{SiO_2-Schott-2011} = P_1 + P_2\lambda^2 + P_3\lambda^{-2} + P_4\lambda^{-4} + P_5\lambda^{-6} + P_6\lambda^{-8} \quad (1\text{-}53)$$

$P_1 = 1.4579$, $P_2 = -0.00365\mathrm{m}^{-2}$, $P_3 = -0.00243\mathrm{m}^2$, $= 0.00012\mathrm{m}^4$, $P_5 = -4.606 \times 10^{-6}\mathrm{m}^6$, $P_6 = 9.635 \times 10^{-8}\mathrm{m}^8$, λ in μm (Perrotton *et al.* 2011b; Perrotton *et al.* 2011c; Perrotton *et al.* 2013), which they use stating it is the Schott industry standard coefficient.

$$n_{SiO_2-P-1981} = c_0 + c_1\lambda^2 + c_2\lambda^4 + \frac{c_3}{\lambda^2 - l} + \frac{c_4}{(\lambda^2 - l)^2} + \frac{c_5}{(\lambda^2 - l)^3} \quad (1\text{-}54)$$

$c_0 = 1.4508554$, $c_1 = -0.0031268\mathrm{m}^{-2}$, $c_2 = -0.0000381\mathrm{m}^{-4}$, $c_3 = 0.0030270\mathrm{m}^2$, $c_4 = -0.0000779\mathrm{m}^4$, $c_5 = 0.0000018\mathrm{m}^6$, $l = 0.035m^2$, λ in μm (Paek *et al.* 1981; A. K. Sharma and B. D. Gupta 2005).

Since several methods of modelling the refractive index of fused silica exist, we must choose the method that is most appropriate to our model. Furthermore, the process for adding SiO_2 to our multilayer OF structure is slightly different; a layer of silicon is added to the sensing structure, after which it is exposed to a fixed quantity of oxygen "in an oven". This forms SiO_2 on the surface of the OF. Thus, the lattice structure of this thin film SiO_2 layer differs than that of the fused silica, and subsequently, the refractive indices will also differ. The following model describes the optical function of thin film silica, which was prepared by thermal decomposition from tetraethylorthosilicate (Postava and Yamaguchi 2001; Ciprian and Hlubina 2013b).

$$n_{SiO_2-PY-2001}{}^2 = 1 + \frac{A\lambda^2}{\lambda^2 - B^2} \quad (1\text{-}55)$$

$A = 1.1336$, $B = 9.261 \times 10^{-2} m^2$, λ in μm.

Plastic has made more of an appearance as a substitute for SiO_2 in fibre optic components (Cennamo *et al.* 2011; Al-Qazwini *et al.* 2015). PMMA (Polymethylmethacrylate) is the most common plastic employed as it demonstrates the best transparency of commercially available plastics (Languy *et al.* 2011; Bodurov *et al.* 2013). It has very good flexibility ie. it can withstand a smaller bend radii than most types of silica (Cennamo *et al.* 2015). Looking at two Sellmeier Dispersion type models in particular, One such model for PMMA comes from Ishigure et al. (Ishigure *et al.* 1996a; Ishigure *et al.* 1996b).

$$n_{PMMA-I-1996}{}^2 - 1 = \sum_{i=1}^{3} \frac{A_i \lambda^2}{\lambda^2 - l_i{}^2} \quad (1\text{-}56)$$

$A_1 = 0.4963$, $A_2 = 0.6965$, $A_3 = 0.3223$, $l_1 = 71.80$, $l_2 = 117.4$, $l_3 = 9237$.

A similar such model is employed by Languy et al.(Languy *et al.* 2011).

$$n_{PMMA-L-2011}{}^2 - 1 = \sum_{i=1}^{3} \frac{B_i \lambda^2}{\lambda^2 - C_i} \quad (1\text{-}57)$$

$B_1 = 4.841120 \times 10^{-1}$, $B_2 = 6.815579 \times 10^{-1}$, $B_3 = 1.028035 \times 10^{-2}$, $C_1 = 3.353637 \times 10^{-4}$, $C_2 = 1.096254 \times 10^{-2}$, $C_3 = 1.184708 \times 10^{-2}$.

In comparing the two, both seem quite feasibly in modelling the refractive index of PMMA. Similarly to SiO_2 above, the differences in the methods of fabrication is the most likely cause for the small discrepancy in the refractive indices of each pure-PMMA model.

We modelled each of the above equations that describe the refractive index of several dielectric material, in order to make a more accurate decision on which models would be included in our optical fibre structure.

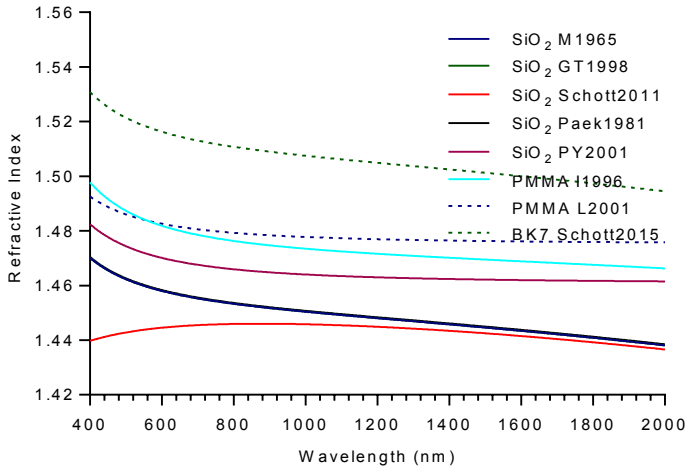

Figure 1-17 – Plot showing the spectral influence that incident wavelength has on refractive index of various dielectric material investigated for use in our optical fibre structure.

Fig. 1-17 demonstrates the refractive indices of several dielectric materials that were considered for our sensor. These include different types of silica, plastic, and glass. Firstly, it is clear that the refractive index of the BK7 glass material is larger than that of the other materials across the spectrum. Since this material has been widely employed by various researchers using Kretschmann based configuration, we adopted this model when employing a glass prism.

Next, looking at the various methods of modelling different types of silica, it can be seen that the refractive index of the thin film silica layer is larger across the observed wavelength spectrum than that of the fused silica typically used an a fibre core component. In terms of the fused silica core, we observe that each of the 4 remaining models follow the same general trend, "decreasing refractive index with increasing wavelength", except for the model from Schott glass which was employed by Perrotton *et al.* The model used by Paek *et al.* produces a slightly lower refractive index than that by Malitson, or Ghatak and Thyagarajan. Both of these models are almost identical.

Finally, while the refractive index of PMMA according to both of the models is slightly larger than SiO_2, there is little difference in both the magnitude of refractive index difference, as well as the behaviour of the optical function across the observed wavelength spectrum. Therefore, little difference is expected in the output between a silica and a PMMA based fibre core. While PMMA has its advantages, plastic typically has more attenuation than silica, thus making good

for short distance applications, however a hydrogen sensing optical fibre device is to be expected to operate in hazardous conditions, and thus remote deployment is a very good advantage. For this reason, silica is a more suitble choice for our sensor, and thus we employed a fibre core.

In light of these findings, we choose to employ Postava and Yamaguchi's model for in determining the optical function of thin film silica, and the old tried and tested "Malistons model" for the fused silica core.

In this section, we have investigated the various methods involving the metallic and dielectric materials that make up our optical fibre sensing structure. In doing this we were able to decide on the most suitable materials, as well as the most appropriate method of modelling the wavelength dependent optical function of each material.

1.2.3 Hydrogen Sensitive Layer

As a final component in our multilayer sensing strucutre, we include a material whose optical function changes with the surrounding hydrogen concentration, thus providing hydrogen sensing functionality. As stated previously, two materials frequently appear across the literature (Pd & Pt-WO_3) due to their miriad of successful applications in hydrogen sensing devices (Lewis 1967; Shaver 1967; Huebert *et al.* 2011; Dai *et al.* 2017; Zhang *et al.* 2017).

The refractive index of WO_3 changes in the presence of hydrogen gas. However, WO_3 is not selective to hydrogen gas, and is also sensitive to other molecules of hydrogen such as C_2H_2 and H_2S. To eliminate this problem, WO_3 is commonly doped with another metallic material with the purpose of lowering the reaction activation energy by dissociating the hydrogen molecules into its atomic form (Shanak *et al.* 2004; X.G. Wang *et al.* 2013a). The resultant material has potential to be highly sensitive and selective to hydrogen, however can fail in application if there is little oxygen present in the ambient atmosphere. Furthermore, the process by which WO_3 reacts with hydrogen is highly exothermic (Zhang *et al.* 2017), which greatly increases the risk of igniting surrounding hydrogen gas. Therefore, the application range of this material is highly restricted. On the other hand, Pd demonstrates excellent application to hydrogen sensing in the absence of electrical components at the point of detection, and the highly-reduced temperature of reaction as compared to WO_3. Pd reacts with gaseous hydrogen forming PdH_x resulting in a nonlinear reduction in both the real and imaginary Pd dielectric

permittivity, where x represents the atomic ratio of hydrogen to palladium. The dielectric permittivity undergoes further decrease with increasing hydrogen concentration.

1.2.4 Pure Palladium

We investigated several different methods of modelling the dielectric permittivity of pure palladium. In the process of our search we found that one source in the literature differed substantially from others (Bevenot *et al.* 2002). In order to understand this discrepancy, we begin by calculating the dielectric permittivity of Pd using the Brendel-Bormann model described previously. As an illustrative example, we will now consider the permittivity that this model predicts at a wavelength of 670nm. At this wavelength, the Brendel-Bormann model predicts a permittivity of approximately -15.56 + i16.61. On the other hand, Bevenot's widely referenced set of experimental data quotes a permittivity of -7.64 + i8.45 at the same wavelength (Bevenot *et al.* 2002), which they determined using ellipsometry measurements of a 12nm thick Pd film.

It is clear that both models differ to a large degree. We looked into another experimental study that aimed to determine the optical function of Pd (von Rottkay *et al.* 1999), which used a 10nm thick Pd film. Next, using von Rottkay's dataset, we fit a 6th order polynomial independently to both the real and imaginary contributions to the Pd dielectric permittivity, and obtained the following equations:

$$\varepsilon_{Pd,VR} = \varepsilon'_{Pd,VR} + \varepsilon''_{Pd,VR} \tag{1-58}$$

$$\varepsilon'_{Pd,VR} = \lambda^6 a_1 + \lambda^5 a_2 + \lambda^4 a_3 + \lambda^3 a_4 + \lambda^2 a_5 + \lambda^1 a_6 + c_{h1} \tag{1-59}$$

$$\varepsilon''_{Pd,VR} = \lambda^6 b_1 + \lambda^5 b_2 + \lambda^4 b_3 + \lambda^3 b_4 + \lambda^2 b_5 + \lambda^1 b_6 + c_{h2} \tag{1-60}$$

Quantity	$\varepsilon'_{Pd,\lambda,VR}$	Quantity	$\varepsilon''_{Pd,\lambda,VR}$
a_1	1.670×10^{-18}	b_1	-2.250×10^{-18}
a_2	-1.097×10^{-14}	b_2	1.276×10^{-14}
a_3	2.700×10^{-11}	b_3	-2.073×10^{-11}
a_4	-3.336×10^{-8}	b_4	-7.240×10^{-9}
a_5	1.325×10^{-5}	b_5	4.921×10^{-5}
a_6	-3.180×10^{-2}	b_6	-2.700×10^{-3}
c_{h1}	5.511	c_{h2}	1.818

Table 1-5 – Table of parameters for a 6th order polynomial function to calculate the real and imaginary components of the complex dielectric permittivity of Pd based on von Rottkay's experimental data.

This allowed us to determine the dielectric permittivity of Pd at 670nm, according to von Rottkay's experimental measurements: -15.77 + i17.27. It is clear that this result is much closer to the Brendel-Bormann model than to Bevenot's measurement. Fig. 1-18 graphically illustrates the close similarity between von Rottkay's experimental results and our theoretical calculation of the complex dielectric permittivity of Pd across a wide wavelength range.

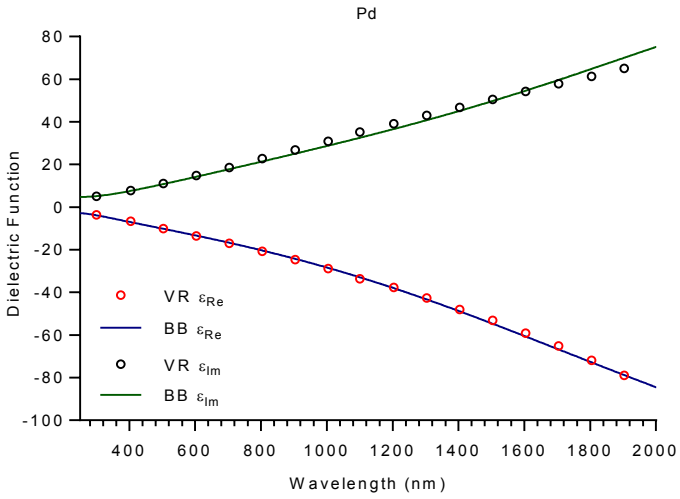

Figure 1-18 – Plot comparing von Rottkay's experimental data directly against our BB model which describes the spectral variation of the real and imaginary components of the dielectric permittivity of Pd.

Another point worth noting is that the multilayer structure of our proposed sensor is similar to that constructed by Perrotton, who employed von Rottkay's experimental results and successfully obtained good agreement between theoretical prediction and experimental results (Perrotton *et al.* 2013). In addition, many others have demonstrated positive results using von Rottkay's data (Vargas *et al.* 2006; Perrotton *et al.* 2011b; Perrotton *et al.* 2011c; Perrotton *et al.* 2013; X.G. Wang *et al.* 2013a).

As a final remark, it is known that the optical properties of Pd depend strongly on the preparation method of the Pd sample (Rakic *et al.* 1998). This could be a contributing factor to the discrepancy between Bevenot's and von Rottkay's results. As a result of this we continued to employ the Brendel Bormann model that closely matches the experimental results from von Rottkay.

1.2.5 Palladium in the Presence of Hydrogen Gas

Bevenot made a first approximation to describe the variation in the dielectric permittivity of Pd in the presence of hydrogen (Bevenot *et al.* 2002):

$$\varepsilon_{PdH,c\%H_2} = h(c\%) \times \varepsilon_{Pd,0\%H_2} \tag{1-61}$$

The value h is a scalar multiple that relates the dielectric permittivity of pure Pd to the dielectric permittivity of Pd in the presence of $c\%$ H_2 gas. This formula has been widely referenced by other researchers (Tobiška *et al.* 2001; Perrotton *et al.* 2011b; Y. Liu *et al.* 2012c; Silva *et al.* 2012). However, looking at von Rottkay's experimental data shown below in Fig. 1-19, we can see that the real and imaginary parts of the dielectric permittivity of Pd and PdH do not in fact vary to the same degree upon hydrogenation.

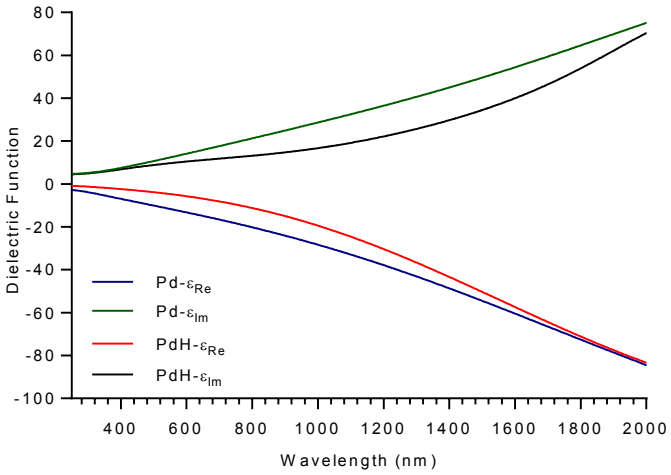

Figure 1-19 – Plot describing the spectral dependence of the dielectric permittivity of Pd and PdH according to our fitting functions derived from von Rottkay's experimental data.

It can be seen that hydrogenation causes the real component of the negative dielectric permittivity to decrease in magnitude across the observed wavelength range. Similarly, absorbing hydrogen causes the positive imaginary component to decrease in magnitude. It is clear that two independent "h-functions" are necessary in order to accurately describe the influence that hydrogen has on Pd permittivity. Perrotton *et al*. realised this fact and introduced the following equation (1-62) containing two such h factors (Perrotton *et al.* 2011c):

$$\varepsilon_{PdH} = h1_{PdH}\varepsilon'_{Pd} + h2_{PdH}\varepsilon''_{Pd} \qquad (1\text{-}62)$$

This describes the relationship between the dielectric permittivity of pure palladium, and palladium in the presence of surrounding hydrogen gas. $h1$ & $h2$ are factors by which the real and imaginary components of the complex permittivity of palladium shift in the presence of hydrogen. In general, these h factors are smooth real functions whose values depend on the wavelength of incident radiation.

To proceed, we require that the spectral relationship of these h-functions be determined within our sensor's operational wavelength range. For the purpose of this work, we will now show how we generated the h-functions for a hydrogen concentration of 4%. We chose this concentration firstly because Perrotton has shown that von Rottkay's data closely agrees with the permittivity behaviour of hydrogen at 4% (Perrotton *et al.* 2011c). Secondly, it is common in the literature (Zhao *et al.* 2006b; Perrotton *et al.* 2011b; Perrotton *et al.* 2011c; Y. Liu *et al.* 2012a) to consider the response of a hydrogen sensor to 4% hydrogen as this represents the

lower explosive limit for hydrogen, Finally, working at a hydrogen concentration of 4% means we are aligned with other workers in the field and will allow us to directly compare our sensor performance with other published results (Perrotton *et al.* 2011b). The functions describing $h1$ and $h2$ have not been published by Perrotton therefore we will now show how we generated them using von Rottkay's data as a starting point. Once again we made a 6th order polynomial fit to von Rottkay's dataset in order to calculate how the spectral dependence of each h function at a given wavelength. We obtained the following relationship:

$$\varepsilon_{PdH} = h1_{PdH}\varepsilon'_{Pd} + h2_{PdH}\varepsilon''_{Pd}$$

$$h1_{PdH,VR} = \lambda^6 a_1 + \lambda^5 a_2 + \lambda^4 a_3 + \lambda^3 a_4 + \lambda^2 a_5 + \lambda^1 a_6 + c_{h1} \quad (1\text{-}63)$$

$$h2_{PdH,VR} = \lambda^6 b_1 + \lambda^5 b_2 + \lambda^4 b_3 + \lambda^3 b_4 + \lambda^2 b_5 + \lambda^1 b_6 + c_{h2} \quad (1\text{-}64)$$

Quantity	$h1_{PdH,VR}$	Quantity	$h2_{PdH,VR}$
a_1	-4.678×10^{-20}	b_1	-7.466×10^{-19}
a_2	2.839×10^{-16}	b_2	5.633×10^{-15}
a_3	-4.547×10^{-13}	b_3	-1.695×10^{-11}
a_4	-4.351×10^{-10}	b_4	2.557×10^{-8}
a_5	1.695×10^{-6}	b_5	-1.940×10^{-5}
a_6	-7.733×10^{-4}	b_6	6.192×10^{-3}
c_{h1}	0.417	c_{h2}	0.280

Table 1-6 – Table of parameters for a 6th order polynomial function to calculate the h1 and h2 values corresponding to the real and imaginary components of the complex dielectric permittivity of PdH based on von Rottkay's experimental data.

Fig. 1-20 demonstrates the influence that hydrogen has on the real and imaginary components of the Pd optical function, where 1 represents no change, and each y value reduces the dielectric permittivity of either the real (black line) and imaginary (blue line) by the factor illustrated.

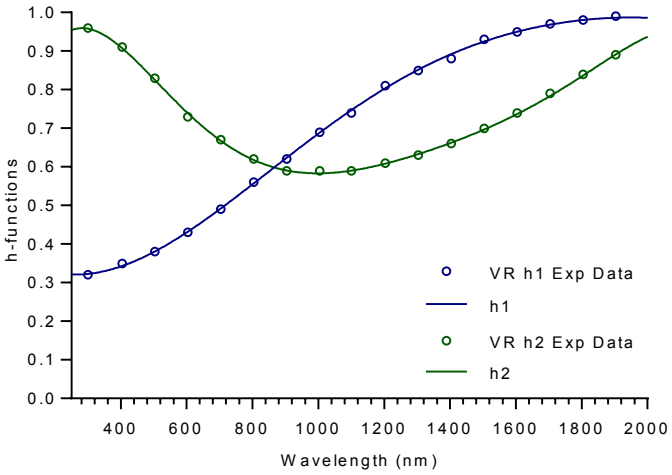

Figure 1-20 – Plot displaying experimental data compiled by von Rottkay of the h1 and h2 values needed to scale the real and imaginary components of Pd dielectric permittivity in the presence of H_2 alongside our 6th order polynomial function that models this relationship.

Below Fig. 1-21 displays the experimental data compiled by von Rottkay along with our fitted polynomial function. Using this model, we were able input the spectrally dependant dielectric permittivity of Pd in the presence of 4% H_2 into our model.

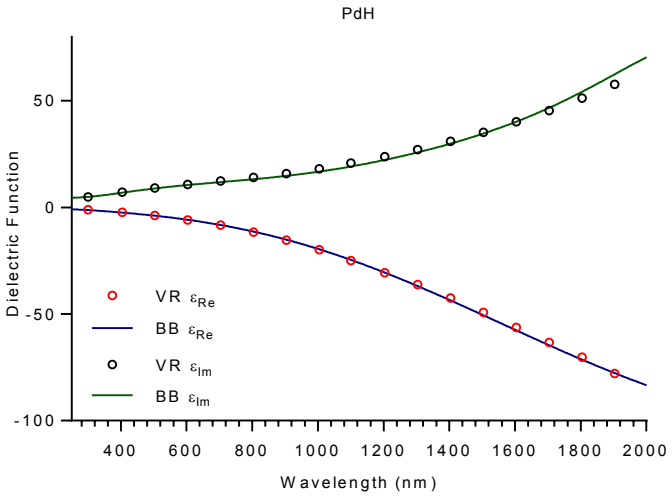

Figure 1-21 – Plot displaying the variation of the real and imaginary components of the complex dielectric permittivity of PdH with incident wavelength.

In conclusion the results generated by von Rottkay that describes the variation in the dielectric permittivity of Pd in terms of $h1$ and $h2$ functions is a more accurate representation than

Bevenot's description of a single h value that relates the real and imaginary permittivity components. We thus employed von Rottkay's model to describe the variation in the dielectric permittivity of Pd in the presence of hydrogen. Armed with the h-functions, we can now accurately predict the permittivity of Pd when exposed to 4% hydrogen at any desired wavelength.

1.3 Validating the Model Section

In previous sections we presented various steps and methods we employed in modelling the interaction of light with our optical fibre structure. This included investigating various materials and methods of modelling their respective optical functions, in order to determine the most suitable for our configuration. In addition to this, we tested our model by replicating a series of results that have been published by other researchers, in order to ensure our model was working accurately. Some of these replications are presented here.

1.3.1 Otto configuration, TM polarized radiation

In order to verify that our transfer matrix model was producing accurate results, we began by modelling the Otto configuration. Fig. 1-22 shows the reflectance of p- polarised radiation from thick Au & Ag films, and how it appears in the literature (Sambles *et al.* 1991).

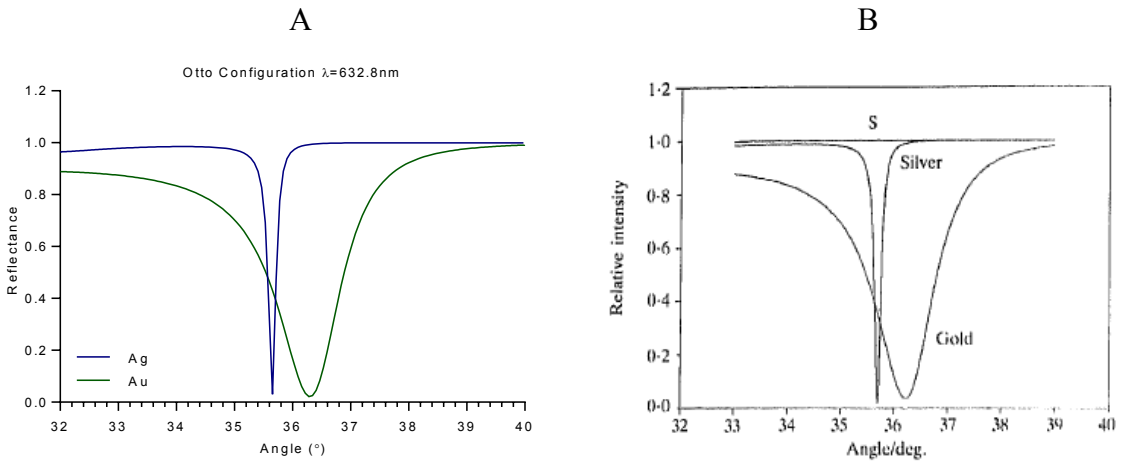

Figure 1-22 – (A) Plot showing reflectance against incident angle of the Otto configurations for Ag and Au layered on a sapphire prism of refractive index (n=1.766), (λ=632.8nm), coupling gap for Ag is (1μm), and (500nm) for Au. (B) As it appears in the literature.

Our model demonstrates near identical results to the computational results published by Sambles (Sambles *et al.* 1991).

1.3.2 Kretschmann configuration, TM, TE polarized radiation, Hydrogen Sensing

Following this, we extended our model such that the metallic layer would cover the prism structure in place of the coupling gap, commonly referred to as the Kretschmann configuration. (Kretschm.E and Raether 1968). Perrotton *et al.* published the results of a computational model consisting of a single palladium layer 12nm thick coated onto the surface of a glass prism (Perrotton *et al.* 2011c). The reflectance of monochromatic light of wavelength 468nm is measured across various angles of input. In order to validate our model, we attempted to replicate these results. Fig. 1-23 shows Perrotton's results for both s- & p- polarized light; in the presence of hydrogen and in a hydrogen free environment (Perrotton *et al.* 2011c). This data set also includes reflectance values from TE radiation, the modelling of which becomes essential when extending the program to optical fibre sensing applications. In the publication, the dielectric permittivity of palladium and palladium hydride was calculated using von Rottkay's experimental data (von Rottkay *et al.* 1999). We used the same parameters to generate the following plot of reflectance against incident light angle (Perrotton *et al.* 2011c).

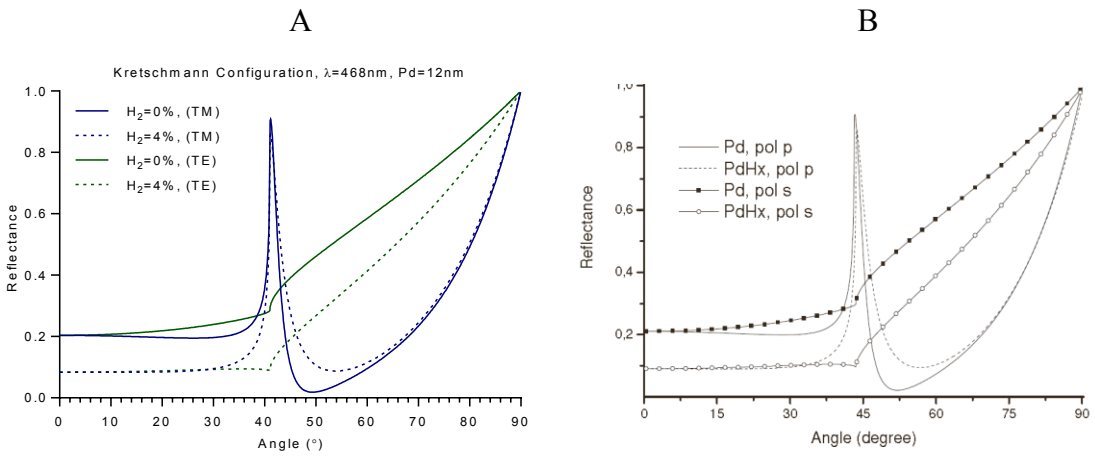

Figure 1-23 – (A) Plot showing reflectance against incident angle for both s and p polarized radiation, in the presence of 0 and 4% H_2 for Pd coated onto a glass prism; (λ=468nm), Pd(d1=12nm). (B) As it appears in the literature.

Another plot appearing in same publication demonstrates the effect of changing the incident wavelength (λ=800.45nm). Once again, using the same input parameters as Perrotton *et al.* we obtained the plot shown below (Perrotton *et al.* 2011c).

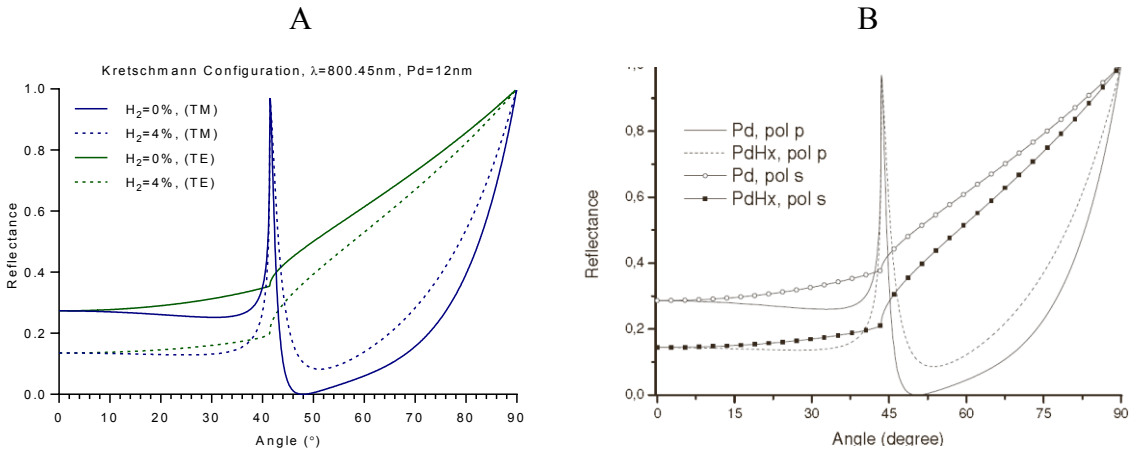

Figure 1-24 – (A) Plot showing reflectance against incident angle for both s and p polarized radiation, in the presence of 0 and 4% H_2 for Pd coated onto a glass prism; (λ=800.45nm), Pd(d1=12nm). (B) As it appears in the literature.

In both sets of data, we found that our model closely resembles Perrotton's results. This gives us confidence that the transfer matrix method we used for calculating reflectance of SPR is working accurately in modelling TM as well as TE polarized radiation using the angular interrogation method, at more than one wavelength. In addition, the close similarity between

our data and Perrotton's allows us to demonstrate that the hydrogen sensitive aspect of our device is producing reliable results.

1.3.3 Multilayer Sensing Structure

Following this, the next step in developing our model was to extend the working hydrogen sensitive Kretschmann model to account for multiple layers in the sensing structure. Perrotton also described the workings of an optical fibre sensor in another journal (Perrotton *et al.* 2011b). This time we employed a multilayer sensing structure consisting of Ag, SiO_2, & Pd. In keeping consistent with Perrotton's modelling methods at the time; von Rottkay's experimental data was used to model the dielectric permittivity of Pd as well as PdH (von Rottkay *et al.* 1999), the Drude model was used to calculate the dielectric permittivity of the Ag layer (Drude 1900a; Drude 1900b), the Schott model was used to calculate the refractive index of the thin film SiO_2 as well as the fused silica fibre core (Refractiveindex.info 2015). We obtained the following plot describing reflectance against input angle.

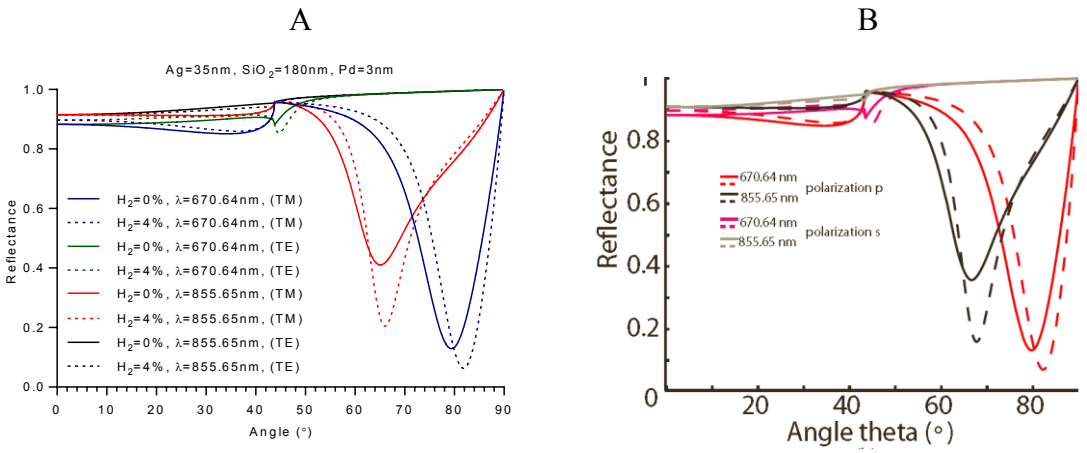

Figure 1-25 – (A) Plot showing reflectance against incident angle for both s- & p- polarized radiation, in the presence of 0 and 4% H_2 for multilayer sandwich structure coated onto a glass prism; (λ=670.64,855.65nm), Ag(d1=35nm), SiO_2(d2=180nm), Pd(d3=3nm). (B) As it appears in the literature.

This proved to be a very close match to Perrotton's data. Another plot appeared in the journal demonstrating the effect that a changing SiO_2 thickness has on the reflectance curve, at a specific wavelength (Perrotton *et al.* 2011b). We also replicated this plot as shown in Fig. 1-26. Once again this is a near perfect match to Perrotton's data.

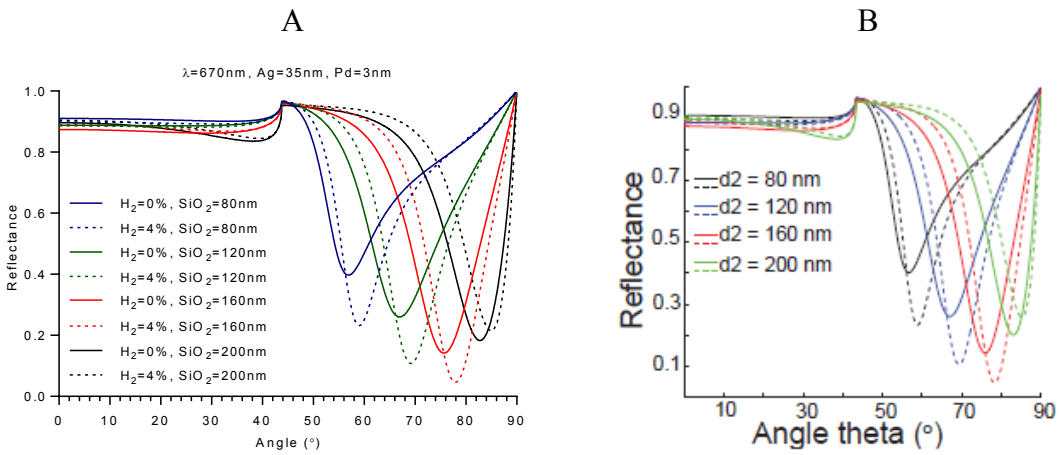

Figure 1-26 – (A) Plot showing reflectance against incident angle for p- polarized radiation, in the presence of 0 and 4% H_2 for multilayer sandwich structure coated onto a glass prism; (λ=670nm), Ag(d1=35nm), SiO_2(d2=80,120,160,200nm), Pd(d3=3nm). (B) As it appears in the literature.

The strikingly close similarity between the output that our model produces and Perrotton's demonstrates that our model can account for the presence of multiple continuous film layers present in the Kretschmann sensing structure. Finally, we extended the model to account for optical fibre operations.

1.3.4 OFSPR Hydrogen Sensor

The final aspect of our model we needed to check was our method of modelling the normalized output power. The following plot of transmitted normalized output power across a wavelength range of (λ=450:900)nm was obtained (Perrotton *et al.* 2011b).

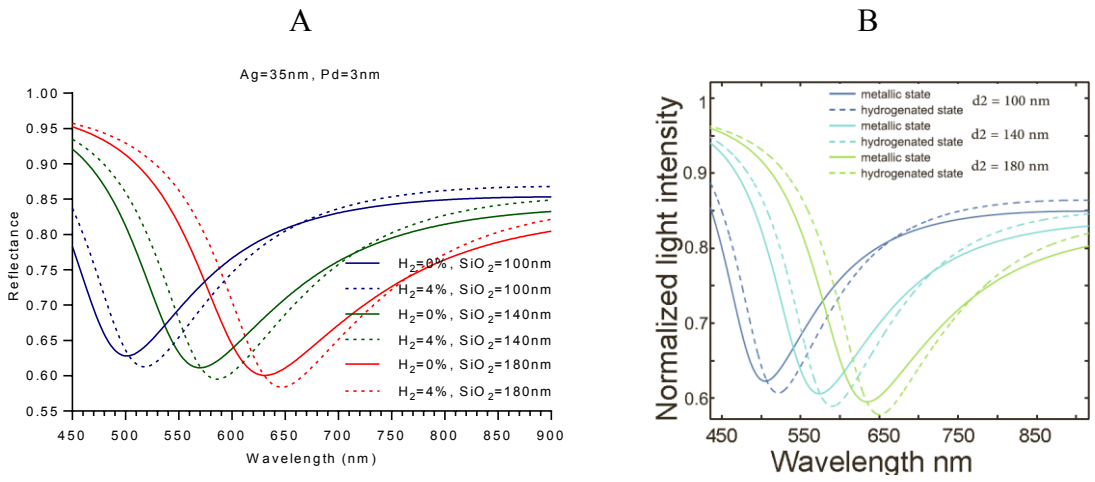

Figure 1-27 – (A) Plot showing transmitted normalized output power across the spectral domain for an OFSPR multilayer structure in the presence of 0 and 4% H_2; (λ=450:900)nm, Ag(d1=35nm), SiO_2(d2=100,140,180nm), Pd(d3=3nm). (B) As it appears in the literature.

Since our data output has repeatedly demonstrated near identical results with that previously published by other researchers, our model must be working accurately. Thus, we can now confidently generate novel structures and investigate the behaviour of different parameters that make up our optical fibre sensing structure.

1.4 Thesis Layout

In each of the subsequent chapters, we conduct research into surface plasmon resonance based sensing devices. We begin each chapter by introducing any relevant additional theory and literature specific to that chapter. We then propose our configuration, and present our findings.

In Chapter 2, we investigate the use of a PdY alloy as the analyte component in our multilayer. This alloy operates with improved durability compared to pure Pd due to the mitigation of an α→β phase transition that normally occurs once Pd interacts with H_2. We study the effects that the thickness of each multilayer component has on sensor performance, as well as the alloy volume fraction, and numerical aperture. We determine a range of optimized configurations that operate with maximum figure of merit for a range of incident unpolarized light sources.

Next, in Chapter 3 we substitute the individual modulation and H_2 sensitive layers for a nanocomposite structure consisting of Pd nanoparticles embedded in a SiO_2 dielectric matrix. We investigated the influence that the nanocomposite metallic and modulation layers have on

sensor performance, and compared the operation to an individual multilayer sensor of equivalent materials and thicknesses. We demonstrate that the nanocomposite device operates with superior performance in the near-IR spectral range, while the individual multilayer based device operates with higher figure of merit in the lower section of the investigated spectral range.

In Chapter 4 we achieved dual channel functionality by including an additional multilayer stack sensing configuration onto our fibre core. We investigated the influence that a change in various dimensions of both channels has on the resonance conditions. We introduce a distinct kind of dual channel sensor that operates with improved sensitivity and fast response time. Lastly, we make preliminary investigations into the operation of a multi-channel sensing device, by including up to 6- sensing channels along the fibre core.

Finally, by careful choice of materials and multilayer film thicknesses, in Chapter 5 we investigate the operation of a device that can stimulate both surface plasmon, and leaky mode resonance. We demonstrate for the first time, a structure that permits the co-operation of surface plasmon and leaky mode resonance through the stimulation of both modes at the same wavelength. We determine the performance of a series of devices that match the resonance wavelength of the surface plasmon resonance mode, and the TE0 mode, and demonstrate significantly improved figure of merit of (323.9%) compared to the optimized SPR sensor. Additionally, we investigate the H_2 applications of higher order waveguide resonance modes, demonstrate further TM & TE based co-operation, and compare their performance to that of the (SPR + TE0) resonance condition.

2 Chapter 2: Palladium Yttrium Alloy

As stated previously in Chapter 1, the first OFSPR hydrogen sensor operating in wavelength modulation was reported in a theoretical study by Perrotton *et al.* (Perrotton *et al.* 2011a) and was realised by depositing a Ag/SiO_2/Pd multilayer on the stripped core of a multimode optical fibre. Hydrogen detection was facilitated by the stimulation of SPR at the Ag/SiO_2 interface which undergoes modulation due to permittivity changes in the Pd layer during exposure to hydrogen. The sensor had excellent sensitivity and a relatively short response time (<15s) (Perrotton *et al.* 2013). In this chapter, we investigate the use of a novel multilayer OFSPR hydrogen sensor, utilizing a PdY alloy.

2.1 Theory

2.1.1 Problem: Durability of pure Pd film

The drawback of such a Pd-based hydrogen sensor is the high susceptibility to mechanical damage during operation due to cracking and blistering of the Pd lattice which occurs during repeated hydrogen loading cycles (Armgarth and Nylander 1982; Choi *et al.* 1986; Mandelis and Garcia 1998). This limitation of Pd-based sensors also applies to those which use a Pd cap layer over another hydrogen sensitive material to facilitate hydrogen dissociation (Kumar and Malhotra 2004; Silva *et al.* 2012). The delamination of Pd stems primarily from the increased mechanical stress on the fcc lattice following repeated transitions between the crystallographic α and β phases of PdH. We explain this in detail below:

As Pd absorbs hydrogen, the thickness of the Pd lattice increases significantly (Tobiška *et al.* 2001; Y. Liu *et al.* 2012a). Fig. 2-1 displays the influence that hydrogen exposure has on the pure Pd lattice structure.

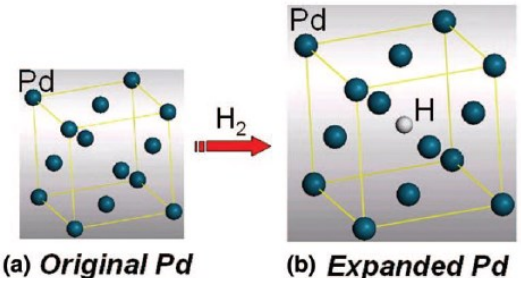

Figure 2-1 – Image showing the fcc lattice structure of pure Pd, and the expansion of the fcc Pd lattice due to interaction with H_2, due to the α→β phase transition; Image from (Y. Liu et al. 2012b).

The reason for this excessive lattice expansion stems from the possibility of Pd existing in more than one lattice structure. Normally solid state Pd exists in the α-phase, where the distance between individual atomic nuclei of Pd is relatively low. Once Pd absorbs a small concentration of H_2, initially it remains in the α-phase, however once the absorbed hydrogen reaches volume fraction above ≈ 1.7% (Manchester *et al.* 1994); some of the PdH alloy structure transitions to the β-phase. While both the α- and β-phases have the same fcc lattice structure as the Pd host structure, the lattice parameters are greater than that of pure Pd. Specifically, the fcc lattice structure of PdH expands significantly upon phase transition from α→β, as is illustrated in Fig. 2-1. During hydrogen loading, the repeated absorption and desorption of hydrogen results in constant fluctuation between phases, and consequently lattice constants. The consequential excessive mechanical stress on the lattice structure results in blistering, cracking, and the rapid degradation of the hydrogen sensitive layer.

2.1.2 Solutions:

2.1.2.1 Chemochromic Materials

To circumvent the aforementioned problem, some alternative hydrogen sensitive materials have been employed over the years. Many recent advances in optochemical sensors used in hydrogen sensing have been mentioned in Ando's review (Ando 2006). The most common chemochromic material used in hydrogen sensing is WO_3 (Benson *et al.* 1999; Sekimoto *et al.* 2000; Buttner *et al.* 2011; Dai *et al.* 2011; Huebert *et al.* 2011; X.G. Wang *et al.* 2013a; Yang *et al.* 2013; Dai *et al.* 2017), which reacts with hydrogen in the visible spectrum, altering the colour of the metal oxide to bronze, which can be easily detected by optical means. The reaction between WO_3 and H_2 can be understood as follows (Huebert *et al.* 2011):

$$WO_3 + 2xH_2 \rightarrow WO_{3-x}(xH_2O) \quad (2\text{-}1)$$

The rate at which the above interaction takes place is quite slow. Therefore, it is common that WO_3 is accompanied by an additional material which acts as a catalyst for H_2 dissociation, such as Pt (Krasnov *et al.* 2008; Zhang *et al.* 2011; X.G. Wang *et al.* 2013a), Pd (Sekimoto *et al.* 2000; Zhang *et al.* 2011; Boudiba *et al.* 2013; Wang *et al.* 2015), or an alloy of both (Shim *et al.* 2009). Wang *et al.* have demonstrated the use of a multilayer sensing structure consisting of $Ag/SiO_2/WO_3/Pt$ (X. Wang *et al.* 2013a). This sensor demonstrated better sensitivity than Perrotton's (Perrotton *et al.* 2013), though there is no information provided on the durability or response time.

Apart from WO_3, some other materials have shown promise in the optical detection of H_2. Composite films composed of Au-Co_3O_4 for example have demonstrated H_2 absorbance changes at (λ=600nm). In these structures, and particle size of Au was (20-40nm). (Ando *et al.* 1997). Also, metallic YH_2 and LH_2 undergo changes in their optical properties during transition to semiconducting YH_3 and LH_3 upon absorption of hydrogen (Huiberts *et al.* 1996; Imai *et al.* 2006).

As a final note, the study by Ando *et al.* must be mentioned. Here, they investigated the use of WO_3 composite films combined with Pd, Pt, and Au (Ando *et al.* 2001). Each of these were prepared on glass substrates in an Ar filled environment by deposition of sputtered species from WO_3. The combinations of Pd-WO_3 and Au-WO_3 demonstrated enhanced absorbance of H_2 in the visible range, and thus enhanced detection of H_2. They observed however that the Pt-WO_3 composite film did not result in a detectable amount of H_2 absorbance change of the film. They hypothesise that the relatively low permeability of Pt suppressed the formation of tungsten bronze.

While there are alternative materials, the highly selective, sensitive, rapid response time, and safe nature of reaction of Pd thin films are ideal for H_2 sensing applications. Consequently, we decided to research possible methods of improving the durability of a Pd based film, while still retaining the exceptional H_2 sensing properties that have brought about its widespread use.

2.1.2.2 Palladium Alloy

One very useful method of improving the durability of a Pd based hydrogen sensor involves alloying Pd with another material, thereby mitigating the α→β phase transition, and subsequently reducing degradation on the Pd based thin film. Hughes and Schubert investigated the use of several Pd-Ni alloys of thickness (50nm), and Ni volume fraction was (8-20%), as the hydrogen sensitive component in a chemiresistor device (Hughes and Schubert 1992). Pd capped Mg_x-Ni alloy films have also been used both in resistance, and transmittance based hydrogen sensors (Yoshimura *et al.* 2008), where *x* is the atomic fraction of Mg. This consisted of a (40nm) thick Mg-Ni alloy coated with a (4nm) Pd film. The sensor operated with a wide hydrogen concentration detection range at room temperature. (50nm) Mg-Ti films accompanied with a (30nm) thick Pd film have been used in H_2 sensing (Slaman *et al.* 2007; Slaman *et al.* 2008). Sengar *et al.* have shown that lower hydrogen induced lattice distortion can be achieved through the use of Pd-Ag and Pd-Cu nanoparticles (Sengar *et al.* 2013), where the nanoparticle agglomerates had a mobility equivalent diameter of (20nm), and the nanoparticle size was (8.9-10.32nm). Zhao *et al.* have investigated the use of a (20nm) Pd-Au film consisting of $Pd_{60\%}$-$Au_{40\%}$ (Zhao *et al.* 2006a). They state that their Pd-Au alloy does not experience an α→β phase transition upon absorption of (0.1-2%) H_2. Tabassum and Gupta investigated the use of a nanocomposite of Pd nanoparticles in a host matrix of ZnO (Tabassum and Gupta 2016a). While the sensor demonstrated good performance, cross-sensitivity to gases other than hydrogen was reported. Recently, Sharma and Kim have demonstrated promising results using a resistance based sensor that employed a Pd-Ag thin film hydrogen sensitive layer with $Pd_{77\%}$-$Ag_{23\%}$ (Sharma and Kim 2017).While each of the above structures demonstrated improved durability than a pure Pd based hydrogen sensitive structure, many involve relatively large volume fractions of another material, that can increase alloy cross sensitivity to gases other than hydrogen. Additionally the sensitivity is reduced if the Pd layer is alloy with a material that is not itself H_2 sensitive.

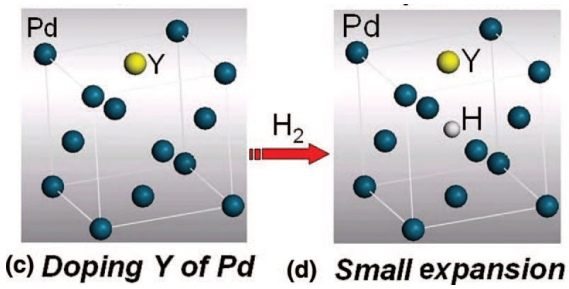

Figure 2-2 – (A) Image showing the fcc lattice structure of PdY. (B) Minimal expansion of the fcc PdY lattice due to interaction with H_2, as the α→β phase transition is mitigated; Image from (Y. Liu et al. 2012b).

Liu *et al.* have demonstrated that alloying Pd with 10% Y is sufficient to mitigate the α→β phase change thus reducing the mechanical stress on the sensor and prolonging its lifetime, as illustrated in Fig. 2-2 (Y. Liu *et al.* 2012b). This alloy concentration also has the additional benefit of increasing the hydrogen permeability 3.76 fold higher than pure Pd (Knapton 1977; Y. Liu *et al.* 2012b). In addition, since the volume fraction of Pd is quite high compared to other previously mentioned alloys, the alloy film is expected to retain a larger quantity of the properties that make Pd an excellent H_2 sensing material.

Finally, unlike the previously mentioned alloy materials, Y is also hydrogen sensitive and forms YH_2 and YH_3 upon hydrogen absorption. We note from the literature that these reactions are slow and generally a continuous Pd cap layer is grown over the Yttrium to facilitate dissociation from molecular to atomic hydrogen and improve uptake (Huiberts *et al.* 1996; Griessen *et al.* 1997). To our knowledge there is no published information on the exact magnitude of the permittivity change in thin film Y or PdY alloys during exposure to various concentrations of hydrogen. However, in a study by van Gogh *et al*. on 300nm Y films with a 15nm Pd cap layer, the real part of the dielectric permittivity of the YH_2 which results from hydrogenation was found to increase (van Gogh *et al.* 2001). So the permittivity change is in the same direction as that undergone by Pd during hydrogenation (von Rottkay *et al.* 1999). Therefore, the wavelength shift of the SPR in PdY, which is dominated by changes in the real part of the permittivity, is accentuated by effects of Y. Van Gogh's paper also shows that the imaginary part of the permittivity, which accounts for absorption and determines the width of the SPR dip, falls when Y is converted to YH_2. Therefore, we can expect that the SPR dip width, and hence the detection accuracy of the PdY sensor, will also improve when Y related effects are accounted for. The same arguments as outlined above also apply for YH_3. Therefore we choose to employ a Pd-Y alloy in our sensor.

In summary, compared to a sensor utilising a pure Pd film, the PdY alloy will operate with improved durability on account of the mitigation of the α→β phase transition. The alloy has demonstrated improved permeability to H_2. Finally, as Y is also sensitive to H_2, and the Y dielectric permittivity shifts in the same direction as Pd during H_2 loading, any decrease in the sensitivity or selectivity of the alloy due to the inclusion of Y is minimal.

2.1.2.3 Palladium Yttrium Alloy

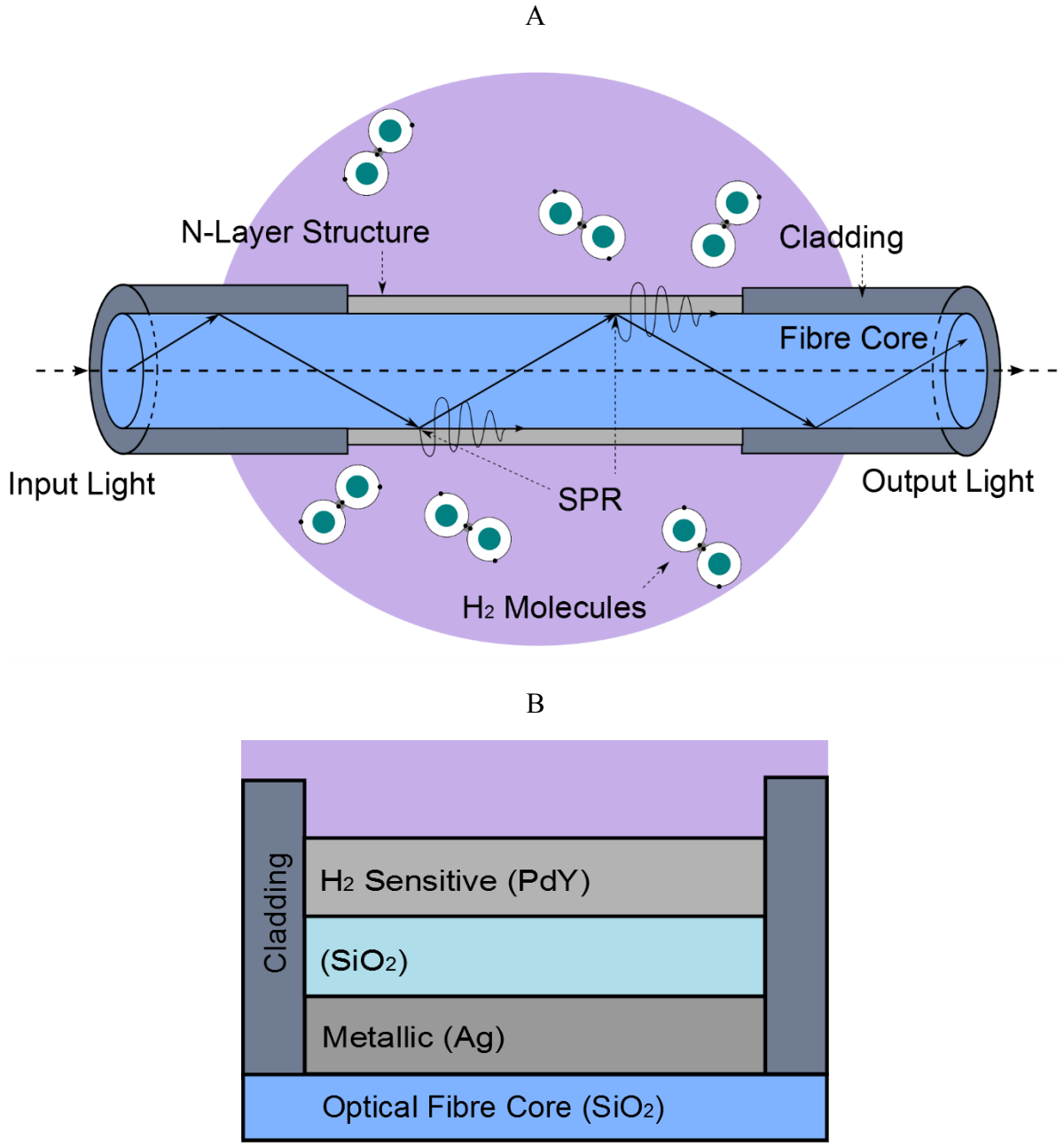

Figure 2-3 – (A) Schematic representation of an optical fibre surface plasmon resonance hydrogen sensor. (B) Close up schematic representation of the multilayer sensing structure (Ag/SiO_2/PdY) within the optical fibre sensing configuration.

We propose a novel optical fibre surface plasmon resonance hydrogen sensor which utilises a sensing multilayer capped with a thin alloy of Pd and Y as the hydrogen sensitive layer, as illustrated in Fig. 2-3(A & B). The PdY alloy mitigates transition of the Pd crystalline lattice from the α→β phase during hydrogen absorption (Y. Liu *et al.* 2012c) reducing mechanical stress on the sensing film during operation and prolonging the lifetime of the device. The optical setup used by Liu *et al.* involved a direct measurement of the light intensity reflected from a thin PdY film placed in the sensing region (Y. Liu *et al.* 2012b). This setup required a reference cell in a hydrogen-free region, which greatly increases the footprint of the sensor. As our proposed sensor operates using OFSPR, it does not necessitate an additional reference cell.

The relatively thick 10nm PdY alloy required for adequate sensing performance used by Liu proved to have a disadvantageous effect on the sensor response time. Since our sensor operates under the principle of SPR, the thickness of the PdY layer can be much less, and consequently allows for a faster response time. Later, Liu and Li have developed a reflectance based sensor which utilises a PdY layer with a thickness of (2.13nm) (Liu and Li 2016a). This film was grown on a fused silica substrate and atomic force microscopy analysis showed it to be uniform and continuous. Therefore, the dielectric permittivity of the alloy can be modelled using the assumption of a continuous film structure.

Several other workers have also reported hydrogen sensors based on PdY alloys, including surface acoustic wave sensors (Vanotti *et al.* 2015), and fibre-optic fabry-perot sensors (Yu *et al.* 2015). The drawbacks of these over the SPR sensor are slow response time, need for a wavelength swept laser source, and requirement for a reference cell in a hydrogen free area respectively. Yang *et al.* have also reported a hydrogen sensor utilising a PdY alloy (Yang *et al.* 2013). In this work, a side-polished fibre Bragg grating (FBG) sputtered with composite films including PdY, PdAg, and PdNi. Sensitivity was found to be largest with the side polished FBG utilising $Pd_{92\%}Y_{8\%}$, which was the Pd volume fraction that was investigated. Each film was (110nm) in thickness, which operated with relatively long response times of (180s, 300s, & 4-5 minutes) for the PdY, PdAg, and PdNi alloys coatings respectively.

In this work, we propose the first use of a PdY in an OFSPR hydrogen sensor. As previously mentioned, using the PdY in SPR sensing mode allows the PdY layer to be significantly thinner than the reflection based sensor reported by Liu *et al.* and will thus retain a fast response time while improving durability and hydrogen permeability. Our novel sensor

involves the growth of a 3-layer stack on the core of a section of multimode optical fibre from which the cladding has been stripped. Within the stack, the first layer is a metal (Ag) which supports SPR. The second layer is a modulation layer (SiO_2) which and allows coupling between guided rays in the fibre and SPR in the metal layer. The third layer is the hydrogen sensitive layer (PdY) whose dielectric function changes upon exposure to hydrogen gas. This sensor leverages the improved robustness and hydrogen permeability of PdY when compared to pure Pd.

2.2 Modelling

Next, we introduce the methods involved in modelling the dielectric permittivity of Y, as well as that of a bimetallic alloy.

2.2.1 Dielectric Permittivity of Yttrium

The Lorentz-Drude model was used to model the dielectric permittivity of Y (Lorentz 1905; Weaver and Olson 1977; Quinten 2011).

$$\varepsilon_Y = \varepsilon_f + \sum \varepsilon_b = 2 - \frac{{\omega_p}^2}{\omega^2 + i\omega\gamma_{fe}} + \frac{S_{IB}{\omega_{IB}}^2}{({\omega_{IB}}^2 - \omega^2 - i\omega\gamma_{IB})} \quad (2\text{-}2)$$

S_{IB} is the harmonic oscillator (HO) strength, ω_{IB} is the frequency of HO, γ_{IB} is the damping constant of the HO, ω_p is the plasma frequency, and γ_{fe} is the damping constant of free electron contribution.

Quantity	Y
S_{IB}	9.63
$\omega_{IB}\ (s^{-1})$	2.9×10^{15}
$\gamma_{IB}\ (s^{-1})$	3×10^{15}
$\omega_p\ (s^{-1})$	5.2×10^{15}
$\gamma_{fe}\ (s^{-1})$	1.5×10^{14}

Table 1 – Table showing the plasma and collision wavelengths for the Lorentz-Drude model approximation of the complex dielectric permittivity of Y (Quinten 2011).

Finally, we compared this model to experimental measurement by Weaver and Olson, as can be seen in Fig. 2-4 (Weaver and Olson 1977; Quinten 2011).

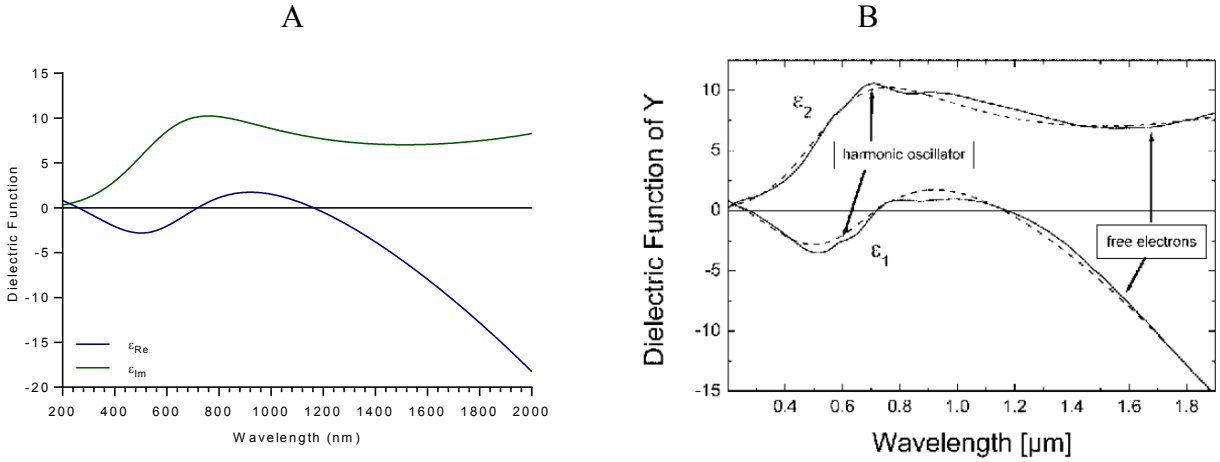

Figure 2-4 – (A) Plot showing the real and imaginary components of the complex dielectric permittivity of yttrium according to the Lorentz-Drude model equation (2-2), (B) Measured data as it appears in Optical Properties of Nanoparticle Systems (Quinten 2011).

We found a good match between our Lorentz-Drude approximation of the complex dielectric permittivity of yttrium and the experimental data shown above.

2.2.2 Effective Dielectric Permittivity of Alloys

Metallic alloys have been widely used in surface plasmon resonance. Typically alloys of Au and Ag have found application in SPR as the resonance condition operates with high durability due to the inclusion of Au, and has a narrow linewidth due to the inclusion of Ag (Ehler and Noe 1995; Sharma and Gupta 2006; Jha and Sharma 2009). The method of

determining the dielectric permittivity of a bimetallic alloy is shown in equation (2-3), where ε_A can be described by as a weighted sum of the dielectric permittivity of each constituent metal and ε_{m1} and ε_{m2} are the dielectric permittivities of each metal composite in the alloy, and x is the alloy concentration of metal 1. This model was employed by Sharma and Gupta to model various Au-Ag alloys for SPR applications (Sharma and Gupta 2006), and was originally introduced by Roy *et al.*, and the original optical constants were taken from Johnson and Christy (Johnson and Christy 1972; Roy *et al.* 2003).

$$\varepsilon_A = x\varepsilon_{m1} + (1-x)\varepsilon_{m2} \tag{2-3}$$

2.3 Results

2.3.1 Materials and Modelling Methods

We will begin by introducing the relevant materials that constitute our OFSPR sensing device. A multilayer stack sensing configuration consisting of a (metallic film / modulation layer / hydrogen sensitive analyte): (Ag/SiO_2/PdY) of thicknesses (d1/d2/d3) respectively was deposited onto an unclad section of a fused silica fibre core. The rationale behind the choice of Ag, SiO_2 and Pd are explained in Chapter 1. Y is employed as an alloy component of the H_2 sensitive layer, primarily in order to improve durability as mentioned previously.

The Brendel Bormann model is used in determining the dielectric permittivity of Ag and Pd (Brendel and Bormann 1992), and Sellmeier Dispersion formulae are used to determine the refractive indices of thin film SiO_2 (Postava and Yamaguchi 2001) and the silica fibre core (Malitson 1965); and the relevant the equations appear in Chapter 1. The normalised output power is determined using the characteristic transfer matrix model as outlined in Chapter 1. The Lorentz-Drude model is used to determine the dielectric permittivity of Y, using equation (2-2), and the effective dielectric permittivity of the PdY alloy is determined using the bimetallic alloy equation (2-3) from this chapter.

We have introduced the materials that make up the multilayer sensing structure, and indicated the methods involved in modelling the propagation of light along the fibre core. Next we will define the parameters of the optical fibre structures that were used throughout our investigations.

2.3.2 General Sensor Parameters

The NA of an optical fibre sensor determines the critical angle for total internal reflection. The higher the NA, the larger the critical angle and the greater the number of rays supported. In our sensor, this will cause an increase in the total number of reflections within the sensing region. The end result is a decrease in sensitivity and a broadening in the width of the SPR spectral dip (A. K. Sharma and B. D. Gupta 2005). Therefore, in general, a low NA sensor is preferred. Here we follow previous workers and choose a fibre (NA=0.22). This choice allows us to probe the general behaviour of the sensor where it is understood that increasing or decreasing the NA will in general reduce or improve sensor performance respectively.

Like the fibre NA, the ratio of sensing length to fibre diameter L/D also influences the number of reflections in the sensing region via the parameter N_{ref}. In general, the sensor performance will degrade as L/D increases. In practice the choice of sensing length L is influenced by structural and fabrication considerations while the fibre diameter must be large enough to ensure multimode operation in order to ensure valid use of the characteristic transfer matrix model (Ciprian and Hlubina 2013a). Here, we choose a sensing length (L=1cm) and a fibre diameter of (D=200μm). These parameters are in line with those used by previous workers and within the range of commonly available multimode fibres (Perrotton *et al.* 2011a; Ciprian and Hlubina 2013a). This choice brings the maximum number of reflections in the sensing region ($N_{ref}\approx100$) and it is clear that choosing these parameters to reduce this number will in general improve the sensing performance.

Our sensor is based on a PdY alloy where the Pd gives hydrogen selectivity while the Y improves hydrogen permeability and sensor robustness. Here we will follow Liu *et al.* and choose an alloy concentration of 10% Y along with 90% Pd as the relative concentrations of each material for the PdY alloy (Liu *et al.* 2013). This ratio is enough to mitigate the unwanted phase change and increases the permeability of Pd to hydrogen, while still retaining the high selectivity and sensitivity of the alloy.

Now that we have defined the parameters that constitute our fibre, and established the relative Pd to Y volume fraction, we will discuss the response time, selectivity, and durability of our device.

2.3.3 Response Time, Selectivity and Durability

The response time of our sensor can be derived by referring to the study of Liu *et al.,* which operated with a response time of (4s) to 4% H_2. This response time was found to increase with increasing H_2 concentration. This is faster than the (<15s) response time of the OFSPR reported by Perrotton *et al.* which was based on a pure Pd hydrogen sensitive layer (3.75nm) thick. The improved response time is due to the increased hydrogen permeability of the PdY alloy over pure Pd (Y. Liu *et al.* 2012b).

With regards to selectivity, Pd is widely employed as a H_2 sensitive material due to the inherent high selectivity to H_2 (Huebert *et al.* 2011). It must be noted however that Pd based sensors have demonstrated minor response to a number of gases including CO, CO_2, H_2S (Palmisano *et al.* 2015), Cl, and N_2 (Tabassum and Gupta 2016a), NO_2, water vapour (Lange *et al.* 2011), and some hydrocarbons (Morjan *et al.* 2009). We note from previous studies into PdY alloys for hydrogen sensing applications, the cross-sensitivity of the alloy to gases other than hydrogen has not always been discussed (Liu *et al.* 2013; Yang *et al.* 2013; Vanotti *et al.* 2015; Yu *et al.* 2015; Liu and Li 2016b). However, we can refer to the findings of Imai *et al*. who showed that a PdY alloy sensor was not sensitive to the presence of methane or isobutane (Imai *et al.* 2004). We can gain further insights into cross-sensitivities by considering the components of the alloy separately. It is known that the presence of CO causes an increase in the response time of Pd-based hydrogen sensors due to the binding of CO to active Pd sites, thus slowing hydrogen dissociation (Zhao *et al.* 2006a). A similar process also makes Pd sensitive to relative humidity changes whereby water absorption on the Pd surface can again decrease the number of active sites available for chemisorption of hydrogen and so slow the sensor response time. We can expect both these sensitivities to be present in the PdY alloy sensor.

Yttrium can be oxidised in air with the result that the response time of the sensor can be negatively impacted as shown in a study by Liu *et al.* (Y. Liu *et al.* 2012b). In that paper, the operation of a sensor stored under oil was compared to one stored in air and it was shown the presence of oxygen in the air led to oxidisation which slowed the response time. However, where a sensor has been damaged by oxidisation, another recent study shows that treating the oxidised PdY film with an annealing process restores the hydrogen absorption and sensitivity of the film (Song *et al.* 2015).

2.3.4 Layer Thickness within the Multilayer

In order to investigate the effect of the metallic layer thickness (d1=Ag), for now, we keep the thickness of the hydrogen sensitive layer (d3=PdY) layer constant at 3nm. It is important to mention that in general, pure Pd films less than 5nm thickness are generally reported as being discontinuous (Huiberts *et al.* 1996). However, recently Liu *et al.* have reported a sensor based on a PdY layer only 2.13nm thick (Liu and Li 2016b). This film was grown on a fused silica substrate and atomic force microscopy analysis showed it to be uniform and continuous. Therefore, in our analysis we assume the PdY film to be continuous and uniform. Perrotton et al. have successfully fabricated a sensor with a Pd layer thickness of 3.75nm (Perrotton *et al.* 2013). A thickness of 3nm is suitable as it is proven to be sufficient for successful hydrogen detection while allowing fast diffusion of hydrogen into the alloy thus giving a fast sensor response.

We proceeded to investigate the influence that the thickness of each material that constitutes the multilayer sensing stack has on sensor performance. In order to achieve this, we determined the normalised power output through the fibre. We repeated this, varying the thickness of one material individually, in order to observe the influence on the output power. Specifically we note the resonance spectral location, depth and width with changing layer thickness.

2.3.4.1 Metallic Layer Thickness

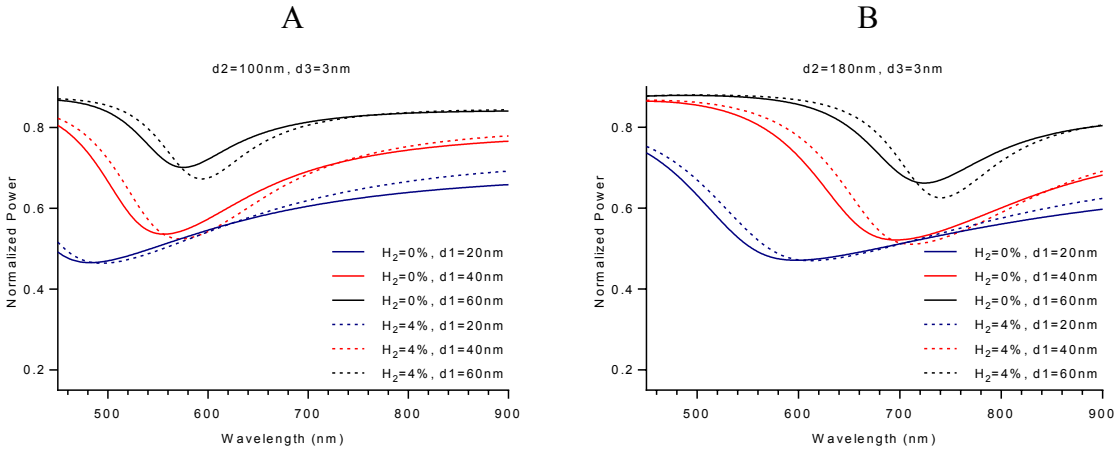

Figure 2-5 – (A) Normalised output power across the spectral domain of a Ag/SiO_2/PdY multilayer sandwich structure OFSPR sensor in the presence of 0% and 4% H_2; (λ=450:900nm), Ag(d1=20,40,60nm), PdY(d3=3nm), Y-fraction(Y=0.1), SiO_2(d2=100nm). (B) SiO_2(d2=180nm).

The normalised output power was determined for three sensing configurations differing in Ag (d1) thickness in shown in Fig. 2-5(A). Here we can see the effect of increasing the Ag thickness is a red shift of the resonance wavelength and a decrease in the depth accompanied by a broadening of the dip. In each figure, the solid line represents the normalised output power through the fibre in the absence of H_2, and the corresponding dashed line of the same colour represents the output power from the same sensor, where the multilayer sensing structure is exposed to an environment with 4% H_2.

The red shift can be understood as the effect of the increase in the real component of the propagation constant of the surface plasmon with increasing Ag thickness. The widening of the resonance dip is due to increased energy absorption in the metal as the layer thickness increases. Finally, the shallowing of the dip is due to a change in the balance between radiation and intrinsic damping. In general it is known that the dip depth will reach a minimum when the Ag thickness is chosen so that the intrinsic and radiation damping losses become equivalent (Raether 1988). Looking again at Fig. 2-5(A), we see that the effect of exposing the sensor to hydrogen is a red shift of the resonance. Again, this can be understood as the effect of an increase in the real part of the propagation constant of the surface plasmon as the permittivity of the PdY film drops upon hydrogenation.

In Fig. 2-5(B), we see the effect of changing the modulation layer thickness (d2=SiO_2) is to shift all resonance dips to longer wavelengths as the real part of the surface plasmon propagation constant increases. Next we investigate the influence of SiO_2 thickness further by keeping the Ag thickness constant, and vary the SiO_2 thickness in steps from (100:180nm).

2.3.4.2 Modulation Layer Thickness

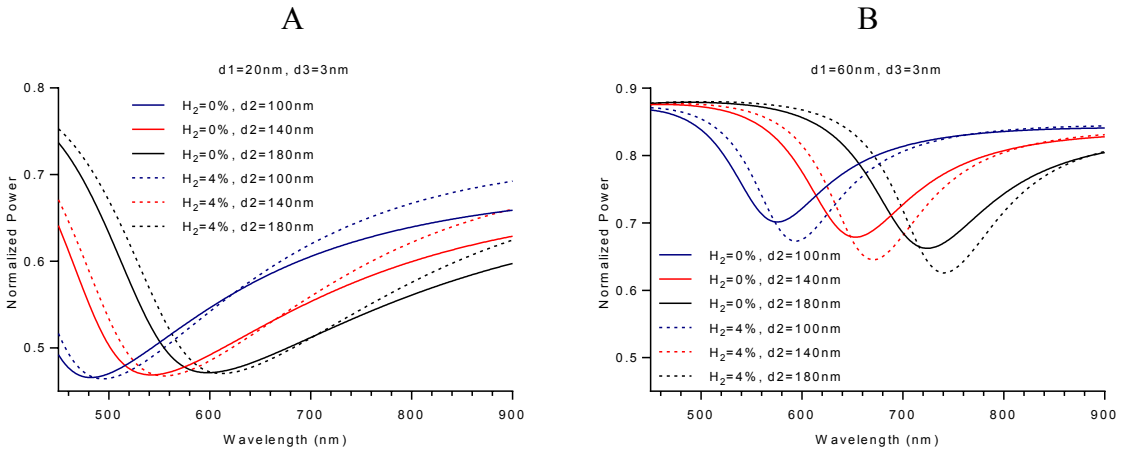

Figure 2-6 – (A) Normalised output power across the spectral domain of a Ag/SiO_2/PdY multilayer sandwich structure OFSPR sensor in the presence of 0% and 4% H_2; (λ=450:900nm), SiO_2(d2=100,140,180nm), PdY(d3=3nm), Y-fraction(Y=0.1), Ag(d1=20nm). (B) Ag(d1=60nm).

In both Fig. 2-6(A & B) we see a red shift in the resonance wavelength with increasing SiO_2 thickness. This effect can be useful in tuning the sensor spectral centre to any desired wavelength; often in practice the spectral centre of the sensor light source. There is very little difference in the depth of the resonance condition with increasing SiO_2 thickness. This is attributed to the fact that the dielectric permittivity of SiO_2 contains only a very minimal imaginary component, and thus, there is very little absorption in the modulation layer.

Other considerations in choosing the SiO_2 thickness include keeping it small enough to allow the evanescent radiation field to interact successfully with the analyte region (Pd layer). The SiO_2 layer must also be small enough to avoid multimodes in the waveguide created by having a dielectric sandwich between two metals (Perrotton *et al.* 2011a). Finally, the SiO_2 thickness must not be so low that the resonance is pushed into the UV where the lack of readily available optics would make the sensor impractical. In Fig. 2-6(B), where the Ag thickness is fixed at 60nm, we see similar behaviour to Fig. 2-6(A), except that all dips have red shifted, broadened and shallowed, due to the aforementioned reasons mentioned from Fig. 2-5.

We have established the primary influence that the metallic and modulation layers have on resonance curve. Next we will investigate the influence that the Pd layer thickness has on sensor performance.

2.3.4.3 Hydrogen Sensitive Layer Thickness

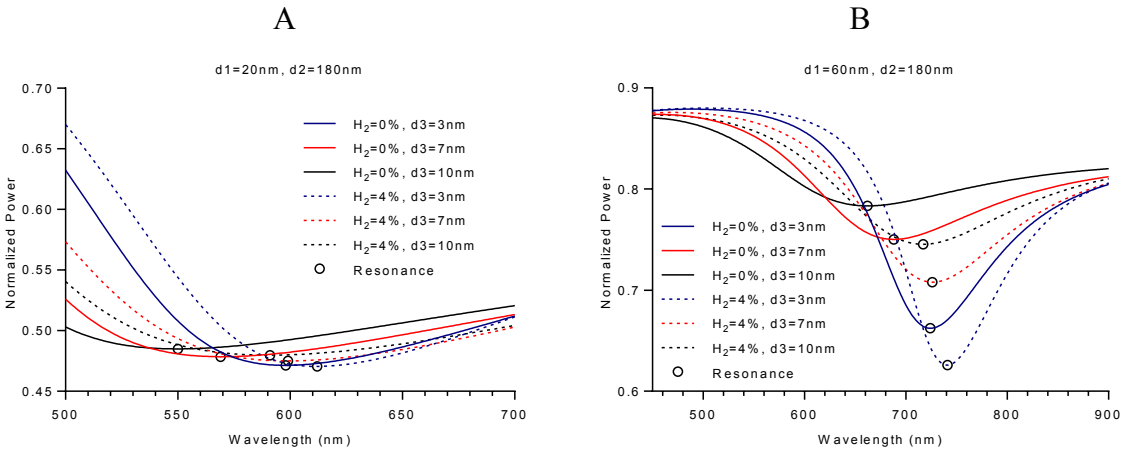

Figure 2-7 – (A) Normalised output power across the spectral domain of a Ag/SiO_2/PdY multilayer sandwich structure OFSPR sensor in the presence of 0% and 4% H_2; (λ=450:900nm), *SiO_2(d2=180nm), PdY(d3=3,7,10nm), Y-fraction(Y=0.1), Ag(d1=20nm). (B) Ag(d1=60nm).*

In Fig. 2-7, we investigate the effects of the PdY layer thickness on the sensor performance. Fig. 2-7(A) illustrates the response of a multilayer with a fixed Ag thickness of 20nm, and SiO_2 thickness of 180nm is presented. The PdY layer thickness is varied in steps with (d3=3, 7, 10nm). These were chosen as Pd continuous films 3nm in thickness has been studied experimentally and theoretically by Perrotton *et al.,* and Liu *et al.* have reported experimental success with PdY alloys of 10nm in thickness (Perrotton *et al.* 2011b; Yi Liu *et al.* 2012; Perrotton *et al.* 2013). While significantly thicker PdY films have been investigated (Minghong *et al.* 2013), the reported response times of (180s) would make the sensor impractical for applications involving rapid H_2 detection.

The effect of increasing the thickness of the PdY layer can be seen clearly in Fig. 2-7(B) where the broadening and shallowing of the SPR dip. This can be understood as the effect of the highly absorbing Pd in the alloy and it is clear that a thinner layer here gives much better performance. Additionally, by observing the spectral locations of each resonance location, it can be seen that the spectral red shift increases with increasing PdY film thickness. Consequently, sensor sensitivity increases with increasing PdY thickness. In Fig. 2-7(A), we observe similar effects with each resonance curves showing a red shift due to the thicker Ag layer, although, since the Ag thickness is quite low, the resonance condition is exceptionally broad. While the improved sensitivity is beneficial, the thickness of the PdY layer has the largest influence on the response time of the sensor, and subsequently should be kept as thin

as possible. As previously mentioned, Liu & Li have shown that a PdY film less than 3nm thick can be homogenously grown (Liu and Li 2016b) and Perrotton *et al.* have shown a pure Pd sensing layer of this size gives acceptable performance with a fast response time (Perrotton *et al.* 2013). Therefore, we suggest this level of thickness for our sensor.

2.3.5 Additional Parameters Investigated

While we have already chosen certain values for the Y volume fraction and NA, based on discussion in the General Sensor Parameters section above, it is important to understand the influence they have on the resonance condition.

2.3.5.1 Yttrium volume fraction

Firstly, we investigated the effect that the Pd-Y alloy volume fraction has on the output power of the sensor.

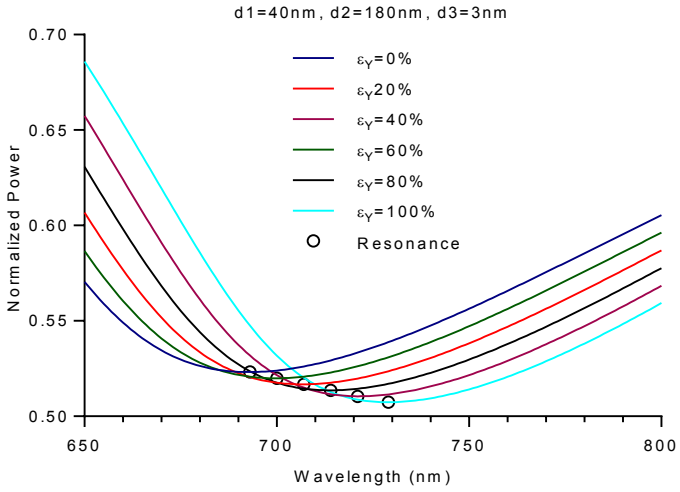

Figure 2-8 – Normalised output power across the spectral domain of a Ag/SiO_2/PdY multilayer sandwich structure OFSPR sensor in the presence of 4% H_2; (λ=450:900nm)*, Ag(d1=40nm), SiO_2(d2=180 nm), PdY(d3=3nm), Y-fraction(Y=0.2,0.4,0.6,0.8,1).*

Fig. 2-8 displays the influence that Y volume fraction has on sensor performance. It can be seen that increasing Y volume fraction results in the shallowing of the SPR dip. This can be understood by noting the difference in the real and imaginary components of Pd and Y dielectric permittivities. For example, at a wavelength of 633nm, ε_{Pd} = -14.32 + 15.29i, whereas ε_Y = -1.50 + 9.20i. The detection accuracy undergoes a mild decrease from

(9.578×10^{-3} to $9.099\times10^{-3}nm^{-1}$) going from 100% Pd to 100% Y respectively. However, the primary function of Y in the alloy is to improve durability and prolong the active lifetime of the sensitive layer. Thus, we need only ensure we choose the alloy fraction that mitigates the unwanted phase transition. Additionally, Yang *et al*. have reported that the PdY alloy of the lowest Y volume fraction operated with the highest sensor sensitivity (Minghong *et al.* 2013). It should also be mentioned that Pd is the primary H_2 sensitive material in this alloy. Overall the Y volume fraction has only a minor effect on the SPR curve. This is good for the sensor as it appears that the presence of yttrium won't unduly affect its operation.

2.3.5.2 Numerical Aperture

Lastly, we briefly investigated the influence that this dimension has on the resonance condition. We employed three values of NA that are widely used commercially (NA=0.12, 0.22, 0.37).

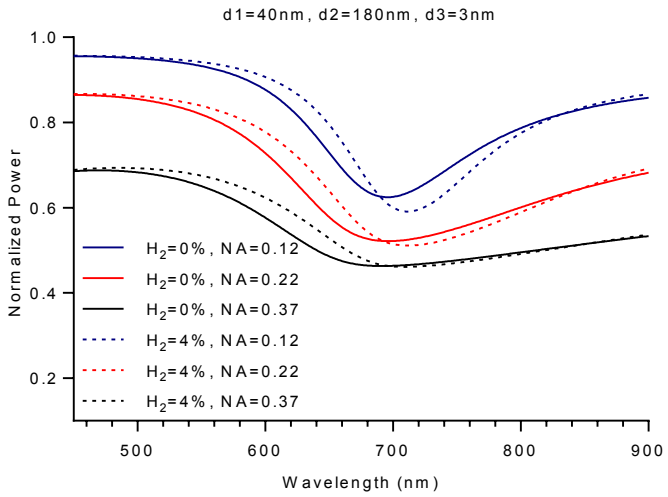

Figure 2-9 – Normalised output power across the spectral domain of a Ag/SiO_2/PdY multilayer sandwich structure OFSPR sensor in the presence of 0% and 4% H_2; (λ=450:900nm), *Ag(d1=35nm), SiO_2(d2=180nm), PdY(d3=3nm), Y-fraction (Y=0.1), (NA=0.12,0.22,0.37).*

Fig. 2-9 demonstrates the influence that numerical aperture NA has on the resonance condition. Increasing the size of NA causes a decrease in the output power at resonance as well as increasing the number of reflections that occurs along the fibre, and subsequently results the broadening of the resonance curve. While the NA does demonstrate a clear influence on sensor performance, it's influence has been studied in detail (Savović and

Djordjevich 2004), and thus the focus of our research will continue to be on parameters and materials that make up the multilayer sensing structure.

Now that we have studied the influence that the thickness of each constitute material in our multilayer has on sensor performance, and have defined most sensor parameters, we determine the sensitivity, detection accuracy, and figure of merit of a series of devices. This is done using the relevant equations for sensitivity and detection accuracy, and figure of merit from Chapter 1.

2.3.6 Performance

In view of the fact that the PdY layer thickness is to a large degree constrained by practical limitations we present a figure which shows how the sensitivity varies with both the SiO_2 and Ag thickness, while keeping the PdY layer thickness fixed at 3nm.

2.3.6.1 Sensitivity and Detection Accuracy

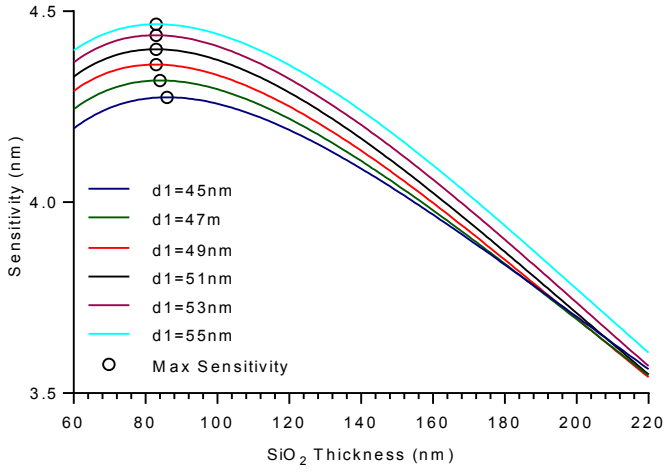

Figure 2-10 – Sensor sensitivity (SPR dip wavelength shift to 1% hydrogen) for several OFSPR configurations in the range Ag(d1=45:55nm), and SiO_2(d2=60:220nm).

The parameters chosen for the range of Ag thicknesses were based that which produced strong resonances when accompanied with various SiO_2 thicknesses. We found that sensitivity increases with Ag thickness. Sensitivity can also be seen to reach a maximum for each Ag thickness when paired with a certain specific thickness of SiO_2. Shalabney *et al.* have described the sensitivity of SPR sensors as being due to the overlap integral between the optical energy in the region of the analyte (in our case, the PdY layer) normalised to the total

energy (Shalabney and Abdulhalim 2010). In their paper, they report that enhancement of the electric field in the region of the analyte was correlated to enhanced sensitivity. Looking at Fig. 2-10, we conclude the optimum sensitivity for each Ag/SiO_2 thickness pair occurs where the electric field enhancement in the PdY layer is at its maximum. For a given Ag thickness, one particular thickness of SiO_2 gives the maximum electric field in the PdY layer and thus the maximum sensitivity. Deviating from this optimum thickness, the field enhancement decreases as does the sensitivity.

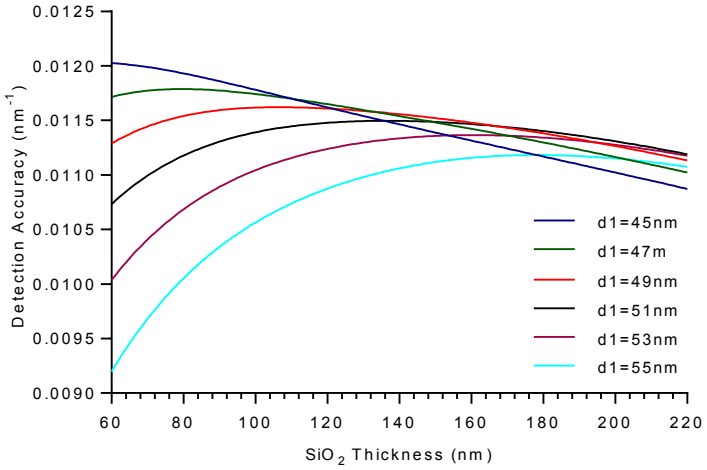

Figure 2-11 – Detection Accuracy (SPR dip wavelength shift to 1% hydrogen) for several OFSPR configurations in the range Ag(d1=45:55nm), and SiO_2(d2=60:220nm).

It is now pertinent to consider the detection accuracy of the sensor. This parameter, which is a robust measure of the width of the resonance dip, is closely related to the signal to noise ratio. For this investigation, the upper and lower limits of the SiO_2 thickness were limited by the highest and lowest wavelengths on the normalised output power simulations that facilitate detection accuracy measurement within the spectral range investigated (λ=450:900nm). This limitation is permitted since in these configurations, the linewidth of the resonance condition exceeds the spectral resonance shift, thus FOM calculations are limited by the linewidth of the resonance curve.

We investigated how each configuration behaves in terms of detection accuracy as seen in Fig. 2-11. We observe that the linewidth of the SPR increases with increasing SiO_2 thickness for low thicknesses of Ag, and we observe a reversal in this behaviour for larger thicknesses of SiO_2. The optimal OFSPR sensor should demonstrate maximal sensor sensitivity and

detection accuracy. Based on the observations made in Fig. 2-11 & 2-12, it is clear that a trade-off between both sensor performance measurements is necessary. Therefore, we employ a sensor figure of merit as defined in Chapter 1 which combines sensor sensitivity and detection accuracy.

2.3.6.2 Figure of Merit

The figure of merit for several OFSPR configurations is demonstrated in Fig. 2-12.

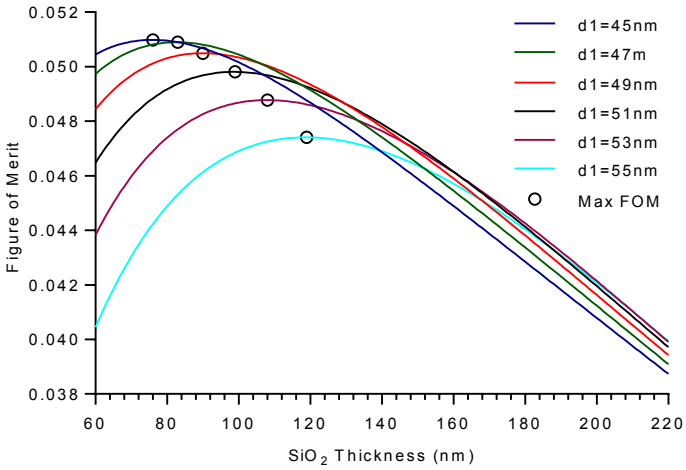

Figure 2-12 – Sensor Figure of Merit (SPR dip wavelength shift to 1% hydrogen) for several OFSPR configurations in the range Ag(d1=45:55nm), and SiO_2(d2=60:220nm).

We observe that sensor FOM for each SiO_2 thickness strongly depends on the corresponding Ag thickness. It is clear that, in order to maximise the FOM for a given SiO_2 thickness, it must be paired with a specific Ag thickness. In view of this, we next determined the maximum FOM for a fixed SiO_2 thickness when paired with all Ag thicknesses in the range (d1=1:90nm). This was subsequently repeated for all SiO_2 thicknesses that permit OFSPR sensing within the spectral range (λ=450:900nm).

2.3.6.3 Optimal Structures

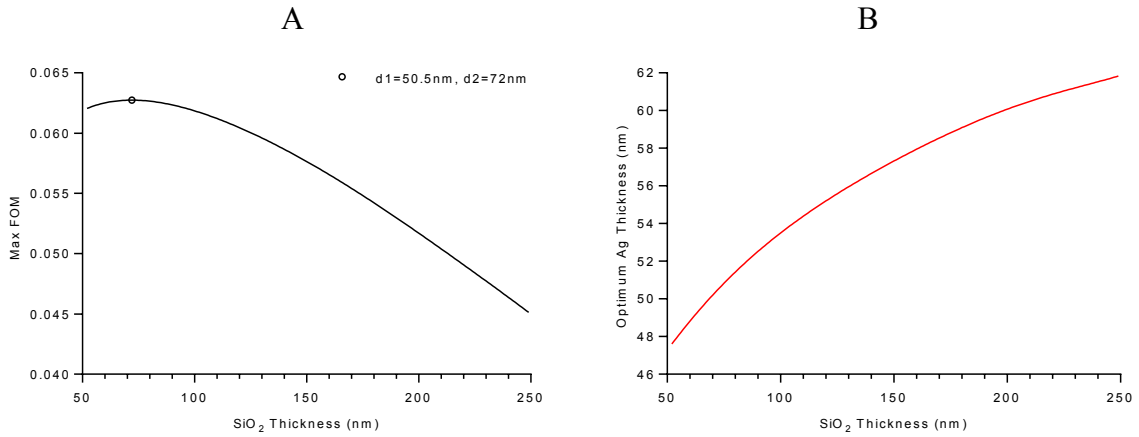

Figure 2-13 – (A) Plot showing the maximum FOM of each OFSPR configurations in the range SiO_2(d2=52:249nm) when combined with Ag(d1=1:90nm). (B) Plot showing the Ag thickness that, when paired with SiO_2(d2=52:249nm), yields optimal sensor performance (highest FOM).

Fig. 2-13(A) displays the maximum FOM, obtained by locating the optimum Ag thickness corresponding to each SiO_2 thickness. It can be seen that after a certain maximum point, the figure of merit decreases with SiO_2 thickness. The sensor with SiO_2 thickness of 72nm performs with (FOM=0.062740) when paired with a Ag thickness of 50.5nm. This sensor demonstrated a sensitivity of 17.64nm to 4% hydrogen and a detection accuracy of 0.014nm^{-1} and operated at a spectral centre of 528.87nm. This is the best sensor FOM performance measurement in this series of simulations. Fig. 2-13(B) demonstrates the relationship between SiO_2 thicknesses and the corresponding Ag thickness that permits maximum FOM.

It can be seen that the optimal Ag thickness increases with SiO_2 thickness. Recalling that the shift in resonance wavelength of the SPR is proportional to the thickness of the SiO_2 film, we expect that the resonance wavelength of each configuration shown in Fig. 2-13(B) will be different. In practical applications it is advantageous that the resonance wavelength of the SP be aligned with the spectral centre of the sensing light source (F. Downes and C. M. Taylor 2017). We determined the resonance wavelength of each configuration shown above in Fig. 2-13(B). This allowed us to determine the optimal sensing configurations based on the resonance wavelength of the SP.

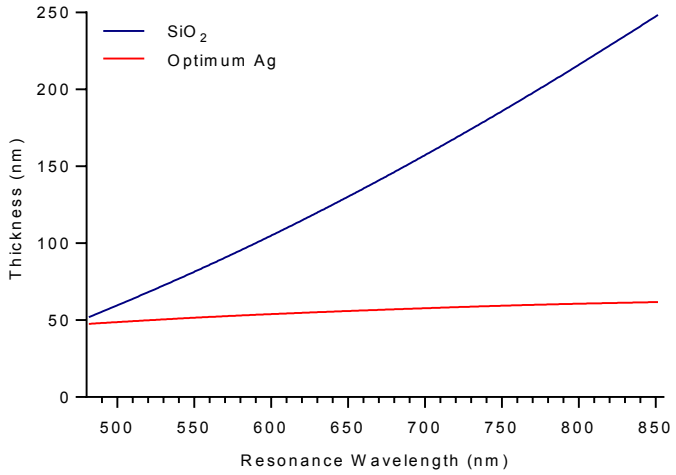

Figure 2-14 Plot showing the Ag(d1=1:90nm) thickness that, when paired with SiO_2(d2=52:249nm), leads to optimal sensor performance (highest FOM) along with the resonance wavelength of the SPR for each configuration.

Using Fig. 2-14, the sensor parameters of Ag and SiO_2 thickness can be chosen such that the resonance wavelength of the SP matches the spectral centre of the incident light source. This allows one to optimize sensor performance "maximize FOM" based on the sensing light source. For example; the optimum parameters for a sensor operating with a sensing light source centred at 633nm would include Ag thickness of 55.2nm accompanied by a SiO_2 thickness of 122nm, and would produce a sensor figure of merit of 0.0603. Similarly, a sensor operating with a sensing light source centred at 750nm would include optimum parameters of (Ag=59.4nm) with (SiO_2=186nm), producing a sensor (FOM=0.0535).

2.4 Conclusion

In conclusion, we have performed a theoretical investigation into the operation of a novel multilayer OFSPR based H_2 sensor that utilizes a PdY alloy. The choice of Y as an alloy component as the volume fraction of $Pd_{90\%}Y_{10\%}$ demonstrates improved film durability, minimal reduction in sensitivity compared to other alloy materials, and improved H_2 permeability. The methods of modelling the interaction between light and our sensor are outlined in Chapter 1. We performed analysis on the normalised output power though the fibre in the presence of 0% and 4% H_2 gas. The spectral resonance location of the surface plasmon underwent a red shift during hydrogen loading, which allowed us to determine sensor sensitivity. The spectral width of the resonance condition was determined by measuring the detection accuracy.

We investigated the influence that metallic layer thickness Ag (d1), modulation layer thickness SiO_2 (d2), hydrogen sensitive layer thickness PdY (d3), Pd volume fraction in the PdY alloy, and numerical aperture have on sensor performance. Following this, we continued investigations into the metallic and modulation layer thickness, and found that a trade-off between sensitivity and detection accuracy is required for an optimum sensing structure. To investigate this trade-off further, a sensor figure of merit (FOM) was used to identify the optimum sensor. We found that the FOM will be a maximum for each SiO_2 thickness, when paired with a particular Ag thickness. We determined the maximum FOM for a range of SiO_2 configurations that permit OFSPR sensing within the spectral range (450:900) nm, along with the corresponding optimal Ag thickness that permits maximum sensor FOM. Finally, we investigated how the resonance wavelength of the sensor varies with layer thickness within the multilayer and found that the optimal Ag and SiO_2 thicknesses are wavelength dependent. For the first time, we presented a figure which can be used to determine the optimal sensing configuration that would maximize sensor performance for a particular sensing light source. The optimal sensor demonstrated a figure of merit of (FOM=0.062740) and comprised of Ag thickness (d1=50.5nm) and SiO_2 thickness (d2=72nm). This sensor demonstrated a sensitivity of (Sn=17.64nm) to 4% hydrogen, a detection accuracy of (DA=0.014228nm^{-1}) and operated at a spectral centre of (λ=528.87nm).

3 Chapter 3: Nanocomposite Structure

3.1 Introduction

In the last chapter, we have investigated the use of an OFSPR PdY based H_2 sensor. The H_2 sensitive component of the sensor employed a continuous Pd based film, and optimal structures were determined for operation across a wide wavelength range. Recently, research into the use of Pd nanoparticles and nanoparticle based composites for H_2 sensing applications has been carried out (Tabassum and Gupta 2016a; Ohodnicki *et al.* 2017), and significant improvements in sensitivity, durability, and selectivity have been demonstrated, compared to pure Pd based continuous film structures.

In this chapter, we perform a series of investigations into the operation of a nanocomposite structure (NC), consisting of Pd nanoparticles embedded in a host dielectric matrix, and compare it to the performance of an individual multilayer based structure (IM) similar to that investigated in Chapter 2. We define a nanocomposite as a material comprised of "nano-sized" particles (<100nm) embedded in the matrix of another material. For the first time we compare the performance of a nanocomposite based device with an OF sensing configuration that employs multiple individual continuous films.

For our nanocomposite, we make the choice of SiO_2 as the matrix which the Pd nanoparticles will be embedded as SiO_2 is known to yield good corrosion protection, have a high permeability to H_2, and low cross-sensitivities to other gaseous compounds. Use of SiO_2 also allows easy comparison of sensing performance to those of Chapter 2. The general performance of the NC sensor will be investigated by looking at the normalized output power spectra of an OFSPR employing such a NC-based sensing layer, and any differences compared to an IM-based sensor will be identified. Finally, we investigate and discuss the sensitivity, detection accuracy and figure of merit of operation of the NC sensor by comparison to an equivalent IM sensor.

3.1.1 History of Nanocomposite Materials

To begin, we'll briefly introduce the history surrounding the development of the first nanocomposite materials. To put a definite date on the creation of the first nanocomposite material is quite difficult, as throughout history, various nanoparticle based materials have been synthesized, and in many cases, the investors may not have necessarily known the

composition of their creation. Given the definition of a nanocomposite, it is feasible to believe that preparation could have taken place as early as the 4th century when objects such as the Lycurgus cup was fashioned by embedding gold nanoparticles in a glass substrate. This artifact comprised of Au nanoparticles approximately (70nm) in diameter embedded in a (15mm) thick glass substrate, as revealed by transverse electron microscopy (TEM) (Barber and Freestone 1990). It has been also suggested that the first nanocomposite structures were created some time in the mid-19th century (Kickelbick 2006), where gold salts were reduced in the presence of natural gum consisting of hardened sap from acacia trees. Furthermore, it could be argued that Michael Faraday was a pioneer in nanocomposite research while he was attempting to create optically translucent Au films. During these experiments, he mechanically cut thin films of Au, and washed them with a solution of potassium cyanide with the aim of further reducing the film thickness. Faraday noticed a faint red colour in the residue leftover from the solution and suggested that there must be Au particles in the solution that are too small to be observed by the naked human eye (Faraday 1857). These gold colloid solutions are currently stored in the Faraday museum at the Royal Institution.

Moving swiftly forward in history, the first patent regarding a nanocomposite structure was filed in 1947, and later approved in 1950 (Carter 1950). Here, the author details the methods involved in suspending organoclay, and subsequently combining this with elastomer latex in order to create a reinforced latex composite. In 1991, the first commercial application of nanocomposite structures came about from a collaboration between Toyota and Ube chemical industries (Ryuichi *et al.* 1991). The researchers embedded montmorillonite (a naturally occurring silicate clay) in a nylon-6 polymer. This process greatly enhanced the thermal resistance and durability of the nylon polymer, and thus was adopted as a cover for their timing belts. This sparked a global interest in nanocomposite materials, and in addition to competition from rival companies, resulted in exponential growth in the research carried out on nanocomposite materials (Gao 2004; Robert 2011).

3.1.2 Pd based Nanocomposite Materials

For this research, we will focus on the developments that have taken place in Pd based nanocomposite structures. Several of these materials have been adapted for gas sensing applications. For example, Meka *et al.* have developed a Pd polycarbonate nanocomposite that undergoes a change in electrical resistance in the presence of SO_2. Transverse electron microscopy (TEM) images have revealed that the volume fraction of their nanocomposite

was (2%) Pd, and the suspended nanoparticles were approximately (15nm) in diameter (Meka D. 2008). A carbonaceous palladium (Pd:C) nanocomposite has similarly been developed (Krawczyk *et al.* 2014), which demonstrates an increase in resistivity upon exposure to ammonia. TEM images show Pd nanoparticles of (5-10nm) in diameter with an fcc lattice structure. A Pd-ZnO nanocomposite has been developed for the purpose of acetone sensing (Alexiadou *et al.* 2017). These devices help to demonstrate the versatility of a Pd based nanocomposite.

Various Pd based nanocomposites have also been developed specifically for the purpose of hydrogen sensing. Mubeen *et al.* have created a single walled carbon nanotube Pd nanocomposite for applications in H_2 sensing (Mubeen *et al.* 2007), however, the response time is of the order of minutes. Similarly, a chemi-resistive based nanocomposite H_2 sensor has been investigated by Kandyla *et al.*, which employed Pd:NiO (Kandyla *et al.* 2014). The authors report success in detecting H_2 at concentrations as low as 300ppb, though the response time of the device was approximately 10 minutes, and thus like the device employed by Mubeen *et al*., was not suitable for rapid H_2 detection.

Synthetization of various kinds of graphene Pd nanocomposite structures has been demonstrated (Sundaram *et al.* 2008; Xu *et al.* 2008; Gotoh *et al.* 2009; Omidvar *et al.* 2017), and H_2 sensitivity has been demonstrated by Lange *et al.* with the use of a graphene Pd nanocomposite (Lange *et al.* 2011), which demonstrated cross sensitivity to NO_2 and water vapour, and operated with a response and regeneration time of a few minutes. Similarly, numerous other Pd based nanocomposites have been exploited for their sensitivity to H_2 gas. Zou *et al.* produced a Pd sodium-carboxymethyl-cellulose nanocomposite which demonstrates sensitivity to H_2 (Zou *et al.* 2012). Single walled carbon nanotube Pd nanocomposites have reported response times of the order of several minutes for H_2 sensing (Mubeen *et al.* 2007).

Alternatively, some researchers have chosen to employ Pd based nanoparticles for H_2 sensing applications. Pd doped ZnO nanoparticles 0.5% wt, of (16.2-16.5nm) in diameter have demonstrated response to H_2 gas 200-300˚C (Do *et al.* 2014). A single mode fibre of (5-10μm) in diameter covered with a with a thin layer of PdAu nanoparticles has been reported (Monzón-Hernández *et al.* 2010), which demonstrates reversible responses to 4% H_2 in a time of (2-4s). The rapid sensor response can be attributed to the change in the dielectric

permittivity of the PdAu nanoparticles upon H_2 exposure. Unfortunately, no information on the cross sensitivity, stability, or the long-term durability of the device was reported.

In another study, Pd nanoparticles were generated on the surface of silica through dewetting of thin Pd films that previously underwent modification of their continuous structure to increase surface roughness by oxidation and reduction (Kracker *et al.* 2014). The magnitude of the optical response to H_2 was found to improve as a result of this process, and a minimal sensor response time was reported. In addition, an irreversible reduction from PdO to Pd was observed on the initial exposure to H_2. Similar responses have been observed previously with a dewetted Pd film initially of 12nm (Kracker *et al.* 2013). While Pd based nanoparticles typically operate with a very fast response time, they are subject to greater damage from chemical poisoning due to surrounding environmental gases than nanocomposite Pd based structure (Sta *et al.* 2016).

Tabassum *et al.* have reported the use of a nanocomposite consisting of Pd nanoparticles embedded in a ZnO dielectric matrix both theoretically (Tabassum and Gupta 2015) and experimentally (Tabassum and Gupta 2016a). The Pd:ZnO NC was synthesised by suspending various concentrations of Pd in in distilled water, and adding 0.05M ZnO. The volume fractions of Pd investigated were (0.15, 0.025, 0.3, 0.4, 0.55, 0.85). In addition, experimental measurements were made using structures consisting of pure ZnO, and pure Pd, for volume fraction values of 0 and 1.0 respectively. This nanocomposite structure was employed in a multilayer optical fibre configuration, where a change in dielectric permittivity of the composite structure was reported during hydrogen loading. This device performed with a response time around (1 minute), with an optimal Pd volume fraction of (0.4). In terms of selectivity, their nanocomposite structure was exposed to H_2S, Cl, and N_2, where a very mild cross sensitivity was reported, thus indicating the sensor is highly selective to H_2. Finally, in terms of durability, there was a diminished response in the transmitted power through the fibre upon subsequent use, as expected with a pure Pd based H_2 sensor.

Ohodnicki *et al.* developed nanocomposite structures consisting of Pd nanoparticles embedded in a SiO_2 matrix at 600˚C and 950˚C (Ohodnicki *et al.* 2015). These structures were used for hydrogen sensing based on evanescent wave absorption spectroscopy. Ultra high resolution transverse electron microscopy demonstrated that the size of the Pd nanospheres in the silica structure were (5-10nm) in diameter, and (3-5nm) in diameter, at the larger and smaller temperatures respectively. The authors observed partial oxidation of the Pd

nanoparticles near the surface of the composite, which is attributed to occur during the calcination process. Since then, the authors have been granted a patent for their H_2 sensing structure (Ohodnicki *et al.* 2017).

3.2 Modelling Nanocomposite structures

Maxwell Garnett presented a two part paper series (Garnett 1904; Garnett 1906) that applied the Lorenz-Lorenz and/or the Clausius-Mossorri relations (Mossotti 1850; Lorenz 1869; Clausius 1879; A. 1881) to allow one to determine the optical function of nanocomposite structures. The effective dielectric permittivity ε_{eff} of a nanocomposite structure consisting of metallic nanoparticles homogeneously embedded in a dielectric matrix can be determined using the Maxwell Garnett relationship shown in equation (3-1), provided the wavelength of light is of a much larger scale than that of the individual nanoparticle dimensions. δ_m is the nanoparticle volume fraction, ε_m and ε_d are the dielectric permittivities of the metal nanoparticles and host dielectric material.

$$\varepsilon_{eff} = \varepsilon_d \left(\frac{2(1-\delta_m)\varepsilon_d + (1+2\delta_m)\varepsilon_m}{(2+\delta_m)\varepsilon_d + (1-\delta_m)\varepsilon_m} \right) \quad (3\text{-}1)$$

Soon after, Mie developed a size dependant theory that describes the optical functions of metallic spheres (Mie 1908). It is possible however to simply use the Maxwell Garnett approximation in place of the size dependent theory, and many researchers have opted to employ this method (Sarika and Gupta 2010; Rani *et al.* 2014; Ohodnicki *et al.* 2015; Tabassum and Gupta 2015; Shah *et al.* 2016).

One constraint of the Maxwell Garnet theory that has on some occasions been ignored is the upper limit of the nanoparticle volume fraction that permits accurate determination of the nanocomposite optical function. Conceptually, the upper limit of spherical particles in close proximity with one another if one employs a geometric fcc lattice packing structure cannot exceed (≈75%) (Sharma and Gupta 2007; O'Toole and Hudson 2011). However, when modelling the optical function NC structures, discrepancies occur between the Maxwell-Garnett first order solution, and optical measurements occur at volume fractions below this value (Doremus 1966; Yoshida *et al.* 1971).

Prior to the Maxwell-Garnett model, many researchers have attempted to derive an empirical solution that describes the optical function of NC materials (Maxwell 1873; Rayleigh 1892). Lord Rayleigh, made a small error in derivation that prevented his model from accurately predicting optical behaviour. These were corrected by Runge and McKenzie *et al*. (Runge 1925; McKenzie and McPhedran 1977). Meredith and Tobias extended Lord Rayleigh's model to account for the order of 2^5 terms (Meredith and Tobias 1960), and McKenzie *et al.* extended this mode further up to 2^7 (McKenzie and McPhedran 1977). In their paper, McKenzie *et al.* determined the NC optical function using their multi-pole model, and compared it to experimental data from both (Meredith & Tobias) (Meredith and Tobias 1960), and (Kharadly & Jackson) (Kharadly and Jackson 1953). They concluded that the Maxwell-Garnett model should be substituted for a multipole model for volume fractions above 0.3 (McKenzie and McPhedran 1977).

It is important to note however that early research carried out on nanocomposite structures may have been hindered by the fact that the shape of the particles might not have been necessarily spherical, and (especially with particularly thick composite films) individual particles may have been partially aggregated. Thus, any attempt at determine the optical properties using a model that necessitates uniform distribution of particles will be hindered. Keeping this in mind, we also look at experiments carried out by Ung *et al.* in the more recent past (Ung *et al.* 2001), where layer-by-layer assembly was used to prepare the Au:SiO_2 films of varying volume fractions. TEM images showed Au nanoparticles embedded in the SiO_2 composite ranging from (1.5-17.5nm) in thickness. The experiments demonstrated agreement between the measured optical function of their Au:SiO_2 nanocomposite and to that predicted by the Maxwell Garnett theory, up to 50% volume fraction, but a divergence thereafter. Singh and Gupta have investigated the used of nanocomposite materials consisting of Au, Ag, ITO embedded in TiO_2, WO_3, and SnO_2 using the Maxwell Garnett model (Sarika and Gupta 2010). In their simulations, volume fractions from (55-85%) were used, however no comparison was made between the results from this paper and experiment. In light of the findings stated in this section we conclude that the volume fraction of the nanocomposite structure should therefore be small enough such that experimental measurement of the dielectric permittivity matches the results of the Maxwell-Garnett model. For this reason, we initially employ a (δ_m=20%) volume fraction in order to investigate the general operation of the nanocomposite device. Later we investigate the influence that the volume fraction has on sensor performance from (δ_m=5-40%).

3.3 Results

In this work, we propose the use of a nanocomposite structure (NC) consisting of Pd nanoparticles embedded in a host SiO_2 dielectric matrix for use in an OFSPR hydrogen sensor. The performance of this device is compared to that of the more commonly investigated individual multilayer (IM) device (F. Downes and C. M. Taylor 2017). A close up schematic representation of each sensing structure is displayed in Fig. 3-1(A & B), where multilayer sensing structures appear on unclad sections of step-index multimode silica optical fibres. We measure the performance of each device by calculating the sensitivity and detection accuracy, which allows us to determine the suitability of each device for various hydrogen sensing applications.

3.3.1 General Sensor Parameters

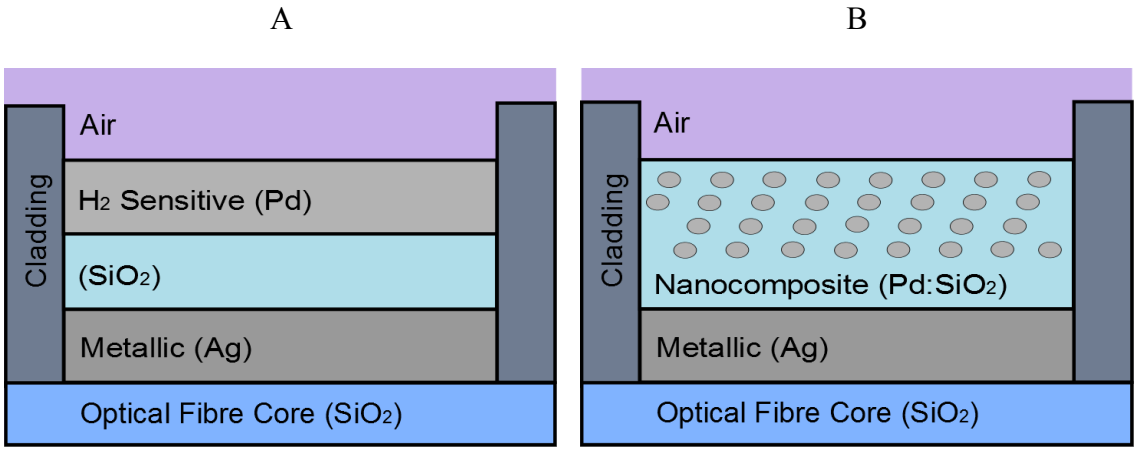

Figure 3-1 – (A) Close up schematic representation of the multilayer sensing structure within the optical fibre sensing configuration consisting of Ag/SiO_2/Pd multilayer sandwich structure. (B) Nanocomposite multilayer sandwich structure consisting of Ag/Pd:SiO_2 nanocomposite.

We will begin by introducing the relevant materials and size of each material used in our OF sensing configuration. Following from Chapter 2, the IM device has parameters (NA=0.22), sensing length (L=1cm), silica core diameter (D=2μm), and consists of a multilayer stack sensing structure Ag, SiO_2 and Pd. Ag, SiO_2, and Pd were chosen as $d1_{IM}$, $d2_{IM}$, and $d3_{IM}$ for the reasons mentioned in Chapter 1. In order to make accurate comparison between the performance of IM and NC sensing devices, the NC structure employs the same fibre parameters as the IM model: NA, sensing length, core diameter, as well as similar multilayer materials and thicknesses. The metallic layer material and thickness of the IM and NC

structures will be equal ($d1_{IM} = d1_{NC}$), where both $d1_{IM}$ and $d1_{NC}$ are continuous Ag films. This ensures that fair comparison can be made between the performances of each device.

Numerous choices are available for the NC-modulation layer, including SiO_2 (Perrotton *et al.* 2011b; Perrotton *et al.* 2013; Ohodnicki *et al.* 2015; Ohodnicki *et al.* 2017) ZnO (Tabassum and Gupta 2015; Shah *et al.* 2016; Tabassum and Gupta 2016b), and Ta_2O_5, (Hosoki *et al.* 2013; Hosoki *et al.* 2014; Hosoki *et al.* 2016). SiO_2 exhibits similar optical function to ZnO and Ta_2O_5, though the real component of the refractive index is smaller over the observational range investigated in this work. In addition SiO_2 has been shown to be highly permeable to H_2 (Fishbein *et al.* 1987; Mrstik *et al.* 1993), which is essential for a hydrogen sensing composite structure. Experimental and theoretical research has been carried out on Pd-SiO_2 nanocomposites, and were found to be in close agreement (Ohodnicki *et al.* 2013; Ohodnicki *et al.* 2015; Ohodnicki *et al.* 2017). Thus, we chose to employ a NC structure consisting of Pd nanoparticles embedded in a SiO_2 dielectric matrix. Additionally, this will allow for easy comparison to be made between the NC device and the previously investigated series of IM structures in Chapter 2.

Similarly to the metallic films $d1_{IM}$ & $d1_{NC}$, the modulation layer thicknesses of each device $d2_{IM}$ and $d2_{NC}$ will be equal where possible, in order to make fair comparison between the performance of each device. The IM-modulation layer $d2_{IM}$ is comprised solely of SiO_2; and the NC-modulation layer $d2_{NC}$ is comprised of SiO_2 embedded with Pd nanoparticles. In terms of modelling; the Brendel Bormann model is used in determining the dielectric permittivity of Ag and Pd (Brendel and Bormann 1992), and Sellmeier Dispersion formulae are used to determine the refractive indices of thin film SiO_2 (Postava and Yamaguchi 2001) and the silica fibre core (Malitson 1965). The normalised output power is determined using the characteristic transfer matrix model, as outlined in Chapter 1. Maxwell-Garnett theory is used to determine the dielectric permittivity of the NC-modulation layer, as illustrated in equation (3-1) (Garnett 1904; Garnett 1906). When considering the volume fraction of Pd in the NC-modulation layer, we recall that McKenzie and McPhedran made note that discrepancies between the Maxwell-Garnett equation, and optical measurement have arose using nanocomposites above a certain volume fraction (McKenzie and McPhedran 1977). Thus, we will initially use a relatively low NC Pd volume fraction of (δ_m=0.2).

Finally, we mention the spectral range of our sensor. Previously, in Chapter 2 the operation of the sensor was investigated in the spectral range (λ=450:900nm) which followed the trend of

numerous other researchers who have reported positive results in this range (Perrotton *et al.* 2013; X.G. Wang *et al.* 2013a; Tabassum and Gupta 2015; F. Downes and C. M. Taylor 2017). Nevertheless, it is possible to expand the spectral sensing range of our device. Von Rottkay's experiments have demonstrated that the Pd dielectric permittivity changes in the presence of hydrogen gas up to 2000nm. Our preliminary results indicate that NC structures exhibits strong resonance in the near-IR part of the spectrum (Fionn Downes and Cian M. Taylor 2017). As a result of this, we expanded the range of input wavelength to (λ=450:2000nm) in modelling the IM and NC devices.

3.3.2 Response Time, Selectivity and Durability

The response time of the the IM structure consisting of a (3nm) thick Pd film is expected to operate similar to that of Liu, 4s to 4% H_2 (Liu and Li 2016b). The response time of the NC based device can be derived by referring to the experiments carried out by Tabassum *et al.*, who reported a sensor response and recovery time of (1 minute), using a Pd-ZnO composite with (δ_m=0.4) volume fraction. The longer response time of the NC based device compared to the individual multilayer structure can be partly attributed to the additional time required for hydrogen to permeate through the dielectric component that makes up the composite structure. While this time could be improved to a few seconds by employing individual Pd nanoparticles (Monzón-Hernández *et al.* 2010), the structure would suffer in terms of the aforementioned problems from Chapter 2 associated with a solely Pd based hydrogen sensor regarding blistering, cracking, flaking, and overall rapid degradation with use.

Insight into the selectivity of the device can be gained by reviewing the highly selective properties of a Pd based hydrogen sensor (Huebert *et al.* 2011), which operate with minimal cross sensitivity to other gases, as previously mentioned in Chapters 1 & 2. Pd based nanocomposites are expected to operate similarly in terms of selectivity to Pd continuous film structures, although the inclusion of an inert material such as SiO_2 as a NC component can help to filter some of the potentially harmful gases such as CO (Ohodnicki *et al.* 2015) which improves the selectivity of the NC structure.

With regards to the durability of the nanocomposite structure, a number of factors are considered. The Pd nanoparticles are expected to undergo excessive expansion contraction during hydrogen loading cycles due to the $\alpha \rightarrow \beta$ phase transition of the Pd lattice structure (Y. Liu *et al.* 2012a). Since the Pd volume fraction is quite low, and the physical volume of the

individual Pd nanoparticles is also small; there exists a large distance between each Pd nanoparticle and its nearest neighbouring Pd nanoparticle. Thus, the damage resulting from Pd lattice expansion upon hydrogenation would be less than that of a Pd continuous film, where each Pd atom is in close proximity with its nearest neighbouring Pd atom. Furthermore, the presence of an inert material such as SiO_2 in the nanocomposite structure provides some protection for the Pd nanoparticles from potentially damaging atmospheric gases such as CO, CO_2, H_2S (Palmisano *et al.* 2015), and thus, extends the longevity of the composite layer compared to a pure Pd continuous film. Hence, the durability of the NC device is expected to be superior to that of the IM that employ a Pd continuous film structure.

Specifically with regards to the NC structure, we refer to refer to the experiments carried out by Tabassum *et al.*, where (0.96 N_2 + 0.04 H_2) gas was introduced into their Pd-ZnO NC gas chamber for (≈1min), left for (≈1min), removed over the course of (≈1min), and left removed for (≈1min); This cycle was repeated a number of times on approximately the same timescale. They reported a minor reduction in response after on the third cycle of H_2 loading compared to the initial response (Tabassum and Gupta 2016a).

The experiments carried out by Ohodnicki *et al.* employed longer H_2 loading and unloading times on the scale of (≈30mins) compared to Tabassum *et al.* (≈1min), using their Pd-SiO_2 NC structure. Similarly, they report a reduction in response with loading cycles (Ohodnicki *et al.* 2015). Consequently, the durability of our NC is expected to be quite high compared to a pure Pd based structure, but ultimately, like the continuous film structure, performance will reduce marginally with hydrogen loading cycles.

3.3.3 Layer Thickness within the Multilayer

3.3.3.1 Normalised Output Power

In order to determine the influence that that metallic layer thicknesses $d1_{IM}$ and $d1_{NC}$ have on performance, the normalized output power was determined for three sensing configurations with ($d1_{IM} = d1_{NC}$) and ($d2_{IM} = d2_{NC}$). The parameters chosen for d1 and d2 chosen such that comparison can be easily made with previous investigations from Chapter 2 Fig. 2-5(A), (d1=20, 40, 60nm) and (d2=100nm), where the hydrogen sensitive layer $d3_{IM}$ comprises solely of Pd. In order to highlight the contrasts in the output from the IM and NC devices, the output power was determined initially in the absence of hydrogen gas. The introduction of

hydrogen gas results in a shift of the resonance conditions in both the IM and NC devices, and has a minor influence of the shape of the normalized power versus wavelength plot.

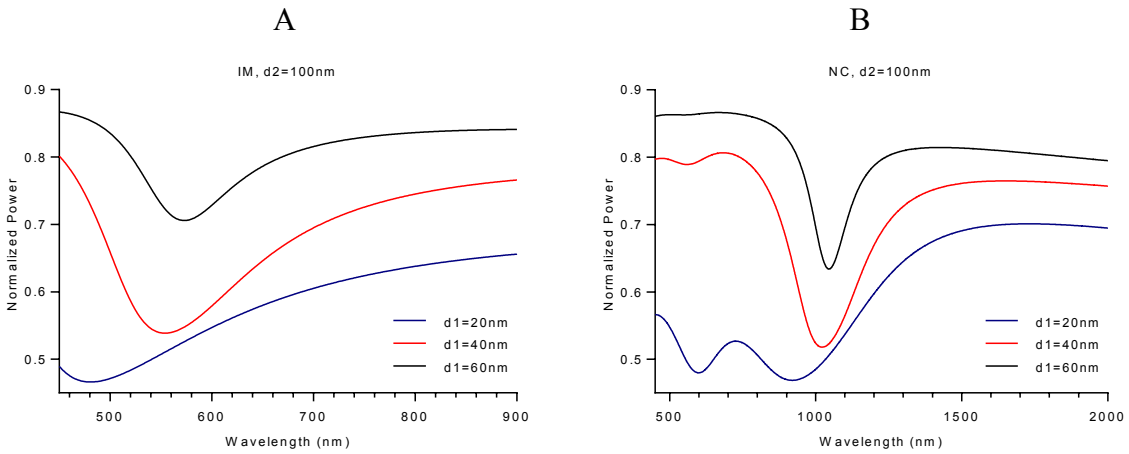

Figure 3-2 – (A) Normalised output power across the spectral domain of Ag/SiO_2/Pd multilayer sandwich structure OFSPR sensor in the absence of H_2; (λ=450:900nm), Ag(d1=20,40,60nm), SiO_2(d2=100nm), Pd(d3=3nm). (B) Nanocomposite structure consisting of Ag/Pd:SiO_2 composite, Pd:SiO_2(d2=100nm), volume fraction of Pd nanoparticles (δ_m=0.2), (λ=450:2000nm).

Fig. 3-2(A) demonstrates the normalised power output through an IM based optical fibre, which is illustrated in Fig. 3-1(A). Fig. 3-2(B) demonstrates the normalised power output through a NC based optical fibre, which is illustrated in Fig. 3-1(B). In the NC device, Fig. 3-2(B), it can be seen that resonance occurs at a much larger wavelength than the IM structure in Fig. 3-2(A). Since the thickness of the modulation in each device ($d2_{IM}$ & $d2_{NC}$) displaces the spectral location of the resonance condition, the observed larger resonance locations of the NC device indicates that the NC-modulation layer causes a greater resonance shift than an equal thickness of the IM-modulation layer. The observed increased displacement in the NC is attributed to the presence of the Pd nanoparticle component of the composite layer, which causes an increase in the real component of the composite refractive index.

The magnitude of the normalised power at resonance of all three NC devices depicted in Fig. 3-2(B) is close to that of each IM device Fig. 3-2(A). This close similarity stems from the equal metallic layer thicknesses $d1_{IM}$ and $d1_{NC}$. As we've mentioned previously in Chapter 1, the thickness of the metallic layer is primarily responsible for the magnitude of the extrinsic (radiation) damping, and consequently, the depth of the resonance condition. This behaviour can be confirmed by looking at Fig. 3-3(A) where the same behaviour of the resonance depth is seen despite the larger modulation layer thickness of 180nm compared to the current thickness of 100nm. In other words, the metallic layer thickness, rather than the modulation

layer thickness is the dominant factor influencing the resonance depth in this case. Finally, observing the influence that $d1_{NC}$ has on the resonance condition in Fig. 3-2(B) it can be seen that increasing $d1_{NC}$ results in a red shift of the resonance dip, and a decrease in resonance depth; similarly to that observed with increasing $d1_{IM}$ in Fig. 3-2(A). These observations made from Fig. 3-2(B) can be understood as a decrease in the real surface plasmon propagation constant, and a change in the extrinsic damping respectively.

Next, in order to further establish the influence that metallic layer thickness has on the NC device, as well as the modulation layer thickness compared to the IM structure; we determined the output power using a range of other parameters of d1 and d2, previously investigated in Chapter 2. These structures appear in Fig. 3-3, where (A, C, E) illustrate the output from IM based devices, and (B, D, F) illustrate the output from the respective NC based devices of equal fibre dimensions and multilayer thicknesses. The $d1_{IM}$ and $d2_{IM}$ in Fig. 3-3(A) are equal in thickness to the $d1_{NC}$ and $d2_{NC}$ in Fig. 3-3(B). The same equivalence applies to the pair of figures Fig. 3-3(C & D), and also to Fig. 3-3(E & F).

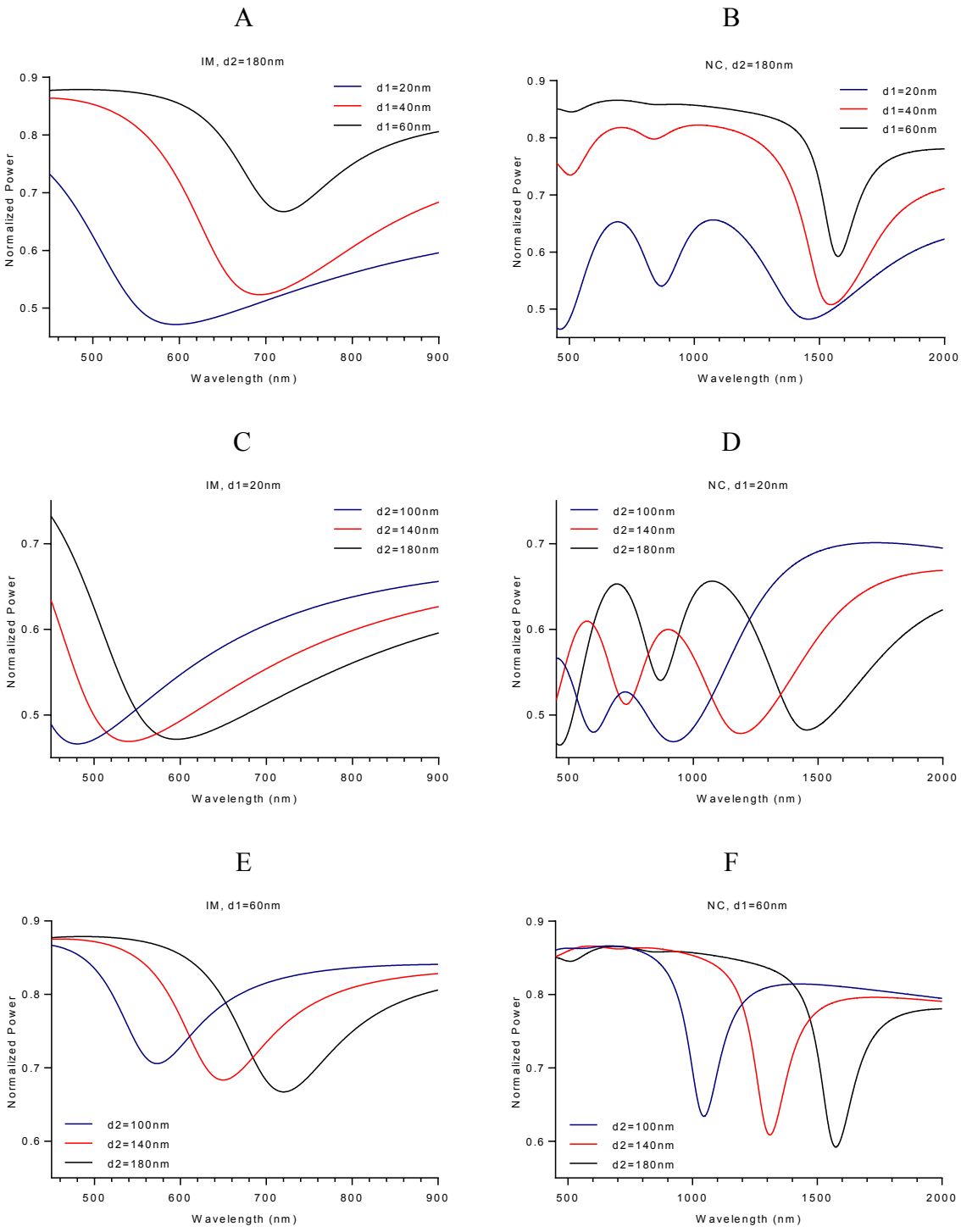

Figure 3-3 – (A) Normalised output power across the spectral domain of a Ag/SiO_2/Pd multilayer sandwich structure OFSPR sensor in the absence of H_2; (λ=450:900nm), Ag(d1=20,40,60nm), SiO_2(d2=180nm), Pd(d3=3nm). (B) Nanocomposite structure consisting of Ag/Pd:SiO_2 composite, Pd:SiO_2(d2=180nm), (δ_m=0.2), (λ=450:2000nm). (C) IM: Ag(d1=20nm), SiO_2(d2=100,140,180nm). (D) NC: Ag(d1=20nm), Pd:SiO_2(d2=100,140,180nm). (E) IM: Ag(d1=60nm), SiO_2(d2=100,140,180 nm). (F) NC: Ag(d1=60nm), Pd:SiO_2(d2=100,140,180nm).

Looking at Fig. 3, we observe that each NC structure displays similar behaviour to its respective IM structure with increasing d1 and d2 thickness in terms of the magnitude of the resonance dip, and spectral shift of the resoance condition. At this stage, it is difficult to determine the influence that $d1_{NC}$ and $d2_{NC}$ have on the spectral width of the resonance condition, and thus further investigation into the detection accuracy of the NC is required.

3.3.3.2 Reflectance

One unusual observation that is evident in Fig. 3-2(B), & 3(B, D) is the presence of additional resonances at shorter wavelengths. In order to investigate the origin of these additional resonance dips, the reflectance from the IM and NC multilayer structures is determined. This simulation is performed by constructing a Kretschmann configuration (as outlined in Chapter 1) where the optical fibre is replaced by a dielectric prism of fused SiO_2, and the IM structure overlays the prism. Similarly a Kretschmann configuration is employed using a NC in place of the IM. The reflectance is measured using the Fresnel coefficients described in Chapter 1.

The reflectance from s- & p- polarised light was determined independently using three angles equally spaced that constitute the operational range of the fibre. This involved a small angle close to the optical fibre critical angle: $\theta_{low} = \theta_C + 1^\circ$, an angle in the middle of the operational range: $\theta_{mid} = \theta_C + (90^\circ - \theta_C)/2$, and a large angle near the upper part of the operational range: $\theta_{high} = 90^\circ - 1^\circ$, where θ_C is the critical angle.

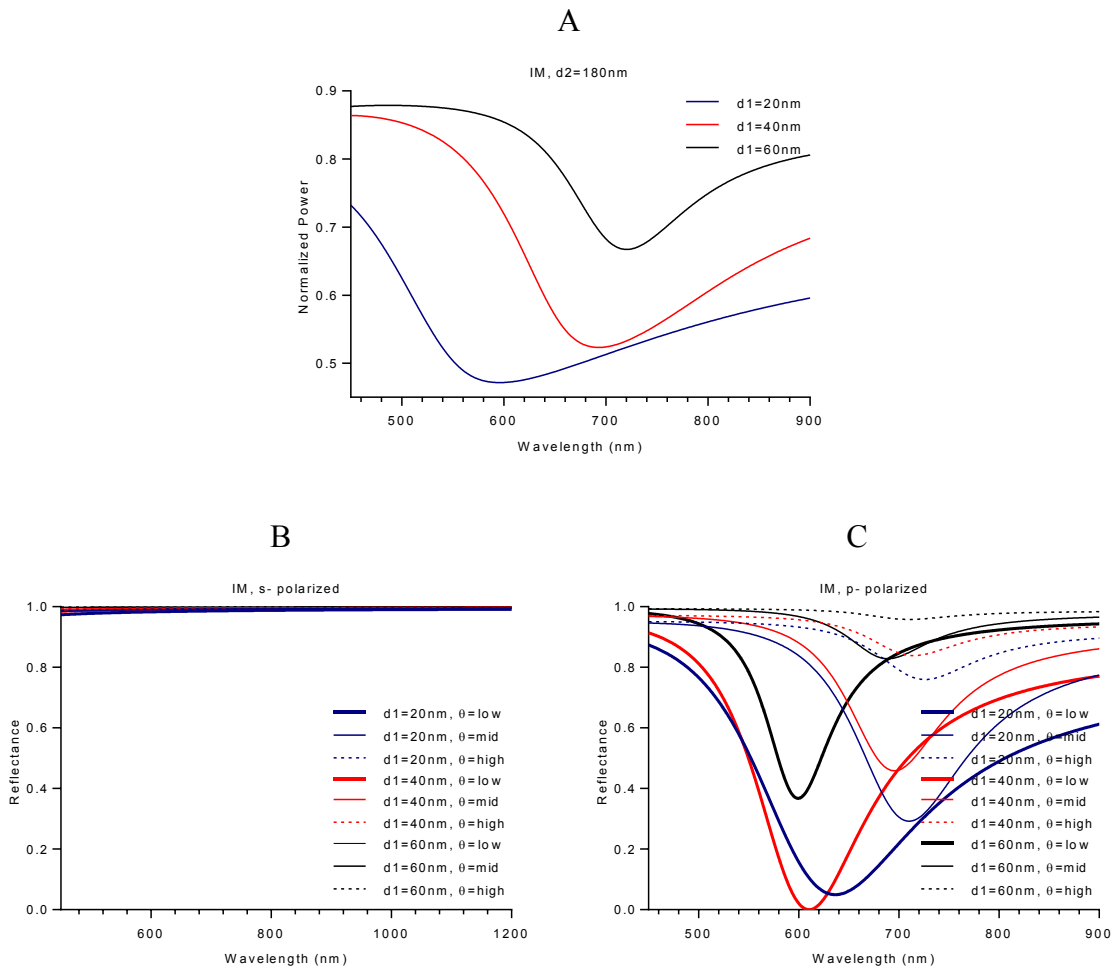

Figure 3-4 – (A) Reprint of Fig. 3-3(A) in this chapter, where (λ=450:900nm), Ag(d1=20,40,60nm), SiO_2(d2=180nm), Pd(d3=3nm). (B) s- polarised reflectance from the IM structure in Fig. 3-4(A) of three angles (ϑ_{low}, ϑ_{mid}, ϑ_{high}) defined above. (C) p- polarised radiation from the IM structure in Fig. 3-4(A).

Fig. 3-4(A) displays the normalised output power from a series of IM configurations. Fig. 3-4(B) shows the s- polarised reflectance, and Fig. 3-4(C) p- polarised reflectance that make up part of the observed output power in Fig. 3-4(A). In Fig. 3-4(B), showing the s- polarised reflectance from a series of IM structures, we observe that most of the light is reflected, and no resonance dip can be detected. As s- polarised light cannot stimulate surface plasmon resonance, this observation is expected. In Fig. 3-4(E), where we shine p- polarised light on the IM structures, we observe resonance at specific angles, resulting from the stimulation of surface plasmons in the metallic layer. This resonance is expected, and manifests as the normalised output power resonance dip seen in Fig. 3-4(A).

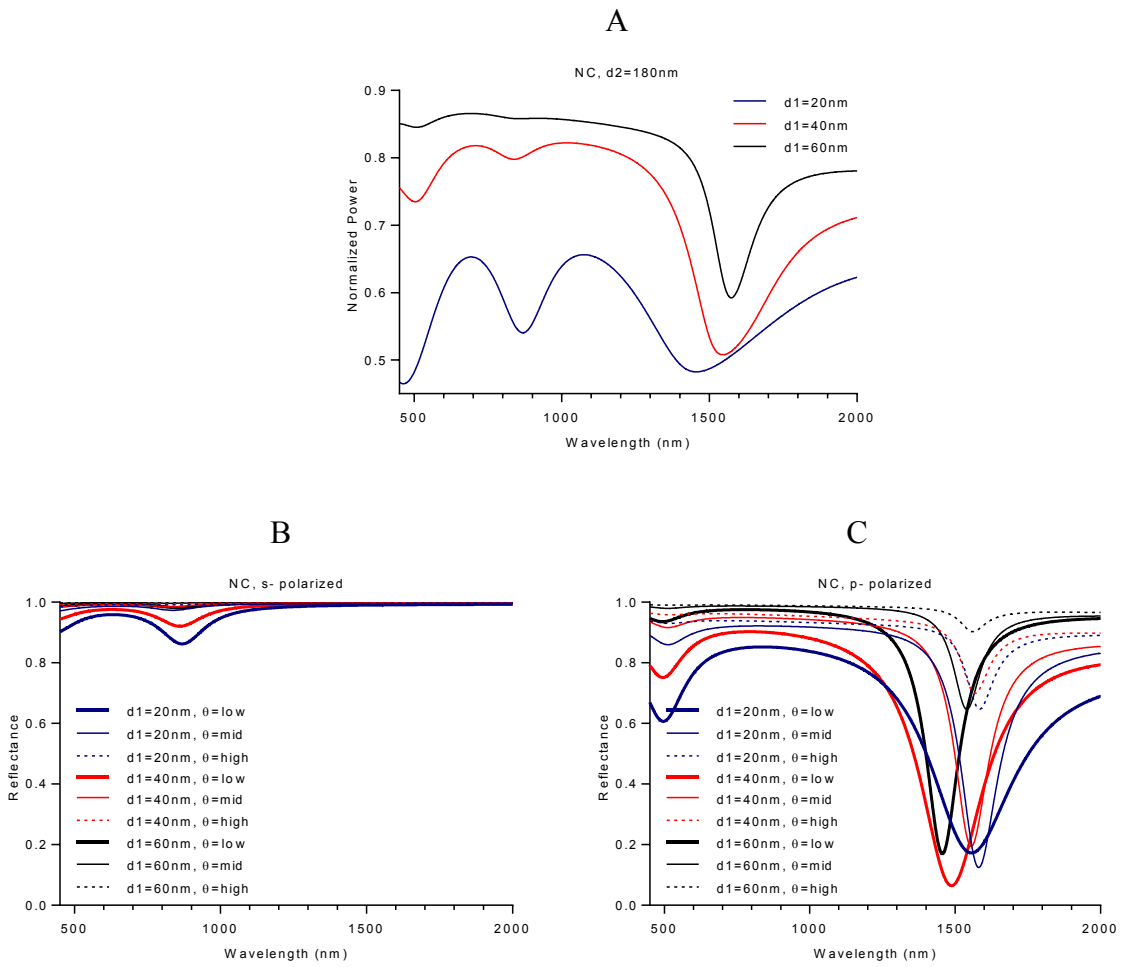

Figure 3-5 – (A) Reprint of Fig. 3-3(B) above in this chapter, where (λ=450:2000nm), Ag(d1=20,40,60nm), Pd:SiO_2(d2=180nm), Pd(d3=3nm). (B) s- polarised reflectance from the NC structure in Fig. 3-5(A) of three angles (ϑ_{low}, ϑ_{mid}, ϑ_{high}) defined above. (C) p-polarised radiation from Fig. 3-4(B).

Fig. 3-5(A) displays the normalised output power from a series of NC structures, and Fig. 3-5(B & C) demonstrate the s- & p- polarised reflectance that make up the output power in Fig. 3-5(A). In Fig. 3-5(B), where s- polarised light is shone on onto a series of NC structures, we observe a small resonance effect, which we attribute to a type of waveguide resonance in the nanocomposite layer (Abbas *et al.* 2011b). In Fig. 3-5(C), showing p- polarised reflectance from the NC structure, we observe a deep resonance at long wavelengths which is attributed to the stimulation of surface plasmons. Additional resonance dips can be seen in Fig. 3-5(C) at shorter wavelengths, which we also attribute to waveguide resonance. Later in Chapter 5, we investigate the stimulation of waveguide resonance further, however for this chapter we will continue to focus on the resonance modes that are formed due the stimulation of surface plasmons in the NC based devices.

3.3.4 Operational Range

Next we investigate the operational range of each device. Typically, the IM structure has operated within the visible and near-IR part of the wavelength spectrum (Perrotton *et al.* 2013; X. Wang *et al.* 2013b; Tabassum and Gupta 2016a). However by increasing the thickness of the dielectric modulation layer, it is possible to push resonance farther into the IR. By increasing the thickness of the modulation layer to a large degree, we were able to achieve resonance above 1500nm. This is demonstrated in Fig. 3-6(A & B).

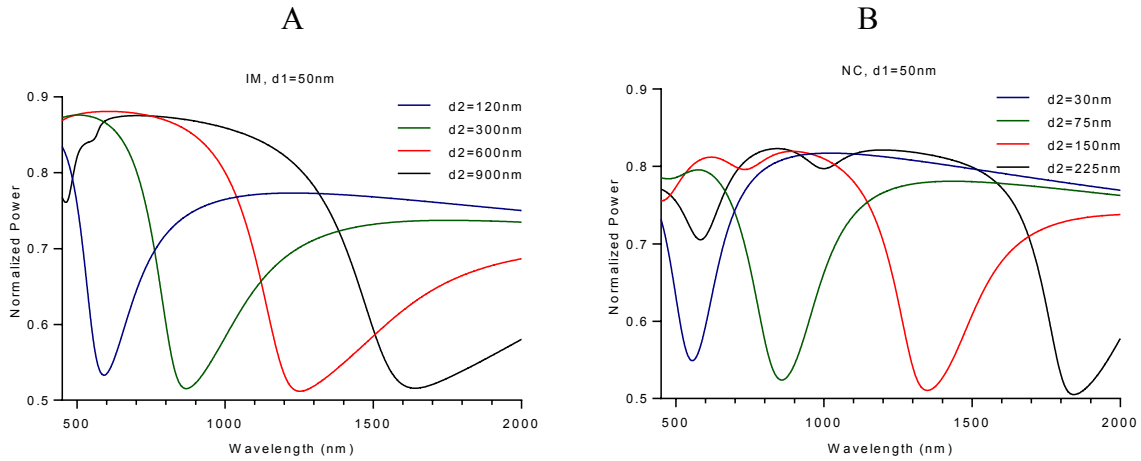

Figure 3-6 – (A) Normalised output power across the spectral domain of a Ag/SiO_2/Pd multilayer sandwich structure OFSPR sensor in the absence of H_2; (λ=450:2000nm), Ag(d1=50nm), SiO_2(d2=120,300,600,900nm), Pd(d3=3nm). (B) Nanocomposite structure consisting of Ag/Pd:SiO_2 composite, with Pd:SiO_2(d2=40,75,150,225nm), a factor of 4 smaller than the corresponding IM-modulation layer thicknesses, and (δm=0.2).

In Fig. 3-6, the normalized output power of various IM and NC structures are investigated with varying modulation layer thicknesses. We observe that the IM structure requires a significantly larger modulation layer thickness than the NC based device for an equivalent wavelength resonance shift, which can be attributed to the increase in the real permittivity component of the composite layer by the inclusion of Pd nanoparticles. It can be observed that the spectral width of the IM structure is narrower than the NC at shorter wavelengths, thus demonstrating superior detection accuracy. However, the spectral width of the IM structures can be seen to increase significantly with resonance wavelength. Thus, in the near-IR spectral range, the spectral width of the observed NC structures is sharper than the corresponding IM structures.

In Fig. 3-6, it should be noted that we have demonstrated that both the IM and NC devices can produce surface plasmon resonance in the near-IR range, which typically has not been explored by many researchers in the past. Although both sensor types can stimulate resonance in the visible as well as the near-IR parts of the wavelength spectrum, at this stage it is unclear what impact the introduction of H_2 will have on the resonance condition of each device. Thus, it is pertinent to investigate the performance of each device with regards to the magnitude of the resonance shift in the presence of H_2 (sensitivity), the spectral width of the resonance condition (detection accuracy), and figure of merit (combination of the both). The methods of determining each of these performance metrics are discussed in Chapters 1 & 2.

3.3.5 Performance of IM and NC structures

The performance of a number of IM and NC devices were determined. Three metallic layer thicknesses ($d1_{IM}$=$d1_{NC}$=Ag=40, 50, 60) are investigated where the parameters were chosen such that they would encompass the previously determined optimal Ag thickness in the IM based structure calculated in Chapter 2. The modulation layer thicknesses investigated are in the range of thicknesses that permit sensing across the observed wavelength spectrum (λ=450:2000nm) in both the IM and NC based devices. The upper and lower limits of performance measurements in the spectral domain were limited by the spectral widths of each resonance condition. For example, once the IM structure: ($d1_{IM}$=50nm), ($d2_{IM}$=960nm) is exposed to 4% H_2; resonance occurs at (λ=1780.74nm). However the longer wavelength at which resonance output power is 10% larger is (λ=1994.16nm). Since our sensing range is (λ=450:2000nm), any further increase in $d2_{IM}$ would not permit accurate measurement of the resonance spectral width, and thus the resonance wavelength of (λ=1780.74nm) is the upper limit of this set of IM configurations. Similarly, in the NC configuration, the thickness of the NC-modulation layer ($d2_{NC}$) was used to control the spectral resonance location. As we have demonstrated that equivalent IM and NC modulation layer thicknesses produce surface plasmon resonance at different spectral locations, we will no longer compare each device based on equivalent d2 thicknesses, and in place, we will determine the performance of each device at various wavelengths across the spectrum (λ=450:2000)nm.

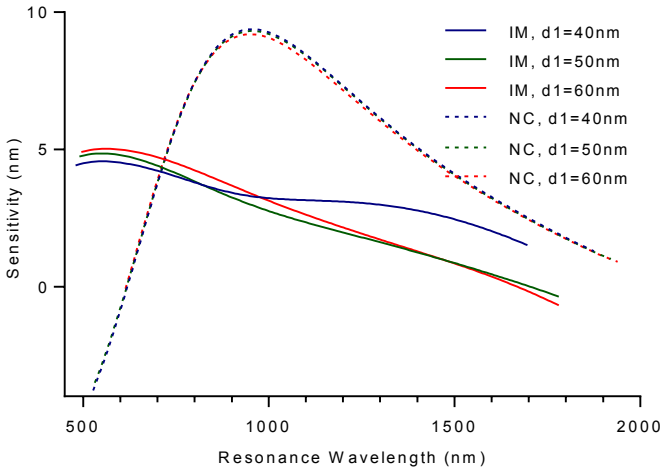

Figure 3-7 – Sensor sensitivity (SPR dip wavelength shift to 1% hydrogen) for several OFSPR configurations with Ag(d1=40,50,60nm), IM: SiO_2(d2=55:940nm), Pd(d3=3nm), NC: Pd:SiO_2(d2=28:234nm), (δ_m=0.2).

Fig. 3-7 displays the sensitivity of several IM sensing configurations (solid continuous lines). As explored previously in Chapter 2, it can be seen that sensitivity of the IM structures is maximum at short wavelengths, and decreases as IM-modulation layer thickness increases. Specifically, where ($d1_{IM}$=50, 60nm), the sensitivity decreases beyond zero into the negative at particularly high wavelengths, thus indicating a blue shift of the resonance condition in the presence of H_2. Observing performance of the NC sensor (dashed lines), it can be seen that sensitivity is initially negative at short wavelengths, and increases to a peak with increasing NC-modulation layer thickness. At this maximum, the sensitivity of each NC device can be seen to operate higher than each equivalent IM sensor. Specifically, when ($d1_{IM}$=$d1_{NC}$=50nm), the maximum sensitivity observed by the NC device is 9.31375nm, when paired with a modulation layer thickness of ($d2_{NC}$=82nm), and operates at a resonance wavelength of 956.01nm. The IM structure that operates at the nearest resonance wavelength has sensitivity 2.965nm, when paired with a modulation layer thickness of ($d2_{IM}$=335nm), and operates at a resonance wavelength of 955.56nm. We make note that this NC structure operates with a higher sensitivity than the corresponding IM structure at the same resonance wavelength by a factor of (314.10%). A further increase in $d2_{NC}$ causes results in a decrease in sensitivity in each structure. It is important to note that over much of the observed wavelength range, the NC structure operates with larger sensitivity than the equivalent IM structure. Finally, we note that the thickness of the Ag layer has very little influence on the sensitivity of the NC based device, as opposed to the IM structure. We can gain some insight

into this behavior in the NC device by following Abdulhalim *et al.* who have described sensor sensitivity as being determined by the overlap integral in the interaction volume as follows (Shalabney and Abdulhalim 2011):

$$\Delta k \approx \frac{k_i}{2} \frac{\int_{V_{in}} \Delta\varepsilon E_i^{\star} E_f dr}{\int_V \varepsilon E_i^{\star} E_i dr} \quad (3\text{-}2)$$

Where k_i and E_i are the wavevector and electric field before hydrogenation of the sensor, while E_f is the electric field after hydrogenation. The integral in the numerator of the fraction is performed over the interaction volume V_{in} which is the physical extent of the NC layer and the hydrogenation causes a shift of Δk in the wavevector and $\Delta\varepsilon$ is the permittivity change in the NC due to hydrogenation. The complex conjugate is represented by operator $\star$. The integral in the denominator is performed across the physical extent of the entire field and so is in effect a normalization term. Noting that the sensor sensitivity is represented by the term $\frac{\Delta k}{\Delta \varepsilon}$, we see that the key drivers of the sensitivity are the permittivity change at the resonance wavelength and the field amplitudes before and after hydrogenation. As these field amplitudes will be modulated by changes in the Ag layer, we conclude the main driver of sensitivity is the permittivity change at the resonance wavelength. This permittivity change in turn is due to the Pd component of the NC and is enhanced as the Pd concentration in the NC is increased. Therefore this term becomes even more dominant in terms of determining the sensitivity. Hence the thickness of the Ag layer has minimal effect on the sensitivity.

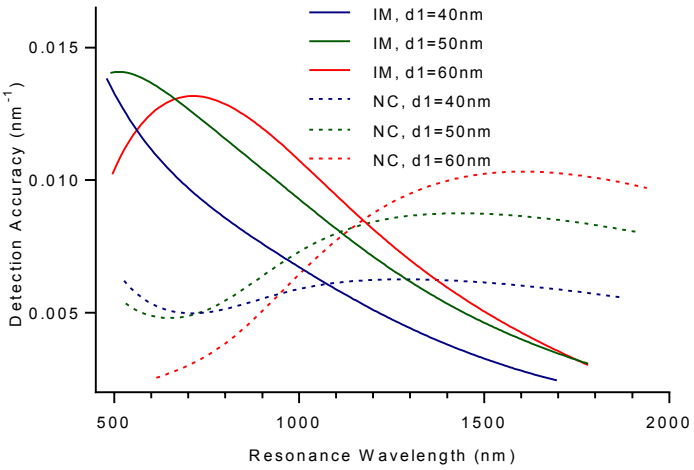

Figure 3-8 – Detection Accuracy (SPR dip wavelength shift to 1% hydrogen) for several OFSPR configurations with Ag(d1=40,50,60nm), IM: SiO_2(d2=55:940nm), Pd(d3=3nm), NC: Pd:SiO_2(d2=28:234nm), (δ_m=0.2).

Next it is appropriate to determine the detection accuracy of each device. Fig. 3-8 demonstrates that the detection accuracy of the IM & NC structures. We note that in the NC structures, the detection accuracy (which represents the linewidth of the resonance) is small at lower wavelengths and rises to a maximum before falling off. This indicates that there is an optimum resonance wavelength which gives the sharpest resonance. In the case of the IM sensor, this optimum resonance occurs in the visible range, whereas for the NC sensor, the sharpest resonance falls in the IR. This highlights the fact the NC sensor performs optimally in the IR, while the IM sensor performs optimally in the visible wavelength range.

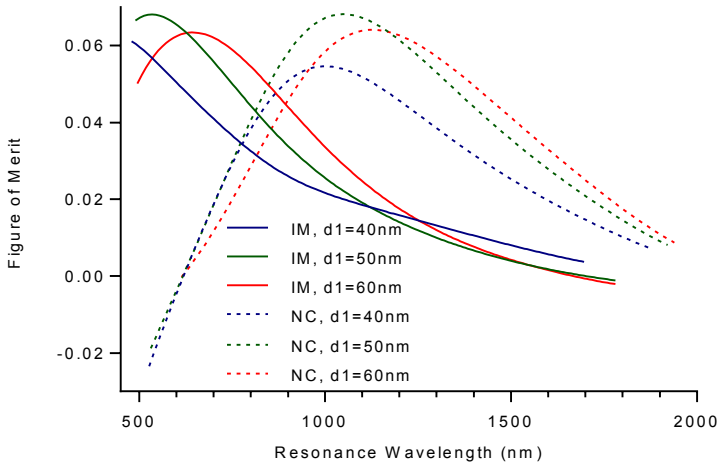

Figure 3-9 – Figure of Merit (SPR dip wavelength shift to 1% hydrogen) for several OFSPR configurations with Ag(d1=40,50,60nm), IM: SiO_2(d2=55:940nm), Pd(d3=3nm), NC: Pd:SiO_2(d2=28:234nm), (δ_m=0.2).

Finally we observe the figure of merit of each set of devices in Fig. 3-9, which is a combination of the sensor sensitivity and detection accuracy. In both structures, maximum figure of merit occurs at (Ag=50nm), thus indicating that the optimal Ag thickness of the NC device is similar to that of the previously determined optical Ag thickness in Chapter 2. It can be seen that the IM structures operates with larger figure of merit at the lower end of the observed spectrum. This gives further justification to previous researchers who have opted to employ this structure when investigating surface plasmon resonance around this observational range (Perrotton *et al.* 2011b; Hosoki *et al.* 2013; Perrotton *et al.* 2013; X.G. Wang *et al.* 2013b). Our findings indicate that the NC structure operates with superior performance in both sensitivity and detection accuracy, in the (λ=900:2000nm) range. Thus, a NC based structure should be employed for H_2 sensing applications involving the near-IR parts of the wavelength spectrum.

The greater penetration depth of surface plasmons in the near-IR range compared to those in the visible spectrum permit better application in areas such as non-invasive, label free bio-sensing. SPR in the near-IR spectral range has found favorable application in a wide range of biological applications including cell and cell-culture (Golosovsky *et al.* 2009), interactions with antibodies such as Immunoglobulin (IgG) (Li *et al.* 2017), hormones such as human chorionic gonadotropin (hCG), and various other bio-sensing applications (Abbas *et al.* 2011a; Petryayeva and Krull 2011).

3.3.6 Volume Fraction

Finally, we investigated the influence that the volume fraction of Pd in the NC has on the performance of the NC based sensing device. We recall the recommendation from McKenzie *et al.* was to substitute the Maxwell-Garnett model for a multipole model above (δ_m=0.3) (McKenzie and McPhedran 1977). Additionally we note that recent advances in the synthesis of NC materials has resulted in the creation of more uniform structures, as demonstrated by Ung *et al.* where the measured optical function of NC structures matched well with the Maxwell-Garnett model up to (δ_m=0.5) (Ung *et al.* 2001). Thus, the measured range of NC volume fractions that we will investigate in this section is (δ_m=0.05, 0.1, 0.2, 0.3, 0.4). The performance of each device in determined in terms of sensitivity, detection accuracy, and figure of merit. The metallic thickness of each device is kept constant at the previously determined optical thickness ($d1_{IM}$=$d1_{NC}$=Ag=50nm). The surface plasmon resonance location was modulated by the thickness of the NC layer ($d2_{NC}$=Pd:SiO_2). As a result, the range of modulation thicknesses used in both configurations will vary, since the IM structure necessitates a larger modulation layer thickness in order to achieve an equivalent spectral shift to the NC. Firstly, we investigated the s- & p- polarised reflectance from the middle angle θ_{mid} in the angular input range between the critical angle and 90˚. These are demonstrated in Fig. 3-10.

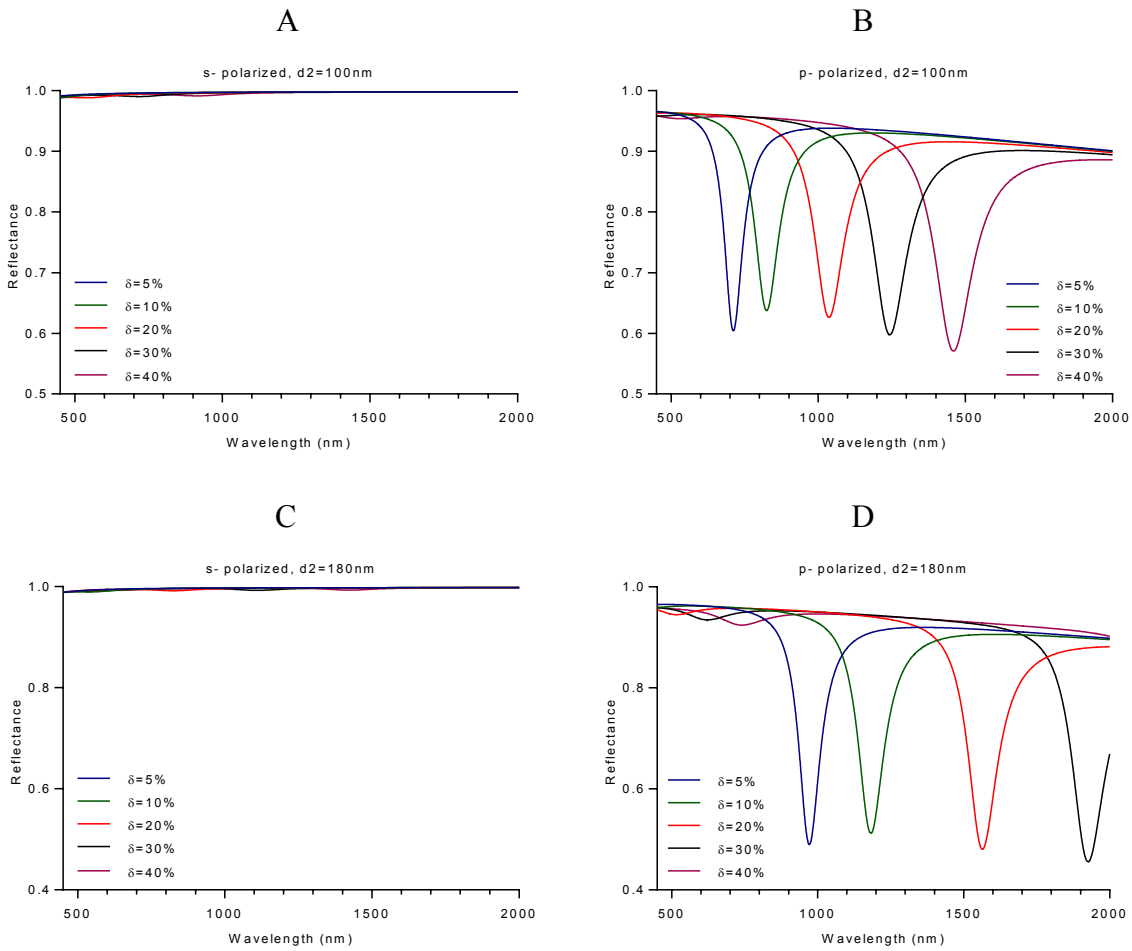

Figure 3-10 – (A) s- polarised reflectance from a series of NC structures with Ag(d1=50 nm), Pd:SiO_2(d2=100 nm), (δ_m=0.05,0.1,0.2,0.3,0.4), as measured using incident light at (θ_{mid}). (B) p- polarised reflectance. (C) s- polarised reflectance with (d2=180 nm). (D) p- polarised reflectance.

In Fig. 3-10 (A, C) no resonance from s- polarized light is evident, regardless of the NC volume fraction, and modulation layer thickness. In our simulations, we found that additional resonance modes were excited when a relatively thin metallic layer thickness was employed. The configurations in Fig. 3-10 employ a metallic layer thickness of ($d1_{NC}$=50nm), which was too large fulfil the stimulation of additional resonance modes. We explore this concept further in Chapter 5. In Fig. 3-10(B, D) dips in reflectance corresponding to the stimulation of SPR can be observed. The spectral location of the p- polarised reflectance resonance conditions increases with increasing volume fraction, due to the increase in the magnitude of the real dielectric permittivity component in the nanocomposite layer. Thus, the displacement of the resonance condition is greater in the structure that employs a large volume fraction, than the structure that employs a low volume fraction. The NC reflectance data in Fig. 3-10 is

presented in order to demonstrate that the subsequent measurements of sensor performance are determined solely from surface plasmon resonance conditions. Next we investigate the influence that volume fraction has on the performance the NC based device.

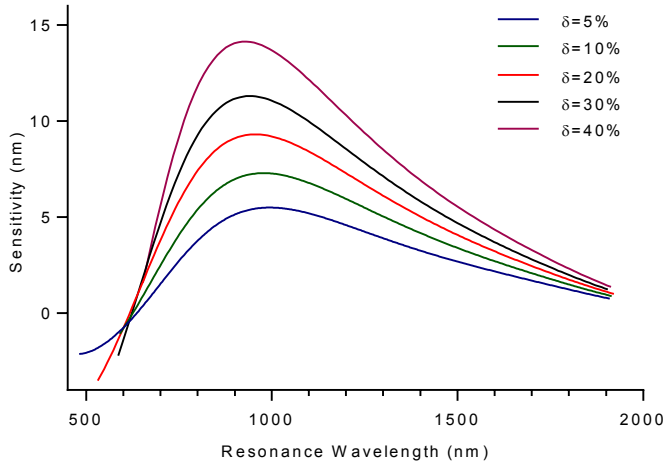

Figure 3-11 – Sensor sensitivity (SPR dip wavelength shift to 1% hydrogen) for several OFSPR configurations with Ag(d1=50nm), Pd:SiO_2(d2=15:470 nm), (δ_m=0.05,0.1,0.2,0.3,0.4).

The sensitivity of each NC volume fraction in Fig. 3-11 follows the same behaviour as the previously investigated (δ_m=0.2), by increasing with composite layer thickness to a maximum, and subsequently diminishing. Additionally, it can be seen that sensitivity increases with volume fraction. This occurs as a consequence of using a larger volume of Pd in the multilayer sensing structure, which results in a larger change in the dielectric permittivity of the NC multilayer structure upon hydrogenation, and thus, a greater spectral shift of the resonance condition. Conceptually, the greatest spectral shift would occur with a structure consisting of pure Pd, and very large in film thickness, but would operate with an exceptionally long response time, and be subject to interaction with hazardous airborne impurities such as sulphur (Hübert *et al.* 2011). At the upper end of the observed wavelength spectrum, the composite volume fraction appears to have very little influence on the sensitivity of the device.

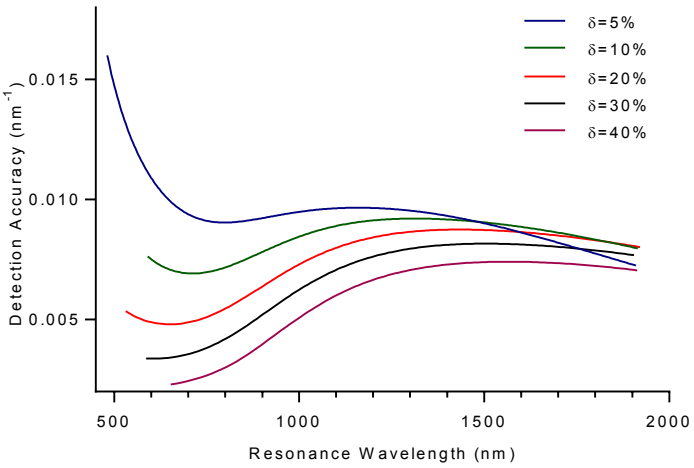

Figure 3-12 – Detection Accuracy (SPR dip wavelength shift to 1% hydrogen) for several OFSPR configurations with Ag(d1=50 nm), Pd:SiO_2(d2=15:470 nm), (δ_m=0.05,0.1,0.2,0.3,0.4).

Fig. 3-12 illustrates the variation of the surface plasmon resonance linewidth with increasing volume fraction. We find that each volume fraction (δ_m=0.1, 0.2, 0.3, 0.4) follows similar behaviour with increasing resonance wavelength in terms of detection accuracy. When the volume fraction is particularly low, such as the case where (δ_m=0.05), we find that the detection accuracy is lower than the larger volume fraction of (δ_m=0.1), at particularly large wavelengths. While the detection accuracy of (δ_m=0.05) is quite large at low wavelengths, it should be recalled that a blue shift is observed in the resonance condition at this range upon H_2 loading.

While H_2 sensing is possible by measuring the blue shift, it is important to note that if the resonance wavelength undergoes a blueshift at one part of the wavelength spectrum, and a red shift at another; then, there will occur a specific localized wavelength range, where sensor sensitivity decreases towards zero, and accurate H_2 detection is no longer permitted.

The detection accuracy of the observed volume fractions can be seen to increase with resonance wavelength, and begin to flatten off at large wavelengths ($\lambda \approx 1400$nm). Finally, we observe that the detection accuracy decreases with increasing volume fraction. This broadening effect is due to the increased magnitude of the imaginary dielectric permittivity component (which is responsible for absorption) of the modulation layer as a greater volume fraction of Pd is present. In Chapter 1 Fig. 1-13 we demonstrated that an increase in the

magnitude of the imaginary permittivity component of the metallic layer results in the broadening of the surface plasmon resonance condition.

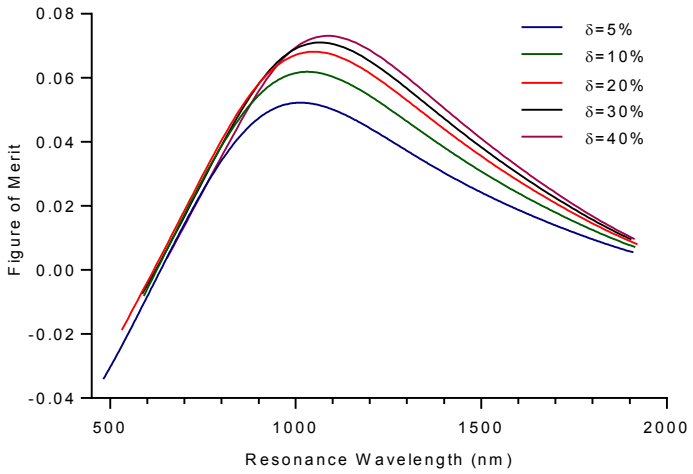

Figure 3-13 – Figure of Merit (SPR dip wavelength shift to 1% hydrogen) for several OFSPR configurations with Ag(d1=50nm), Pd:SiO_2(d2=15:470 nm), (δ_m=0.05,0.1,0.2,0.3,0.4).

Finally observing Fig. 3-13, we note that the figure of merit of each device increases with increasing composite thickness to an optimal point, and decreases thereafter, regardless of volume fraction. The resonance location of the optimal figure of merit corresponding to a volume fraction can be seen to increase with volume fraction. Figure of merit is affected very little by the NC volume fraction across the visible range of the wavelength spectrum. This is not necessarily important as we have previously observed, the IM based device operates with superior performance across this wavelength range, and should therefore be employed for operations in this wavelength range.

While an increase in volume fraction leads to an increase in figure of merit, the magnitude of the increase reduces with volume fraction. For example, increasing the volume fraction from (δ_m=0.1-0.2) results in the maximum figure of merit being increased from (FOM=0.052263-0.061904), thus, an (18.5%) increase in max FOM from a (5%) increase in volume fraction. However, increasing the volume fraction from (δ_m=0.3–0.4) results in a rise in the maximum figure of merit from (FOM=0.071039-0.073113), a significantly lower (2.9%) increase from a (10%) increase in volume fraction. Tabassum also found that FOM increases to an optimal value with increasing volume fraction, and decreases thereafter (Tabassum and Gupta 2015;

Tabassum and Gupta 2016a). As the maximum FOM can be seen to increase marginally with further increase in volume fraction (δ_m=0.4), we infer that further increase in volume fraction will result in a negligible increase in FOM, but will reduce the durability of the device substantially due to the previously mentioned problems associated with a Pd based sensor.

The sensor figure of merit observations can be understood by examining the fact that increasing the Pd volume fraction results in an increase in the magnitude of change in dielectric permittivity permitted in the H_2 sensitive layer, and consequently, a greater resonance shift (higher sensitivity). On the other hand, increasing the Pd volume fraction results in an increase in the real component of the dielectric, permittivity thus, increasing the resonance linewidth (lower detection accuracy), as demonstrated in Chapter 2.

3.4 Conclusion

In conclusion, we have performed a theoretical investigation into the operation of multilayer OFSPR Pd based H_2 sensor, and compared its performance to a novel nanocomposite based multilayer OFSPR Pd based H_2 sensor. The methods of modelling the interaction between light and our sensor are outlined in Chapter 1. We performed analysis on the normalised output power though the fibre in the presence of 0% and 4% H_2 gas, and scaled our results in order to determine performance upon the introduction of 1% H_2. The spectral resonance location underwent a red shift during hydrogen loading, which allowed us to determine sensor sensitivity. The spectral width of the resonance condition was determined by measuring the detection accuracy.

We investigated the influence that metallic layer thicknesses ($d1_{IM}$ & $d1_{NC}$) the modulation layer thicknesses ($d2_{IM}$ & $d2_{NC}$) have on the performance of each device, where ($d1_{IM}$=$d1_{NC}$) and ($d2_{IM}$=$d2_{NC}$). We investigated the reflectance from various Kretschmann configurations, employing IM and NC over-layers, in order to establish the origin of additional resonance dips in the output power. We established that the surface plasmon resonance generated using the NC occurred at a longer wavelength than that of the IM device of equivalent multilayer thicknesses due to the higher refractive index of the SiO_2:Pd NC layer when compared to a pure SiO_2 layer.

We determined the sensitivity, detection accuracy, and figure of merit, of numerous IM and NC devices with varying metallic thickness, where the resonance locations were controlled by the thickness of each modulation layer ($d2_{IM}$ & $d2_{NC}$). Both sensitivity and detection accuracy were found to be maximum in the visible part of the wavelength spectrum for the IM based devices. Correspondingly, the NC structures operated with high figure of merit in the near-IR part of the spectrum.

Finally, we investigated the influence that NC volume fraction has on sensor performance. In doing this, we found that the figure of merit increases with increasing Pd volume fraction, however the magnitude of the increase is reduced at high volume fractions. The NC structure operated with high figure of merit in the near-IR part of the wavelength spectrum, and thus, should be employed for H_2 sensing applications in this range. Additionally, due to the highly penetrating nature of surface plasmons in the near-IR range, NC structures have great potential in biological based sensing applications. Utilizing NC based SPR allows one to increase the SP penetration depth, while still retaining high performance, and thus, provides a non-invasive method of detecting bulk refractive index changes within biological organisms. In addition, utilizing both IM and NC based sensors with corresponding short and long SP penetration depths, enables the used to distinguish between surface refractive index changes at the analyte interface, and bulk index changes within the analyte.

4 Chapter 4: Multi-Channel Sensor

Previously in Chapters 2 & 3, we investigated the operation of various OFSPR H_2 sensing configurations. Each of these structures consisted of a single multilayer sensing structure, which permitted the stimulation of SPR. In this chapter, we consider the use of a multi-channel sensor in which more than one detection channel is present with the primary benefit of multi-point sensing wherein multiple physically separate locations can simultaneously be monitored.

Additional advantages of employing multiple sensing channels include: the aforementioned combination of IM based SPR and NC based SPR (see Chapter 3) for biological sensing applications, where distinctions can be made between surface refractive index changes, and bulk analyte index changes. Various channels can incorporate different methods of shielding in order to improve durability. The gas sensitive layer could be exchanged in certain channels thus increasing the range of gases that can be detected. Performance can be improved by employing different metallic layers in each channel, for the detection of the same gas, thereby combining the high sensitivity of one material with the large penetration depth of another. Finally, the environment around one channel can be strictly controlled and regulated, thus, acting as a reference channel in order to reduce the potential for error during gaseous measurement using the second channel.

In this section, we investigate the use and operation of an OFSPR multi-channel H_2 sensor. We place a particular focus on understanding how the response in one channel affects the response in another by investigating the effects of the thicknesses of each layer in the multilayer, on performance. We suggest a design strategy for such a dual-channel sensor which involves placing one resonance in the visible wavelength range and the other in the near-IR range. We measure the sensor performance by looking at sensor sensitivity, detection accuracy and figure of merit. Finally, we investigate the operation of three, four, and six-channel sensors and illustrate the fundamental limitations which limit the number of channels which can be used.

4.1 Literature Regarding Multi-Channel Sensing

Many examples of multi-channel sensing devices have appeared throughout the literature, each detailing advantages over single channel operation. In some cases, one channel is used

as a reference (Nenninger *et al.* 1998; Homola *et al.* 2002; Liu *et al.* 2017), in order to more accurately determine an optical change around the analyte region. An example of this sensor type is that developed by Homola *et al.*, which was used for investigations into the detection of staphylococcal enterotoxin B (SEB) in milk (Homola *et al.* 2002). Here, one channel was used as a reference, and the other was used to determine surface refractive index changes in the 5nm thick bio-layer. Liu *et al.* also developed a dual channel OFSPR biochemical sensor which comprised a (50nm) Au film coated into a silica fibre of (NA=0.37), diameter (D=400μm), sensing length 4cm (Liu *et al.* 2017). The sensor utilized a detection and reference channel, and was used in the detection of lectin concanavalin A, and ribonuclease B, where a spectral resonance red shift was evident upon increase in the analyte refractive index. A reflectivity based dual-channel biosensor was employed by Nenninger *et al.* that employed a lightpipe design, where the functionalization differed between the two channels (Nenninger *et al.* 1998). One channel was used as a reference. Prism configurations were used to couple light both into and out of the lightpipe. Two resulting TM reflectivity versus wavelength plots were determined, and resonance was achieved.

It is possible to achieve simultaneous detection using a multichannel OFSPR sensor by ensuring that each channel operates within an independent spectral range. This is known as wavelength division multiplexing (WDM), which is more commonly employed in fibre optic telecommunications. Many applications of WDM have appeared in the literature that involve sensing. One such method is involves excitation by attenuated total reflection using a specific type of prism coupler, with modified geometry, such that by total internal reflection, light interacts with the metallic film at two different angles of incidence. Thus surface plasmon resonance is permitted two resonance wavelengths. This modified prism configuration is illustrated in Fig. 4-1.

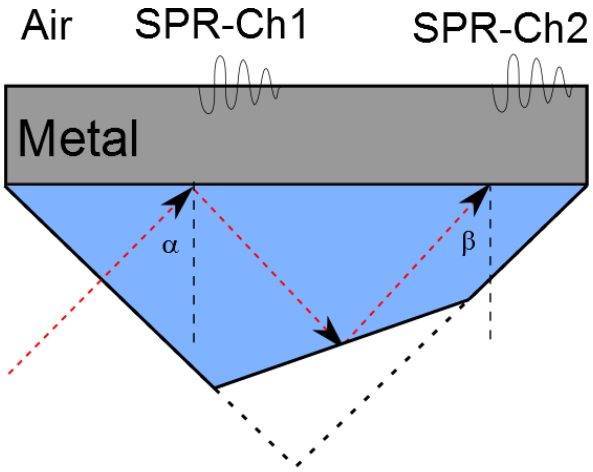

Figure 4-1 – (A) Schematic representation of a Kretschmann prism configuration structure with modified geometry such that ATR of polychromatic light is permitted in the prism, and incident radiation interacts with the metallic film at more than one angle of incidence. Thus surface plasmon resonance occurs at two distinct resonance wavelengths.

Homola *et al*. investigated the use of a multi-channel sensor based on WDM, which employs an ATR structure. This device consisted of (SF14 glass / Au=55nm / dielectric aqueous medium). In their experiment the incident angles were (α=54.6˚) and (β=52.5˚), which resulted in two distinct resonance dips occurring at separate wavelengths in the measured reflectivity. Following the equations presented in Chapter 1; the shorter angle of incidence gives rise to the stimulation of surface plasmon polarization at a longer resonance wavelength. Dostálek *et al*. have also made use of a modified prism structure for the stimulation of ATR based WDM for bio sensing applications. Their sensor consisted of a Au film coated with a thin dielectric layer of (n=1.43) (Dostálek *et al.* 2005). Similarly to Homola, two independent resonance dips were observed in the measured transmitted intensity through the fibre. Another method of achieving WDM involves modulating the resonance wavelength of the surface plasmon in one channel using a dielectric overlayer on the metallic film. This is illustrated in Fig. 4-2.

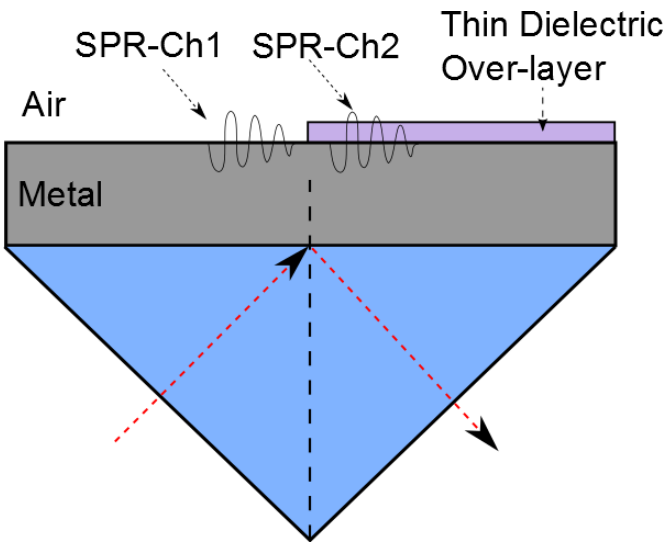

Figure 4-2 – (A) Schematic representation of a Kretschmann prism configuration structure with a dielectric overlayer covering part of the metallic film. SPR is permitted at the bare metallic interface. Additionally, SPR of a different resonance wavelength is permitted at the metallic interface component that is covered by the dielectric film.

Homola *et al*. investigated the use of a dual-channel reflectivity based biosensor, which was used to detect anti-dinitrophenyl antibody interactions (Homola *et al.* 2001). This consisted of a Kretschmann configuration (glass prism / Au film), where half of the metallic layer was covered with a Ta_2O_5 dielectric film. Polychromatic light (λ=500:2000nm) was shone through the prism at incident angle (θ_i=55˚). The reflectivity from the prism structure was measured, and two distinct resonance dips were observed at different wavelengths. The bare Au section of the sensing film facilitated the stimulation at short wavelengths, and the Ta_2O_5 overlayer over the other half of the Au film permitted resonance to occur at longer wavelengths. The IR region has greater penetration depth than that of the visible, and thus, can provide a greater magnitude of information relating to the bulk change in analyte regions, as opposed to surface changes. Accordingly, surface index changes can be determined at short wavelengths, and bulk refractive index changes are better determined using longer wavelengths.

Akowuah *et al.* simulated a dual channel planer waveguide SP biosensor (Akowuah *et al.* 2010). In this work, a dual channel silica core is accompanied by thin films of Au on one channel, and Ag on another. The transmission of p- polarized light through the fibre was determined. An overlayer was included on the outer surface of the Ag film in order to provide some protection against hazardous environmental gases. Both channels successfully detected changes their respective analyte regions from (n=1.33-1.6).

Peng *et al.* developed an optical fibre dual channel refractive index sensor that operates under the principle of WDM (Peng *et al.* 2005). Their sensor consisted of two sensing regions, spaced (5mm) apart on a (400μm) diameter core. Both sensing regions comprised of a (5nm) thick chrome film (to improve adhesion), covered in a (50nm) Au layer. Only the second channel was polymerized. The normalized output power displayed two resonance dips at separate wavelengths. The surface plasmon resonance wavelength of the second channel is longer than that of the first channel due to polymer component in the second channel.

Wang *et al.* investigated the operation of a dual channel OFSPR H_2 sensor (X. Wang *et al.* 2013b). In this paper, the transmitted power from p- polarized radiation was determined from a dual channel optical fibre sensing configuration. This consisted of two multilayer sensing configurations: (Ag=35-45nm), (SiO_2=80nm), (WO_3=160nm), (Pt=3nm), both over layering a silica fibre core. Wavelength division multiplexing was achieved by using a larger thickness of both SiO_2 and WO_3 layers in one channel, which resulted in shifting the resonance wavelength of channel (2) towards higher wavelengths. A blue shift of the resonance condition was observed from both channels, using various sensors differing in multilayer thicknesses.

Another method of achieving dual channel functionality involves fusing tapered optical fibres. Wei *et al*. developed a dual channel OFSPR refractive index sensor (Wei *et al.* 2017), where two optical fibres (polymer cladded & vitreous cladded) of different diameter were tapered at a specific grinding angle, and fused together. At the location where the fibres are joined together, the fibre grinding angle is set up such that the incident angle of light propagating from one fibre to another changes. Both sensing surfaces employed metallic films (Au=50nm). The resultant output power though the fibre illustrated two distinct resonance dips due to SPR stimulation from light at the sensing surface at the original incident angle, and also from light which changed its propagation angle at the tilted region. The motivation for this research was that no effective method to adjust the operational range of the resonance wavelength exists in a single SPR sensor. We know however, that the inclusion of a dielectric overlayer achieves this outcome.

Similarly, Kim *et al.* investigated the operation of a tapered dual channel OFSPR sensor (Kim *et al.* 2005). A single dual tapered fibre of (NA=0.12) was employed to measure refractive index changes of media in both the vapor channel (1) and liquid phases channel (2). The simulations were run using MATLAB. Changes in both the vapour and liquid phases of the

analyte region were measured simultaneously using each channel. Liu *et al*. also developed an OFSPR sensor that operates with multiple sensing channels through WDM (Liu *et al.* 2015). By adjusting the geometry of the fibre tip, and connecting together two sensing channels, the propagation angle along the fibre is different for each sensing region, and thus, each channel operates in a unique resonance wavelength range.

Certain materials whose dielectric function exhibits metallic properties at certain wavelengths, translucent properties at others, have proven to be interesting candidates for stimulation of multiple surface plasmon resonance polarizations. Specifically, ITO has been employed for application on a dual channel sensor (Li *et al.* 2017). In this paper, a multilayer of (Au=35nm) / (ITO=100nm) was employed. Since the refractive index of ITO is larger than the SiO_2 core, from (λ=400:755nm), a Kretschmann like configuration is present, and thus the stimulation of surface plasmon resonance is permitted within this wavelength range. The Otto configuration necessitates that the real component of the dielectric prism refractive index is larger than the real component of the air gap refractive index, so that an evanescent wave can propagate towards the metallic film. In Li's paper, since the refractive index of ITO is smaller than the core in the near-IR spectral range; The ITO layer acts like the air gap in the Otto configuration. Thus, within this higher wavelength range, an Otto like configuration is present, and surface plasmon resonance can be stimulated using the second Au film. The device was used in biomolecular sensing applications. ITO has also been employed in a device by Lu *et al.* as a component in a capillary based SPR sensor (Lu *et al.* 2017). This consisted of (air core/Ag/Capillary layer/Au/ITO/analyte region). A blue shift with increasing sensing medium refractive index was reported with both surface plasmon resonance polarizations.

Multi-channel functionality has also been achieved through WDM using Bragg grating of different periods (Špačková *et al.* 2009) in a structure (core/cladding/Au/analyte region). Here, the Bragg gratings of length (1-3mm) are inscribed on a single-mode fibre core, with period (288nm), and a (Au=50nm) is coated around the cladding. Multi-channel sensing is realized by two Bragg grating structures are inscribed onto the fibre core, with different refractive index periods of modulation, and thus different surface plasmon resonance wavelengths. Additionally, WDM of a single fibre has been demonstrated using tilted Bragg gratings (Baiad and Kashyap 2015). This device consisted of channels, with three corresponding series of gratings at different tilt angles. By changing the grating tilt angle at each channel, the operational range of each channel was different.

Berger *et al.* investigated the use of a multi-channel surface plasmon resonance immunosensor (Berger *et al.* 1998). This consisted of an Au film, with a 4 channel flow cell overlayer that measured 4 immunoreactions simultaneously. The first surface plasmon resonance sensor to detect bio molecular interactions, based on angular modulation that allowed for multi-channel functionality was developed by Löfås *et al.* (Löfås *et al.* 1991). This device operated with 4 sensing channels. The sensor chip consisted of glass / (Au=40-50nm) / (coupling matrix=100-200nm) of n=1.33.

A dual channel OFSPR refractive index sensor has also been developed by Verma *et al.* based on Au and Ag (Verma *et al.* 2012). Given that the real components of the dielectric permittivity of Au and Ag are inherently different, they will stimulate surface plasmon polarizations at different resonance wavelengths. In their research, Verma *et al.* determined the output power of p- polarized light through an OF structure, which consisted of two sensing channels. One coated with (Au=50nm), and another with (Ag=40nm), along with a small adhesion layer of Cr on each channel. The resonance wavelength corresponding to both channels were quite close however, which made it difficult to determine the performance of each channel. They employed a series of equations that determines normalized output power through a dual channel OF structure, where the net reflectance is determined as the product of the two individual reflectance calculations corresponding to each channel.

Later Verma *et al.* investigated the operation of a refractive index dual channel sensor for operation in the near-IR region, where (Au=50nm) was used in both channels, but with two different dielectric over-layers of (Si=8nm) in channel (1), and (TiO_2=35nm) in channel (2) (Verma and Gupta 2013). The large difference in the real component of the refractive indices of Si and TiO_2 ensured that the surface plasmon polarizations of each channel occurred at different spectral locations. This model also determines net reflectance as the product of the two individual reflectance measurements from each channel. The authors expanded on this model to include a third sensing channel, where channels (1, 2, 3) consisted of (Ag=40nm, Au=50nm, Cu+TiO_2=40+10nm), respectively (Verma and Gupta 2014b). Experimental work was carried out by Verma *et al*. into a dual channel OFSPR sensor for the detection of urea (Verma and Gupta 2014a). Channel (1) consisted of (Ag=30nm, with an overlayer of Si=4nm), and channel (2) comprised of (Cu=40nm, with an overlayer of SnO_2=8nm). The

authors observed a blue shift of the resonance wavelength with increasing urea and glucose concentration.

An OFSPR sensor that utilizes ion-printed nanoparticles has been developed by Srivastava and Gupta (Shrivastav and Gupta 2018). In their research, channel (1) consisted of (Cu=40nm covered in Pb^{+2} nanoparticles), and channel (2) consisted of (Ag=40nm, covered in Cu^{+2} nanoparticles). Once a solution of Pb^{+2} or Cu^{+2} ions are introduced into the sensor flow cell, the effective refractive index of each channel changes, and this the corresponding surface plasmon wavelength.

With regards to Pd based multi-channel sensing, very little research has been carried out. Simulations were carried out by Alam *et al*. (Alam *et al.* 2007; Alam *et al.* 2008); In both papers the authors investigate the operation of Pd based hydrogen sensors, and go on to state that each device could be easily extended to multichannel sensing with the use of a wavelength division multiplexed chip, however no results using this concept were presented. Therefore the opportunity to investigate a Pd based multi-channel sensor is open. For the first time we investigate the use a step-index multi-channel OFSPR Pd based H_2 sensor.

4.2 Modelling

The series of equations from Chapter 1 that make up the transfer matrix model along with the Fresnel terms were used to determine the reflectance of polychromatic s- & p- polarized radiation. Wang *et al*. employs a model that determines the output power of the p -polarized light in a dual channel optical fibre. This model includes the term T_p that represents the intensity transmittance corresponding to the optical fibre end face for p- polarization (X.G. Wang *et al.* 2013b). Wang *et al.* also employed this intensity transmittance term in modelling the operation of a single channel OFPSR device (X.G. Wang *et al.* 2013a), however we did not find any other mention of this term in the literature, and it was not experimentally verified. Verma *et al*. employed the same dual-channel equation as Wang, without T_p (Verma *et al.* 2012; Verma and Gupta 2013; Verma and Gupta 2014b), and demonstrated favorable results. Thus, we extended our own model that determines the normalized output power of both s- and p- polarized light, to include multichannel functionality. Recalling the method we employed for determining the output power through the fibre from Chapter 1, rewritten here as equation (4-1).

$$P_{nor} = \frac{{}^{1}/_{2}\int_{\theta_c}^{\pi/2}(|r_s(\theta)|^{2N_{ref}} + |r_p(\theta)|^{2N_{ref}})dPd\theta}{\int_{\theta_c}^{\pi/2} dPd\theta} \quad (4\text{-}1)$$

By including additional terms that describe both the s- and p- polarized reflectance of a second channel, equation (4-1) has been modified to account for the excitation of surface plasmon polarizations on a second channel overlaying the optical fibre core, as per equation (4-2).

$$P_{nor} = \frac{{}^{1}/_{2}\int_{\theta_c}^{\pi/2}\left[\begin{matrix}\left[|r_{s(ch1)}(\theta)|^{2N_{ref}}|r_{s(ch2)}(\theta)|^{2N_{ref}}\right] \\ +\left[|r_{p(ch1)}(\theta)|^{2N_{ref}}|r_{p(ch2)}(\theta)|^{2N_{ref}}\right]\end{matrix}\right]dPd\theta}{\int_{\theta_c}^{\pi/2} dPd\theta} \quad (4\text{-}2)$$

Finally, this model has been extended to account for n channels along the optical fibre core as per equation (4-3).

$$P_{nor} = \frac{{}^{1}/_{2}\int_{\theta_c}^{\pi/2}\left[\begin{matrix}\left[|r_{s(ch1)}(\theta)|^{2N_{ref}}|r_{s(ch2)}(\theta)|^{2N_{ref}}\ldots|r_{s(chN)}(\theta)|^{2N_{ref}}\right] \\ +\left[|r_{p(ch1)}(\theta)|^{2N_{ref}}|r_{p(ch2)}(\theta)|^{2N_{ref}}\ldots|r_{p(chN)}(\theta)|^{2N_{ref}}\right]\end{matrix}\right]dPd\theta}{\int_{\theta_c}^{\pi/2} dPd\theta} \quad (4\text{-}3)$$

4.3 Results

In this section, we propose an investigation into the use of a dual-channel OFSPR H_2 sensor, illustrated in Fig. 4-3. This is realized by including an additional multilayer sensing structure along the optical fibre core, spaced apart from the initial channel. Provided there is a substantial difference in the modulation layer thickness of between channel (1) and channel (2), the surface plasmon polarization at each channel will stimulate surface plasmon resonance at different resonance wavelengths. The resultant output power through the fibre core will therefore, reveal two distinct dips, corresponding to the resonance conditions of each channel. By including an outer Pd film in both channels, both of the resonance locations will undergo a shift in the presence of H_2. We investigate the influence that the thickness of each multilayer component (Ag/SiO_2/Pd) in both channels has on the output power through the fibre.

Later, we propose a specific type of dual channel sensor, where one channel is expected to operate with a fast sensor response time of (4s to 4% H_2), thus providing an early warning indication of H_2 leakage, and the other channel operates with a (267%) increase in sensitivity,

in (<15s to 4% H_2), thereby providing a more accurate measurement of H_2 concentration over time. Finally we make preliminary investigations into the operation of an N-channel sensor, where N>2.

4.3.1 General Sensor Parameters

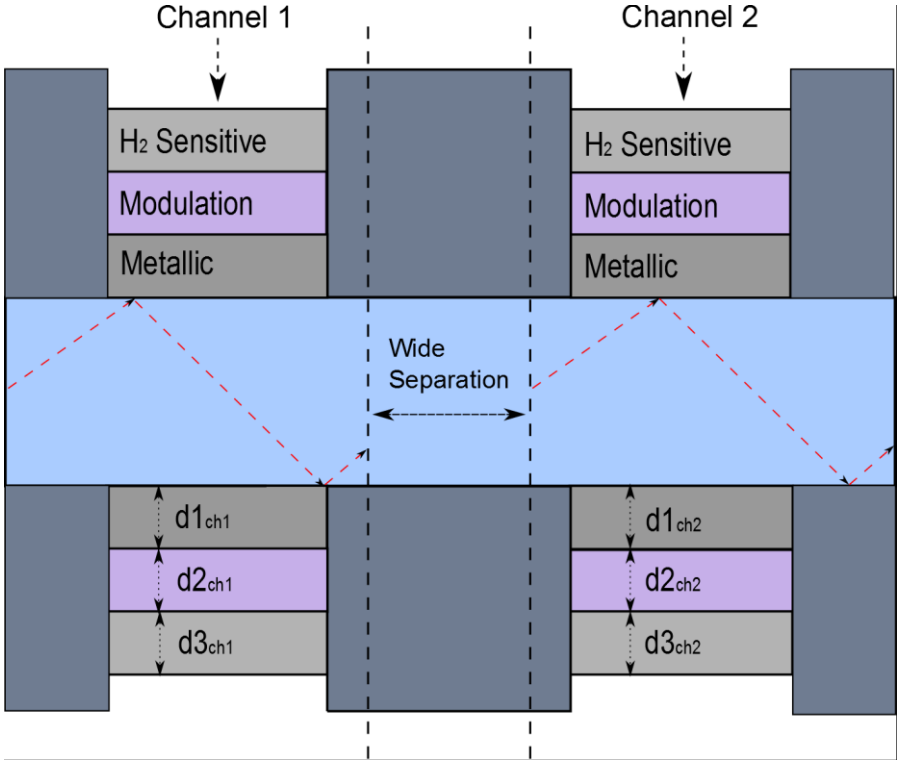

Figure 4-3 – (A) Schematic representation of dual channel OFSPR multi-layer H_2 sensor. Both channels consist of multi-layer sensing stack configurations (Ag/SiO_2/Pd). Channel (1) and channel (2) are widely separated along a step-index multimode OF. The thickness of the modulation layer ($d2_{ch2} > d2_{ch1}$), and thus the resonance wavelength ($\lambda res_{ch2} > \lambda res_{ch1}$). Consequently two independent resonance dips appear in the normalised output power spectrum.

Following from Chapters (2 & 3), our sensor is comprised of a silica fibre core diameter (D=2µm), with (NA=0.22), and the sensing length of each channel (L=1cm). Each channel consists of a multilayer stack sensing structure Ag, SiO_2 and Pd continuous films. The materials (Ag, SiO_2, Pd) were employed with thicknesses (d1, d2, d3) of each channel. The rationale behind the choice of Ag, SiO_2 and Pd are explained in Chapter 1. Provided there is a sufficiently large difference in the modulation layer thickness of each channel ($d2_{ch1}$ and $d2_{ch2}$), the surface plasmon polarisations corresponding to each channel should occur at

separate resonance wavelengths. Thus the resultant output power will demonstrate two distinct independent resonance dips as separate spectral locations.

The Brendel Bormann model is used in determining the dielectric permittivity of Ag and Pd (Brendel and Bormann 1992), and Sellmeier Dispersion formulae are used to determine the refractive indices of thin film SiO_2 (Postava and Yamaguchi 2001) and the silica fibre core (Malitson 1965); and the relevant the equations appear in Chapter 1. The normalised output power is determined using the characteristic transfer matrix model as outlined in Chapter 1, and the extension for dual-channel, and multi-channel functionality are outlined in equations (4-2, & -3) respectively.

The range of input wavelengths permitted in our multichannel structure is (λ=450:2000nm), however as we've observed in in Chapter 3 Fig. 3-7; the sensitivity of an IM based device decreases with increasing resonance wavelength, and is negative at the upper extreme of this spectrum. We recall that while H_2 sensing is possible by measuring the blue shift, it is important to note that if the resonance wavelength undergoes a blue shift at one part of the wavelength spectrum, and a red shift at another; then, there will occur a specific localized wavelength range, where sensor sensitivity decreases towards zero, and accurate H_2 detection is no longer permitted. In addition, from Chapter 3 Fig. 3-7, we concluded that sensor performance was greatest around at the lower end of the wavelength spectrum. Thus, we will employ structures that permit the stimulation of surface plasmons polarisations at resonance wavelengths in the visible, and lower parts of the near-IR spectrum; in order to avoid a localised section of the wavelength range where sensitivity approaches zero, and additionally generate resonance within the range where figure of merit is high.

4.3.2 Response Time, Selectivity and Durability

The response time of the the IM structure consisting of a (3nm) thick Pd film is expected to operate similar to that of Liu, 4s to 4% H_2 (Liu and Li 2016b). The sensor response time is expected to increase with Pd layer thickness, as explained in Chapter 2. Insight into the selectivity of the device can be gained by reviewing the highly selective properties of a Pd based hydrogen sensor (Huebert *et al.* 2011), which operate with minimal cross sensitivity to other gases, as previously mentioned in Chapter 2. The durability of each channel can be derived from investigation into the durability of each multichannel sensing component. While Ag is subject to hazardous interaction with atmospheric gases, the protective overlayer of

SiO_2 improves the longevity of the Ag film. Thus, the durability of the multichannel sensor primarily stems from the durability of the Pd component in the multilayer sensing structure. As explained in Chapter 2, Pd undergoes a α→β phase transition during hydrogenation, causing excessive expansion of the Pd fcc lattice structure, and increased mechanical strain. Thus, repeated H_2 loading cycles causes rapid degradation of the Pd continuous film structure.

We begin by investigating the operation of a dual-channel sensor. In doing this, we investigated the influence that the thickness of each multilayer component had on the surface plasmon polarisations that corresponded to each channel. We aim to investigate the relative thicknesses of each material that permits dual channel functionality by WDM. Dual channel operation necessitates that two independent resonance dips occur at separate wavelengths. In addition, to ensure accurate measurement of performance, the magnitude of each resonance dip must be deep enough such that the spectral width can be determined using equation (1-28). This equation necessitates that the spectral width of the resonance condition generated in the presence of H_2 be measured where the normalized output power is 10% greater than that at resonance. In order to highlight the influence that each multilayer component has on the resonance condition, we initially plot the normalised output of a series of structures in the absence of H_2. The performance metrics (sensitivity, detection accuracy, and figure of merit), are determined upon the interaction with 4% H_2 gas.

4.3.3 Metallic Layer Thickness (d1)

In order to determine the influence that the thickness of the metallic layer in each channel has on the sensor performance, we keep the thicknesses of all other multilayer components constant. Following from our previous chapters, a H_2 sensitive layer thickness (d3=3nm) was used for both channels, in order to minimize the sensor response time, while maintaining a continuous film structure. Two constant modulation layer thicknesses were employed ($d2_{ch1}$=100nm, $d2_{ch2}$=300nm). These values were chosen such that each channel excited resonances at separate spectral locations, in order to realize wavelength division multiplexing in our optical fibre device. For simplicity, the larger d2 thickness (300nm) is employed in the second channel. Since the thickness of this layer has the largest influence on the spectral resonance location; the surface plasmon polarization will be stimulated at a longer resonance

wavelength in channel (2). Finally, a range of d1 thicknesses were chosen in order to determine the influence that d1 thickness has on the performance of a dual channel sensor.

4.3.3.1 Channel (1)

First, we kept the $d1_{ch2}$ constant at the previously determined optimal value in Chapter 2 of ($d1_{ch2}$=50nm), and varied the ($d1_{ch1}$=10:90nm).

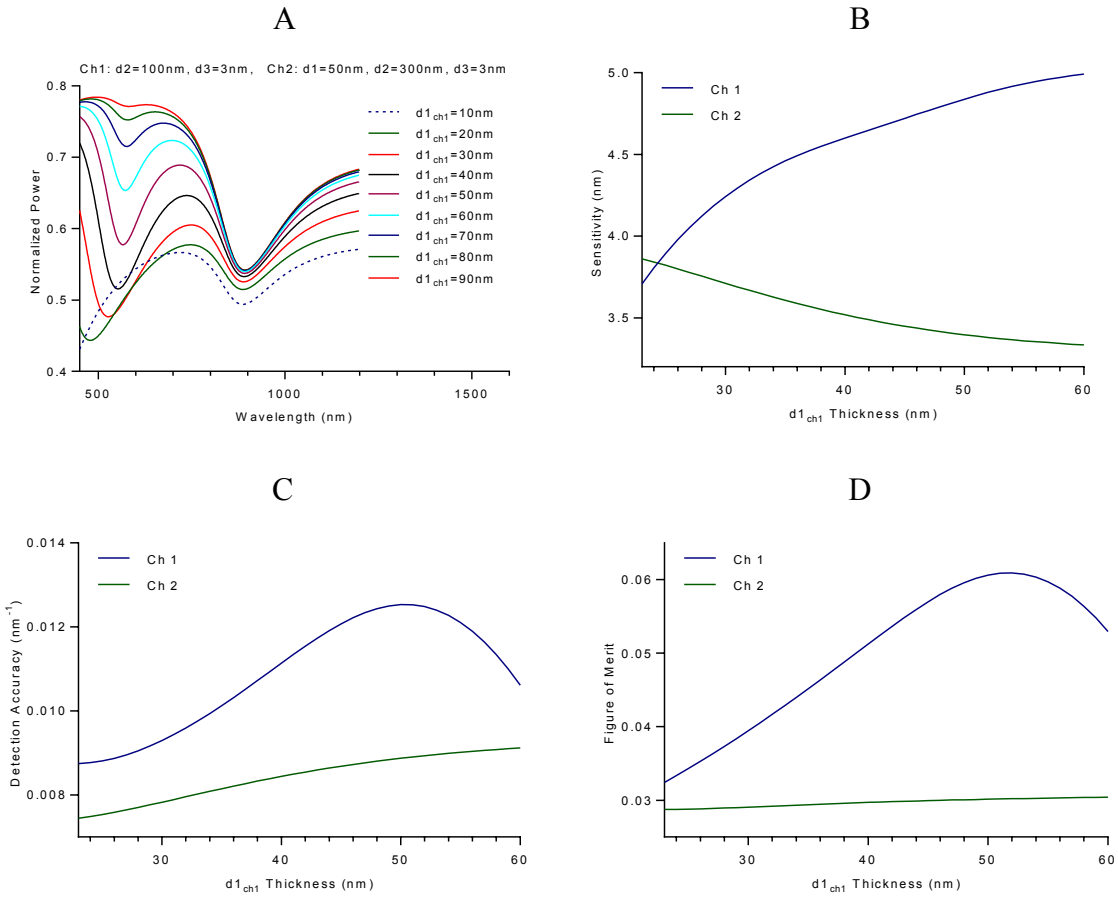

Figure 4-4 – (A) Normalised output power across the spectral domain of a (Ag/SiO_2/Pd) multilayer dual-channel sandwich structure OFSPR sensor in the presence of 0% H_2; (λ=450:1200nm), Ag($d1_{ch1}$=10:90nm, $d1_{ch2}$=50nm), SiO_2($d2_{ch1}$=100nm, $d2_{ch2}$=300nm), Pd($d3_{ch1}$=3nm, $d3_{ch2}$=3nm). (B) Sensitivity of the resonance conditions stimulated at channel (1) and channel (2) as measured by the introduction of 4% H_2. (C) Detection accuracy. (D) Figure of merit.

Fig. 4-4(A), displays the normalized output power from a range of dual channel sensing configurations where the thickness of the metallic layer in channel (1) ($d1_{ch1}$) was varied in steps from ($d1_{ch1}$=10:90nm), with the purpose of illustrating the general behavior of the dual-channel sensing device. We also determined the performance of channel (1 & 2), of the various structures that make up the range ($d1_{ch1}$=10:90nm) in terms of sensitivity (B),

detection accuracy (C), and figure of merit (D). As the thickness of the dielectric layer is lower in channel (1) than in channel (2), the spectral locations of each resonance condition appear at a shorter wavelength than compared to channel (2). In Fig. 4-4(A) we observe a red shift of the resonance condition and a decrease in the resonance depth with increasing metallic thickness $d1_{ch1}$.

Again, looking at Fig. 4-4(A), the influence that $d1_{ch1}$ has on the resonance stimulated in the second channel (right), we observe that there is very little change in the spectral location of the channel (2) resonance location. The magnitude of the resonance condition in channel (2) decreases with increasing $d1_{ch1}$ however the variation in dip depth changes very little with $d1_{ch1}$ once the $d1_{ch1}$ thickness is quite large. We can understand this as an effect of the evanescent field at the Ag/SiO_2 interface which, at low values of $d1_{ch1}$ significantly overlaps the SiO_2 layer allowing leakage of light into it. The end result is that the background level in the spectral response is reduced. As $d1_{ch1}$ is increased the part of the evanescent field overlapping the SiO_2 layer is much decreasing giving less light leakage and a higher background level. The sensitivity of channel (1) and channel (2) is demonstrated in Fig. 4-4(B). Similar to that observed in Chapter 2, the sensitivity of channel (1) increases with increasing $d1_{ch1}$. In contrast, the sensitivity of channel (2) however, decreases with increasing $d1_{ch1}$. Once the thicknesses of the metallic layers in each channel are equal ($d1_{ch1}$=$d1_{ch2}$=50nm), the sensitivity of the resonance associated with channel (1) is significantly larger than that of channel (2). This can be understood by reviewing the findings in Chapter 3 where the sensitivity of the IM structure decreased with increasing wavelength.

In Fig. 4-4(C), the detection accuracy can be seen to reach a maximum at around ($d1_{ch1}$=50nm) of channel (1), similarly to that observed in Chapter 2. In addition the detection accuracy of channel (2) increases slightly with increasing $d1_{ch1}$. Again this can be explained by considering the aforementioned evanescent field of the light wave incident at the Ag/SiO_2 interface. The overlap of this field with the SiO_2 layer determines the background level in the spectral response due to light leakage. At high values of $d1_{ch1}$ the overlap is minimal and the background reflectance is much increased. This allows the channel (2) dip to take on a deeper shape with higher resulting detection accuracy. Finally, we observe the figure of merit of both channels in Fig. 4-4(D). Similarly to Chapter 2, we observe a maximum at around ($d1_{ch1}$=50nm) of channel (1). In addition, the opposing effects of the decreased sensitivity and increased detection accuracy of the resonance in channel (2) with increasing $d1_{ch1}$ tend to cancel each other out with the result that the figure of merit changes very little as $d1_{ch1}$ varies.

The lower limit of $d1_{ch1}$ thicknesses ($d1_{ch1}$=23nm) used in Fig. 4-4(B, C, D), was determined to be the minimum $d1_{ch1}$ thickness that permitted accurate measurement of the detection accuracy within the observed spectral range (λ=450:2000nm). As further decrease in $d1_{ch1}$ would result in a surface plasmon polarization generated at a lower resonance wavelength, where the spectral width can no longer be determined; when ($d1_{ch1}$=22nm), we find that ($\lambda_{\leftarrow}$<450nm). The upper limit of ($d1_{ch1}$=60) was determined as the maximum that permitted accurate measurement of the spectral width of ch1 resonance; in that above this thickness, the dip depth of the resonance location is too shallow to permit measurement of the spectral width using equation (1-28) from Chapter 1. Above this $d1_{ch1}$ thickness, the resonance condition flattens off, as observed in Fig. 4-4(A). In summary, only a certain range of $d1_{ch1}$ thickness ($d1_{ch1}$=23:60) permit the stimulation of dual channel SPR, in the investigated configurations.

4.3.3.2 Channel (2)

Next we investigate the influence that the thickness of the metallic component of the second channel has on sensor performance. This is done using the same parameters as in Fig. 4-4, but with ($d1_{ch1}$=50nm), and ($d1_{ch2}$=10:90nm).

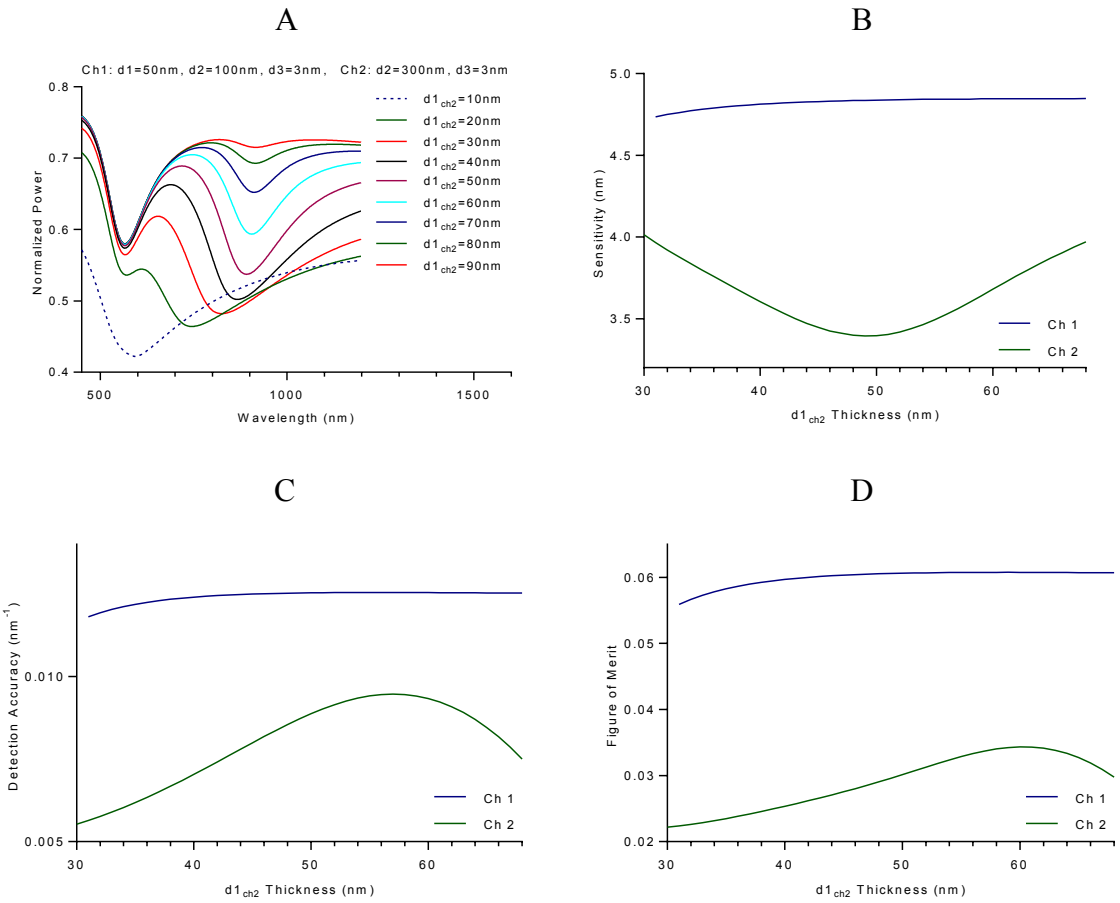

Figure 4-5 – (A) Normalised output power across the spectral domain of a (Ag/SiO_2/Pd) multilayer dual-channel sandwich structure OFSPR sensor in the presence of 0% H_2; (λ=450:1200nm), Ag($d1_{ch1}$=50nm, $d1_{ch2}$=10:90nm), SiO_2($d2_{ch1}$=100nm, $d2_{ch2}$=300nm), Pd($d3_{ch1}$=3nm, $d3_{ch2}$=3nm). (B) Sensitivity of the resonance conditions stimulated at channel (1) and channel (2) as measured by the introduction of 4% H_2. (C) Detection accuracy. (D) Figure of merit.

Fig. 4-5(A) displays the influence that $d1_{ch2}$ has on the normalized output power, and Fig. 4-5(B, C, D) illustrate the performance of the range of configurations represented in Fig. 4-5(A). Similarly, to $d1_{ch1}$, we observe that increase in $d1_{ch2}$ causes a red shift, and shallowing of the resonance condition in channel (2). This shallowing with increasing metallic thickness was also observed by Wang *et al.* in their dual channel OFPSR sensor (X.G. Wang *et al.* 2013b). The sensitivity of channel (2) decreases to a minimum around ($d1_{ch2}$=50nm) with increasing $d1_{ch2}$, and increases thereafter. The detection accuracy of channel (2) increases to a

maximum around ($d1_{ch2}$=57nm), and decreases with further increase in $d1_{ch2}$. Finally, the resultant figure of merit of channel (2) increases to a maximum with increasing $d1_{ch2}$ at around ($d1_{ch2}$=60nm), and decreases upon further rise in $d1_{ch2}$ thicknesses. This optimal d1 thickness is larger than that of the channel (1) value of 50nm. This is in correspondence to our findings in Chapter 3 Fig. 4-9, where we found that while the IM structure operated with maximum figure of merit at (d1=50nm), the resonance wavelength of this surface plasmon polarization was quite low, in the visible spectrum. In Chapter 3 Fig. 4-9, we found that IM structures with (d1=60nm) operated with the largest figure of merit across the near-IR spectrum. In the current chapter, the surface plasmon polarization in channel (2) occurs at longer resonance wavelengths, and thus the corresponding optimal metallic component thickness ($d1_{ch2}$) is expected to larger.

The sensitivity, detection accuracy, and figure of merit of channel (1) varies very little with $d1_{ch2}$. We make note that once the thickness of the metallic component in channel (2) is thin enough ($d1_{ch2}$=10nm), only a single broadened resonance dip can be observed. This occurs as the resonance wavelength of the surface plasmon polarizations in each channel becomes too close together due to the blue shift of the channel (2) resonance condition with decreasing $d1_{ch2}$ thickness, and thus the observed resonance dip is a combination of the surface plasmon polarizations stimulated in channel (1 & 2). The lower limit of ($d1_{ch2}$=31nm) was determined as the lowest $d1_{ch2}$ thickness that permitted accurate determination of the spectral width of the resonance generated in the channel (1) multilayer sensing structure. Similarly, the upper limit of ($d1_{ch2}$=68nm) was determined as the largest $d1_{ch2}$ thickness that permitted accurate measurement of the spectral of channel (2).

In summary, we have investigated the influence that a range of metallic layer thickness have on the performance of both sensing channels. We have observed that only a range of $d1_{ch1}$ and $d1_{ch2}$ thicknesses permit the stimulation of two independent surface plasmon resonance conditions, whose performance can be measured. In light of these findings. 50nm was the determined optical thickness of $d1_{ch1}$ in Fig. 4-4(D), and 60nm was the optimum thickness of $d1_{ch2}$. Thus we choose to employ optimal parameters of ($d1_{ch1}$=50nm), and ($d1_{ch2}$=60nm), in the subsequent investigations. Next we investigated the influence that the modulation layer thickness $d2_{ch1}$ and $d2_{ch2}$ has on the dual channel sensing device.

4.3.4 Modulation Layer Thickness (d2)

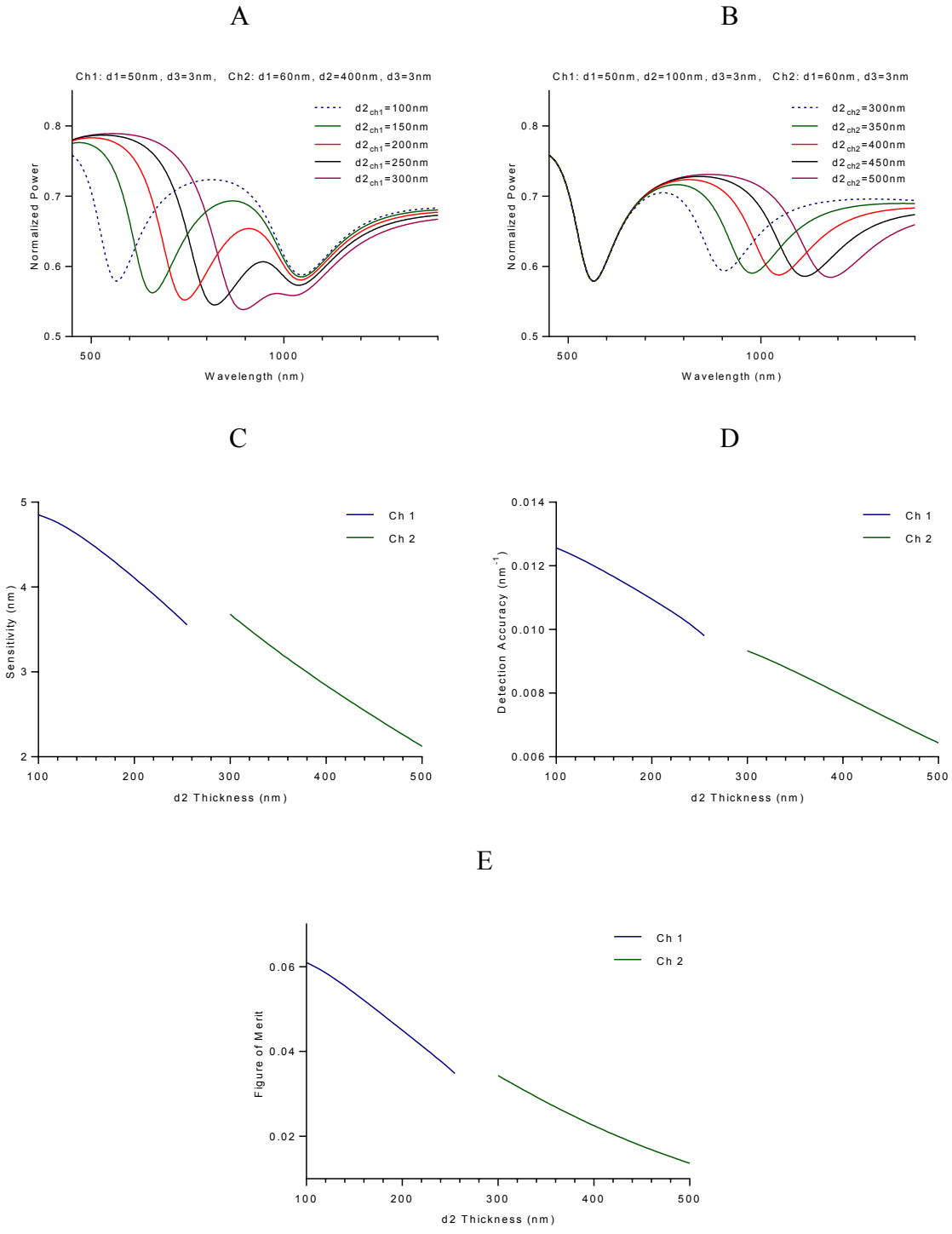

Figure 4-6 – Normalised output power across the spectral domain of a (Ag/SiO_2/Pd) multilayer dual-channel sandwich structure OFSPR sensor in the presence of 0% H_2; (λ=450:1400nm), Ag($d1_{ch1}$=50nm, $d1_{ch2}$=60nm), SiO_2($d2_{ch1}$=100:300nm, $d2_{ch2}$=400nm), Pd($d3_{ch1}$=3nm, $d3_{ch2}$=3nm). (B) SiO_2($d2_{ch1}$=100nm,$d2_{ch2}$=300:500nm). (C) Sensitivity of the resonance conditions stimulated at channel (1) from (A), and the sensitivity of the resonance conditions stimulated at channel (2) from (B) as measured by the introduction of 4% H_2. (D) Detection accuracy. (E) Figure of merit.

In Fig. 4-6(A), $d2_{ch1}$ is varied in steps from ($d2_{ch1}$=100:300nm). As we have previously observed in Chapter 2, the modulation layer thickness has little influence on the magnitude of the resonance condition, and this is also true for the dual-channel sensor, as can be seen in Fig. 4-6(A, B). We observe that increasing the thickness of the modulation layer in channel (1) causes the spectral location of the channel (1) resonance condition to move towards longer wavelengths. The shape, resonance location and magnitude of the resonance generated in channel (2) is affected very little by a change in $d2_{ch1}$. Similar observations are made in Fig. 4-6(B), where ($d2_{ch2}$=300:500nm), and a red shift of channel (2) can be observed with increasing $d2_{ch2}$, with a very marginal influence on the surface plasmon polarization in channel (1). In light of these observations, the influence that $d2_{ch1}$ has on the channel (1) surface plasmon polarization will not be presented here, as $d2_{ch1}$ has almost no influence on the performance of the channel (1) surface plasmon polarization. Similar action is taken with the performance of $d2_{ch2}$ on channel (1).

Fig. 4-6(C) displays the influence that $d2_{ch1}$ and $d2_{ch2}$ has on sensor sensitivity, of the surface plasmon polarizations corresponding to their channels. The sensitivity of both channels decreases with increasing modulation layer thickness. A similar reduction in performance can be seen in the detection accuracy Fig. 4-6(D) of each device with increasing modulation layer thickness, and subsequently the figure of merit Fig. 4-6(E). This can be understood by considering the fact that as the modulation layer thickness (d2) increases, the resonance is pushes to higher wavelengths where the sensitivity is decreased (see chapter 2). At these higher wavelengths, the amount of absorption in the metallic Pd layer also increases, causing a broadening in the dip and a resulting reduction in detection accuracy.

We note that the performance of channel (1) could not be determined once the modulation thickness exceeded a certain value ($d2_{ch1}$=255nm), as the resonance depth was too shallow. From Fig. 4-6(A & B), it can be seen that a minimum difference in the thickness of each modulation layer is necessary in order to establish independent resonance conditions corresponding to each channel. As a result, we maintain a difference in modulation thickness of 200nm, where ($d2_{ch1}$=100nnm), and ($d2_{ch2}$=300nm), in the subsequent investigation; where we observe the influence that the Pd layer thickness has on the resonance condition.

4.3.5 H_2 Sensitive Layer Thickness (d3)

We have previously investigated the influence that the thickness of the Pd layer has on the resonance condition in Chapter 2. Here we will investigate the influence that the Pd layer thickness has on the performance of both channels along the fibre.

4.3.5.1 Channel (1)

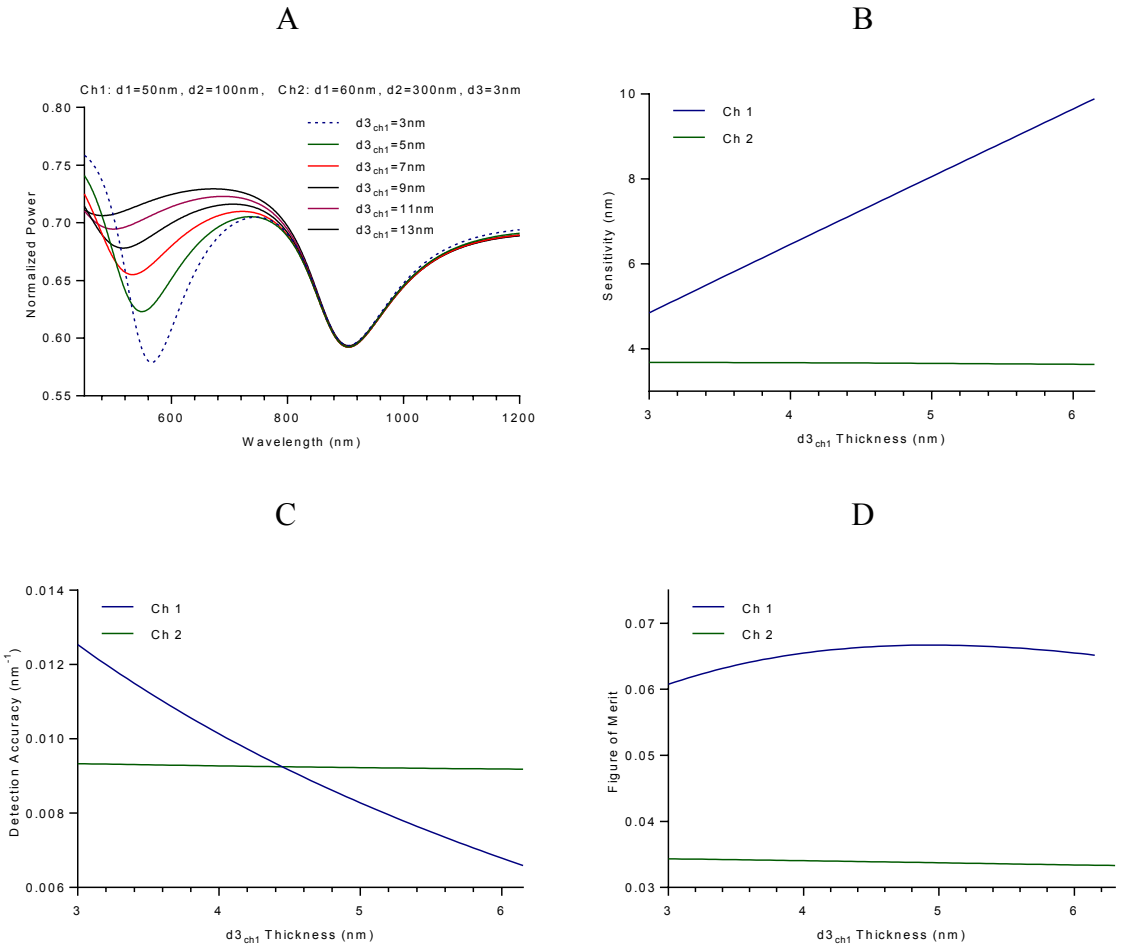

Figure 4-7 – (A) Normalised output power across the spectral domain of a (Ag/SiO_2/Pd) multilayer dual-channel sandwich structure OFSPR sensor in the presence of 0% H_2; (λ=450:1200nm), Ag($d1_{ch1}$=50nm, $d1_{ch2}$=60nm), SiO_2($d2_{ch1}$=100nm, $d2_{ch2}$=300nm), Pd($d3_{ch1}$=3:13nm, $d3_{ch2}$=3nm). (B) Sensitivity of the resonance conditions stimulated at channel (1) and channel (2) as measured by the introduction of 4% H_2. (C) Detection accuracy. (D) Figure of merit.

Fig. 4-7(A) displays the normalized output power from a series of structures varying in the thickness of the Pd layer in channel (1) ($d3_{ch1}$=3:13nm). It can be seen that as the thickness of this layer decreases, so too does the depth of the resonance condition in channel (1). This is due to increased absorption of light which occurs as the Pd layer thickness increases. The

sensitivity of the channel (1) structure increases with increasing $d3_{ch1}$ thickness, as seen in Fig. 4-7(B), and is in correlation with that observed in Chapter 2. The spectral width of channel (1) increases with increasing $d3_{ch1}$, as observed in Fig. 4-7(A, C). Again, this is due to absorption increases which occur as the Pd thickness increases. The upper limit of the $d3_{ch1}$ thickness is that which permits a resonance condition with enough depth such that the spectral width can be measured using the detection accuracy equation (1-28) from Chapter 1, and was found to be ($d3_{ch1}$=6.15nm). The figure of merit changes very little with $d3_{ch1}$ thickness due to the opposing influences that this layer thickness has on sensitivity (increases with d3) and detection accuracy (decreases with d3) as observed in Fig. 4-7(B, C, D). The thickness of $d3_{ch1}$ has little influence on the performance of the resonance condition stimulated in channel (2).

4.3.5.2 Channel (2)

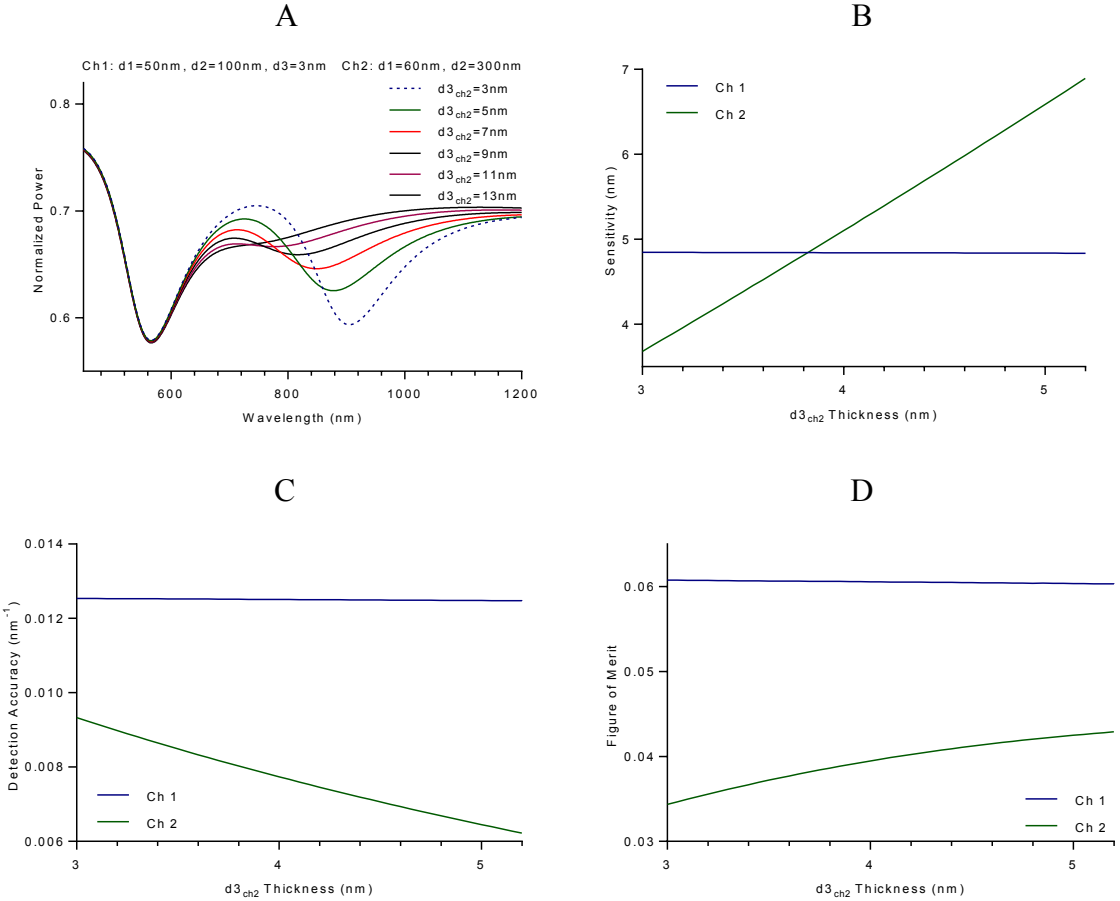

Figure 4-8 – (A) Normalised output power across the spectral domain of a ($Ag/SiO_2/Pd$) multilayer dual-channel sandwich structure OFSPR sensor in the presence of 0% H_2; (λ=450:1200nm), Ag($d1_{ch1}$=50nm, $d1_{ch2}$=60nm), SiO_2($d2_{ch1}$=100nm, $d2_{ch2}$=300nm), Pd($d3_{ch1}$=3nm, $d3_{ch2}$=3:13nm). (B) Sensitivity of the resonance conditions stimulated at channel (1) and channel (2) as measured by the introduction of 4% H_2. (C) Detection accuracy. (D) Figure of merit.

Finally, we investigated the influence that $d3_{ch2}$ has on the performance of each channel. Similar to channel (1), we see a blue shift of the resonance condition due to a decrease in the effective index of the surface plasmon with increasing $d3_{ch2}$ thickness. Additionally we observe shallowing, and broadening with increasing $d3_{ch2}$ in Fig. 4-8(A), again due to increasing absorption in the Pd layer as its thickness increases. Sensitivity increases with increasing $d3_{ch2}$ thickness, and surpasses the sensitivity of channel (1) once the $d3_{ch2}$ thickness is above (≈4nm). Once again, the upper limit of the thickness of the Pd layer was that which allowed for accurate determination of the resonance linewidth. The detection accuracy of channel (2) can be seen to decrease with $d3_{ch2}$, (again due the increased absorption in Pd). By careful comparison of Fig. 4-7(C) and Fig. 4-8 (C), we see that the decrease in detection accuracy in both cases is very similar in nature however the detection accuracy in Fig. 4-7(C) has a higher starting point (at $d3_{ch1}$=3nm). This is due to the fact the channel (1) resonance occurs at much shorter wavelengths where absorption in the metallic components of the sensor is inhibited therefore giving a narrower resonance. Therefore, we begin with a higher detection accuracy which falls away as the thickness of the Pd layer is increased. In Fig. 4-8(C) by comparison, the resonance, occurring at a longer wavelength, is broader but follows the same trend as the Pd layer thickness is increased.

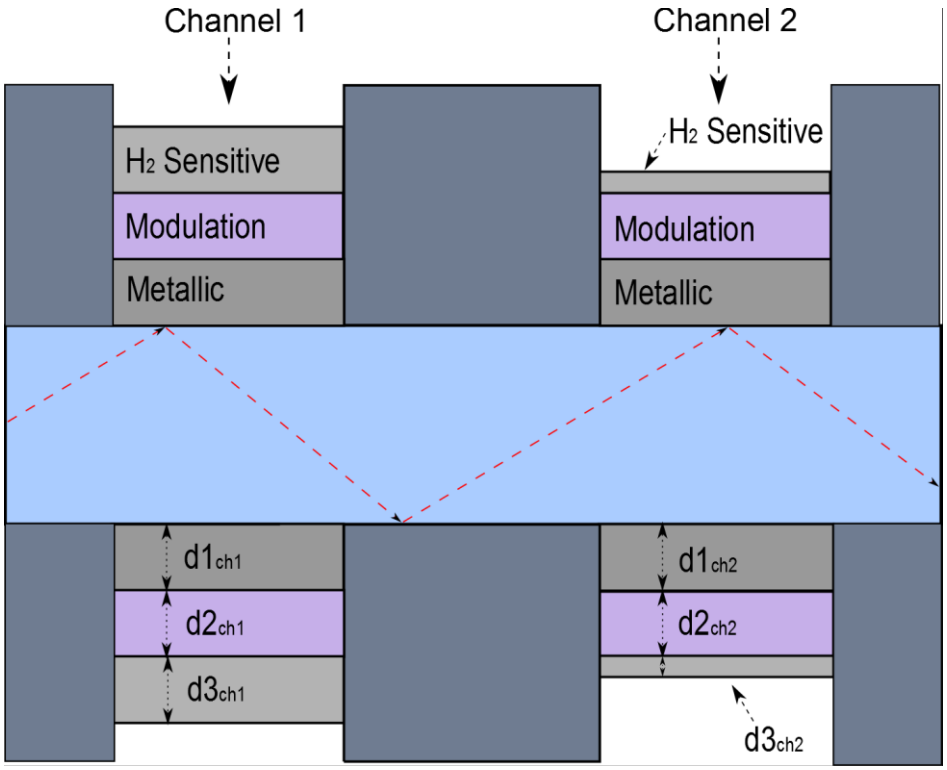

Figure 4-9 – (A) Schematic representation of a specific dual channel sensor, consisting of a relatively thick Pd layer in channel (1), and a thinner Pd layer in channel (2).

In light of these findings, we propose a specific type of dual-channel sensor, which consists of a thick and thin Pd film. The relatively thick Pd film will undergo a greater spectral resonance shift upon hydrogenation, thus leading to higher sensitivity, compared to the thinner Pd film. The relatively thin Pd film is expected to operate with a very fast response time however. Thus, an early warning response is achieved through the thin Pd layer channel, and a more accurate determination of H_2 concentration. From the results illustrated in Fig. 4-7 & 8, we conclude the device operates with higher sensitivity at lower wavelength. Thus, the thick Pd film will be employed in channel (1), overlaying the thinner modulation layer of the two channels. We suggest using the configuration that operated with the highest sensitivity in Fig. 4-7. The normalized output power of this configuration Ag($d1_{ch1}$=50nm, $d1_{ch2}$=60nm), SiO_2($d2_{ch1}$=100nm, $d2_{ch2}$=300nm), Pd($d3_{ch1}$=6.15nm, $d3_{ch2}$=3nm), is presented in Fig. 4-10.

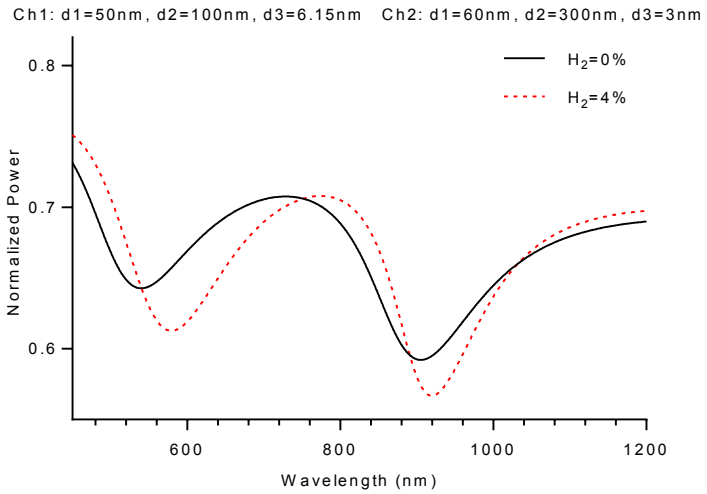

Figure 4-10 – Normalised output power across the spectral domain of a specific type of dual channel multilayer OFSPR sensor in the presence of 0% and 4% H_2 consisting of relatively thick and thin Pd films; (λ=450:1200nm), Ag($d1_{ch1}$=50nm, $d1_{ch2}$=60nm), SiO_2($d2_{ch1}$=100nm, $d2_{ch2}$=300nm), Pd($d3_{ch1}$=6.15nm, $d3_{ch2}$=3nm).

In Fig. 4-10, the continuous black line illustrates the normalized output power in the absence of H_2, and the dashed red line demonstrates the influence on the output power upon the introduction of 4% H_2. This device operates with a sensitivity of (Sn=9.8875nm) in channel (1) to 1% change in H_2 concentration, with a corresponding sensitivity of (Sn=3.68nm) in channel (2). The response time of channel (2) is expected to be (4s) to 4% H_2, which is derived from (Liu and Li 2016b). The response time of channel (1) is expected to be longer than channel (2), but is still expected to operate faster than (15s) to 4% H_2, as derived from (Perrotton *et al.* 2013).

4.3.6 Further Multi-Channel Extension

In this section, we extend the dual channel model equation (4-2) to account for the inclusion of a third channel as per equation (4-3). We investigate the performance of this device by measuring the sensor sensitivity, detection accuracy, and figure of merit. Following this, we investigate the possibility of including additional channels along the fibre core.

4.3.6.1 Triple Channel

The normalized output power of the sensor is illustrated in Fig. 4-11(A). In addition, the performance of each channel in Fig. 4-11(A) is demonstrated in Fig. 4-11(B, C, D).

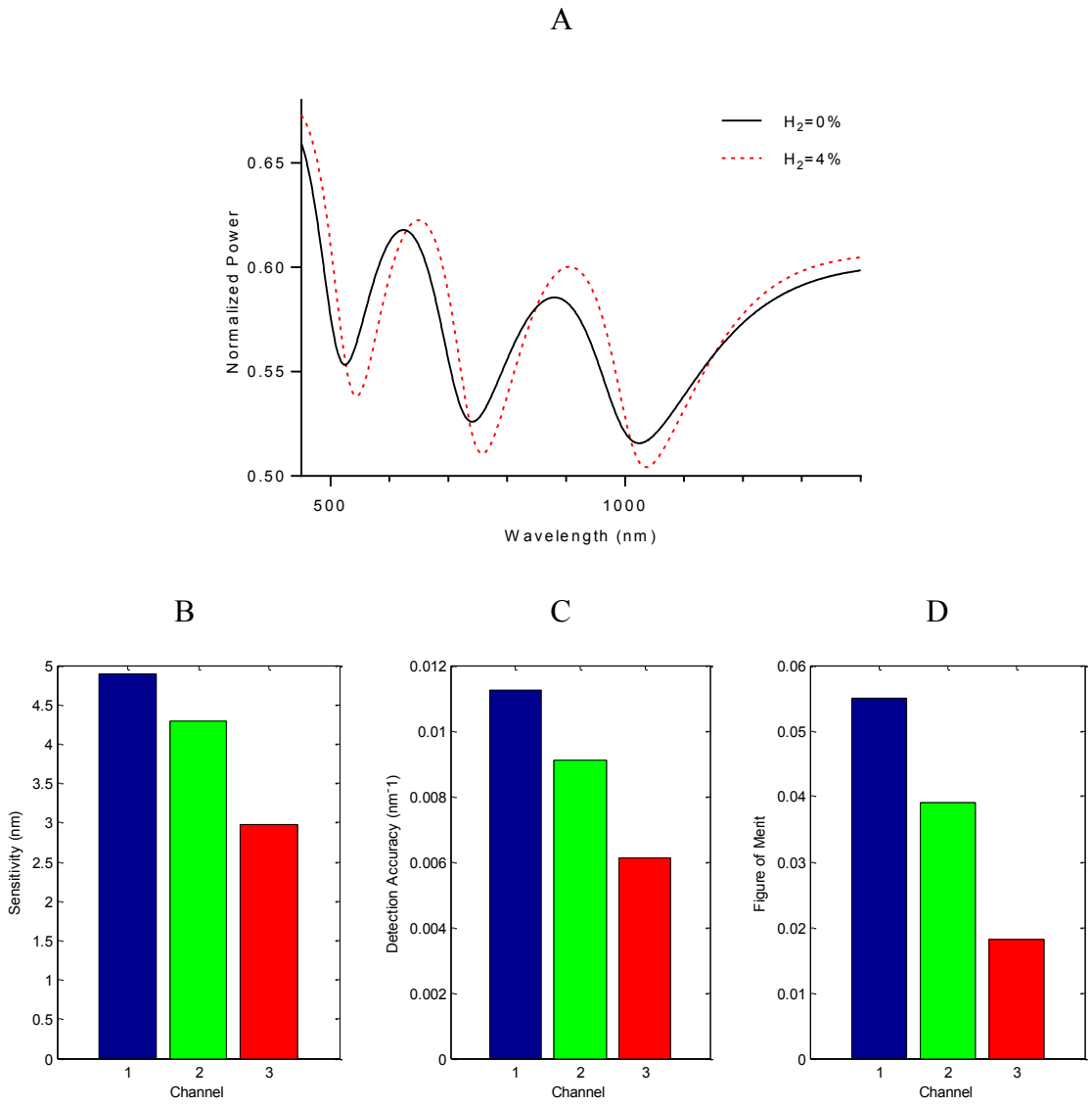

Figure 4-11 – (A) Normalised output power across the spectral domain of a specific type of triple-channel multilayer OFSPR sensor in the presence of 0% and 4% H_2 consisting of relatively thick and thin Pd films; (λ=450:1400nm), Ag($d1_{ch1}$=$d1_{ch2}$=$d1_{ch3}$=50nm), SiO_2($d2_{ch1}$=80nm, $d2_{ch2}$=200nm, $d2_{ch3}$=400nm), Pd($d3_{ch1}$=$d3_{ch2}$=$d3_{ch3}$=3nm). (B) Sensitivity. (C) Detection Accuracy. (D) Figure of Merit.

Similarly to the dual channel sensor, surface plasmon polarizations at each channel stimulates surface plasmon resonance at different wavelengths, due to the difference in modulation layer thickness at each channel. In Fig. 4-11(B), sensitivity decreases with channel, due to the

increase in modulation layer thickness. The resonance wavelength of the first channel in our triple-channel sensor is near 550nm. We recall from Chapter 3 Fig. 3-7, where we determined the sensitivity of IM based structures with (d1=50nm), and the resonance wavelength was modulated using d2; sensitivity increased to a maximum at (λ≈550nm), and decreased thereafter. Thus, the triple channel device follows the same behavior as the previously investigated single channel counterpart in Chapter 3 Fig. 3-7, and dual channel sensor in Fig. 4-6(C) where sensitivity decreases with increasing modulation thickness. Fig. 4-11(B) illustrates the detection accuracy of each channel. Similarly to the sensitivity measurement, the detection accuracy of the triple channel sensor decreases with increasing channel, like the single channel sensor in Chapter 3 Fig. 3-8 and the dual channel sensor in Fig. 4-5(D). Consequently, the resultant figure of merit decreases with increasing channel in the triple channel sensor, as illustrated in Fig. 4-11(D). A common trend observed in each multi-channel configuration is that performance decreases with increasing resonance wavelength, again a behavior consistent with what we've seen in Chapter 2.

While sensor performance decreases with increasing modulation layer thickness as we move towards higher channels, improvements to sensitivity and detection accuracy can be made in a number of ways. As we've seen in Fig. 4-7, 8, & 10; the sensitivity can be improved by increasing the thickness of the Pd layer. In Chapter 1 Fig. 1-15, we demonstrated that the real component of metallic layer dielectric permittivity has a large influence on the sharpness of the resonance condition. Thus, the metallic material (Ag) could be substituted for another material with greater magnitude of the real permittivity component; for example Al (Sharma 2012).

4.3.6.2 Quadruple Channel

We've found that the greatest limiting factor in the number of channels that can be employed along the fibre, is the methods of measuring sensor performance. Specifically, the method of determining the spectral width of the resonance condition at a location where the normalized output power is equal to $1.1 \times P_{min}$, as once the difference in the modulation thickness between channels is small enough, the depth of the resonance conditions decrease to a point where the detection accuracy can no longer be determined. In the previous figures, while it is has not been presented, the detection accuracy of the resonance condition in the absence of H_2 gas could be determined as the criteria for the detection accuracy equation (1-28) from Chapter 1 is fulfilled. If we were to disregard this and only ensure that the spectral width of

the resonance condition in the presence of 4% H_2 can be measured using Chapter 1 equation (28), then an additional channel can be included along the spectral range (λ=450:2000 nm). Fig 12 illustrates the normalized output power from a 4-channel OF sensor, where the detection accuracy of the resonance condition in the absence of H_2 (continuous black line) cannot be measured using the previously defined equation for detection accuracy, but the detection accuracy of the resonance condition in the presence of 4% H_2 is presented. The performance of each channel is illustrated in Fig. 4-12 (B, C, D).

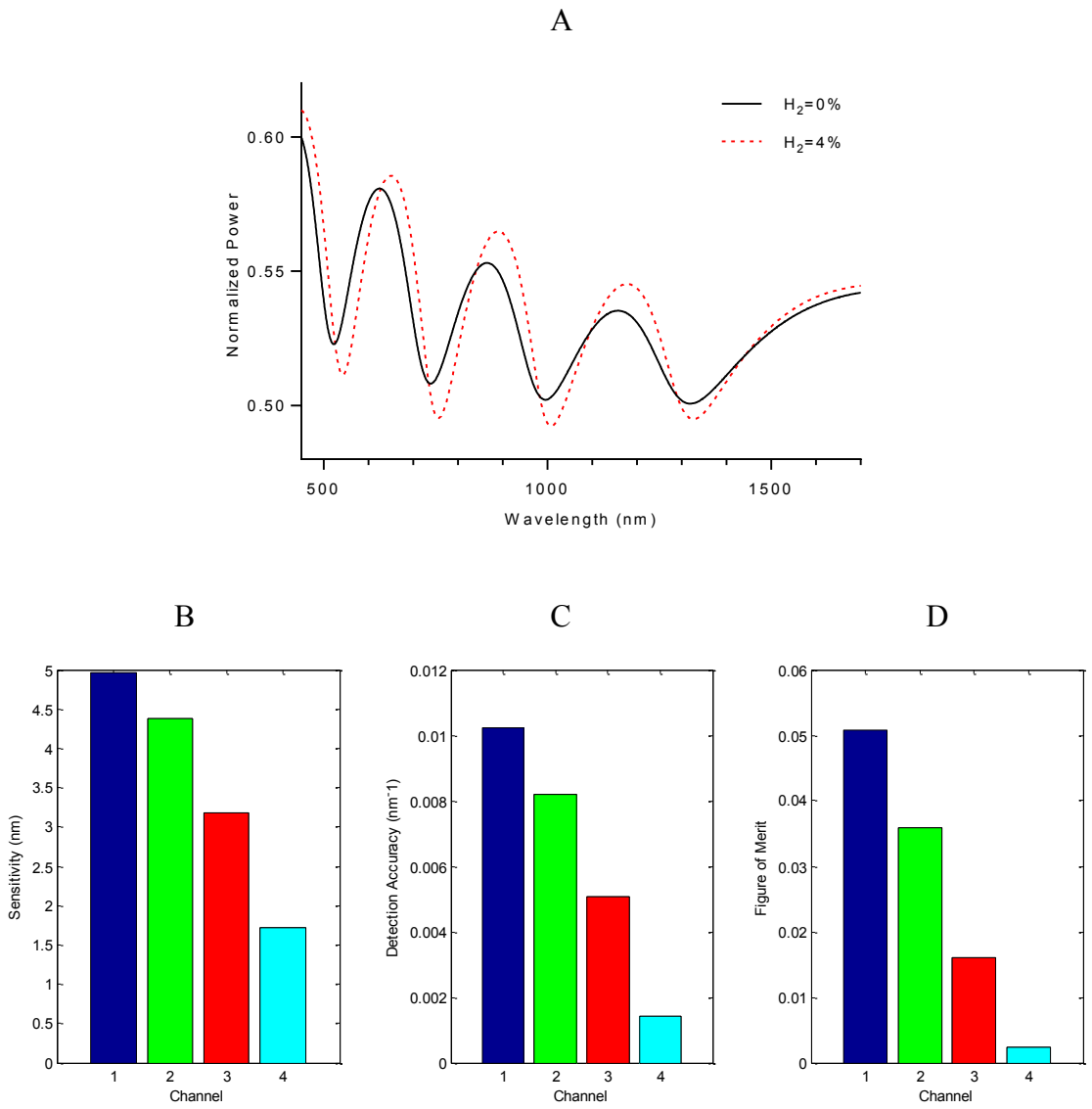

Figure 4-12 – (A) Normalised output power across the spectral domain of a specific type of quadruple-channel multilayer OFSPR sensor in the presence of 0% and 4% H_2 consisting of relatively thick and thin Pd films; (λ=450:1700nm), Ag($d1_{ch1}$=$d1_{ch2}$=$d1_{ch3}$=$d1_{ch4}$=50nm), SiO_2($d2_{ch1}$=80nm, $d2_{ch2}$=200nm, $d2_{ch3}$=380nm, $d2_{ch4}$=640), Pd($d3_{ch1}$=$d3_{ch2}$=$d3_{ch3}$=$d1_{ch4}$=3nm). (B) Sensitivity. (C) Detection Accuracy. (D) Figure of Merit.

Sensor performance can be seen to decrease with increasing channel / modulation layer thickness in Fig. 4-12, similarly to that of the triple channel senor. We note that the figure of merit in the fourth channel is particularly low (4.92% of that observed in channel (1)). Which is driven by enhanced broadening due to increased absorption in the metallic components of the sensor at longer wavelengths. The reduction in sensitivity of channel (4) compared to channel (1) is much less however (35%). As mentioned previously, the decrease in

performance occurs due to the increase modulation layer thickness that accompanies an increase in resonance wavelength.

4.3.6.3 Sextuple Channel

Attempts to include additional channels are hindered by the reduction in resonance depth that accompanies the greater modulation thicknesses necessary in order to generate additional independent resonance conditions. If resonance conditions can be identified, even though the resonance depth is shallower than that which permits measurement using the detection accuracy formula in Chapter 1; then the number of sensing channels can be further increased. Fig. 4-13 demonstrates proof of this concept, where 6 multilayer sensing channels are employed along the OF structure.

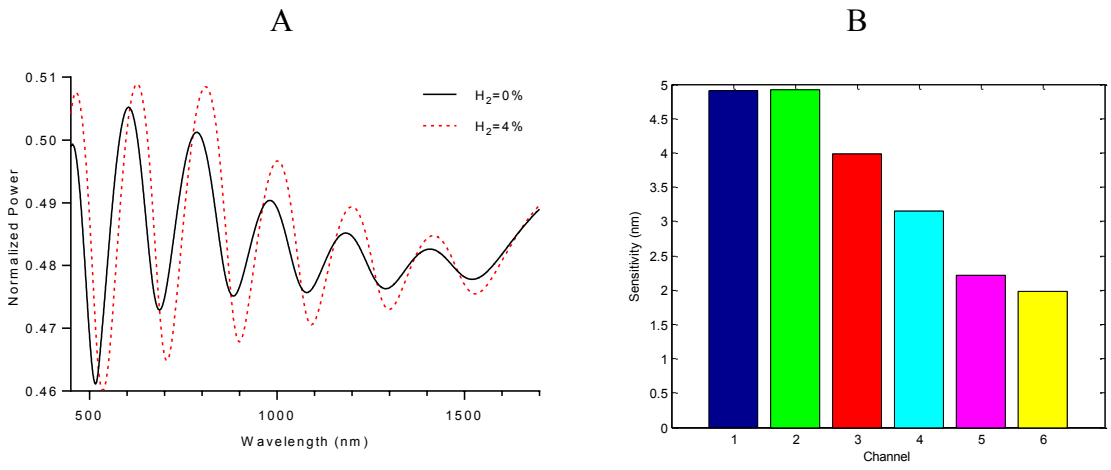

Figure 4-13 – (A) Normalised output power across the spectral domain of a specific type of sextuple-channel multilayer OFSPR sensor in the presence of 0% and 4% H_2 consisting of relatively thick and thin Pd films; (λ=450:1700nm), Ag($d1_{ch1}$=$d1_{ch2}$=$d1_{ch3}$=$d1_{ch4}$=$d1_{ch5}$=$d1_{ch6}$=50nm), SiO_2($d2_{ch1}$=80nm, $d2_{ch2}$=170nm, $d2_{ch3}$=300nm, $d2_{ch4}$=450nm, $d1_{ch5}$=625nm, $d2_{ch6}$=825nm), Pd($d3_{ch1}$=$d3_{ch2}$=$d3_{ch3}$=$d1_{ch4}$= $d1_{ch5}$=$d1_{ch6}$=3nm). (B) Sensitivity.

In Fig. 4-13(A) we observe that normalized output power from a 6-channel OFSPR multilayer structure. A reduction in resonance depth with increasing channel is evident, that stems from the use of thickener modulation layers at larger channels. In Fig. 4-6(A), we observed that the resonance depth of channels (1 & 2) decreased as the resonance wavelengths of each channel approached the same value. This effect can be observed in Fig. 4-13(A) as an overall reduction in the resonance depth across the wavelength spectrum, due

to the inclusion of more channels that generate independent resonance conditions across the finite observed wavelength spectrum.

In summary, additional channels can be added to the dual channel sensing device. These operate with decreasing performance as the modulation layer thickness increases. The increase in modulation layer thickness is necessary in order to generate independent surface plasmon resonance modes through wavelength division multiplexing. The largest limiting factor when it comes to the number of additional channels that can be added is the minimum depth that constitutes a resonance condition. With the continued advent of affordable high accuracy spectrometers it is possible that this problem of reduced resonance depth in the higher channels could be overcome to some degree when measurements of the spectrum attain sufficient accuracy.

4.4 Conclusion

In conclusion, we performed a series of investigations into the operation of a dual channel multilayer ($Ag/SiO_2/Pd$) OFSPR H_2 sensor. We determined the influence that the thickness of each multilayer component has on the performance of both channels. This was achieved by first determining the normalized output power through the fibre, and then measuring the performance of each configuration in terms of sensitivity, detection accuracy, and figure of merit. We found that the optimal $d1_{ch1}$ thickness was approximately 50nm, where the thinner modulation layer thickness was employed in channel (1). In addition, we found a larger thickness of the metallic layer demonstrated the largest figure of merit with channel (2), due to the spectral location of channel (2) resonance wavelength. We observed that a minimum difference in the modulation layer thicknesses of channel (1 & 2) is necessary such that the independent resonance dips can be observed.

We propose a specific type of dual channel sensor, where one channel is expected to operate with a fast sensor response time of (4s to 4% H_2), thus providing an early warning indication of H_2 leakage, and the other channel operates with (267%) improvement in sensitivity, in (<15s to 4% H_2), thereby providing a more accurate measurement of H_2 concentration over time. Finally we make preliminary investigations into the operation of an N-channel sensor, where N>2. We demonstrate the operation of a 3- and 4- channel sensor, and determine the corresponding performance of each channel. Finally, we extend the model to include 6

multilayer sensing structures along the fibre core, and determine the sensitivity of each channel.

H_2 has proven to be an excellent clean, renewable, abundant source of fuel. However, given the nature of H_2 gas: (4%) lower explosive limit, high volatility, and storage at (-253˚C); it has been difficult to harness. Employing a remote sensing optical fibre device with multipoint detection capabilities significantly increases safety by ensuring rapid accurate H_2 leak detection, and helps to facilitate a continued change towards clean energy.

5 Chapter 5: Waveguide Coupled Surface Plasmon Resonance

5.1 Introduction

In Chapter 3, we observed the presence of additional resonance terms relating to incident s-polarized light. This encouraged us to carry out investigations into the origin of these additional resonance modes, and inquire if they can be exploited for H_2 sensing applications. In this chapter, we carry out investigations in to a unique waveguide coupled optical fibre surface plasmon resonance H_2 sensor that permits co-operation between SPR and TE waveguide resonance modes. The sensor operates with significantly improved performance compared to the previously defined optimal SPR sensor. This is the first example of a device that permits the stimulation of SP and TE mode resonance at the same resonance wavelength.

5.1.1 Leaky Mode Resonance

A surface wave propagates along the interface between two media provided the admittance exhibited by the adjoining medium is positive imaginary, with extinction coefficient similar to that of the metal. Thus, only materials with a relatively small refractive index, and a large wavevector (metals) can facilitate the stimulation of surface waves (Salamon *et al.* 1997). This condition is fulfilled only using TM polarized light, within a small range incident angles, since the admittance is always negative imaginary for TE polarized light. Thus, a surface wave has characteristics as follows; propagation along the interface between two media, is not subject to attenuation parallel to the surface, and is attenuated perpendicular to the surface.

By including a dielectric overlayer on the metallic film, it is possible however to transform the admittance of the emergent medium such that it is positive imaginary for both TM and TE polarized light which can give rise waveguide modes within the dielectric film. When a mode ceases to be supported beyond a particular wavelength, that wavelength is said to be the cut-off. If the mode of a dielectric slab of larger refractive index than that of the adjoining media reaches the cut-off wavelength, then the nature of the mode changes from a fully guided mode to one whose propagation constant becomes complex. Consequently, this mode is subject to attenuation both parallel and perpendicular to the guiding surface (Haus and Miller 1986). Accordingly, this mode continually “leaks” energy away from the plane associated

with its propagation, and can be categorized as a leaky mode. For that reason, leaky waves differ to surface waves in that a leaky wave is not a proper modal solution whereas a surface wave is.

The existence of leaky waves on a surface interface was conceived by Zucker (Zucker 1954). The leaky wave theory for slab waveguides was first hypothesised in 1956. A book published by Barone while working at the Polytechnic Institute of Brooklyn (BARONE and INST. 1956), detailed investigations into a structure consisting of an electric line source located over a dielectric slab structure, and discovered the presence of resonance modes. The same year, a paper was published by Marcuvitz (who was working at the same institute), where he noted their close analogy to quantum mechanical tunnelling (Marcuvitz 1956). In this paper, Marcuvitz derived non-modal solutions to the wave propagation constant, and thus, indicates the presence of "leaky" waves.

The first measurement of a leaky mode was carried out 5 years later (Cassedy and Cohn 1961) using the a form of the configuration mentioned by both Barone and Marcuvitz. The authors performed experimental measurements of the output spectrum through a dielectric loaded trough waveguide and confirmed the presence of leaky modes. The existence of whispering gallery leaky waves has been demonstrated using a dielectric cylinder configuration (Wait 1967). Soon after, solutions to the characteristic equation that defines wave propagation were determined along a lossless thin cylinder "rod" structure indicating the presence of axial leaky waves (Arnbak 1969).

The influence of the inclusion of a metal overlayer on the optical modes within a dielectric slab was investigated by Otto and Sohler (Otto and Sohler 1971). Hall and Yeh carried out investigations into the nature of leaky modes located inside and dielectric waveguide (Hall and Yeh 1973). Specifically, they experimentally demonstrated the hypothesis that in a three layer configuration where ($\varepsilon_1 < \varepsilon_2 < \varepsilon_3$), leaky modes can exist in the middle layer. This experiment was performed by focusing TM and TE light of wavelength (λ=632.8nm) onto the cleaved edge of various materials (ZnSe, GaAs), and the respective resonant modes were observed. The attenuation for the TM resonance mode was higher than that of the TE mode. Haus and Miller developed a formula that determines the attenuation constant of higher order cuttoff modes and of leaky modes in a dielectric slab (Haus and Miller 1986).

Further investigation was performance by Salamon *et al*., using a prism based configuration (Salamon *et al.* 1997). In their publication, two propagation modes (TM and TE) of incident

monochromatic light of (λ=632.8nm) were shone incident on a Kretschmann configuration, analogous to Fig. 5-1(D). This consisted of a glass prism coated with Ag(d1=50nm), TiO_2(d2=50nm), and material with refractive index (n=1.35), (d3=750nm). Salamon *et al.* experimentally observed both TM and TE resonance using a single configuration at different angles of incidence. The presence of TE-stimulated resonance is attributed to the inclusion of a dielectric overcoat on the metallic layer. The presence of both propagation modes in a single structure gave rise to the title coupled plasmon-waveguide resonance sensor for the device. Since then, much research has been carried out on various surface plasmon resonance based configurations with the aim to exploit any attractive properties that the coupled plasmon-plasmon waveguide resonance sensor can exhibit. We introduce six different multilayer configurations that permit the stimulation of resonance in Fig. 5-1 in order to illustrate the configurations used by other researchers.

5.1.2 Resonance Configurations

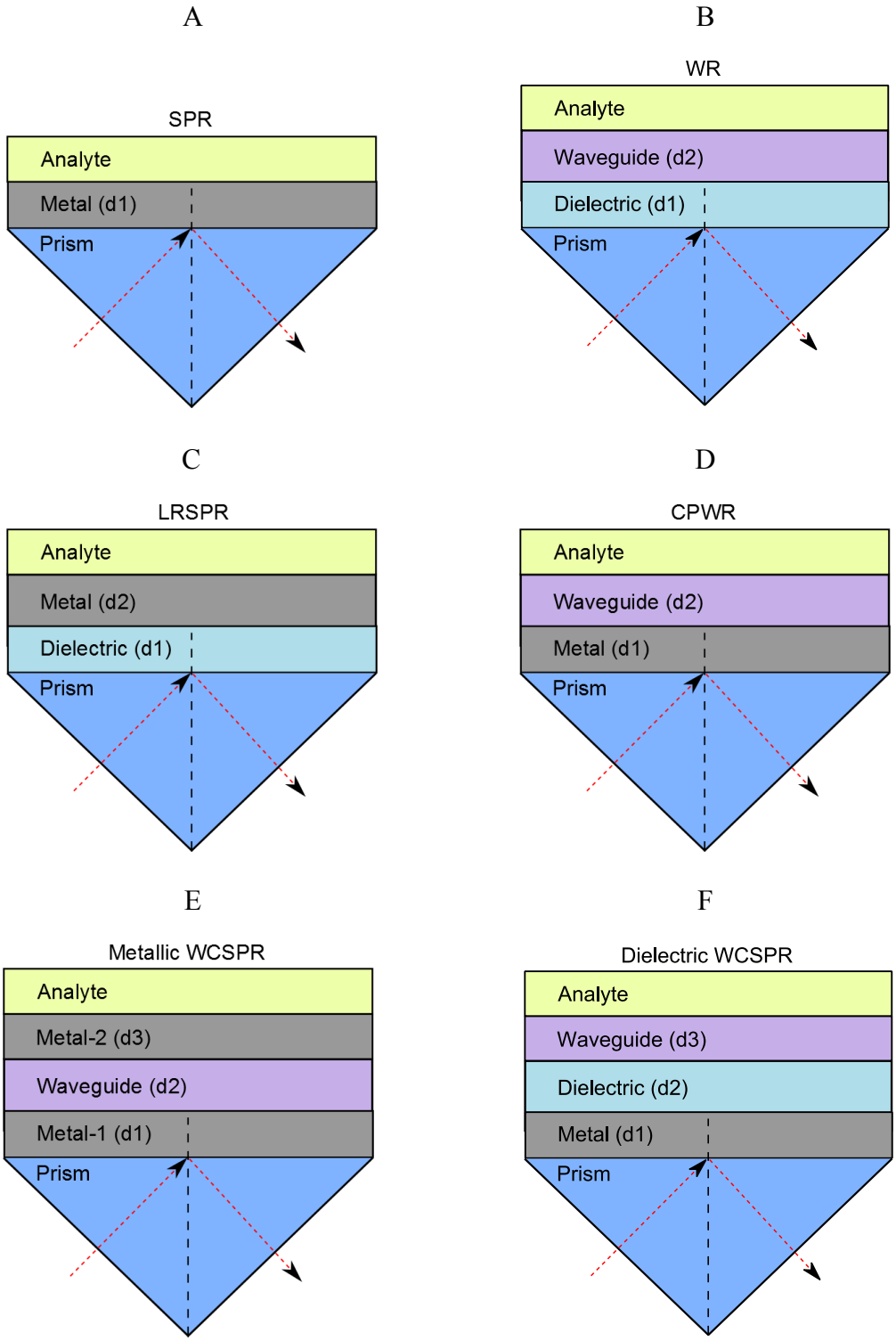

Figure 5-1 – (A) Schematic representation of a Kretschmann prism configuration that permits the stimulation of SPR (dielectric prism, metal film, analyte). (B) Waveguide Resonance (WR) sensor consisting of (dielectric prism, dielectric layer, waveguide layer, analyte). (C) LRSPR sensor consisting of (dielectric prism, dielectric layer, metal film, analyte). (D) CPWR sensor consisting of (glass prism, metal film, waveguide layer, analyte). (E) Metallic WCSPR sensor consisting of (dielectric prism, metallic film, waveguide layer, another metallic film, analyte). (F) Dielectric WCSPR sensor consisting of (dielectric prism, metallic film, dielectric layer, waveguide layer, analyte).

Several kinds of SPR sensors are presented in Fig. 5-1. They differ in terms of the components of their respective multilayer sensing structure. Fig. 5-1(A) displays the standard SPR sensor which consists of a metallic layer, and the analyte region, deposited onto a prism, in a Kretschmann configuration format. As we've mentioned in Chapter 1, incident monochromatic TM polarized radiation propagates through the prism structure and interacts with the metallic film. At a specific angle, SPR occurs between the incident radiation and the surface electrons at the metallic-analyte interface. The analyte region is the material whose properties are being measured, and can consist of a myriad of substances.

Fig. 5-1(B) illustrates a structure consisting of a dielectric prism, coated with two dielectric overlayers. The first overlayer modulates the incident angle through the dielectric material. The second material acts a waveguide, where the stimulation of both TM and TE waveguide modes are possible, thus it is labelled as a waveguide resonance (WR) sensor.

Fig. 5-1(C) displays a similar structure to Fig. 5-1(A), however, a dielectric layer is included between the prism and the metallic overlayer. Provided the refractive index of the prism matches that of the dielectric overlayer, the resultant penetration depth of the SPR increases. This enables the device to determine bulk changes in the analyte rather than focusing on surface changes near the metal-analyte interface. It is difficult however, to reliably generate a structure where the refractive indices of the prism and dielectric overlayer are equal, and thus, this structure is rarely adopted for sensing applications. Regardless, only TM polarized light is permitted to stimulate resonance within this sensing configuration.

Fig. 5-1(D) illustrates a coupled plasmon-waveguide resonance sensor (CPWR). Like the standard SPR sensor, this configuration consists of a metallic prism layered onto a dielectric prism. An additional dielectric layer is included onto the surface of the metallic film which acts as a waveguide. The analyte layer is then included on the surface of the waveguide layer. This configuration is capable of stimulating SPR at the metallic layer surface. Additionally, both TM and TE resonance can be achieved through resonance modes within the waveguide and are typically much narrower in existence than SPR modes.

Fig. 5-1(E) is comprised of a dielectric prism covered with a multilayer structure with a metallic layer, dielectric waveguide layer, another metallic layer, and analyte region. Both metallic films are capable of stimulating SPR using TM light, and waveguide resonance can be stimulated using the dielectric waveguide layer. This configuration is referred to as a metallic waveguide coupled surface plasmon resonance (WCSPR) sensor.

Finally the configuration in Fig. 5-1(F) consists of a dielectric prism, metallic overlayer, dielectric layer, waveguide film, and analyte region. The metallic film is spatially separated from the waveguide by a dielectric film, thus this configuration is known as a dielectric WCSPR sensor. Similarly to the previous WCSPR sensor in Fig. 5-1(E), both TM and TE resonance conditions are can be stimulated within this configuration.

A theoretical comparison between 4 of the different types of surface plasmons resonance sensing devices in Fig. 5-1(A, C-E) has been presented Chien and Chen (Chien and Chen 2004). They found that the LRSPR sensor operates with the largest sensitivity when used in a wavelength modulation based device, and the standard SPR operated with superior sensitivity in an angular interrogation based sensor. The results were as follows: (SPR, LRSPR, CPWR, WCSPR) operated with sensitivity of (0.2714, 0.0293, 0.0329, 0.1523˚) in angular interrogation, and (6.6, 15.3, 4.1, 7.1nm) in wavelength interrogation both in response to an absorbed self-assembly monolayer ($HS\text{-}(CH_2)_{15}COOH$).

Another theoretical review into various types of surface plasmon resonance sensing devices Fig. 5-1(A, D-F) has been performed by Grotewohl *et al.* (Grotewohl *et al.* 2016). In their paper, the authors also refer to 4 sensing types, (SPR, CPWR, metallic WCSPR Fig 1(D), and dielectric WCSPR). An incident wavelength of (λ=632.8nm) was shone onto each strucutre. The materials employed were: prism (glass), metallic (Ag), dielectric film (polymer with n=1.34), waveguide (TiO_2). The computed senstivities of each device were (150, 3100, 180, 14000 RIU^{-1}), with full width half maximums of ($1.8x10^{-3}$, $3.4x10^{-5}$,$1.6x10^{-3}$, $9.0x10^{-6}$ RIU). The dielectric WCSPR demonstrated the largest sensitivty compared to the other strucutres, but also yielded the lowest dynamic range.

Now that we have introduced several different configurations that permit the stimulation of resonance conditions, we will discuss some of the research that has been carried out to date by other researchers using these structures.

5.1.2.1 SPR

The configuration in Fig. 5-1(A) has been investigated by numerous researchers. Taking one example, Gwon *et al.* employed a configuration primarily consisting of a glass prism, Au(d1=30-70nm), surrounded by air (analyte region) (Gwon and Lee 2010). Very narrow thicknesses of index matching fluid, pyrex glass, and chromium were also applied between the glass prism and the Au film. TM polarized light was shone incident on the prism

configuration, and the corresponding reflectance revealed a single resonance condition within a very small range of incident angles. This dip in reflectance is attributed to SPR. This concept has been investigated in pervious Chapters 1-4.

Perrotton applied this structure to investigate an optical fibre configuration (Perrotton *et al.* 2011c). In their paper, the employed a silica prism, covered with a Pd film. Both TM and TE polarized light were shone through the silica fibre, at various angles of incidence, (thus acting like a prism). The authors demonstrated that only TM polarized light permitted the stimulation of resonance using this configuration.

5.1.2.2 WR

Sensing solely using waveguide modes have also been demonstrated. In particular we mention a device that permits the stimulation of leaky waveguide mode resonance. This configuration consists of a multilayer structure consisting of glass prism, Teflon cladding layer, SiO_2 waveguide layer, water analyte region (Okamoto and Yamaguchi 1997). Various TM and TE resonance modes were found as different resonance angles, and the depth of the TM dip was shown to vary with the imaginary component of the analyte refractive index.

5.1.2.3 LRSPR

The LRSPR structure has been applied for optical fibre applications (Jiang *et al.* 2015). In this paper, Jiang *et al.* used OF to stimulate both long and short range SPR simultaneously. This configuration consisted of a multilayer structure consisting of a hollow fibre core, OC300 (d1=260nm) - similar refractive index to SiO_2, Ag(d2=90nm), surrounded fused silica cladding. The dielectric and the cladding layers have similar refractive indices. In their paper, the authors state that since the Ag layer is located in between two dielectric materials, both long range, and short range SPR can be simulated simultaneously. The sensed liquid is introduced through the hollow fibre core. TM polarized light propagates along the hollow fibre core. The measured transmitted power reveals a dip at a specific resonance wavelength corresponding to the refractive index of the sensed liquid.

5.1.2.4 CPWR

Many researchers have employed this type of sensing configuration, however many different titles have been given to the structures, such as the aforementioned CPWR, plasmon waveguide resonance (PWR), and a metal clad waveguide (MCW) sensor.

A CPWR sensor has also been developed by Mahajna *et al.* (Mahajna *et al.* 2016). Their device consisted of a glass prism, covered in a thin film of Ag(d1=45nm), SiO_2(d2=1200nm), and the analyte medium, Fig. 5-1(D). Due to various conditions involving the thickness of the SiO_2 layer, incident angle, and wavelength, and refractive indices of each material; the SiO_2 acts as a waveguide, thus permitting the stimulation of resonance modes by either TM or TE polarized light. Monochromatic TM polarized light of (λ=632.8nm) was shone through the prism, proceeded to interact with the metallic film, and the corresponding reflectivity was determined. Three resonance modes were revealed, two very narrow and one wide. The narrow resonance conditions were attributed to waveguide resonance, and the wider mode was attributed to the stimulation of surface plasmon resonance. Additionally, TE polarized light of the same wavelength was shone incident onto the device, and two TE resonance modes were found, and attributed to waveguide guide resonance. All of the discovered resonance modes were stimulated at different angles of incident light.

Recently, a theoretical study into the operation of an optical fibre based coupled plasmon waveguide sensor was performed (Liu *et al.* 2018). Their configuration consisted of a multilayer sensing structure (metal, dielectric, analyte) deposited onto a step-index multimode fibre core. Various combinations of Ag, Au, ZnO, and TiO_2 were investigated as components in the multilayer structure. Three different propagation modes were investigated through the fibre, (unpolarized, TM, TE). Several dips in the output power were detected, and were labelled as (SPR, CPWR-1, CPWR-2), however, no method of characterization was implemented in defining each resonance condition. Metallic thicknesses (d1=10-70nm) were investigated, using unpolarized light, and the thickness of the dielectric layers were used to control the resonance wavelengths. Each resonance condition occurred at a separate resonance wavelength.

Bahrami *et al*. conducted research into the operation of a plasmon waveguide resonance sensor Kretschmann configuration consisting of a glass prism, Au(d1=48nm), SiO_2(d2=1200nm). In addition, a very thin Ti adhesion layer (2nm) was employed between the glass prism and Au. Incident TM and TE polarized light was shone on the structure separately of wavelength (λ=632nm) (Bahrami *et al.* 2013). The device was employed as a

refractive index based sensor, and operation was compared to that of the standard surface plasmon resonance structure. The plasmon waveguide resonance sensor operated with superior resolution in the refractive index, and this was attributed to the increase in the sharpness of the plasmon waveguide resonance condition.

Comparison between the sensitivity of the standard SPR and the plasmon waveguide resonance sensor has been carried out (Abbas *et al.* 2011b). For the SPR configurations, they used incident TM polarized light (λ=650nm), and employed structures with Au and Ag films (d1=50-54nm), with a small dielectric overlayer SiO_2(d2=3-6nm). The CPWR configurations were generated by increasing the dielectric layer thickness to (d2=510-520nm). A single dip in the measured reflectance was found in each of the investigated configurations at different angles of incidence. It was reported that the CPWR sensor operated with a greater penetration depth, and reduced sensitivity.

Another plasmon-waveguide resonance sensor based on angular interrogation has been developed by Zhang *et al*. (Zhang *et al.* 2015). Their configuration consists of a dielectric prism coated in a thin film of Au followed by SiO_2, and accompanied by a water analyte region. Au thickness of (d1=40, 55, 70nm) were investigated, and optimized at (d1=55nm). A very large dielectric thickness of (d2=1000nm) was used. Incident monochromatic TM polarized light (λ=632.8nm) is shone at various incident angles, and resonance occurs at two different angles of input corresponding to TM1 & TM2. SiO_2 was substituted for MgF_2 with (d2=1650nm) and two modes of TM resonance were stimulated once again. The three configurations mentioned here are analogous to the CPWR (Abbas *et al.* 2011b; Bahrami *et al.* 2013; Zhang *et al.* 2015).

A MCW sensor was developed by Skivesen *et al.* as an alternative to the commonly employed surface plasmon resonance sensor for biological sensing applications (Skivesen *et al.* 2007). The sensor consisted of a glass substrate, metallic layer, polystyrene (n=1.57), adlayer (n=1.33-1.45) (analyte) of varying thicknesses (0-1000nm). TM and TE resonance were demonstrated at separate resonance angles. This configuration is also analogous to the CPWR sensor illustrated in Fig. 5-1(D).

5.1.2.5 Metallic WCSPR

Apart from the previous mentioned study carried out by Salamon *et al.* (Salamon *et al.* 1997), the authors carried on research into the design of WCSPR sensors (Salamon and Tollin

2001). This sensor consisted of a Kretschmann configuration design; glass prism, Ag film, SiO2, Teflon spacer layer, aqueous material (analyte). TM and TE polarized light (λ=543.5, 632.8nm) was used in their experiments. Polarization modes at separate angles of incidence were demonstrated using both polarization modes of light, and were sensitive to the concentration of lipids present in the aqueous solution (analyte region).

A metallic WCSPR optical fibre sensor was developed by Ahn *et al.* which consisted of: Au(d1=18nm), ZnS:SiO_2(d2=220nm), Au(d1=18nm), deposited onto a 200μm diameter SiO_2 core, and was used in the detection of sucrose in solution (Ahn *et al.* 2012). By determining the transmittance of s- and p- polarized light through the fibre, the authors observed both surface plasmon, and waveguide modes at different resonance wavelengths. The number of plasmonic modes increased with the thickness of the ZnS-SiO_2 waveguide layer. Different aqueous solutions of concentration (0-25%w/w) were introduced in the flow cell, and the resonance conditions were analysed. While the guided modes demonstrated little to no response to the change in the refractive index of the liquid in the flow cell; the SPR mode underwent a red shift with increase in sucrose concentration.

5.1.2.6 Dielectric WCSPR

A dielectric WCSPR sensor has been investigated by Grotewohl *et al.* as mentioned previously (Grotewohl *et al.* 2016). Similarly to the CPWR, this structure has been employed by other researchers, using a different title such as low loss waveguide (LLW), and metal multilayer dielectric surface plasmon resonance (MMDSPR) senor.

A LLW sensor was developed (Sekkat 2016). This consisted of a Kretschmann configuration structure, which is comprised of a glass prism, metallic film (Au), low index spacer layer (n=1.3395), waveguide layer (PMMA), low index sensing media (water). The structure supported the excitation of independent TM and TE modes. This configuration is analogous to the dielectric WCSPR sensor.

A theoretical investigation into the operation of a MMDSPR sensor has been performed (Ilchenko *et al.* 2017). In this paper incident light (λ=532nm) was shone onto a Kretschmann structure consisting of a glass prism, Ag(d1=43nm), followed by a series of high and low index materials: TiO_2 and SiO_2 respectively. The thickness of the dielectric layers were determined using the formula $h_i = \frac{\lambda\alpha}{4\sqrt{\varepsilon_i}\cos(\phi)}$, which works out at approximately (d2=76nm)

for the first layer, and (d2=297nm) for the final layer, assuming that it is SiO_2. The structure supports both TM and TE resonant modes. This configuration has similarities to the WCSPR sensor, in that the same order is used in stacking the multilayer structure (prism, metal, dielectric, waveguide), but additional pairs of (dielectric, waveguide) layers are included overlaying the multilayer stack device.

5.1.2.7 MCLW

One final structure that is not analogous to any of the images illustrated in Fig. 5-1 is that investigated by Zourob *et al*. (Zourob *et al.* 2003). This configuration consisted of a Kretschmann based metal clad leaky waveguide (MCLW) sensor, for application in the detection of biological warfare agents. The structure consisted of a glass substrate (modulation) (d1=1mm), Ti(d2=8.5nm), SiO_2(300nm), with a water based analyte region. The design of the device (materials and relevant thicknesses) resulted in enhancement of the evanescent field from surface to bulk sensing.

5.1.3 Our Proposed Sensor

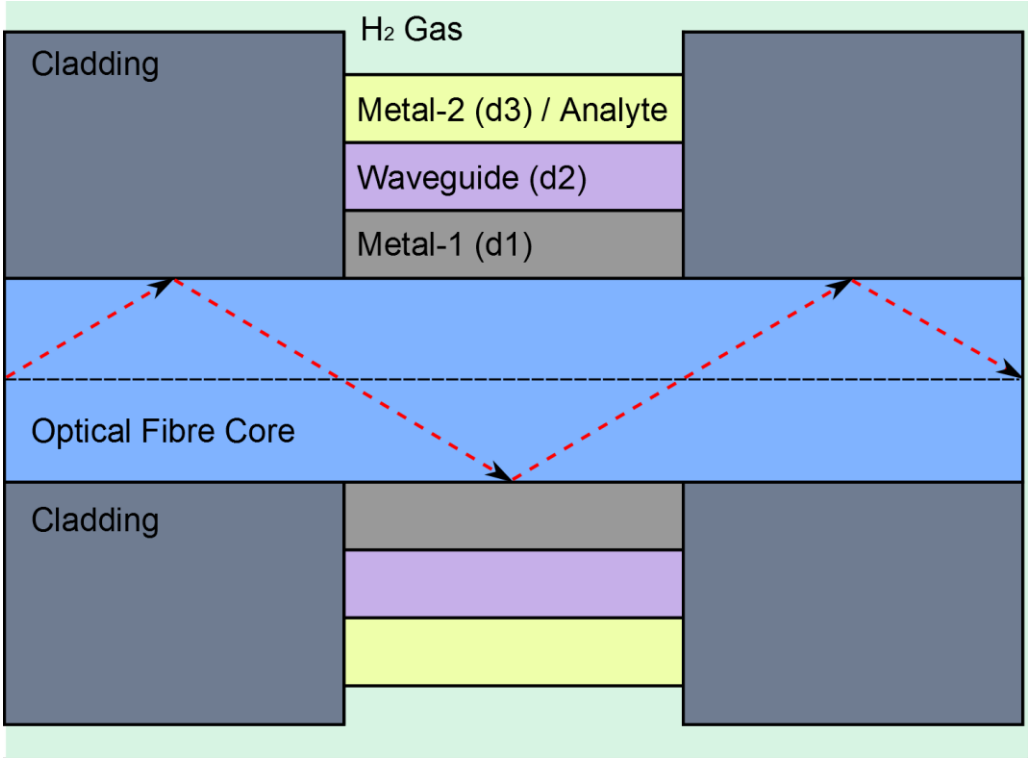

Figure 5-2 – (A) Schematic representation of our proposed optical fibre waveguide resonance sensor which consists of a multilayer stack sensing structure which consists of a silica fibre core, metal-1, dielectric waveguide, metal-2 (analyte).

Our final configuration consists of a multilayer sensing stack structure (Ag, Ta_2O_5, Pd) with (d1, d2, d3) deposited onto an unclad section of a fused silica fibre core as illustrated in Fig. 5-2. Given the nature of the materials that constitute our multilayer sensing structure, and the order in which they are stacked, our device could be defined as various sensors that have appeared throughout the literature, including; a CPWR sensor (Salamon *et al.* 1997; Grotewohl *et al.* 2016; Mahajna *et al.* 2016), also referred to as a PWR sensor (Abbas *et al.* 2011b; Bahrami *et al.* 2013; Zhou *et al.* 2014; Zhang *et al.* 2015), and a (MCW) (Skivesen *et al.* 2007). Additionally, due to the fact that our analyte layer is metallic (Salamon *et al.* 1997; Salamon and Tollin 2001; Chien and Chen 2004; Ahn *et al.* 2012). Regardless, of the title given to this type of sensor, the stimulation of surface plasmon resonance is permitted by the inclusion of the metallic layers, and the stimulation of TM and TE leaky resonance modes is permitted within the modulation layer. But through carefully choice metallic and dielectric materials, as well as the thickness of each multilayer sensing component, we demonstrate for

the first time that is possible to stimulate surface plasmon and leaky mode resonance at the same resonance wavelength using s single sensing configuration. Consequently, the magnitude of the resonance dip in the resultant output power through the optical fibre, which takes into account both TM and TE oscillation modes of propagation, will be greatly increased. The resultant unpolarized resonance condition has improved detection accuracy due to the inclusion of the leaky resonant mode, and thus, the figure of merit is greatly enhanced.

5.2 Theory

5.2.1 Output Power

In previous chapters, we determined the normalized output power through the fibre by considering both s- and p- polarized contributions. In this chapter, in order to understand the origin of certain resonance conditions, it is necessary to also determine the output power according to each individual propagation mode according to equations (5-1 & -2).

$$P_{TM-nor} = \frac{\int_{\theta_c}^{\pi/2} |r_p(\theta)|^{2N_{ref}} dPd\theta}{\int_{\theta_c}^{\pi/2} dPd\theta} \quad (5\text{-}1)$$

$$P_{TE-nor} = \frac{\int_{\theta_c}^{\pi/2} |r_s(\theta)|^{2N_{ref}} dPd\theta}{\int_{\theta_c}^{\pi/2} dPd\theta} \quad (5\text{-}2)$$

Where P_{TM-nor} and P_{TE-nor} correspond to the normalised output power of p- and s-polarized light respectively.

5.2.2 Dielectric Permittivity of Ta_2O_5

An additional material (Ta_2O_5) is included in the multilayer that has two primary functions; to shift the surface plasmon resonance angle to greater than the critical angle, and additionally to fulfil the stimulation of leaky mode resonance. The dielectric function of Ta_2O_5 is determined using the Lorentz-Drude relationship (Bright *et al.* 2013).

$$\varepsilon = \varepsilon_\infty + \frac{{\omega_{p,0}}^2}{\omega^2 + i\omega\gamma_0} + \sum_{j=1}^{N} \frac{{\omega_{p,j}}^2}{{\omega_j}^2 - \omega^2 - i\omega\gamma_j} \quad (5\text{-}3)$$

Where ε_∞ is determined from Equation (5-4).

$$\sqrt{\varepsilon_\infty} = A + \frac{B}{\lambda^2} \quad (5\text{-}4)$$

A = 2.10, B = 0.024 μm^2, $\omega_{p,0}$ = 6490 cm^{-1}, γ_0 = 6.5 x 105 cm^{-1}.

5.2.3 Electric Fields

Additionally, in order understand the nature of each resonance condition, we observe the behaviour of the electric field along our multilayer sensing structure.

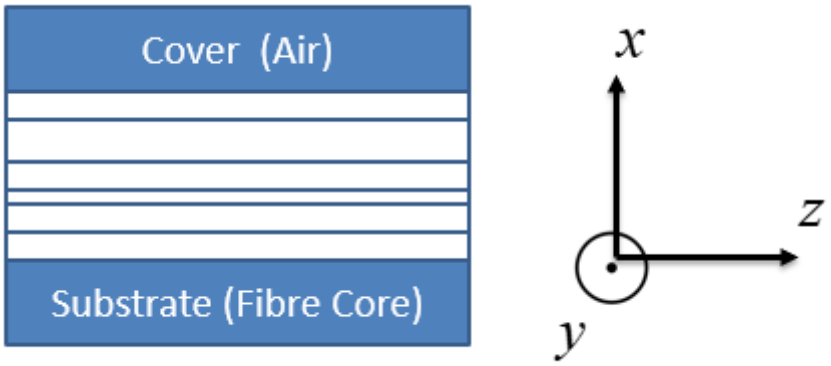

Figure 5-3 – The figure shows a multilayer sandwiched between cover and substrate layers. The orientation of the co-ordinate axes used in the equations which follow is also given.

We now introduce mode theory for a multilayer sandwiched between a cover layer and a substrate as shown above. The z direction represents the direction of mode propagation, and the x direction traverses the layers of the multilayer.

Following Chen *et al.*, Maxwell's equations for source-free time-harmonic Electric and Magnetic fields E, H, in isotropic media can be expressed as (Chen *et al.* 2000).

$$\nabla \times E = -i\omega\mu_0 H \quad (5\text{-}5)$$

$$\nabla \times H = i\omega\varepsilon_0\varepsilon_r E \quad (5\text{-}6)$$

For a TE mode ($E_x, E_z, H_y = 0$) propagating the $+z$ direction in the jth layer ($x_j \leq x \leq x_{j+1}$), the non-zero magnetic and electric field components are:

$$H_j = \left[\hat{x}H_{xj}(x) + \hat{z}H_{zj}(x)\right]\exp(iwt - i\tilde{\gamma}z) \quad (5\text{-}7)$$

$$E_j = \hat{y}E_{yj}(x)\exp(iwt - i\tilde{\gamma}z) \tag{5-8}$$

Where $\hat{x}, \hat{y}, \hat{z}$ are unit vectors in the $x, y,$ and z directions and $\tilde{\gamma} = k_0(\beta - i\alpha)$ is the complex mode propagation constant with β and α the normalised phase and attenuation constants and $k_0 = {}^{2\pi}/_{\lambda_0}$ where λ_0 is the free space wavelength of the light.

Combining the equations above, we can arrive at the following:

$$\begin{pmatrix} E_{yj}(x_j) \\ \dfrac{dE_{yj}(x_j)}{dx} \end{pmatrix} = \begin{pmatrix} cos[\kappa_j(x - x_j)] & -\dfrac{1}{\kappa_j} sin[\kappa_j(x - x_j)] \\ \kappa_j sin[\kappa_j(x - x_j)] & cos[\kappa_j(x - x_j)] \end{pmatrix} \begin{pmatrix} E_{yj}(x) \\ \dfrac{dE_{yj}(x)}{dx} \end{pmatrix} \tag{5-9}$$

Imposing appropriate boundary conditions, we can arrive at:

$$\begin{pmatrix} E_{ys} \\ \dfrac{dE_{ys}}{dx} \end{pmatrix} = \prod_{j=1}^{r} M_j \begin{pmatrix} E_{yc} \\ \dfrac{dE_{yc}}{dx} \end{pmatrix} \tag{5-10}$$

$$\begin{pmatrix} E_{ys} \\ \dfrac{dE_{ys}}{dx} \end{pmatrix} = \begin{pmatrix} M_{11} & M_{12} \\ M_{21} & M_{22} \end{pmatrix} \begin{pmatrix} E_{yc} \\ \dfrac{dE_{yc}}{dx} \end{pmatrix} \tag{5-11}$$

Where:

$$M_j = \begin{pmatrix} \cos(\kappa_j d_j) & -\dfrac{1}{\kappa_j}\sin(\kappa_j d_j) \\ \kappa_j \sin(\kappa_j d_j) & \cos(\kappa_j d_j) \end{pmatrix} \tag{5-12}$$

for $j = 1,2,3, \ldots r$

For guided modes, the tangential fields in the cover and substrate must be exponentially decaying so that:

$$\left.\begin{array}{l} E_{ys}(x) = A_s \exp(\tilde{\gamma}_s x) \\ \dfrac{dE_{ys}(x)}{dx} = \tilde{\gamma}_s A_s \exp(\tilde{\gamma}_s x) \end{array}\right\} \quad \text{for } x \leq 0 \tag{5-13}$$

$$\left.\begin{array}{c} E_{yc}(x) = B_c \exp[-\tilde{\gamma}_c(x - x_{r+1})] \\ \frac{dE_{yc}(x)}{dx} = -\tilde{\gamma}_c B_c \exp[-\tilde{\gamma}_c(x - x_{r+1})] \end{array}\right\} \quad \text{for } x \geq x_{r+1} \tag{5-14}$$

where

$$\tilde{\gamma}_s = \pm\sqrt{\tilde{\gamma}^2 - {k_0}^2 {n_s}^2} \tag{5-15}$$

$$\tilde{\gamma}_c = \pm\sqrt{\tilde{\gamma}^2 - {k_0}^2 {n_c}^2} \tag{5-16}$$

and n_s and n_c are the substrate and cover refractive indices. These equations together allow the dispersion equation to be derived for TE modes as:

$$F(\tilde{\gamma}) = \tilde{\gamma}_s M_{11} + \tilde{\gamma}_c M_{22} - M_{21} - \tilde{\gamma}_s \tilde{\gamma}_c M_{12} = 0 \tag{5-17}$$

In a similar way, the dispersion relation for the TM modes can be derived as:

$$F(\tilde{\gamma}) = \frac{\tilde{\gamma}_s}{{n_s}^2} M_{11} + \frac{\tilde{\gamma}_c}{{n_c}^2} M_{22} - M_{21} - \frac{\tilde{\gamma}_s \tilde{\gamma}_c}{{n_s}^2 {n_c}^2} M_{12} = 0 \tag{5-18}$$

The zeros of this function give the complex propagation constants of the allowed TE and TM modes in the structure.

We note, for guided modes, the complex propagation constant must meet the following condition: $\beta > n_s, n_c$ (guided modes).

In the case of our sensor, modes can only be excited by guided light which originates the fibre core (substrate). These means the above condition cannot in general be met and therefore any propagating modes will be leaky modes and will progressively leak from the multilayer back into the fibre core as they propagate.

Such leaky modes can be identified using the aforementioned dispersion relations, however, as explained by Chilwell and Hodgkinson some restrictions must be placed on $\tilde{\gamma}_c$ and $\tilde{\gamma}_s$ as a result (Chilwell and Hodgkinson 1984). Specifically, when calculating $\tilde{\gamma}_c$ and $\tilde{\gamma}_s$ using the equations above we must take either the negative or positive root as appropriate such that the following conditions are met:

$\left.\begin{matrix} Re\{\gamma_s\} > 0, & Im\{\gamma_s\} < 0 \\ Re\{\gamma_c\} < 0, & Im\{\gamma_c\} > 0 \end{matrix}\right\}$ for leaky modes excited from guided rays propagating the fibre core.

5.2.4 Mode Theory

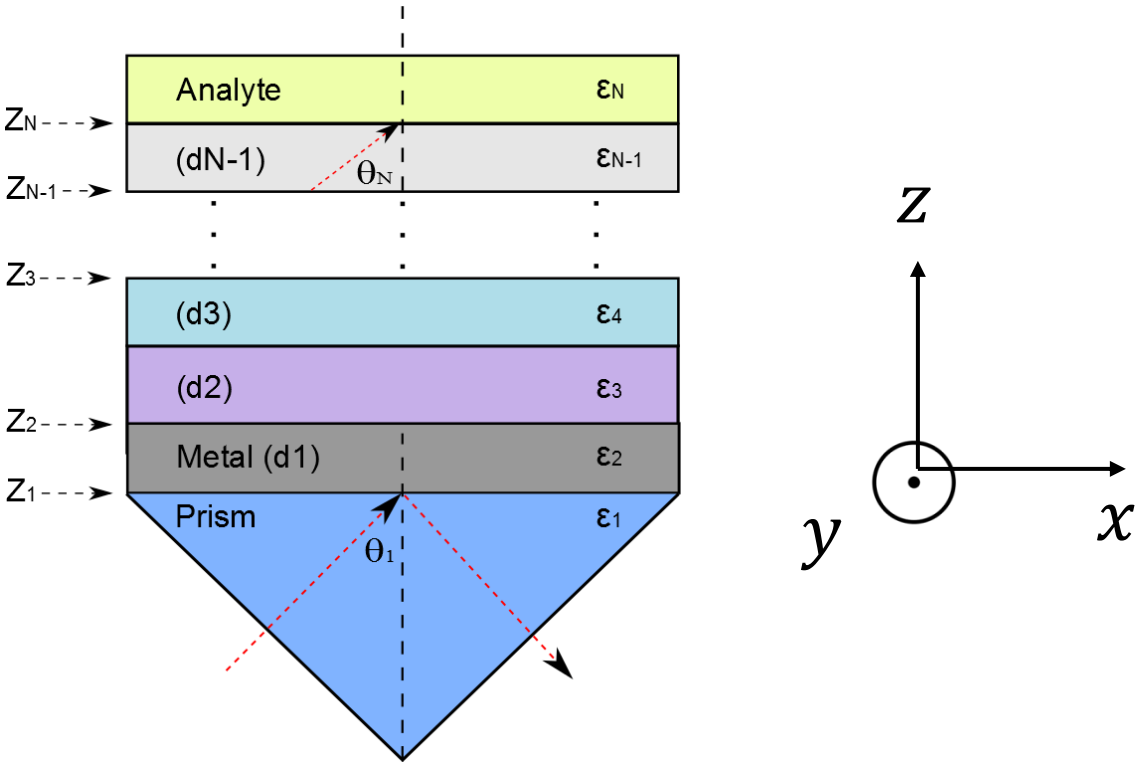

Figure 5-4 – (A) Schematic representation of a Kretschmann prism configuration comprised of a multilayer sensing configuration where d1 represents thickness of layer 1, ε_1 is the dielectric permittivity of material 1, and Z_1 is the interface between material 1 & 2.

For the purposes of deriving the electric field equations, we refer to the figure above where the multilayer structure is defined.

Following the approach of Shalabney *et al.*, we assume a multilayer structure consisting of N layers so that there are $N-1$ boundaries in the structure. Each layer, j, is assumed to be uniform and isotropic and has permittivity ε_j, permeability μ_j, and thickness d_j. The interfaces between the layers are found along the z direction at $Z_1, Z_2, \ldots., Z_{N-1}$, with $Z_1 = 0$. We take the plane of incidence to be the xz plane.

5.2.4.1 TM Radiation

We first consider incident TM radiation so that $E_y = H_x = H_z = 0$. The angle of incidence at the first layer is $\theta_1$and for each layer j the following condition holds according to Snell's law:

$$n_1 \sin\theta_1 = n_j \sin\theta_j = \alpha_j \tag{5-19}$$

It follows that the TM fields in layer j can be represented as follows:

$$H_{yj}(x,z,t) = H_{yj}(z)exp\left[i(k_0\alpha_j x - \omega t)\right] \tag{5-20}$$

$$E_{xj}(x,z,t) = E_{xj}(z)exp\left[i(k_0\alpha_j x - \omega t)\right] \tag{5-21}$$

$$E_{zj}(x,z,t) = E_{zj}(z)exp\left[i(k_0\alpha_j x - \omega t)\right] \tag{5-22}$$

Following Shalabney, we can then calculate the fields in 3 steps (Shalabney and Abdulhalim 2010):

Step 1: Calculate the characteristic matrix (M_{TOT}) for the multilayer structure as follows:

$$M_{TOT} = \prod_{j=2}^{N-1} M_j \tag{5-23}$$

with:

$$M_j = \begin{bmatrix} cos\beta_j & -\frac{i}{q_j}sin\beta_j \\ -iq_j sin\beta_j & cos\beta_j \end{bmatrix} \tag{5-24}$$

and:

$$\beta_j = k_0 n_j d_j cos\theta_j \tag{5-25}$$

$$q_j = \sqrt{\mu_j/\varepsilon_j}\, cos\theta_j \tag{5-26}$$

Knowledge of the characteristic matrix M_{TOT} allows derivation of the reflection co-efficient r using:

$$r = \frac{(M_{11} + M_{12}.q_N).q_1 - (M_{21} + M_{22}.q_N)}{(M_{11} + M_{12}.q_N).q_1 + (M_{21} + M_{22}.q_N)} \quad (5\text{-}27)$$

Step 2: Calculate the fields in the second layer (H_{y2}, E_{x2}) using

$$\begin{bmatrix} H_{y2}(z) \\ -E_{x2}(z) \end{bmatrix} = P_2(z) \begin{bmatrix} (1+r) \\ q_1(r-1) \end{bmatrix} H_y^{inc} \quad (5\text{-}28)$$

$Z_1 \leq z \leq Z_2$

Here, the propagation matrix P is used to derive the fields after any distance z in the second layer and is defined as:

$$P_2(z) = \begin{bmatrix} \cos(k_0 n_2 z \cos\theta_2) & \frac{i}{q_2}\sin(k_0 n_2 z \cos\theta_2) \\ iq_2 \sin(k_0 n_2 z \cos\theta_2) & \cos(k_0 n_2 z \cos\theta_2) \end{bmatrix} \quad (5\text{-}29)$$

Step 3: Calculate the fields in any layer $j \geq 3$ (H_{yj}, E_{xj}) using

$$\begin{bmatrix} H_{yj}(z) \\ -E_{xj}(z) \end{bmatrix} = P_j(z).\prod_{l=j-1}^{2} P_l(d_l) \begin{bmatrix} (1+r) \\ q_1(r-1) \end{bmatrix} H_y^{inc} \quad (5\text{-}30)$$

In all of the above, the value of the incident field H_y^{inc} is determined by the type of field normalisation used as shown in the table below.

Normalising to…	Value of H_y^{inc}
Incident Magnetic Field ($H = 1$)	$H_y^{inc} = 1$
x-comp of Electric Field ($E_x = 1$)	$H_y^{inc} = n_1 / \cos\theta_1$
z-comp of Electric Field ($E_z = 1$)	$H_y^{inc} = n_1 / \sin\theta_1$
Incident Electric Field ($E = 1$)	$H_y^{inc} = n_1$

Finally, (see Hansen *et al.* Equation (107)) the remaining field component E_{zj} can be calculated from (Hansen 1968):

$$E_{zj}(z) = H_{yj}(z) n_1 \sin\theta_1 / \varepsilon_j \qquad (5\text{-}31)$$

5.2.4.2 TE Radiation

For incident TE radiation, $H_y = E_x = E_z = 0$ and the non-zero components of the fields in any layer j (H_{xj}, H_{zj}, E_{yj}) can be derived by replacing the field column $\begin{bmatrix} H_{yj}(z) \\ -E_{xj}(z) \end{bmatrix}$ in the equations above with $\begin{bmatrix} E_{yj}(z) \\ H_{xj}(z) \end{bmatrix}$. Replacing any occurrences of q_j with $p_j = \sqrt{\varepsilon_j / \mu_j}\, cos\theta_j$ and substituting the incident field E_y^{inc} in place of H_y^{inc}. Finally, (see Hansen *et al.* Equation (99)(Hansen 1968)) the remaining field term (H_{zj}) can be calculated from:

$$H_{zj}(z) = E_{yj}(z) n_1 \sin\theta_1 \qquad (32)$$

5.3 Results

In this section, we propose an investigation into the use of a multilayer stack sensing OF structure that facilitates the stimulation of both surface plasmon and leaky mode resonance.

5.3.1 General Sensor Parameters

We choose to employ Ag due to its relatively narrow spectral dip, which greatly enhances the sensor signal to noise ratio as compared to other metals. In order to ensure that resonance occurs above the optical fibre critical angle, it's location is modulated by adding an additional high index dielectric material onto the surface of the metallic layer. Furthermore, the high potential for atmospheric poisoning of the metallic layer is reduced by the inclusion of a modulation layer. Numerous materials were considered for this here including SiO_2, ZnO, and Ta_2O_5. SiO_2 has been commonly employed in OFSPR for hydrogen sensing applications (Perrotton *et al.* 2011b; Perrotton *et al.* 2013; F. Downes and C. M. Taylor 2017), however preliminary results have shown that Ta_2O_5 demonstrate superior performance in terms of sensitivity (Fionn Downes and Cian M. Taylor 2017), and the fact that a higher index material cause a greater shift in the angular location of the SPR thus a smaller modulation material thickness is necessary to overlayer the metallic film. Furthermore, Ta_2O_5 operates with high chemical stability, as well as a resistance to corrosion (Toki *et al.* 1996; Bright *et al.* 2013). Both Ag and Ta_2O_5 have previously demonstrated success for OFSPR hydrogen sensing applications (X.G. Wang *et al.* 2013b; Hosoki *et al.* 2014; Fionn Downes and Cian M. Taylor 2017). Finally, as we will see, Ta_2O_5, having a higher refractive index than SiO_2 allows support of guided modes at a lower cut-off thickness: given a more compact sensor which is easier to fabricate. The final multilayer sensing structure takes the form (Ag, Ta_2O_5, Pd) as (d1, d2, d3) respectively, with Ag first being layer onto an unclad silica fibre core, and finally with Pd in direct contact with the external environment.

Similar to the SPR phenomenon, a substrate (in our case the fibre core), coated with a high index dielectric or certain polymer compounds can support many number of modes. Provided the real component of the dielectric layer refractive index is less than that of the substrate and the analyte; these modes constantly radiate energy back into fibre and are known as leaky modes. If thin dielectric film thickness is increased, leaky modes cross the cut-off condition and start guiding in the thin dielectric film, leaving the fibre core. Furthermore, coupling of a specific leaky mode takes place, at a particular value of film thickness.

Maximum coupling requires two conditions: There is considerable overlap between the mode fields, and the phase matching condition is sufficiently satisfied; (ie. the equality of the real parts of the respective propagation constants). Thus, under certain conditions of incident angle, wavelength, and index of refraction; this guided wave can give rise to leaky mode resonance in the dielectric film. Given the nature of the materials that constitute our

multilayer sensing structure, and the order in which they are stacked, our device could be referred to as a number of structures such as a coupled plasmon-waveguide resonance sensor, or a waveguide coupled surface plasmon resonance sensor as discussed in the introduction. For brevity, for the remainder of the chapter, will we refer to the device as a waveguide coupled surface plasmon resonance (WCSPR) sensor. While surface plasmon resonance can only be stimulated by TM polarized light, leaky mode resonance can be stimulated by both TM and TE polarized light. In addition, the thickness of the dielectric overlayer controls the mount of modes permitted.

Typically, researchers have opted to improve sensor performance by employing new metallic material, alloys, new higher index dielectric films, substituting a new hydrogen sensitive material, changing mechanical fibre dimensions, choice of film thicknesses, and this has brought about steady predictable improvements in sensitivity and detection accuracy. But through carefully choice metallic and dielectric materials, as well as the thickness of each multilayer sensing component, we demonstrate for the first time that is possible to stimulate surface plasmon and leaky mode resonance at the same resonance wavelength. Consequently, the magnitude of the resonance dip in the resultant output power through the optical fibre, which takes into account both TM and TE oscillation modes of propagation, will be greatly increased, giving improved sensing performance.

The Brendel Bormann model is used in determining the dielectric permittivity of Ag and Pd (Brendel and Bormann 1992), and Sellmeier Dispersion formulae are used to determine the refractive indices of thin film SiO_2 (Postava and Yamaguchi 2001) and the silica fibre core (Malitson 1965); and the relevant the equations appear in Chapter 1. An adjustment is made using the model derived from Von Rottkay as per equations (1-58, -59, -60) from Chapter 1 account for the presence of 4% H_2 interacting with the Pd layer.

Numerous materials were considered for the modulation layer that permits the stimulation of leaky mode resonance including SiO_2, ZnO, and Ta_2O_5. SiO_2 has been commonly employed in OFSPR for hydrogen sensing applications (Perrotton *et al.* 2011b; Perrotton *et al.* 2013; F. Downes and C. M. Taylor 2017), however preliminary results involving Ta_2O_5 demonstrates superior performance in terms of sensitivity (Fionn Downes and Cian M. Taylor 2017), and the fact that higher index materials cause a greater shift in the angular location of the SPR thus a smaller modulation material thickness is necessary. Ta_2O_5 was chosen as the modulation material as it demonstrated high sensitivity and largest angular resonance.

Furthermore, this material operates with high chemical stability, as well as a resistance to corrosion (Toki *et al.* 1996; Bright *et al.* 2013). Experimental success has been demonstrated by Hosoki *et al*. using an OF multilayer structure containing Ta_2O_5 as a modulation material for H_2 sensing applications (Hosoki *et al.* 2014).

The normalised output power is determined using the characteristic transfer matrix model as outlined in Chapter 1, and the output power corresponding to each individual oscillation mode (TM & TE) are determined using equations (5-1 & -2). The range of input wavelengths permitted in our OF sensing device is (λ=450:2000nm). Following from our previous chapters, our sensor is comprised of a silica fibre core diameter = 2μm, with NA = 0.22, and the sensing length of each channel = 1cm.

The electric field intensities through the multilayer structure will be determined using equations (5-3, & -16), and as we will show, analysis of these field profiles allows identification of the mode designations of supported modes. For TM modes, the E_x field intensity will be used to represent the field behaviour while for TE modes, the E_y field intensity will be employed. In all cases the fields as normalised to assume a total incident electric field of 1.

5.3.2 Response Time, Selectivity and Durability

The response time of the the device consisting of a Pd film with (d3=3nm) is expected to operate similar to that of Liu, 4s to 4% H_2 (Liu and Li 2016b), and is expected to increase with Pd thickness as explained in Chapter 2. Insight into the selectivity of the device can be gained by reviewing the highly selective properties of a Pd based hydrogen sensor (Huebert *et al.* 2011), which operate with minimal cross sensitivity to other gases, as previously mentioned in Chapter 2. The durability of each channel can be derived from investigation into the durability of each multichannel sensing component. While Ag is subject to hazardous interaction with atmospheric gases, the protective overlayer of Ta_2O_5 improves the longevity of the Ag film. Thus, the durability of the multichannel sensor primarily stems from the durability of the Pd component in the multilayer sensing structure. As explained in Chapter 2, Pd undergoes an α→β phase transition during hydrogenation, causing excessive expansion of the Pd fcc lattice structure, and increased mechanical strain. Thus, repeated H_2 loading cycles causes rapid degradation of the Pd continuous film structure. In Chapter (2 & 3) we employed

a PdY alloy, and a Pd nanocomposite structure, both which are expected to operate with greater durability to the pure Pd film. In Chapter 2 Fig. 2-8, we demonstrate that the presence of a small volume fraction of Y has little influence on the resonance condition, thus durability could be improved with little influence on the resultant performance of the device. In this chapter, our focus is investigation into the stimulation of surface plasmon and leaky mode resonance for applications in H_2 sensing. Thus, for simplicity, we will employ a pure Pd film to act as the H_2 sensitive layer.

5.3.3 Results Summary

We begin by investigating the operation of the device by measuring the normalized output power using two different modulation layer materials (SiO_2 & Ta_2O_5). We extend this investigation by determining the output power at three specific angles of incidence (which traverse the range of angles guided in the fibre), for a range of modulation layer thicknesses. We demonstrate that in our proposed sensor, Ta_2O_5 is a suitable material for stimulation of multiple resonance modes, whereas SiO_2 permits the stimulation of only a single resonant mode at the thicknesses examined (100nm & 250nm), which is attributed to surface plasmon resonance.

Next, we investigate the influence that metallic layer thickness has on the resonance conditions using Ta_2O_5 as the modulation layer material. Here we demonstrate that when the metallic layer thickness is large, more than one resonance mode is observed. A decrease in the metallic layer thickness results in the disappearance of individual resonance dips in the normalized output power spectrum, and the appearance of a single widened resonance condition with great depth.

In order to further investigate the nature of each resonance condition, we model the output power of various sensing configurations differing metallic layer thickness using un-, p- & s-polarized light in Fig. 5-(7-12). In addition, we determine the output power of each configuration using three angles of input that make up the angular sensing range of our fibre. This allows us to characterize each unpolarized output power resonant mode as originating from p- or s- oscillations.

Next, we plot the resonance wavelengths of the first modes stimulated using p- & s- polarized light, and observe that they cross over within a very small metallic thickness range. We also demonstrate depth of the single resonance condition generated using low metallic layer

thicknesses reaches a minimum within the same very small metallic thickness range. Next, we determine the electric field of each configuration that permits stimulation of a mode. Due to the shape of the electric field we are able to characterize each resonance mode further as being due to surface plasmon resonance, or a particular leaky waveguide mode. Finally, we determine the performance (sensitivity, detection accuracy, and figure of merit) of various devices upon the interaction with 4% H_2 gas, using un-, p-, and s- polarized light, where each configuration differs metallic thickness and the modulation thickness was used to control the resonance wavelength. We demonstrate that the sensor figure of merit is significantly greater in the configurations that employ a thin metallic thickness of (d1=3, 5nm) compared to the widely referenced optimal thickness of (d1≈50nm). The improved performance is attributed to matching the resonance wavelengths of the individual (SPR + TE0) resonance modes. Additionally, we investigate the performance of higher order waveguide modes, and demonstrate the co-operation of (TM0 + TE1).

5.3.4 Modulation Thickness

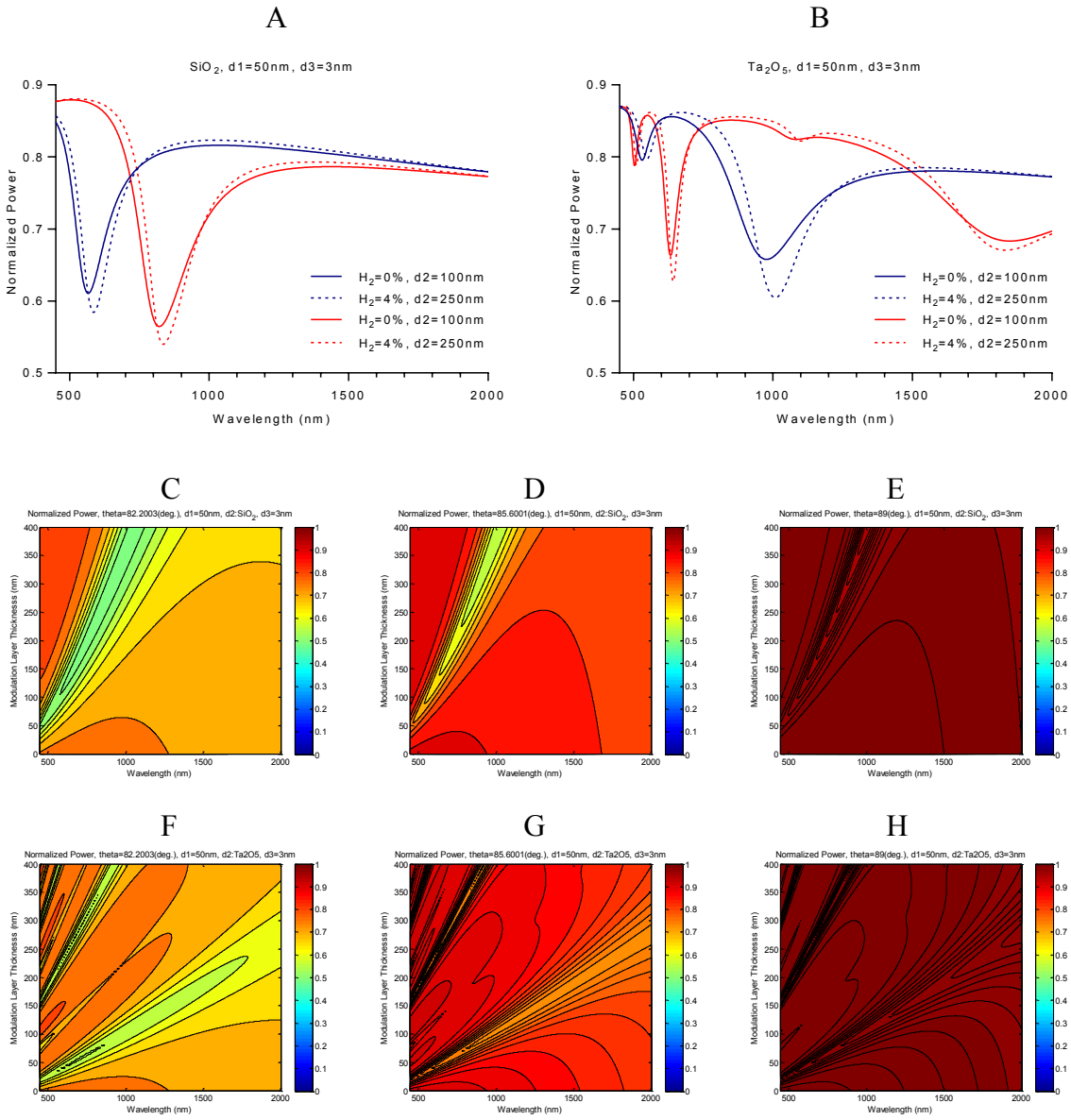

Figure 5-5 – (A) Normalised output power across the spectral domain of a (Ag/SiO_2/Pd) multilayer step-index OFSPR sensor in the presence of 0% and 4% H_2; (λ=450:2000nm), Ag(d1=50nm), SiO_2(d2=100,250nm), Pd(d3=3nm). (B) Output power from a series of structures utilizing (Ta_2O_5) as the modulation layer component in place of (SiO_2). (C, D, E) Contour plots illustrating variation in the output power with wavelength and modulation thickness (SiO_2) at three distinct angles (ϑ_{low}, ϑ_{mid}, ϑ_{high}) respectively, in the absence of H_2. (F, G, H) Contour plots with modulation layer (Ta_2O_5).

Fig. 5-5(A) illustrates the normalized output power from two structures differing in modulation thickness (d2=100, 250nm), where SiO_2 was employed as the modulation material. The solid lines indicates the output power of the device in the absence of H_2 gas, where the dielectric permittivity of the Pd layer is solely determined using the Brendel-Bormann model for Pd. The dashed lines illustrate the output power of the structure in the

presence of 4% H_2 gas. We observe the presence of a single resonance dip in each configuration, regardless of the change in the modulation thickness.

Fig. 5-5(B) displays the normalized output power from structures with identical dimensions to that in used in Fig. 5-5(A), however, the modulation material has been replaced with Ta_2O_5. In the structure containing a Ta_2O_5 thickness of 100nm, two independent resonance conditions can be observed, unlike the single resonance condition evident in Fig. 5-5(A). Once the modulation layer thickness is increased to 250nm, we observe four independent resonance conditions, differing sensitivity, spectral linewidth, and resonance depth. At this stage, it is pertinent to identify the origin of each resonance mode stimulated when using Ta_2O_5 in place of SiO_2. In order understand how the additional modes are stimulated, we determined the normalized output power for all d2 thicknesses in the range (d2=0:400nm), for both SiO_2 and Ta_2O_5. This should help establish some criteria for the stimulation of each resonance condition. This has been carried out in Fig. 5-5(C-H).

Fig. 5-5(C) displays a plot showing incident wavelength (x-axis) against modulation layer thickness (y-axis), with the normalized output power illustrated in the contour (z-axis), with fixed parameters (d1=50nm), (d3=3nm), and ($\theta_{in}=\theta_{low}$). The angles (θ_{low}, θ_{mid}, θ_{high}) are defined in Chapter (3). Fig. 5-5(D, E) displays the data generated using alternative incident angles of light, where ($\theta_{in}=\theta_{mid}$), and ($\theta_{in}=\theta_{high}$) respectively. Resonances (regions where the output power is relatively low) can be observed by locating cold colours in Fig. 5-5(C-H). Looking at Fig. 5-5(C-E); a single resonance can be observed once the SiO_2 thicknesses rises above (d2≈50nm), particularly at low angles of incidence. We make note that regardless of the incident angle ($\theta_{in}=\theta_C$:90˚), incident wavelength (λ=450:2000nm), or modulation thickness SiO_2(d2=0:400nm); no more than one resonance condition is evident when using SiO_2 as the modulation layer material. Finally, we observe similar behaviour to that investigated in previous chapters, where an increase in the modulation thickness results in a red shift of the resonance condition.

Fig. 5-5(F-H) illustrates similar contour plots generated using Ta_2O_5 in place of SiO_2. A resonance mode appears once the modulation thickness increases above (d2≈20nm), and is primarily stimulated using low angles of incidence. The slope of this initial resonance condition is less steep than that stimulated using SiO_2, thus indicating that an equal thickness of Ta_2O_5 causes resonance to occur at a longer wavelength than compared to SiO_2. Further increase in Ta_2O_5 thickness results in the stimulation of multiple more resonance modes. At

this stage, we also make note that the slope of each mode is different, thus indicating that the difference in the resonance wavelength of each mode is a function of the modulation thickness.

In summary, we have established that the only one resonant mode can be stimulated using SiO_2 (within the range of thicknesses examined), regardless of incident angle and wavelength. Previous papers have attributed the origin of this resonance condition to the stimulation of surface plasmon resonance (Perrotton *et al.* 2013; F. Downes and C. M. Taylor 2017). We have investigated the influence that replacing the SiO_2 modulation layer with Ta_2O_5 has on the output power of the sensing device, and observed the stimulation of additional resonance modes. Moreover, the number of modes increases with Ta_2O_5 thickness. At this stage we will solely employ Ta_2O_5 as the modulation layer material. Now that we have studied the influence that the modulation layer thickness has on the additional resonance modes, it is sensible to investigate the influence that the thickness of the metallic layer when utilizing a Ta_2O_5 based modulation layer.

5.3.5 Metallic Thickness

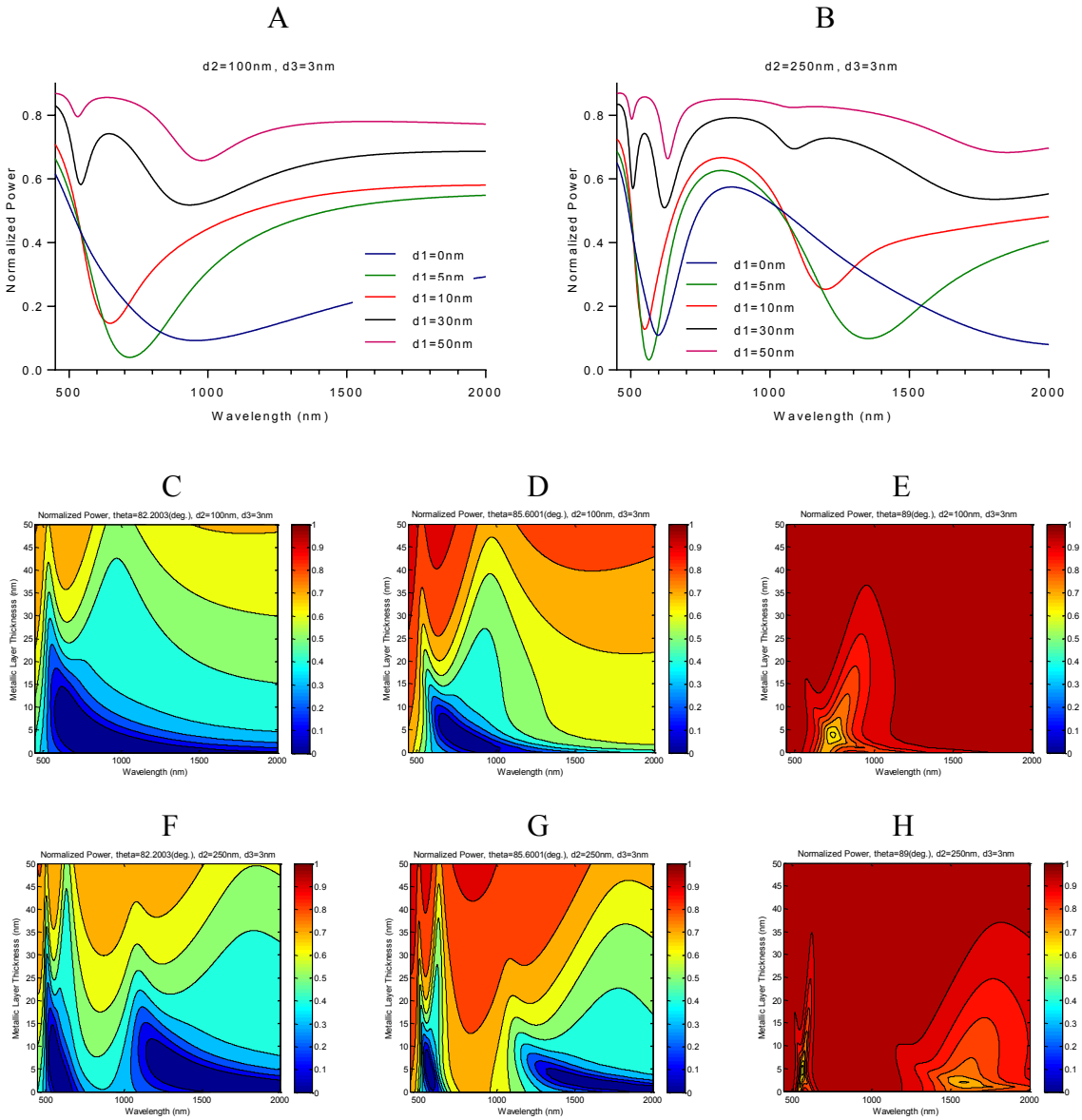

Figure 5-6 – (A) Normalised output power across the spectral domain of a ($Ag/Ta_2O_5/Pd$) multilayer step-index OFSPR sensor in the absence of H_2; (λ=450:2000nm), Ag(d1=0,5,10,30,50nm), Ta_2O_5(d2=100nm), Pd(d3=3nm). (B) Ta_2O_5(d2=250nm). (C, D, E) Contour plots illustrating variation in the output power with wavelength and metallic thickness, with modulation layer SiO_2(d2=100nm) at three distinct angles (ϑ_{low}, ϑ_{mid}, ϑ_{high}) respectively. (F, G, H) Contour plots with modulation layer SiO_2(d2=250nm).

Fig. 5-6(A) displays the normalized output power from several structures differing in metallic thickness with (d1=0, 5, 10, 30, 50nm), coupled with a relatively small modulation layer thickness (d2=100nm), and in the absence of H_2 gas. It can be seen that using a large metallic thickness (d1=50nm), results in the stimulation of two individual resonance conditions, as we've observed in Fig. 5-6(A). As d1 thickness decreases to (d1=10nm), the two individual

resonance dips disappear, and in their place a single resonance dip appears with greater depth. Similarly in Fig. 5-6(B), where the modulation thickness is increased to (d2=250nm), multiple independent resonance dips can be observed at large metallic thicknesses (d1=30, 50nm). In Fig. 5-6(A & B), the largest resonance depths are observed once the metallic thickness is (d1=5nm), for both sets of modulation layers. The depth of this resonance condition is significant because the normalized output power is composed of equally weighted TM and TE polarized light contributions as per equation (1-25) in Chapter 1. Therefore, if the normalized output power drops well below 50% at resonance, we postulate the stimulation of an s- polarized based resonance mode. The increase in magnitude of the resonance dip at very low thickness of Ag may lead to improved performance, compared to the previously investigated structures in Chapter (2-4).

Fig. 5-6(C-E) illustrates variation in normalized output power with incident wavelength, and metallic layer thickness; at three distinct angles. In the set of structures that employ a modulation thickness of (d2=100nm), resonance occurs mostly at the lower half of the range of angles permitted in the fibre. At low metallic thicknesses, a wide single resonance condition can be observed (deep blue colour across the lower section of the y-axis). The strong blue colour indicates very deep resonance depth of resonance conditions generated around this area. As the metallic thickness decreases, the initially deep and wide resonance condition can be seen to decrease in depth and width, and the formation of two individual resonance conditions can be observed clearly in Fig. 5-6(C & D). The difference in the resonance wavelength of each of these now independent resonance dips increases with further increase in metallic layer thickness. Specifically, increase in the metallic thickness results in the blue shift of the shorter resonance mode, and the red shift of the longer mode. This is important as it is clear that the metallic thickness can be used to tune the resonance location of each mode. Unlike the modulation layer thickness which causes the resonance wavelength of each mode to change in the same direction, the thickness of the metallic layer can be used to generate two resonance conditions around the same resonance wavelength.

When (d2=250nm) in Fig. 5-6(F-H) resonance also occurs mostly within the lower and middle sections of the incident angular range. Numerous more resonance conditions can be seen compared to Fig. 5-6(A-C) when the modulation layer thickness was lower. Similarly, increase in metallic thickness results in a reduction in resonance depth, and above a certain metallic thickness; the splitting up of each observed resonance mode into constituent resonance conditions.

To summarize, we investigated the influence that the metallic layer thickness has on the resonance conditions produced using Ta_2O_5 as the modulation layer component. We discovered that relatively wide, independent resonance conditions can be observed once the metallic layer thickness is low (d1=0, 5, 10nm). An increase in this metallic layer thickness beyond these values to (d1=30, 50nm) results in the splitting up of each initial resonance conditions (formed once d1 was low), into two constituent independent dips. The resonance wavelengths of these now independent dips undergo displacement in opposite directions upon further increase in metallic layer thickness. Finally, we observed that the normalized output power can be as low as 5% at resonance once the metallic layer thickness is (d1=5nm). This indicates the presence of an s- polarized resonance contribution in addition to the expected p-polarized resonance condition. Next we attempt to characterize each of the observed resonance conditions by measuring the normalized output power in two stages; when only p-polarized light propagates through the fibre, an when only s- polarized light propagates through the fibre.

5.3.6 Output Power (Unpolarized, TM, & TE)

5.3.6.1 d1=50nm

In order to understand the origin of each resonance condition, we can determine the normalized output power according to equation (5-1), where only p- polarized light is permitted to propagate along the fibre core. Similarly, we can model the output power that is generated solely using s- polarized light according to equation (5-2). By plotting these alongside the output power of the combined s- & p- contributions illustrated in Fig. 5-7(A & B), the origin of each resonance dip in the combined output power can be chacterized as originating from either s- or p- polarized resonance contributions.

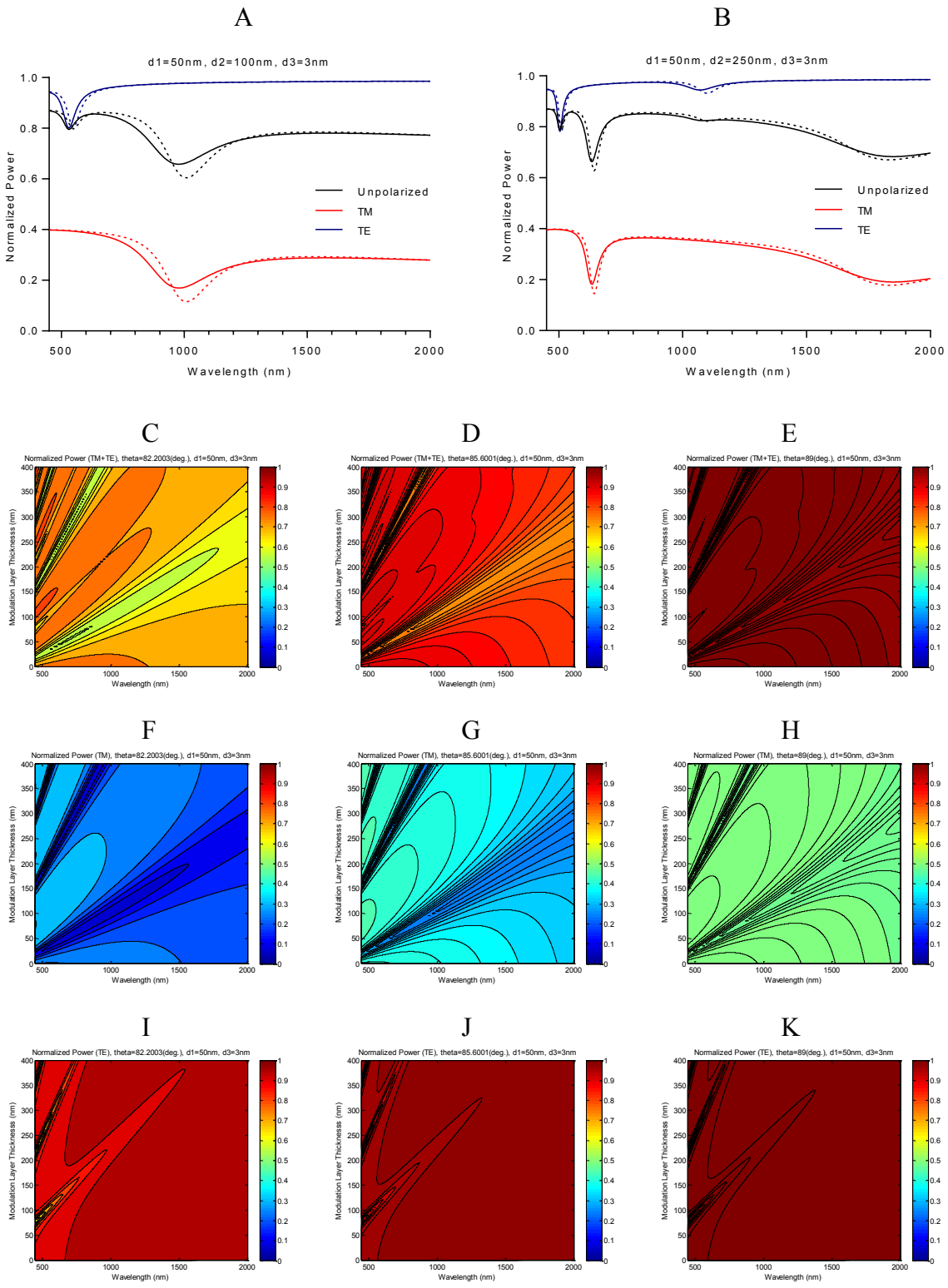

Figure 5-7 – (A) Normalised output power across the spectral domain of a (Ag/Ta_2O_5/Pd) multilayer step-index OFSPR sensor in the presence of 0% and 4% H_2; (λ=450:2000nm), Ag(d1=50nm), Ta_2O_5(d2=100nm), Pd(d3=3nm) are demonstrated; where (TM+TE) is the combined contribution of p- and s- polarized light, (TM) is the output power determined solely using p-polarized light, and (TE) is the output power solely determined using s- polarized light. (B) Ta_2O_5(d2=250nm). (C, D, E) Contour plots illustrating variation in the (TM+TE) output power with wavelength and modulation thickness at three distinct angles (ϑ_{low}, ϑ_{mid}, ϑ_{high}) respectively, in the absence of H_2. (F, G, H) (TM) output power. (I, J, K) (TE) output power.

Starting with (d1=50nm), Fig. 5-7(A) illustrates the normalized output power an unpolarized light source (TM+TE-black), as well as the normalized ouput power from two more light sources, polairzed such that only (TM-red) or (TE-blue) oscillations are permitted. Thus, in these figures, the combined output power is equal is made up of the individual TM and TE contributions, (TM+TE = TM + TE). Fig. 5-7(B) displays the normalized power output from structres similar to Fig. 5-7(A), except with a larger modulation layer thickness (d2=250nm). For conciseness, from this point we will refer to the output power generated using both (TM+TE) as the "unpolarized" output power. From Fig. 5-7(A), it is clear that the resonance mode stimulated at the shorter wavelength of the unpolarised plot originates from a shallow s- polarized resonance mode as indicated by the presence of a resonance dip in the TE output power around the same wavelength. Similarly, the longer unpolarised resonance mode can be seen to originate from a particularly deep p- polarized resonance. In Fig. 5-7(B) each resonance mode in the unpolarised dataset can also be seen to originate from stimulation by either s- or p- polarized resonance.

We expanded this investigation further by modelling the output power from a range of structures differing in modulation layer thickness (d2=0:400nm). Fig. 5-7(C-E) illustrates the output power from three fixed angles of incidence (θ_{low}, θ_{mid}, θ_{high}) respectively. The deepest resonance can be seen to occur at the lowest investigated angle of incidence; Fig. 5-7(C). The distinct unpolarized resonance modes in Fig. 5-7(A & B) can be easily identified in Fig. 5-7(C). Similarly, TM resonance modes in Fig. 5-7(A & B) can be found in Fig. 5-7(F-H), and the TE resonance modes in Fig. 5-7(A & B) can be located in Fig. 5-7(I-K). Fig. 5-7(F) indicates that the depth of TM resonance dip is large, for all investigated values of modulation layer thickness. Every s- polarized resonance condition is quite shallow compared to the corresponding p- polarized resonance modes in Fig. 5-7(F-H), thus indicating that regardless of the modulation layer thickness, when (d1=50nm) in this configuration only very weak TE resonance modes can be stimulated. We make note that the propagation of the TM modes as they behave with incident wavelength and modulation thickness "mode map" in Fig. 5-7(F-H) do not match up with those illustrated by the TE modes as illustrated in Fig. 5-7(I-K), and thus each polarized resonance mode in Fig. 5-7(F-K) appear as independent resonance modes (at separate wavelengths) when using unpolarized light in Fig. 5-7(C-E). Next, we will replicate each of the above figures in Fig. 5-7, but using smaller metallic layer thickness, in order to observe the behaviour of the individual TM & TE and how they contribute to the unpolarized output power.

5.3.6.2 d1=30nm

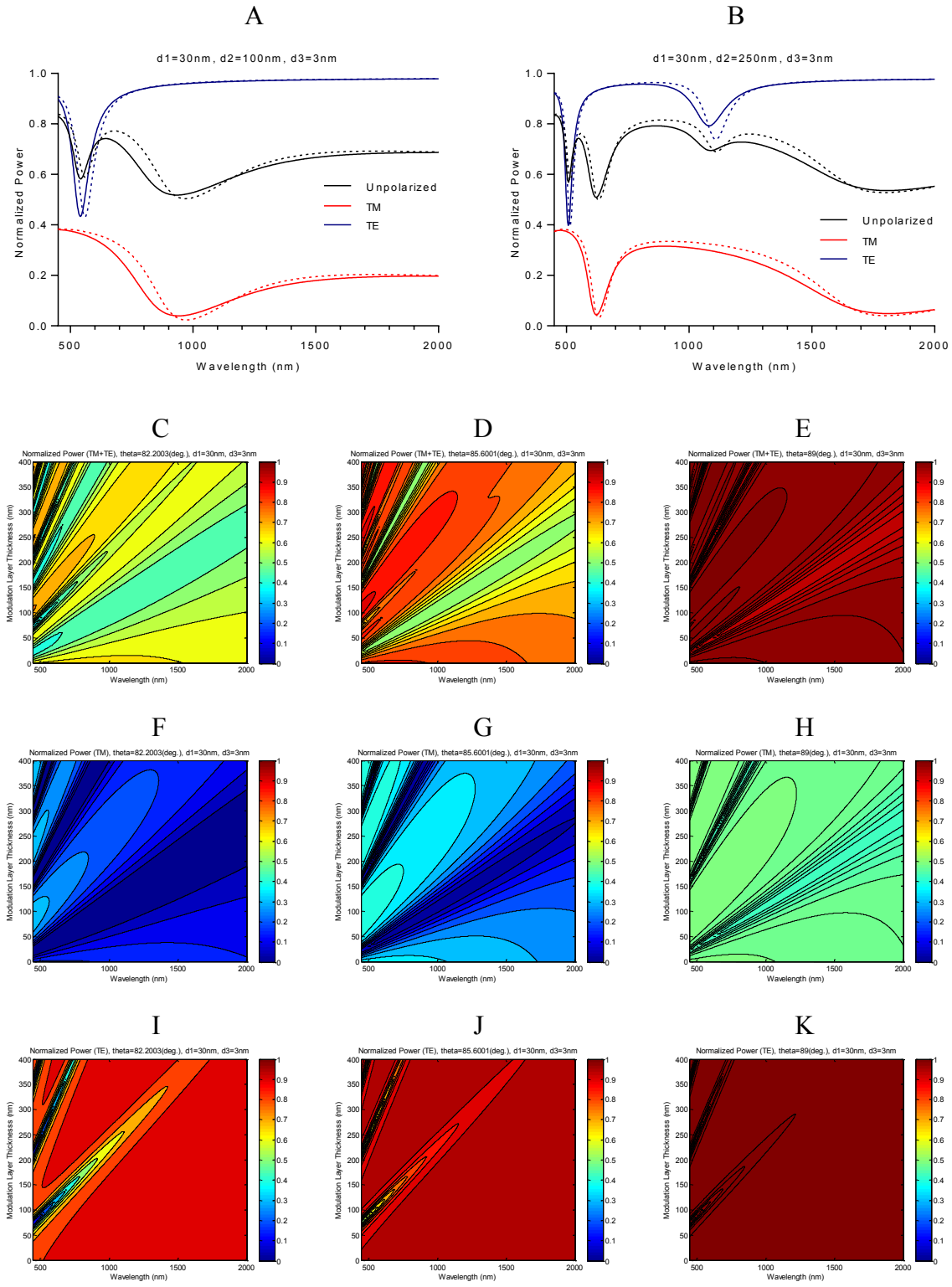

Figure 5-8 – (A) Normalised output power across the spectral domain of a (Ag/Ta_2O_5/Pd) multilayer step-index OFSPR sensor in the presence of 0% and 4% H_2; (λ=450:2000nm), Ag(d1=30nm), Ta_2O_5(d2=100nm), Pd(d3=3nm) are demonstrated; where (TM+TE) is the combined contribution of p- and s- polarized light, (TM) is the output power determined solely using p-polarized light, and (TE) is the output power solely determined using s- polarized light. (B) Ta_2O_5(d2=250nm). (C, D, E) Contour plots illustrating variation in the (TM+TE) output power with wavelength and modulation thickness at three distinct angles (ϑ_{low}, ϑ_{mid}, ϑ_{high}) respectively. (F, G, H) (TM) output power. (I, J, K) (TE) output power.

In Fig. 5-8, we observe the influence that a smaller metallic layer thickness has on each resonance condition. We observe that the depth of each unpolarized resonance condition increases compared to those stimulated with (d1=50nm) in Fig. 5-7. This is primarily due to an increase in the resonance depth of each TE polarized resonance condition as the metallic layer thickness decreased. At this stage, in Fig. 5-8(A) we still observe two individual unpolarized resonance conditions. We do note however that a distinct blue shift of the TM resonance wavelength has occurred once the metallic thickness has decreased from (d1=50-30nm). Consequently, the resultant difference in the resonance wavelengths between the individual TM and TE has decreased. Next, we decrease the metallic thickness further to (d1=10nm).

5.3.6.3 d1=10nm

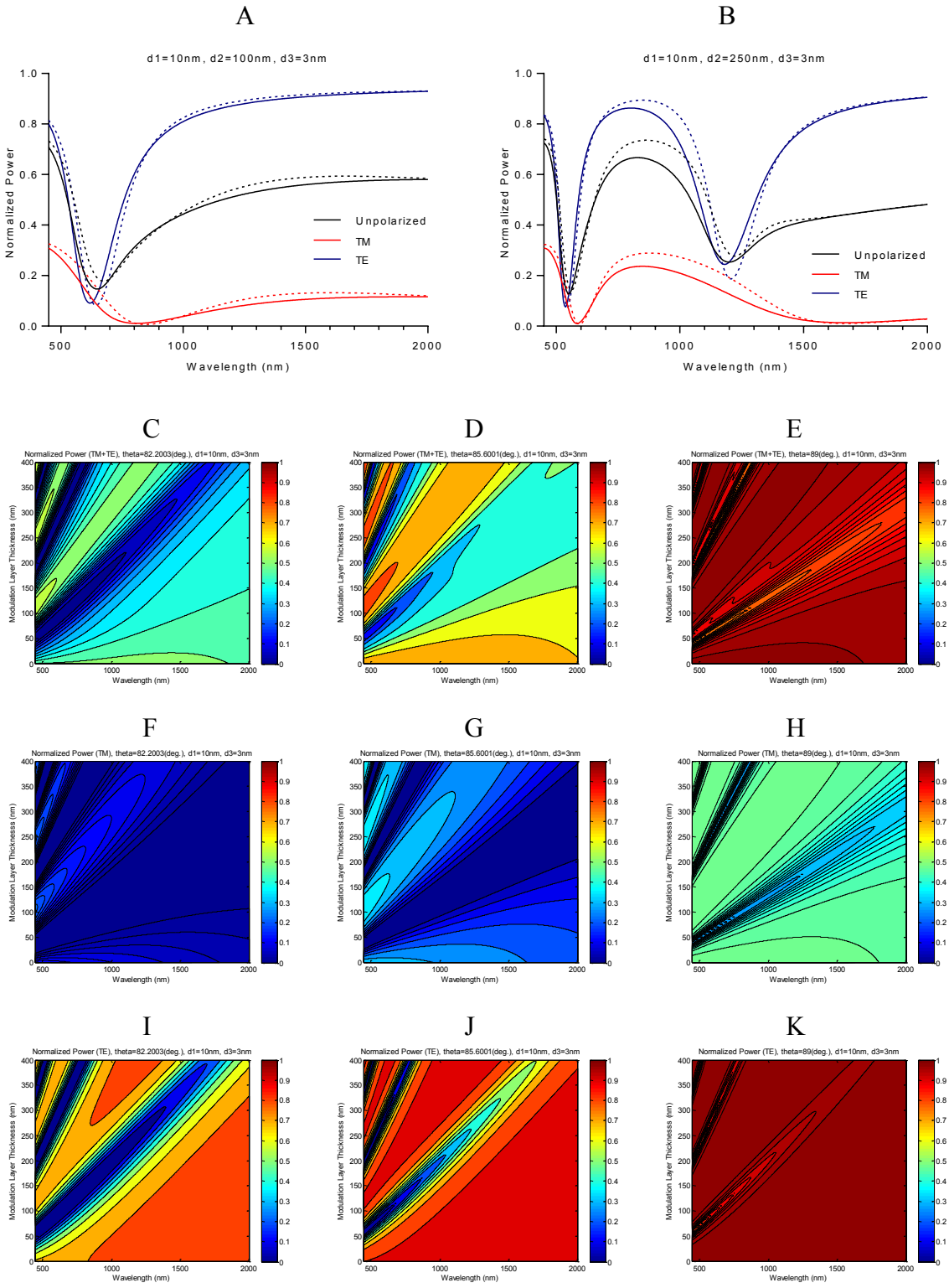

Figure 5-9 – (A) Normalised output power across the spectral domain of a (Ag/Ta_2O_5/Pd) multilayer step-index OFSPR sensor in the presence of 0% and 4% H_2; (λ=450:2000nm), Ag(d1=10nm), Ta_2O_5(d2=100nm), Pd(d3=3nm) are demonstrated; where (TM+TE) is the combined contribution of p- and s- polarized light, (TM) is the output power determined solely using p-polarized light, and (TE) is the output power solely determined using s- polarized light. (B) Ta_2O_5(d2=250nm). (C, D, E) Contour plots illustrating variation in the (TM+TE) output power with wavelength and modulation thickness at three distinct angles (ϑ_{low}, ϑ_{mid}, ϑ_{high}) respectively. (F, G, H) (TM) output power. (I, J, K) (TE) output power.

In Fig. 5-9(A) we now observe a single broadened unpolarized resonance condition. In addition, the depth of the TE dip has increased further from when (d1=30nm), and resultantly increasing the depth of the unpolarized resonance dip more. We observe that the resonance wavelength of the TM has undergone a further blueshift, and the TE has experienced a red shift compared to Fig. 5-8 when (d1=30nm). Thus, the resultant unpolarized output power displays a single resonance condition that can be seen to be comprised of both TM and TE contributions. The mode map in Fig. 5-9(F-H) matches up with that observed in Fig. 5-9(I-K) somewhat, thus indicating that as the modulation layer thickness increases, both the individual TM and TE resonance conditions can be observed as a single broad resonance condition when determining the output power of unpolarized light.

As we've seen previously in each set of contour figures, the mode maps of all three investigated angles match up. While the TM mode map is difficult to make out using the angle at which the resonance condition is strongest; it is easily distinguishable at large angles of incidence. The result of this overlap of the individual TM & TE mode maps results in the appearance of single, wide, and deep resonance modes when modelling unpolarized light through the fibre. In addition, from Fig. 5-9(A & B), it can be seen that both the individual TM and TE resonance conditions undergo a red shift in the presence of H_2. Thus, this single unpolarized resonance condition can be easily utilized for OF based H_2 sensing applications. Following these observations, we decrease the metallic layer thickness further in an attempt to further improve overlap area of the individual TM and TE mode maps.

5.3.6.4 d1=5nm

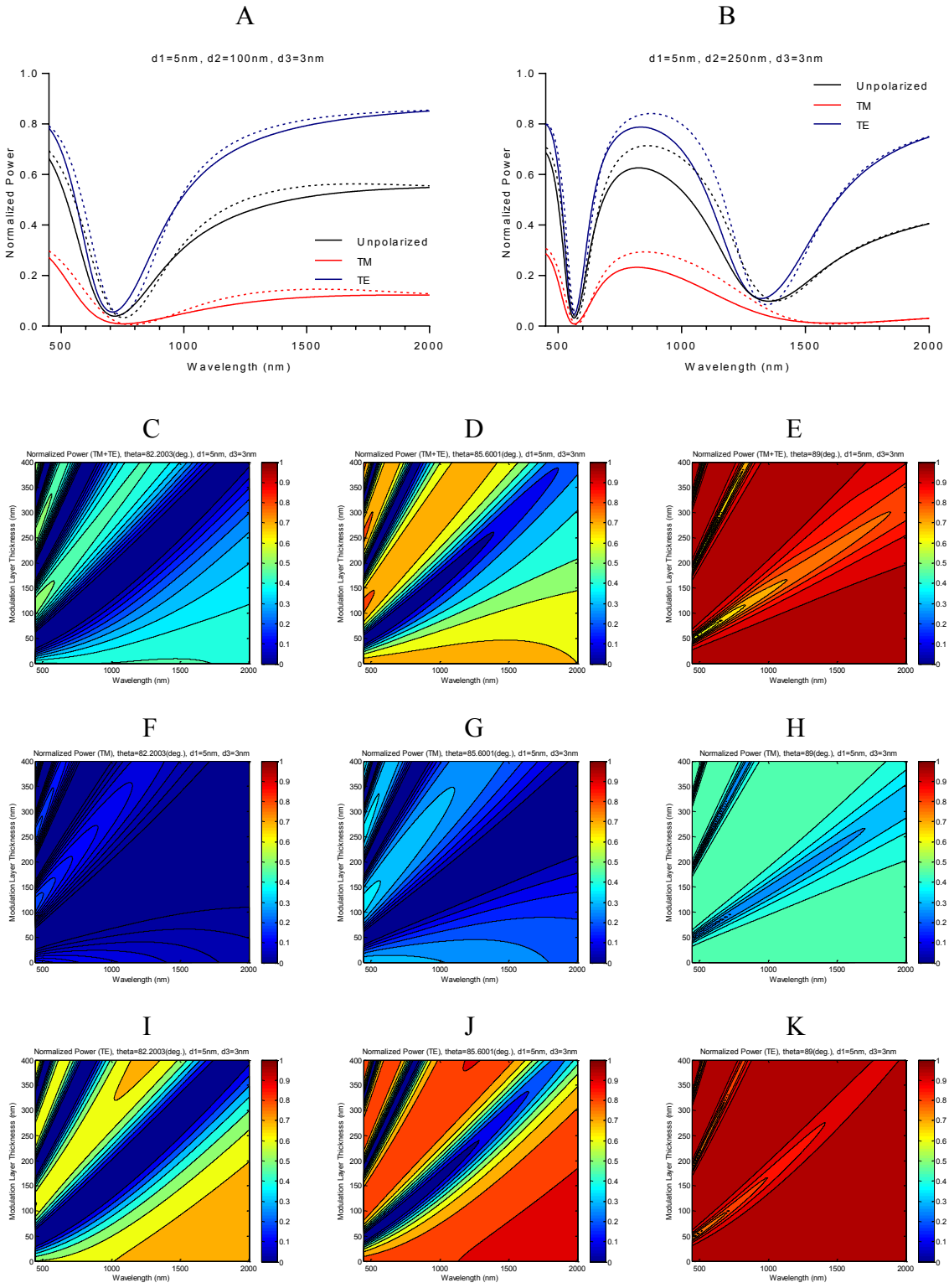

Figure 5-10 – (A) Normalised output power across the spectral domain of a (Ag/Ta_2O_5/Pd) multilayer step-index OFSPR sensor in the presence of 0% and 4% H_2; (λ=450:2000nm), Ag(d1=10nm), Ta_2O_5(d2=100nm), Pd(d3=3nm) are demonstrated; where (TM+TE) is the combined contribution of p- and s- polarized light, (TM) is the output power determined solely using p-polarized light, and (TE) is the output power solely determined using s- polarized light. (B) Ta_2O_5(d2=250nm). (C, D, E) Contour plots illustrating variation in the (TM+TE) output power with wavelength and modulation thickness at three distinct angles (ϑ_{low}, ϑ_{mid}, ϑ_{high}) respectively. (F, G, H) (TM) output power. (I, J, K) (TE) output power.

In Fig. 5-10 the thickness of the metallic layer has been decreased to 5nm. The depth of the TE resonance condition has increased further, and consequently, the depth of the unpolarized resonance condition has increased. Overlap between the two individual TM and TE resonance conditions has improved, as the resonance wavelengths of each individual polarization mode are almost equal. Next, we decrease the metallic thickness further.

5.3.6.5 d1=3nm

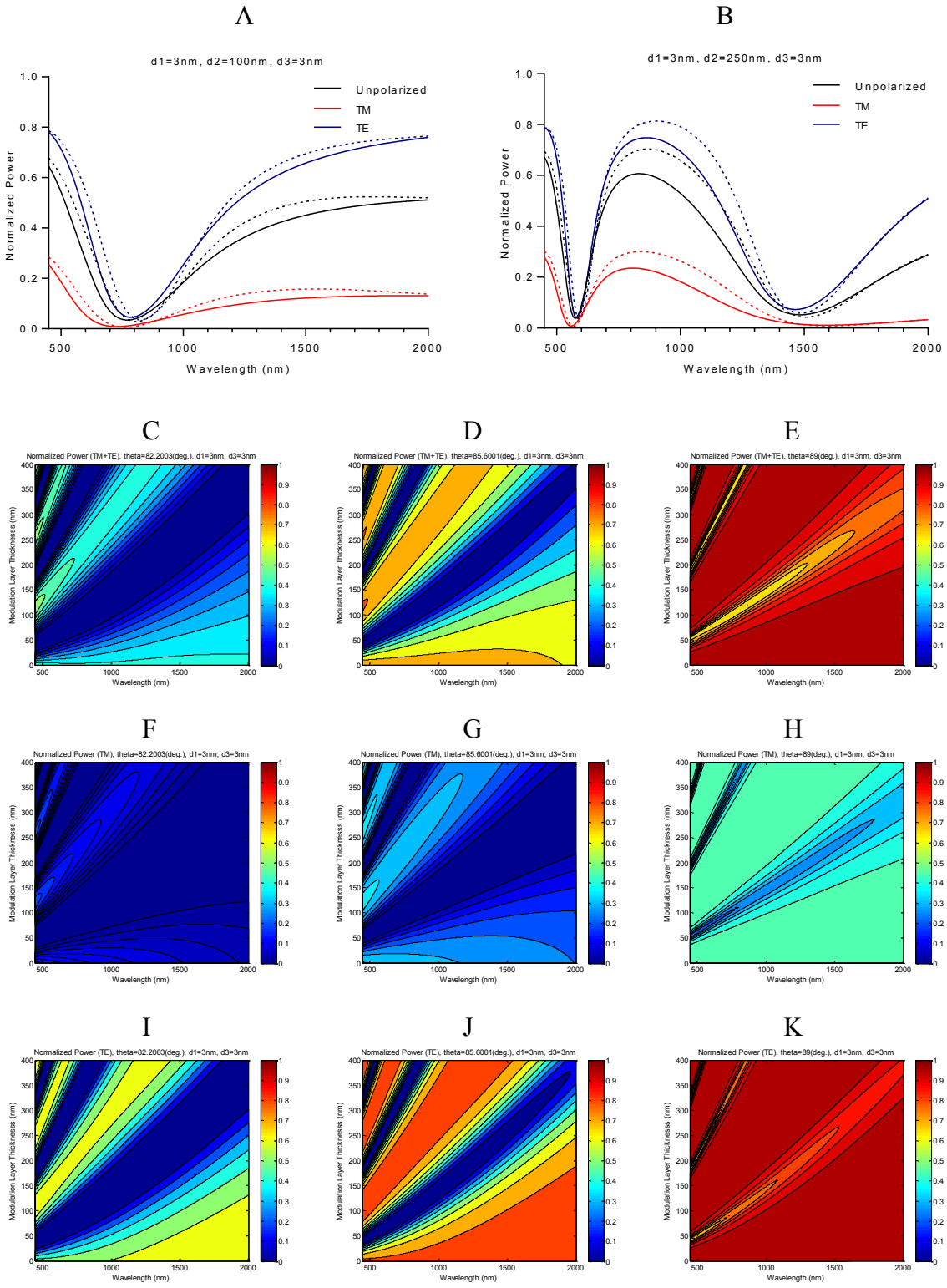

Figure 5-11 – (A) Normalised output power across the spectral domain of a (Ag/Ta_2O_5/Pd) multilayer step-index OFSPR sensor in the presence of 0% and 4% H_2; (λ=450:2000nm), Ag(d1=10nm), Ta_2O_5(d2=100nm), Pd(d3=3nm) are demonstrated; where (TM+TE) is the combined contribution of p- and s- polarized light, (TM) is the output power determined solely using p-polarized light, and (TE) is the output power solely determined using s- polarized light. (B) Ta_2O_5(d2=250nm). (C, D, E) Contour plots illustrating variation in the (TM+TE) output power with wavelength and modulation thickness at three distinct angles (ϑ_{low}, ϑ_{mid}, ϑ_{high}) respectively. (F, G, H) (TM) output power. (I, J, K) (TE) output power.

In Fig. 5-11 we decrease the metallic thickness further to (d1=3nm), and observe that the TM resonance condition now occurs at a shorter resonance wavelength than the corresponding TE resonance condition. Finally, we remove the metallic layer, and observe the output power from each individual polarization mode.

5.3.6.6 d1=0nm

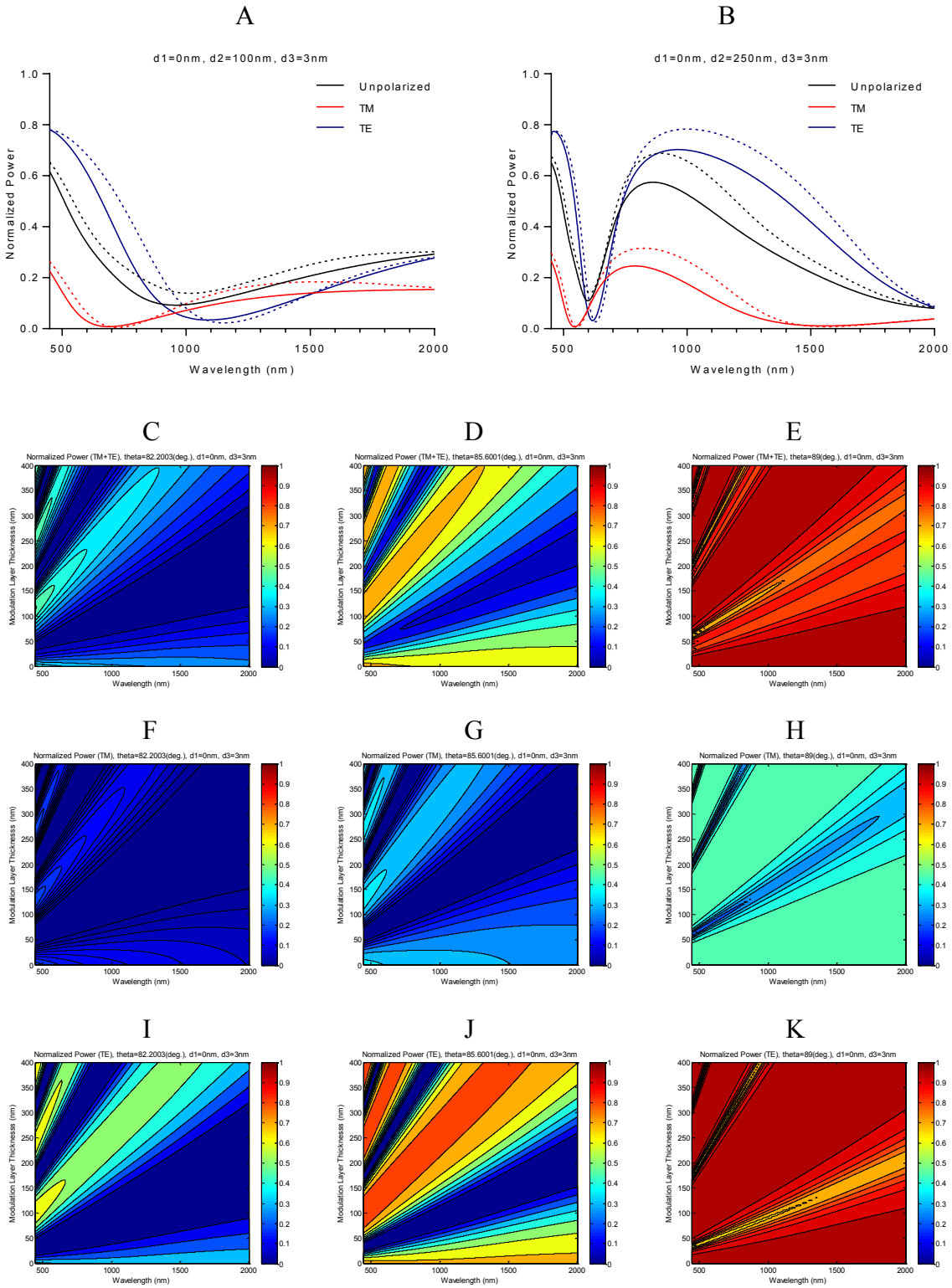

Figure 5-12 – (A) Normalised output power across the spectral domain of a (Ag/Ta_2O_5/Pd) multilayer step-index OFSPR sensor in the presence of 0% and 4% H_2; (λ=450:2000nm), Ag(d1=10nm), Ta_2O_5(d2=100nm), Pd(d3=3nm) are demonstrated; where (TM+TE) is the combined contribution of p- and s- polarized light, (TM) is the output power determined solely using p-polarized light, and (TE) is the output power solely determined using s- polarized light. (B) Ta_2O_5(d2=250nm). (C, D, E) Contour plots illustrating variation in the (TM+TE) output power with wavelength and modulation thickness at three distinct angles (ϑ_{low}, ϑ_{mid}, ϑ_{high}) respectively. (F, G, H) (TM) output power. (I, J, K) (TE) output power.

In Fig. 5-12, the metallic layer has been removed (d1=0nm). While we observe a resonance condition resulting from incident unpolarized light, it is more shallow and broad than that observed when (d1=3, 5nm). This is a consequence of the reduction in the overlap of the individual TM & TE resonance modes. In addition, the depth of the unpolarized resonance condition has decreased.

In this section, we attempted to identify the origin of the additional resonance modes observed in Fig. 5-(5 & 6). We determined the output power of a series of structures differing in metallic and modulation layer thickness, where three different kinds of incident light was used in the fibre; TM polarized, TE polarized, and unpolarized (TM+TE). We were able to identify whether each resonance mode in the unpolarized plots originates in from TM or TE oscillations. We then determined the output using the three different input methods of light, for three specific angles that make up the optical fibre sensing range. These contour plots allowed us to identify resonance modes, and their behaviour with various metallic and modulation layer thicknesses. These contour figures also allowed us to identify the typical angular range that stimulates each resonance mode.

We demonstrated that additional TM and TE resonance modes occur as the modulation layer thickness is increased. The contour images provided an easy medium by which the unpolarized resonance conditions can be identified as originating from wither TM or TE polarized light. They also illustrate that when the individual TM and TE resonance modes occur at separate resonance wavelengths, independent resonance modes appear in the unpolarized light spectrum. However, when the individual TM and TE resonance modes occur at the same resonance wavelength, a single resonance condition is evident in the unpolarized light spectrum. Next we present a figure showing how the resonance wavelengths of the first modes of both the individual TM and TE polarized light behave with metallic thickness.

5.3.7 Identification of Waveguide Modes

In order to identify the mode designations of the resonance modes appearing in our reflectance spectra we will now investigate the behaviour of the electric field through the multilayer stack structure. By looking at the shape of the fields and the number of nodes/anti-

nodes present within the waveguiding layer, we can identify and characterize any modes that appear. In the figures which follow, the layers interfaces are represented by red vertical lines. E_x fields are used to identify TM resonances and E_y fields to identify TE resonances. All fields are normalised to an initial total electric field of 1. The co-ordinate axes are oriented as shown in Fig. 5-4.

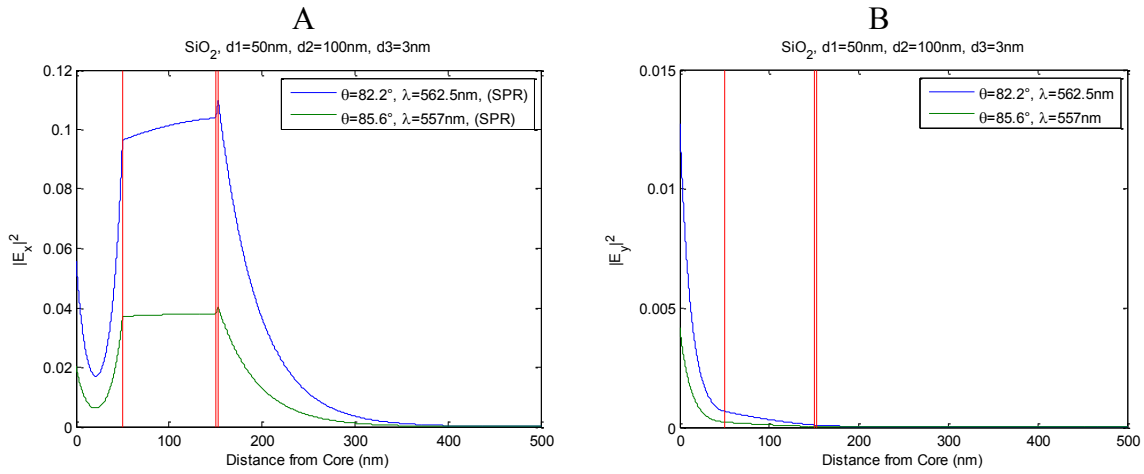

Figure 5-13 Electric field intensities through an (Ag/SiO_2/Pd) multilayer step-index OFSPR sensor. Ag(d1=50nm), SiO_2(d2=100nm), Pd(d3=3nm). The fields were investigated at two distinct angles (ϑ_{min}=82.2˚), (ϑ_{mid}=85.6˚). Resonance wavelengths are indicated in the figure legend. (A) E_x field intensity. (B) E_y field intensity.

In the figure above we investigated the electric fields for a structure consisting of Ag(50nm)/SiO_2(100nm)/Pd(3nm). Two light propagation angles were investigated: (θ_{min}=82.2°) which is close to the critical angle, and (θ_{mid}=85.6°) which is approximately half way between the critical angle and 90˚. The resonance wavelengths (shown) were calculated from the TM reflectance spectrum, there was no resonance present in the TE reflectance spectrum. Fig. 5-13(A) shows the field intensity profile of the E_x component of the electric field (normalised to a total incident electric field of 1). A field profile which is characteristic of surface plasmon resonance is present with the field being a local maximum at the distal surfaces of both the Ag and Pd layers. It is seen that the maximum field decreases as the propagation angle is increased. In Fig. 5-13(B), the field intensity profile of the E_y component (normalised to a total incident electric field of 1) is shown. The fields confirm that no resonance is present.

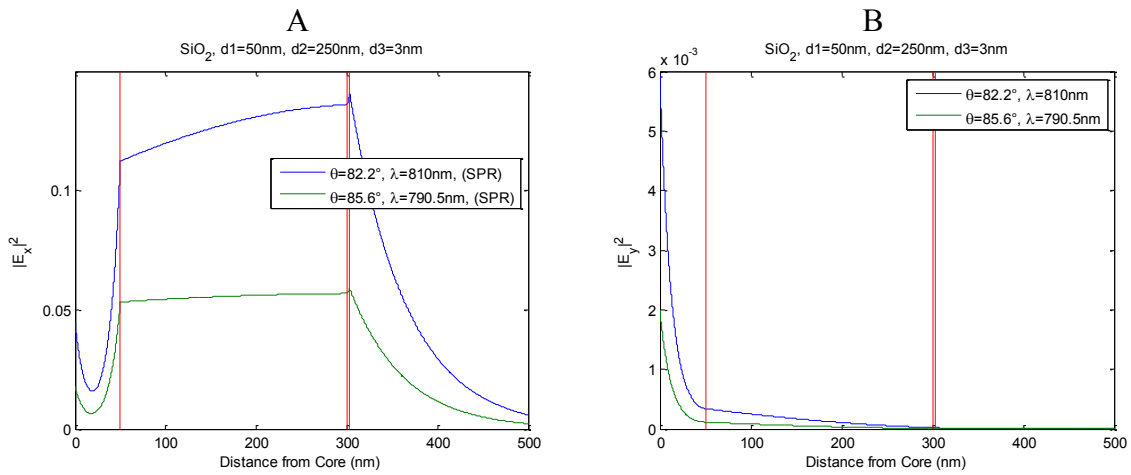

Figure 5-14 Electric field intensities through an (Ag/SiO_2/Pd) multilayer step-index OFSPR sensor. Ag(d1=50nm), SiO_2(d2=250nm), Pd(d3=3nm). The fields were investigated at two distinct angles (ϑ_{min}=82.2˚), (ϑ_{mid}=85.6˚). Resonance wavelengths are indicated in the figure legend. (A) E_x field intensity. (B) E_y field intensity.

In the Fig. 5-14 above we investigated the electric fields for a structure consisting of Ag(50nm)/SiO_2(250nm)/Pd(3nm). Again two light propagation angles were investigated. The resonance wavelengths (shown) were calculated from the TM reflectance spectrum, there was no resonance present in the TE reflectance spectrum. Fig. 5-14(A) shows the field intensity profile of the E_x component of the electric field (normalised to a total incident electric field of 1). A field profile which is characteristic of surface plasmon resonance is present with the field being a local maximum at the distal surfaces of both the Ag and Pd layers. It is seen that the maximum field decreases as the propagation angle is increased. In Fig. 5-14(B), the field intensity profile of the E_y component (normalised to a total incident electric field of 1) is shown. The fields confirm that no resonance is present.

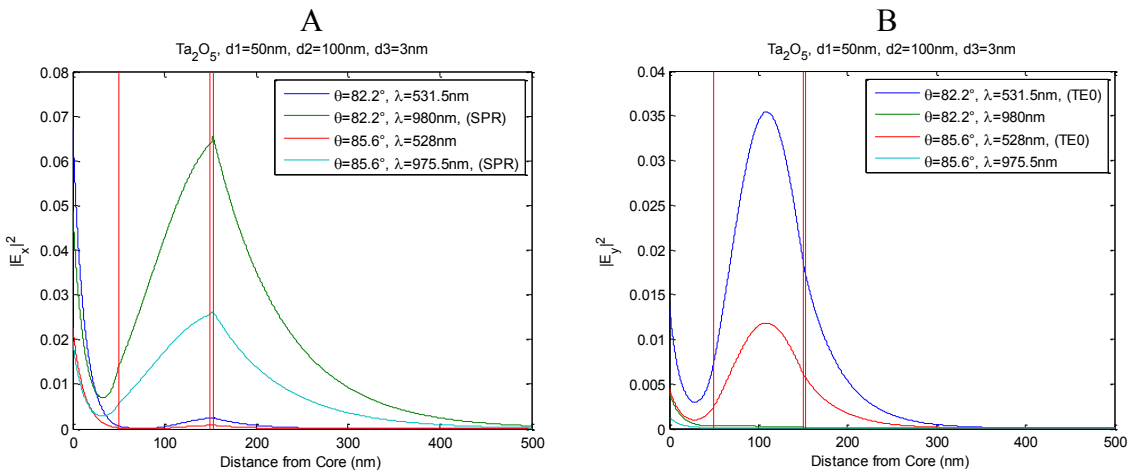

Figure 5-15 Electric field intensities through an (Ag/Ta_2O_5/Pd) multilayer step-index OFSPR sensor. Ag(d1=50nm), Ta_2O_5(d2=100nm), Pd(d3=3nm). The fields were investigated at two distinct angles (ϑ_{min}=82.2˚), (ϑ_{mid}=85.6˚). Resonance wavelengths are indicated in the figure legend. (A) E_x field intensity. (B) E_y field intensity.

In Fig. 5-15 we investigated the electric fields for a structure consisting of Ag(50nm)/Ta_2O_5(100nm)/Pd/(3nm). Two light propagation angles were investigated. The resonance wavelengths (shown) were calculated from both the TM ($\lambda_{res\text{-}TM}$=980, 975.5nm) and TE ($\lambda_{res\text{-}TE}$=531.5, 528nm) reflectance spectra. Fig. 5-15(A) shows the field intensity profile of the E_x component of the electric field intensity. A field profile which is characteristic of surface plasmon resonance is present at the TM resonance wavelengths with the field being a maximum at the distal surfaces of both the Ag and Pd layers. It is seen that the maximum field decreases as the propagation angle is increased. As expected, the fields of the TM resonance ($\lambda_{res\text{-}TM}$=531.5, 528nm) do not show this behaviour. In Fig 15(B), the field intensity profile of the E_y component is shown. The fields confirm the presence of waveguide modes at both TE resonance wavelengths ($\lambda_{res\text{-}TE}$=531.5, 528nm). This field profile corresponds to a TE0 mode (Zhang *et al.* 2015; Sekkat 2016). For comparison, the fields at two wavelengths which are off the TE resonances are shown and confirm the absence of this mode off resonance.

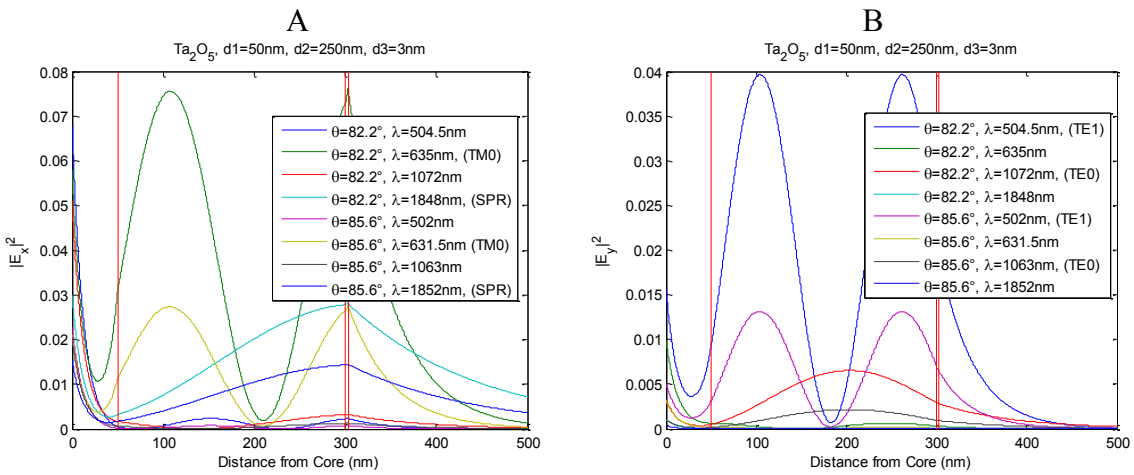

Figure 5-16 Electric field intensities through an (Ag/Ta_2O_5/Pd) multilayer step-index OFSPR sensor. Ag(d1=50nm), Ta_2O_5(d2=250nm), Pd(d3=3nm). The fields were investigated at two distinct angles (ϑ_{min}=82.2˚), (ϑ_{mid}=85.6˚). Resonance wavelengths are indicated in the figure legend. (A) E_x field intensity. (B) E_y field intensity.

In Fig. 5-16 we investigated the electric fields for a structure consisting of Ag(50nm)/Ta_2O_5(250nm)/Pd(3nm). Two light propagation angles were investigated. The resonance wavelengths (shown) were calculated from both the TM and TE reflectance spectra. spectra. For a light propagation angle of (θ_{min}=82.2°), TM resonances were found at 635nm and 1848.5nm and TE resonances at 504.4nm and 1072nm. When the propagation angle was (θ_{mid}=85.6°), the TM resonances shifted to ($\lambda_{res\text{-}TM}$=631.5, 1852nm) and the TE resonances to ($\lambda_{res\text{-}TE}$=502, 1063nm. Fig 16(A) shows the field intensity profile of the E_x component of the electric field intensity. Looking first at the cyan curve (θ_{min}=82.2°), ($\lambda_{res\text{-}TM}$=1848.5nm) we see a field profile which is characteristic of surface plasmon resonance. This is the sensor SPR mode. Looking next at the green curve (θ_{min}=82.2°), ($\lambda_{res\text{-}TM}$=635nm) we see a field profile which is characteristic of a TM guided mode. This mode was not present when SiO_2 was used as the modulation layer in Fig. 5-5 as it is below cut-off in that case. Due to the higher refractive index of Ta_2O_5, the TM0 mode is above cut-off in this structure and causes a resonance peak in the spectrum. The mode order can be identified by counting the number of antinodes (N_A) in the field within the wave-guiding layer and can be written TM (N_A-1). The existence of the mode is confirmed by the mode dispersion function. The figure also shows that the fields for wavelengths which are off ($\lambda_{res\text{-}TM}$=504.5, 1072, 502, 1063nm) do not show either SPR or TM guided modes.

In Fig 16(B), the field intensity profile of the E_y component is shown. Looking at the blue curve (θ_{min}=82.2°), ($\lambda_{res\text{-}TE}$=504.5nm), we see a field profile characteristic of a guided mode. The mode designation can be identified by counting the number of anti-nodes within the wave-guiding layer and is given by TE (N_A). We can see that this mode is a TE1 mode and the other modes can be identified in a similar way. Finally, we see that at off-resonance wavelengths, these mode fields are absent.

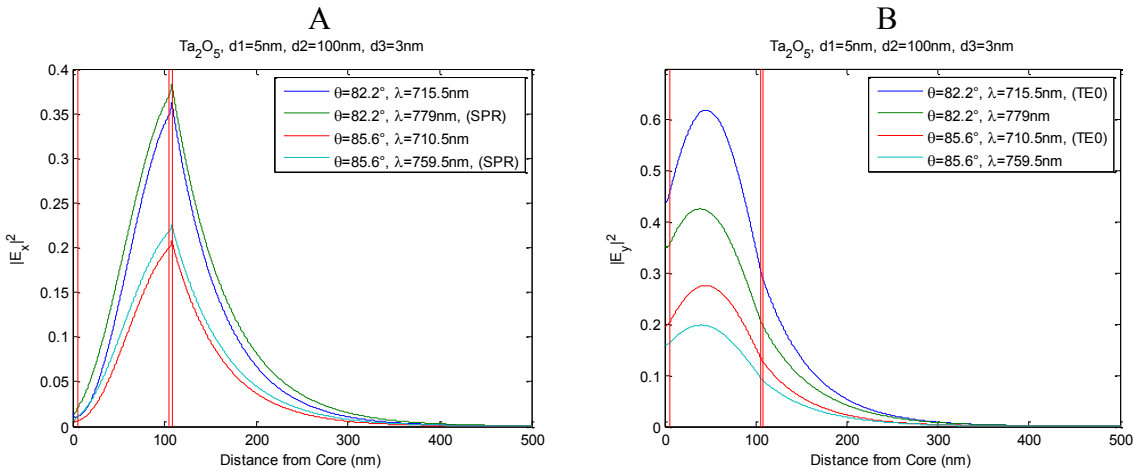

Figure 5-17 Electric field intensities through an (Ag/Ta_2O_5/Pd) multilayer step-index OFSPR sensor. Ag(d1=5nm), Ta_2O_5(d2=100nm), Pd(d3=3nm). The fields were investigated at two distinct angles (ϑ_{min}=82.2˚), (ϑ_{mid}=85.6˚). Resonance wavelengths are indicated in the figure legend. (A) E_x field intensity. (B) E_y field intensity.

In Fig. 5-17 above we investigated the electric fields for a structure consisting of Ag(5nm)/Ta_2O_5(100nm)/Pd(3nm). At a light propagation angle of (θ_{min}=82.2) resonances were found at ($\lambda_{res\text{-}TM}$=779nm) due to SPR and ($\lambda_{res\text{-}TE}$=715.5nm) due to TE0. At the higher propagation angle of (θ_{mid}=85.6), resonances were present at ($\lambda_{res\text{-}TM}$=759.5nm) due to SPR, and ($\lambda_{res\text{-}TE}$=710.5nm) due to TE0. The mode designations are shown in the figure legend. It is noticeable that due to the spectral proximity of the TM and TE modes in each case, fields which are characteristic of SPR Fig. 5-17(A) and TE0 modes Fig. 5-17(B) can be seen even at the off-resonance wavelengths. We note the highest fields in each case are found at the resonance wavelength as expected. As we will show, the spectral proximity of the two modes is advantageous for the sensor as the modes (SPR &TE0) will combine in the spectrum to form a deeper resonance with a resulting improvement in sensing performance.

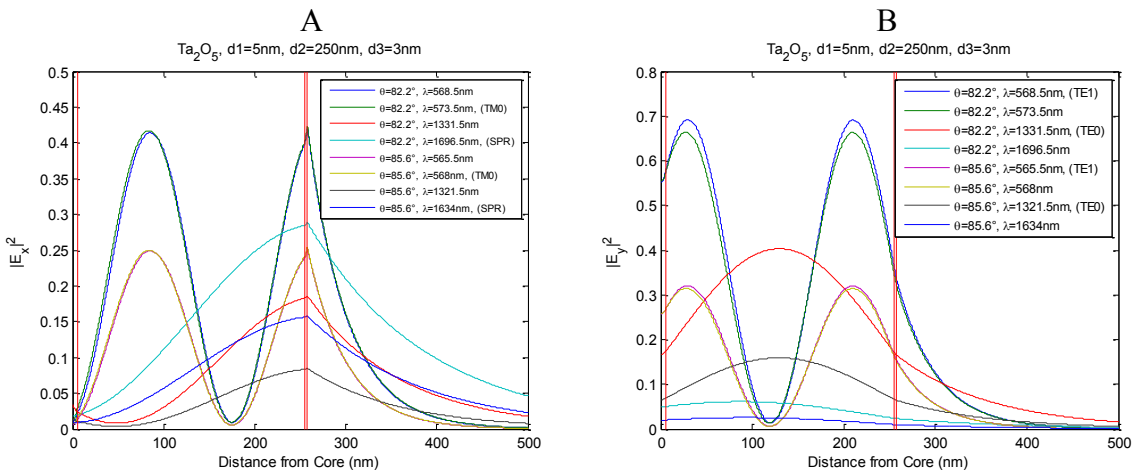

Figure 5-18 Electric field intensities through an (Ag/Ta_2O_5/Pd) multilayer step-index OFSPR sensor. Ag(d1=5nm), Ta_2O_5(d2=250nm), Pd(d3=3nm). The fields were investigated at two distinct angles (ϑ_{min}=82.2˚), (ϑ_{mid}=85.6˚). Resonance wavelengths are indicated in the figure legend. (A) E_x field intensity. (B) E_y field intensity.

In Fig. 5-18 above we investigated the electric fields for a structure consisting of Ag(5nm)/Ta_2O_5(250nm)/Pd(3nm). At a light propagation angle of (θ_{min}=82.2) resonances were found at ($\lambda_{res\text{-}TM}$=573.5, 1696.5nm) due to (TM0 & SPR) respectively. Additionally, ($\lambda_{res\text{-}TE}$=568.5, 1331.5nm) due to (TE1 & TE0) respectively. The spectral proximity of the TM0 and TE1 modes is again advantageous for the aforementioned reasons. At the higher propagation angle of (θ_{mid}=85.6), resonances were found at ($\lambda_{res\text{-}TM}$=568, 1634, $\lambda_{res\text{-}TE}$=565.5, 1321.5nm) due to (TM0, SPR, TE1, TE0) respectively.

In summary, we determined the electric field through our multilayer stack sensing structure. Using the shape that the electric field takes at certain points along the multilayer allowed us to identify and characterize resonance modes.

5.3.8 TM, TE resonance wavelengths + unpolarized resonance depth

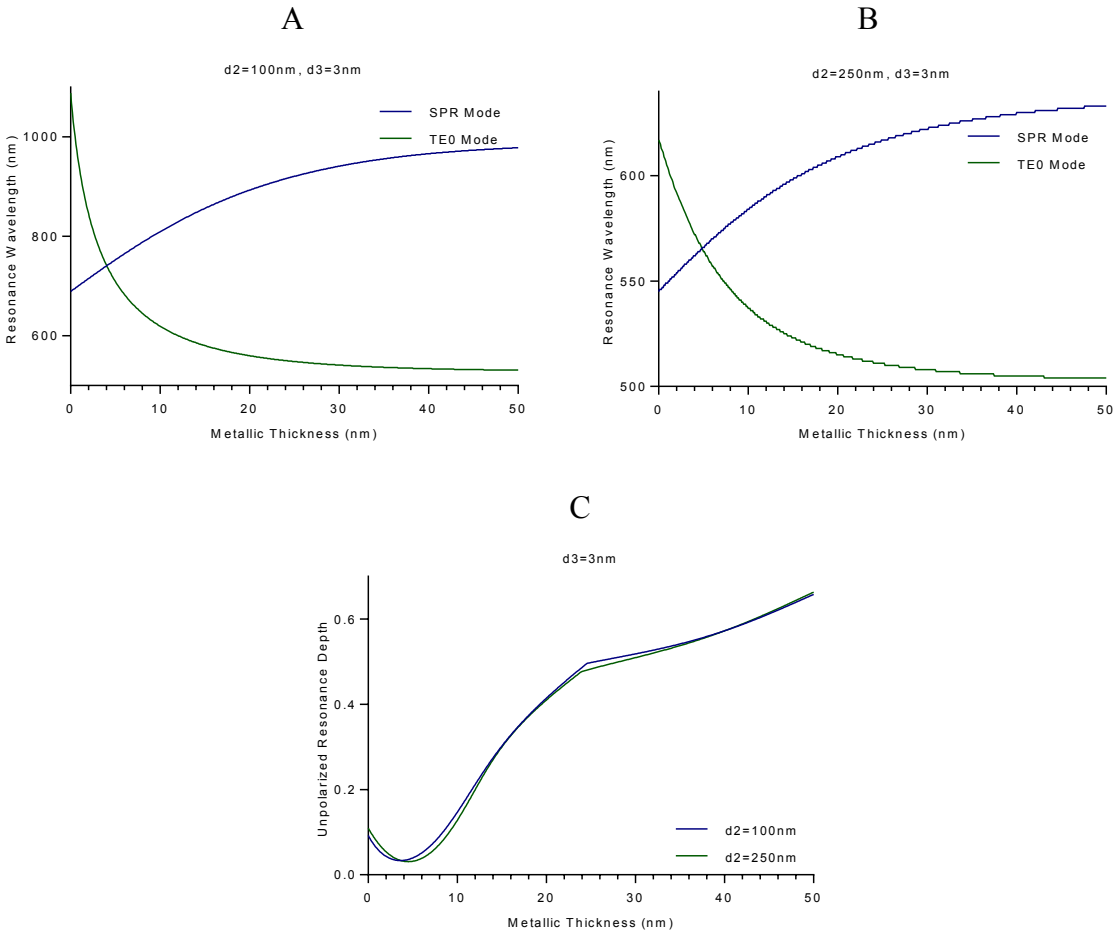

Figure 5-19 – (A) Resonance wavelength of the first mode in the series of OFSPR based structures demonstrated in Fig. 5-(3-8), where only TM or TE polarized light are input through the fibre, Ta_2O_5(d2=100nm), Pd(d3=3nm). (B) Ta_2O_5(d2=250nm). (C) Resonance depth of the first mode in the series of OFSPR based structures demonstrated in Fig. 5-(3-8), where unpolarized light is input through the fibre.

Fig. 5-19(A) illustrates the influence that the metallic layer thickness has on the resonance wavelength of each individual polarization mode. The TM resonance mode (SPR) undergoes a red shift with increasing metallic layer thickness, while the TE mode (TE0) undergoes a blueshift. At a modulation layer thickness of (d2=100nm), the individual TM and TE resonance modes occur at the same resonance wavelength at a metallic thickness of (d1=5nm). In Fig. 5-19(B), while the modulation layer thickness has been increased to (d2=250nm), the behaviour of each resonance mode with increasing metallic layer thickness follows the same trend, (respective red and blue shift). Once the modulation layer thickness is increased, the individual TM and TE resonance modes occur at the same resonance

wavelength at a slightly larger metallic layer thickness than when the modulation layer thickness was thinner in Fig. 5-19(A).

Next, we illustrate the resonance depth of first resonance mode stimulated using unpolarized light. We find that the resonance depth reaches a minimum at (d1=4, 5nm), when (d2=100, 250nm) respectively. We make note that the minimum resonance depth in these series of structures occurs at the same location where the individual TM and TE resonance modes overlap. At (d1=24nm), the slope of both plots in Fig. 5-19(C) becomes less steep. This occurs as the difference in the resonance wavelengths between the individual TM and TE resonance modes has become too great, and no longer form a single resonance mode. Above this metallic thickness, we determine the resonance wavelength of the deepest resonance condition, which in both cases; (d2=100, 250nm), is the TM resonance mode.

In summary, we have investigated the behaviour of the resonance wavelength of the first mode stimulated using TM polarized light. We observed a red shift with increasing metallic layer thickness. We then investigated the behaviour of the resonance wavelength of the first mode stimulated using TE polarized light, and found a blue shift with increasing metallic layer thickness. The resonance modes crossover within a very small metallic thickness range, regardless of the modulation layer thickness. We also determined the depth of the first resonance mode generated using an input of unpolarized light, and found that minimums in the same very small metallic layer thickness range. These findings suggest that this metallic thickness range may yield optimal results. In light of these findings, we determined the performance of the sensor, in terms of sensitivity, detection accuracy, and figure of merit.

5.3.9 Sensitivity

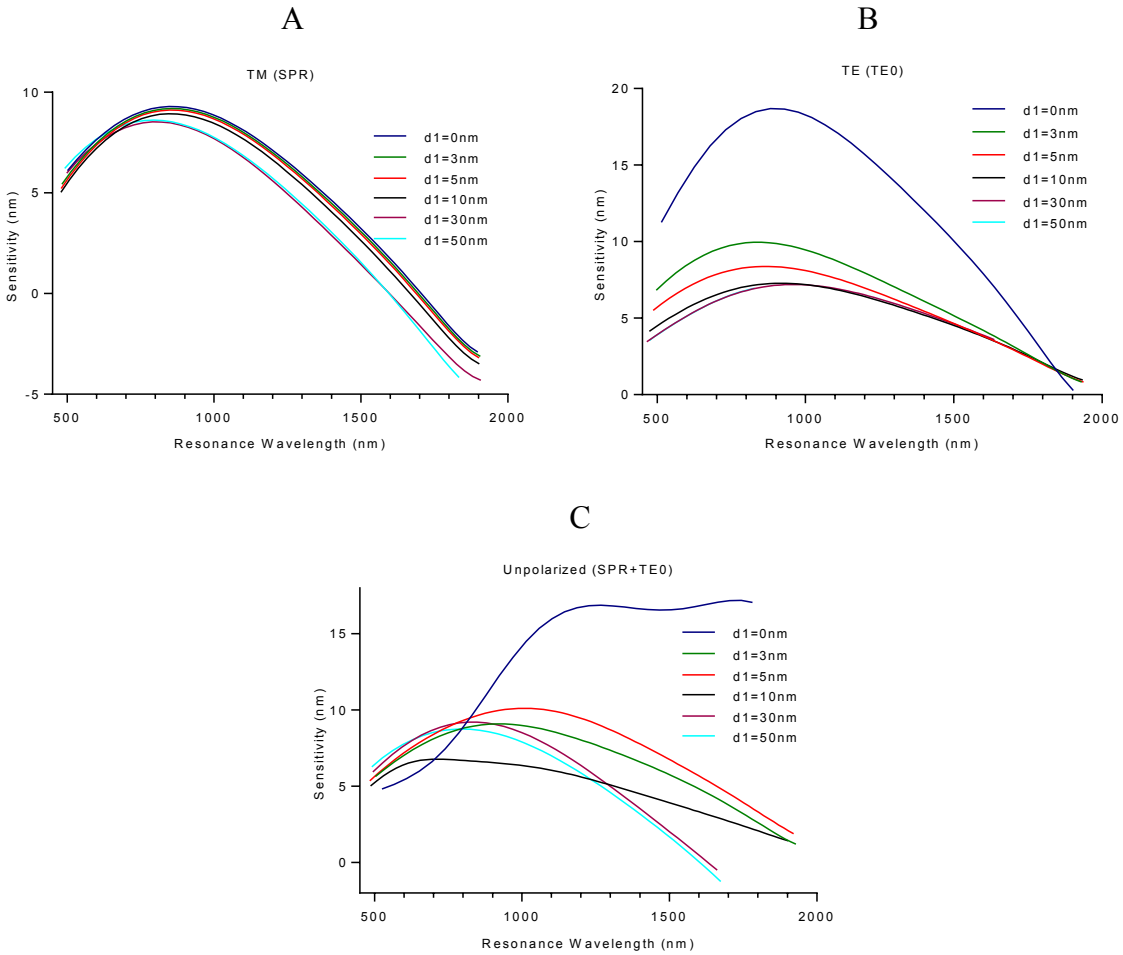

Figure 5-20 – (A) Sensor sensitivity (dip wavelength shift to 1% hydrogen) for several OF configurations with Ag(d1=0,3,5,10,30,50nm), Pd(d3=3nm), TM light (λ=450:2000nm), where the resonance wavelength of each mode was modulated using the thickness of the modulation layer (Ta_2O_5). (B) TE polarized light. (C) Unpolarized light.

Fig. 5-20(A) displays the sensitivity of several OF structures differing in metallic thickness, where the modulation layer thickness was used to control the resonance wavelength of each respective mode, and TM polarized light was incident through the fibre. When the metallic thickness was low (d1=3nm), relatively large upper and lower limits of the modulation thickness range was needed (d2=55:310nm) in order to shift the resonance location along the investigated spectral range. In the case of (d1=50nm) lower limits (d2=20:250nm) were necessary in order to shift resonance along the investigated wavelength spectrum. For each of the configurations in Fig. 5-20(A), sensitivity can be seen to increase to a maximum with increasing modulation layer thickness, and then fall off. Sensitivity is maximum across the majority of the investigated wavelength range for the configurations that do not include an

initial metallic layer. It is also noted that the presence of the metallic layer has little influence on the overall sensitivity of the structures when using incident TM light, as can be seen by the minor difference in sensitivity between (d1=0nm) and (d1=3nm) across the wavelength spectrum.

It should be noted that once a particularly large dielectric thickness is employed, the sensitivity of TM contributions decreases to negative values, thus indicating a blueshift of the resonance condition. as previously mentioned in Chapter 3; while H_2 sensing is possible by measuring the blue shift, it is important to note that if the resonance wavelength undergoes a blue shift at one part of the wavelength spectrum, and a red shift at another; then, there will occur a specific localized wavelength range, where sensor sensitivity decreases towards zero, and accurate H_2 detection is no longer permitted.

In Fig. 5-20(B), the sensitivity of various structures are determined once again, but using incident TE polarized light. Similarly to Fig. 5-20(A), sensitivity increases to a maximum optimal value with increasing modulation layer thickness followed by a decline with further increase in the Ta_2O_5 layer. Unlike Fig. 5-20(A) however, the sensitivity of the TE based configuration increases dramatically upon removing the metallic layer, as can be seen by the sudden increase in sensitivity when the metallic layer thickness decreases from (d1=3nm) to (d1=0nm).

Finally Fig. 5-20(C) illustrates the sensitivity for each OF configuration where unpolarized light is incident through the fibre. For each of the investigated structures that utilize an initial metallic layer, sensitivity reaches maximum corresponding to a specific modulation layer thickness. The structures that do not include Ag demonstrates very high sensitivity, primarily due to the TE component of the unpolarized light. Next, we investigated the spectral width of the resonance condition. A narrow resonance, (high detection accuracy) is preferred.

5.3.10Detection Accuracy

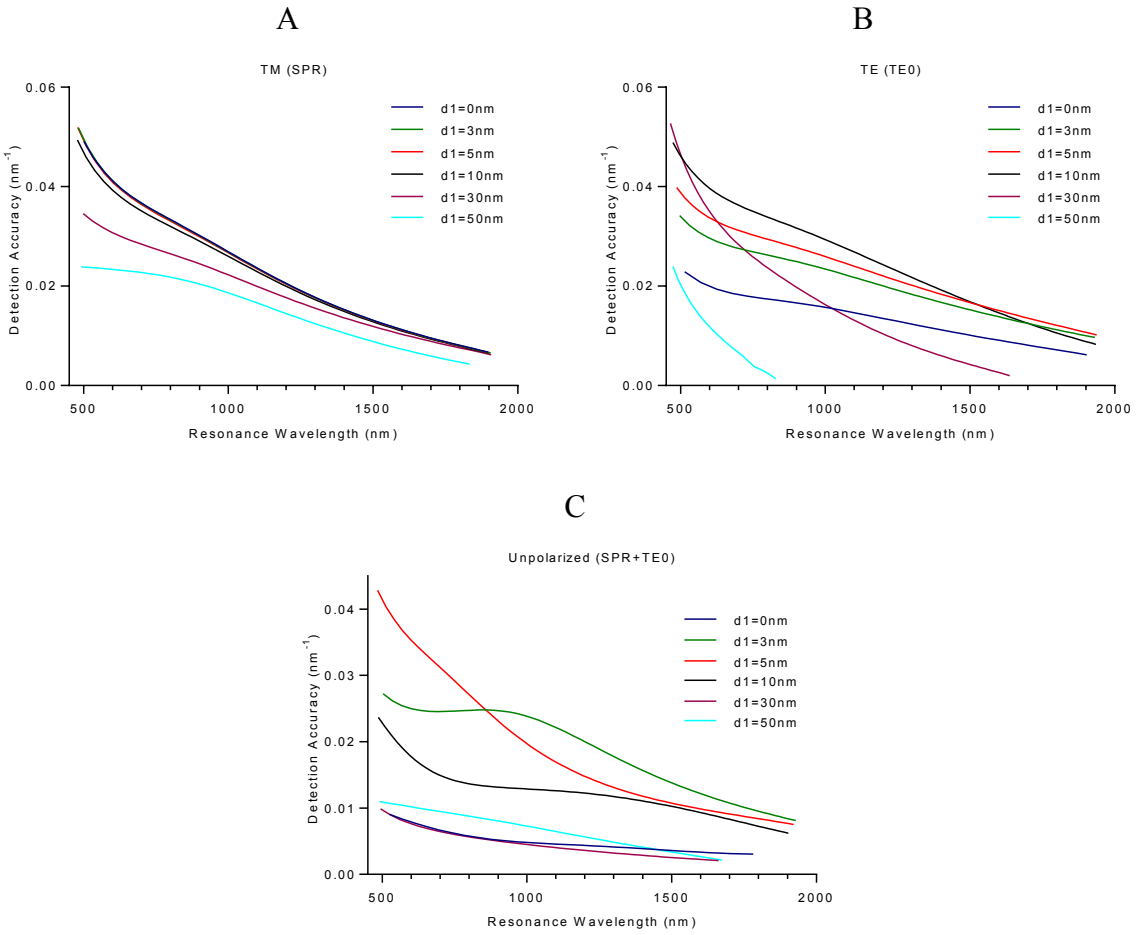

Figure 5-21 – (A) Detection accuracy (dip wavelength shift to 1% hydrogen) for several OF configurations with Ag(d1=0,3,5,10,30,50nm), Pd(d3=3nm), TM light (λ=450:2000nm), where the resonance wavelength of each mode was modulated using the thickness of the modulation layer (Ta_2O_5). (B) TE polarized light. (C) Unpolarized light.

It can be observed in Fig. 5-21(A & B) that that detection accuracy of each independent oscillation mode TM and TE, decreases with increasing resonance wavelength. Additionally, the configurations that employ a metallic thickness of (d1=50nm) demonstrate the lowest detection accuracy (widest resonance width) in both Fig. 5-21(A & B) when only one oscillation mode is permitted though the fibre. In Fig. 5-21(A), there is little difference in the detection accuracy of the resonance mode between the configurations that do not employ any initial metallic layer, and those that employ a very thin metallic layer thickness (d1=3, 5, 10nm). This is similar to what was observed in the sensitivity measurements in Fig. 5-21(A).

In Fig. 5-21(B), sensitivity is maximum at low wavelengths when using a large metallic thickness of (d1=30nm). As the modulation layer increases, the metallic thickness that

generates the highest sensitivity decreases to (d1=10nm), and further to (d1=5nm). It is also evident from Fig. 5-21(B) that the inclusion of a small metallic thickness improves the detection accuracy of the device, as can be seen by the fact that, the detection accuracy is greater when (d1=3, 5, 10nm), than when (d1=0, 50nm), regardless of the modulation layer thickness.

Finally in Fig. 5-21(C), we determine the detection accuracy of the series of devices, using unpolarized light as the input through the fibre. We observe that the detection accuracy is greatest when (d1=5nm) at the lower end of the investigated wavelength spectrum, and detection accuracy is greater when (d1=3nm), at the upper end. This can be understood recalling that the unpolarized input is made up of independent TM and TE polarized contributions. From Fig. 5-(7-12) we found that both of these propagation modes give rise to independent resonance conditions. From Fig. 5-19(A & B) it can be seen that the resonance wavelengths of each of these independent resonance modes overlap at (d1=3, 5nm), when (d2=100, 250nm), which give rise to resonance conditions with resonance wavelengths at lower and upper sections of the investigated wavelength spectrum respectively. Thus, when the two independent TM and TE resonance modes occur at the same resonance wavelength, it can be concluded that the width of the single unpolarized resonance condition will be minimal. Finally we determine the overall performance of each of the investigated configuration by demining the sensor figure of merit.

5.3.11 Figure of Merit

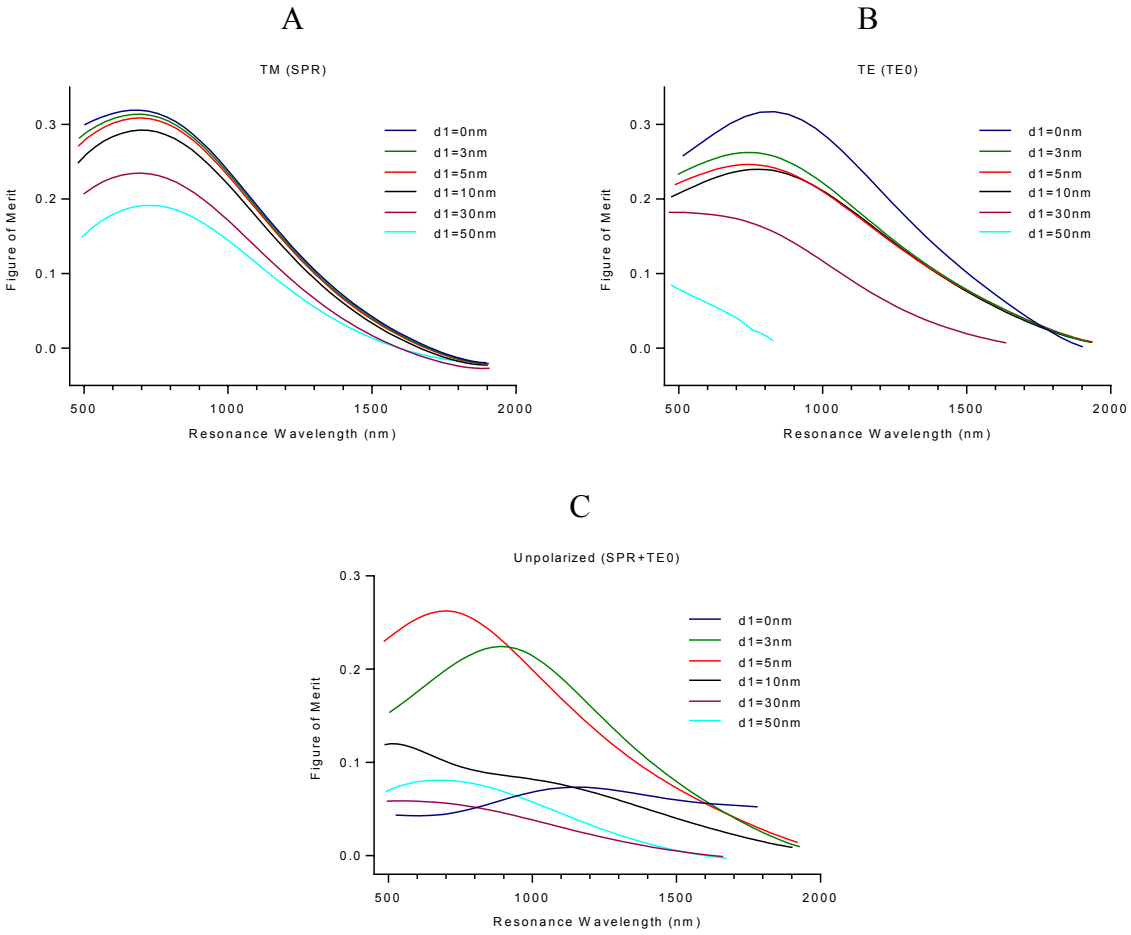

Figure 5-22 – (A) Figure of merit (dip wavelength shift to 1% hydrogen) for several OF configurations with Ag(d1=0,3,5,10,30,50nm), Pd(d3=3nm), TM light (λ=450:2000nm), where the resonance wavelength of each mode was modulated using the thickness of the modulation layer (Ta_2O_5). (B) TE polarized light. (C) Unpolarized light.

In Fig. 5-22(A & B), the sensor figure of merit can be seen to increase with increasing resonance wavelength for both independent TM and TE polarisation modes of light, and decreases thereafter. When considering each independent oscillation mode, the maximum sensor figure of merit occurs when the metallic layer is removed. In the Fig. 5-22(A), where TM light is input through the fibre, the figure of merit can be seen to reach negative values at large resonance wavelengths, resulting from the negative sensitivity values at this resonance wavelength, which originates from the blueshift of the resonance condition. Since there was little variation between the absence of an initial metallic layer thickness, and the inclusion of a small thickness of (d1=3, 5, 10nm) on the sensitivity or detection accuracy in Fig. 5-20(A)

and Fig. 5-21(A); there is consequently little observed difference in the figure of merit in Fig. 5-22(A).

In Fig. 5-22(B) the figure of merit is determined using TE polarized incident light. Since the configurations in Fig. 5-20(B) and Fig. 5-21(B) that employ a metallic thickness of (d1=50nm) demonstrate the lowest performance of those metallic thickness investigated; the resultant figure of merit in Fig. 5-22(B) when (d1=50nm) is very low. The relative difference between the sensitivity of (d1=0nm) in Fig. 5-20(B) that of the other investigates metallic thickness is very large. The relative difference in the detection accuracy of (d1=0nm) in Fig. 5-21(B) than the other investigated metallic thickness is smaller. Thus, the resultant TE figure of merit displays optimal performance for the majority of the investigated wavelength spectrum for configurations that employ no initial metallic thickness (d1=0nm).

Finally, Fig. 5-22(C) displays the figure of merit as calculated using incident unpolarized light through the fibre. Optimal performance is exhibited once s thin metallic layer thickness is employed. Specifically, once (d1=3nm) for operation at the lower part of the investigated wavelength spectrum, and (d1=5nm) at the upper section of the wavelength spectrum. These metallic thickness that exhibit optimal performance exist in the very small range of metallic thicknesses in Fig. 5-19(A & B) that cause independent TM and TE resonance wavelengths overlap.

It is noted that the largest exhibited figure of merit occurs when only one oscillation mode (either TM or TE) is permitted though the fibre. As a result, most researchers consider only one oscillation mode when looking as sensor performance as typically only TM. However these configurations are unrealistic when considering operation with a multimode optical fibre for most real world applications, as polarisation of one oscillation mode is very difficult to achieve in a cylindrical multimode optical fibre, thus for practical applications the presence of both modes must be accounted for. By optimising the metallic thickness and choosing suitable high index dielectric material, co-operation between TM and TE modes can be achieved by closely matching the spectral locations of each resonance condition, thus producing significantly enhanced results than was possible when the resonance locations of each oscillation mode occurred far apart. Specifically, using a very small metallic thickness of (d1=5nm) in order to match the resonance wavelengths of the independent TM and TE modes has resulted in significantly improved performance of (FOM=0.262469). While we could compare this to the optimal figure of merit determined in Chapter 2 of

(FOM=0.062740), it would not provide much insight as the modulation and H_2 sensitive materials are different. We can however compare this figure of merit to that produced using the configuration form this chapter along with the widely referenced value for Ag thickness, which was also the previously determined optimal in Chapter 2 of (d1=50nm); (FOM=0.081045). Using (d1=5nm) corresponds to a 323.9% improvement in the figure of merit compared to the widely referenced optimal of (d1=50nm). The dramatic improvement is attributed to matching the resonance wavelengths of individual TM and TE resonance conditions.

5.3.12 Co-operation of Higher Order Resonance Conditions

5.3.12.1 Sensitivity

Fig. 5-(7-12) revealed the presence of additional resonance modes once the thickness of the dielectric layer was high enough. In Fig. 5-(13-18) we were able to characterize each of these additional resonance modes. We determined the performance of some of these additional modes, using a specific metallic thickness (d1=5nm) that permits the overlap of (SPR + TE0), as well as (TM0 + TE1).

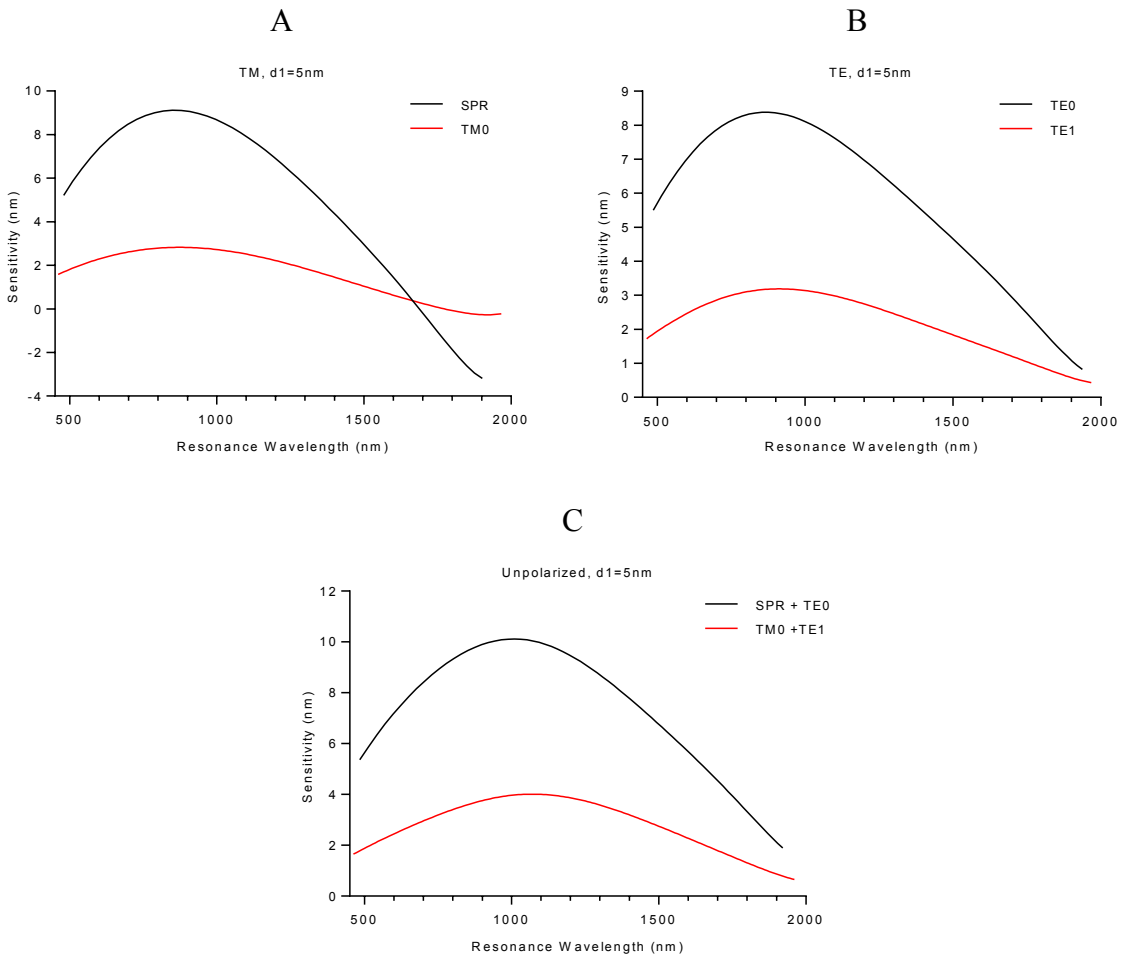

Figure 5-23 – (A) Sensor sensitivity (dip wavelength shift to 1% hydrogen) of the first two resonance modes that appear for several OF configurations with Ag(d1=5nm), Pd(d3=3nm), TM polarized light (λ=450:2000nm), where the resonance wavelength of each mode was modulated using the thickness of the modulation layer (Ta_2O_5). (B) TE polarized light. (C) unpolarized light.

Fig. 5-23(A) illustrates the sensitivity of two resonance conditions stimulated using TE light (TE0 & TE1). Similarly, Fig. 5-23(B) displays the sensitivity of two resonance conditions stimulated using incident TM polarized light (SPR & TM0). Finally, Fig. 5-23(C) illustrates the sensitivity of both resonance conditions stimulated with unpolarized light, where once resonance condition is comprised of (SPR + TE0) resonance contribution, and the other is composed of (TM0 + TE1). The sensitivity of the first unpolarized resonance mode is significantly larger than the second. This can be understood by considering the fact that a significantly larger modulation layer thickness is necessary in order to achieve the same spectral shift of the (TM0 + TE1) unpolarized resonance condition compared to the (SPR + TE0). For example, in order for resonance to occur above (λ=1990nm), where (d1=5nm); the

(SPR + TE0) mode necessitates a modulation thickness of (d2=405nm). In order to shift the (TM0 + TE1) resonance to a similar resonance wavelength, a modulation thickness of (1085nm) is necessary, and thus, coupling between the generated resonance conditions and the analyte region (Pd layer) is reduced.

5.3.12.2 Detection Accuracy

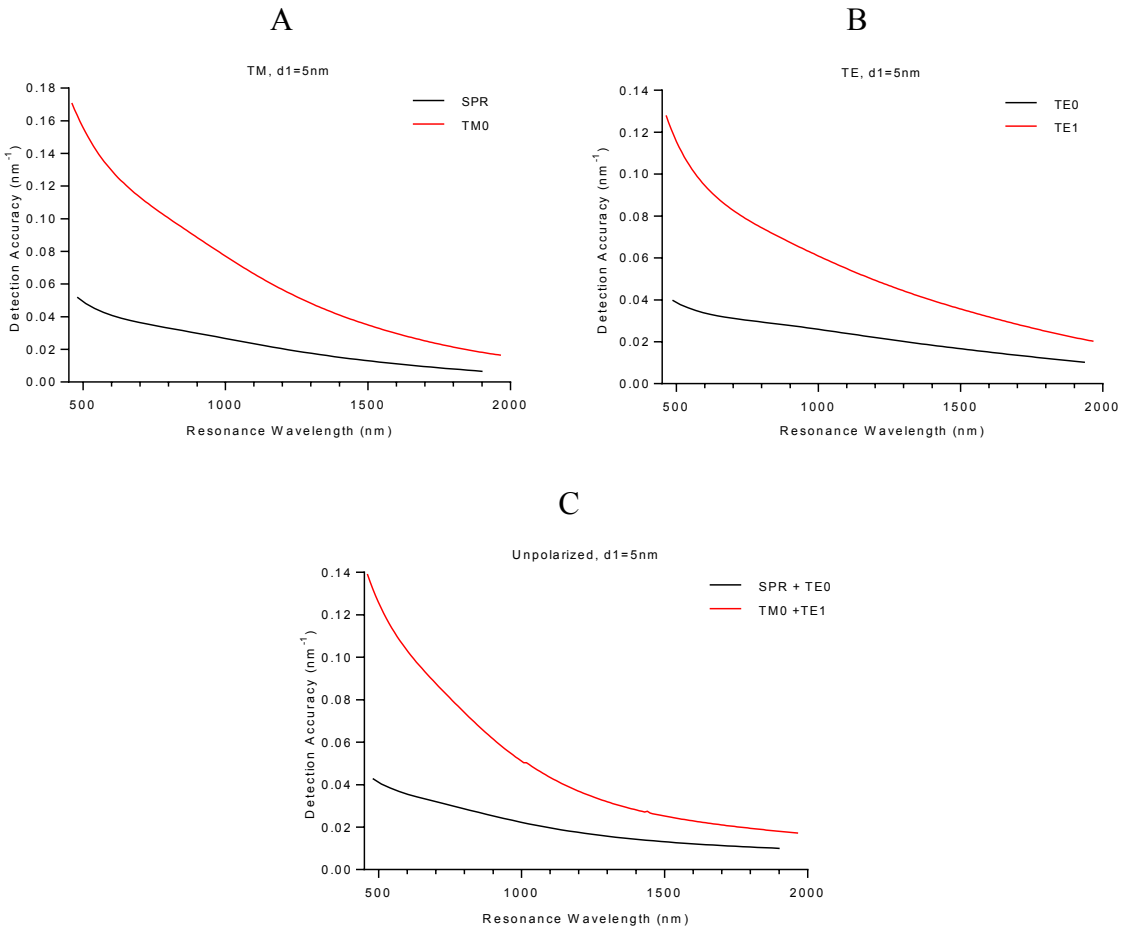

Figure 5-24 – (A) Detection Accuracy (dip wavelength shift to 1% hydrogen) of the first two resonance modes that appear for several OF configurations with Ag(d1=5nm), Pd(d3=3nm), TM polarized light (λ=450:2000nm), where the resonance wavelength of each mode was modulated using the thickness of the modulation layer (Ta_2O_5). (B) TE polarized light. (C) unpolarized light.

Fig. 5-24 displays the data relating to the spectral width of each resonance condition in the presence of 4% H_2 gas. The detection accuracy of the waveguide resonance conditions is larger than the stimulated surface plasmons resonance condition.

5.3.12.3 Figure of Merit

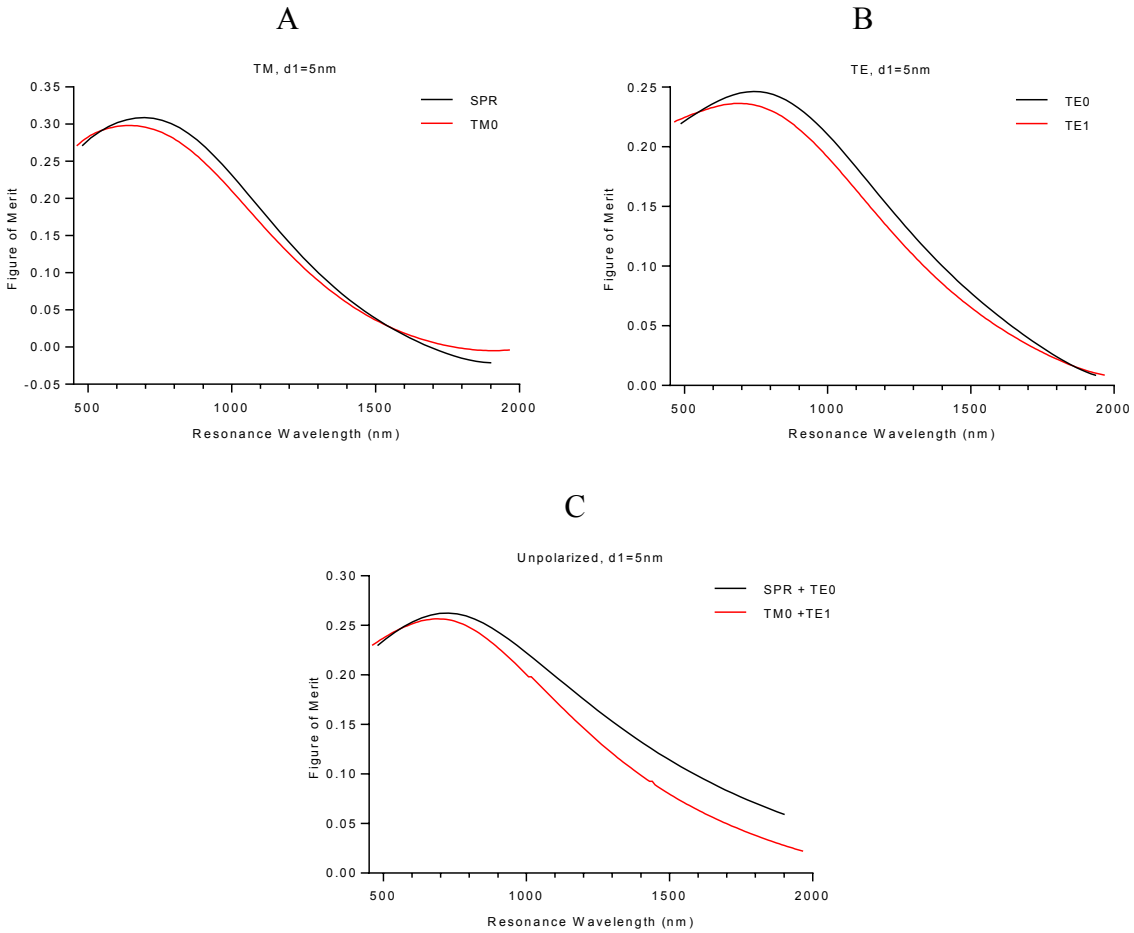

Figure 5-25 – (A) Figure of Merit (dip wavelength shift to 1% hydrogen) of the first two resonance modes that appear for several OF configurations with Ag(d1=5nm), Pd(d3=3nm), TM polarized light (λ=450:2000nm), where the resonance wavelength of each mode was modulated using the thickness of the modulation layer (Ta_2O_5). (B) TE polarized light. (C) unpolarized light.

Fig. 5-25 displays the figure of merit of each resonance mode. It can be seen that the figure of merit (metric by which sensor performance is measured) is larger for the combined (SPR + TE0) resonance condition, than the combination of the higher order resonance modes (TM0 + TE1). Nevertheless, the performance of the combined (TM0 + TE1) resonance modes is significantly higher than the previously determined optimal figure of merit. In addition to the significant improvement in performance, Fig. 5-25 demonstrates that it is possible to simultaneously measure gaseous concentration using unpolarized light, at two different resonance wavelengths, using a single channel sensor.

5.4 Conclusion

In conclusion, we have performed an investigation into the operation of a waveguide coupled surface plasmon resonance H_2 sensor. This device permits the stimulation of both surface plasmon and leaky mode resonance within the incident wavelength range (λ=450:2000nm). The methods of modelling the propagation of light along our structure are outlined in Chapter 1, and the theory section of this chapter. Our configuration consists of (SiO_2 fibre core, Ag metallic film, Ta_2O_5 modulation layer, Pd analyte layer). Ta_2O_5 was chosen as the modulation layer material as it facilitates the stimulation of leaky resonant modes using our multilayer dimensions within the observed wavelength range. Additionally, the associated real component of Ta_2O_5 refractive index is large, which permits the stimulation of guided modes at a lower cut-off thickness when compared to SiO_2 for example.

We investigated the influence that the modulation layer thickness has on performance using both SiO_2 and Ta_2O_5. Both structures yield surface plasmon resonance conditions, while the Ta_2O_5 structures also produces additional resonance modes. We determined the output power through a series of configurations at three fixed angles of incidence that make up the operational angular range of our fibre. This allowed us to study the behaviour of particular modes as the modulation layer thickness increased, and determine the approximate resonance angle corresponding to each mode. We also investigated the influence that the metallic layer thickness has on output power. In doing this, we discovered that a large metallic layer thickness yields independent spectrally separated resonance conditions. As the thickness of this metallic film decreases, the independent resonance conditions shift closer together, and a single resonance dip with increased depth is evident. Next, we determined the normalized output power through the fibre, using three different types of incident light; TM polarized, TE polarized, and unpolarized (TM+TE), for a range of metallic and modulation layer thicknesses. This allowed us to characterize each unpolarized resonance mode as originating from either TM or TE resonance contributions. Studying the individual oscillation modes led us to discover that the single unpolarized resonance condition, which is observed once a low metallic thickness was employed; is comprised of independent TM and TE resonance contributions.

We then determined the electric field throughout multilayer configuration. Using the shape of the electric field, we were able to characterize each resonance mode as being SPR, TE0, TM0, or TE1. We plotted the resonance wavelengths of the surface plasmon, and TE0 resonance modes stimulated using TM & TE polarized light respectively. We observed that

the resonance wavelength of the SPR and TE0 modes overlap within a very small metallic thickness range. The deepest resonance conditions in the unpolarized output power were also demonstrated within the same very small metallic thickness range.

We investigated the performance in terms of sensitivity, detection accuracy, and figure of merit of various devices using three incident sources of light, TM, TE, & unpolarized light. We demonstrated that, when using incident unpolarized light, the figure of merit is maximum in the configurations where the metallic thickness is within the aforementioned low thickness range. The highest observed figure of merit was determined using (d1=5nm) which corresponds to a (323.9%) improvement in the figure of merit compared to the highest figure of merit determined in this chapter using the previously determined, and widely referenced optimal thickness of (d1=50nm). The drastic improvement is attributed to the co-operation of the surface plasmon, and TE0 leaky resonance mode. To our knowledge, this is the first evidence of the stimulation of surface plasmon and waveguide mode resonance at the same resonance wavelength using a single OFSPR sensing structure.

Lastly, we compare the operation of the SPR, TE0, TM0, & TE1 resonance modes, using structures that permit co-operation between (SPR + TE0) and the (TM0 + TE1). We demonstrate that the figure of merit in the combined (SPR + TE0) resonance mode is larger than the (TM0 + TE1). We also demonstrate that it is possible to simultaneously measure gaseous concentration using unpolarized light, at two different resonance wavelengths, using a single channel sensor.

Conclusion

In conclusion, we have performed a theoretical investigation into the operation and optimization of multiple optical fibre surface plasmon resonance hydrogen sensing devices. We began by giving a brief introduction into the history of surface plasmon resonance, and highlighted several key publications relating to Pd, H_2 sensing, & optical fibre based sensing. We introduced the relevant theory relating to SPR. We defined the characteristic transfer matrix model which allowed us to determine the propagation of light through a multilayer structure, and extended this model to optical fibre based application. We investigated numerous materials related to OFSPR H_2 sensing. This involved determining suitable methods of modelling the spectrally dependent optical functions of each material. We investigated the Drude, Lorentz-Drude, and Brendel-Bormann models to determine the dielectric permittivity of metallic films. We modelled the reflectance of numerous Kretschmann based configurations in order to determine the influence that the metallic layer has on the surface plasmon resonance condition. We also investigated several dielectric materials to be included in our device, as well as methods of modelling their respective refractive indices. Using von Rottkay's experimental measurements, we generated a method of determining the influence that exposure of 4% H_2 has on the Pd film in our multilayer sensing structure. From this result, it became evident that the widely referenced change in Pd dielectric permittivity of 0.8h to 4% H_2 was incorrect. Finally we proceeded to validate our model by replicating a series of structures that have been published by other researchers. These included the Otto configuration, numerous Kretschmann configurations, and an OFSPR based H_2 sensor. The final sensing configuration we employed consisted of a multilayer stack (Ag/SiO_2/Pd) embedded onto an unclad section of a silica optical fibre core.

In Chapter 2, we acknowledged the fundamental problem associated with a purely Pd based H_2 sensing device that is the rapid degradation with use due to an α→β phase transition upon hydrogen loading. We discussed solutions taken by various other researchers including using other hydrogen sensitive materials, and alloys. We arrived at a solution of employing a PdY alloy (volume fraction Pd90%:Y10%) that operates with improved film durability, minimal reduction in sensitivity compared to other alloy materials, and improved H_2 permeability. Investigating the normalised output power through the fibre revealed a redshift of the SPR

condition upon H_2 exposure, which allowed us to determine the sensor sensitivity. The width of the resonance condition was used to determine the detection accuracy. We investigated the influence that metallic layer thickness Ag (d1), modulation layer thickness SiO_2 (d2), hydrogen sensitive layer thickness PdY (d3), Pd volume fraction in the PdY alloy, and numerical aperture have on sensor performance. Next, we continued investigations into the metallic and modulation layer thickness, and found that a trade-off between sensitivity and detection accuracy is required to optimise the figure of merit of the device. We observed FOM is largest for each of the investigated Ag thicknesses when paired with a specific SiO_2 thickness. This prompted us to carry our next series of investigations which involved determining sensor performance at specific SiO_2 thicknesses, when paired with all Ag thicknesses in the range (1:90nm). This allowed us to create a plot showing the specific Ag thickness yielded the highest FOM with each SiO_2. The optimal sensor demonstrated a figure of merit of (FOM=0.062740) and comprised of Ag thickness (d1=50.5nm) and SiO_2 thickness (d2=72nm). This sensor demonstrated a sensitivity of (Sn=17.64nm) to 4% hydrogen, a detection accuracy of (DA=0.014228nm^{-1}) and operated at a spectral centre of (λ=528.87nm). This has been the first OFSPR based on wavelength modulation that employs a durable PdY alloy. The durability of the device is significantly greater than that of a purely Pd based device, while still retaining the high performance. In Chapter 2, we observed some researchers that have employed sensing devices that incorporate nanocomposite films. This provoked us to conduct research in this area.

In Chapter 3, we compared the operation of an individual multilayer sensing structure (similar to that Chapter 2) to a nanocomposite based device. We began by introducing the history of nanocomposite structures, and discussing various Pd based nanocomposites that have been employed for hydrogen sensing applications. We chose to employ a NC structure consisting of Pd nanoparticles embedded in a SiO_2 dielectric matrix. We discussed methods of modelling the dielectric permittivity of a nanocomposite structure, and detailed limitations involving the upper limits of the nanoparticle volume fraction. We investigated the influence that metallic layer thicknesses ($d1_{IM}$ & $d1_{NC}$) the modulation layer thicknesses ($d2_{IM}$ & $d2_{NC}$) have on the performance of each device, where ($d1_{IM}$=$d1_{NC}$) and ($d2_{IM}$=$d2_{NC}$). We established that the surface plasmon resonance generated using the NC occurred at a longer wavelength than that of the IM device of equivalent multilayer thicknesses due to the higher refractive

index of the SiO_2:Pd NC layer when compared to a pure SiO_2 layer. We determined the performance of several IM & NC devices with varying metallic and modulation thicknesses. Both sensitivity and detection accuracy were found to be maximum in the visible part of the wavelength spectrum for the IM based devices. Correspondingly, the NC structures operated with high figure of merit in the near-IR part of the spectrum, and thus we conclude that the NC based configuration should be employed for H_2 sensing applications in this range. Finally, we investigated the influence that NC volume fraction has on sensor performance. We found that the figure of merit increases with increasing Pd volume fraction, however the magnitude of the increase is reduced at high volume fractions. Specifically, due to the increased penetration depth that accompanies sensing in the near-IR spectrum, NC based devices are ideal for applications that involve bulk sensing as opposed to surface sensing, such as non-invasive method of measuring dielectric permittivity changes in biological organisms. In Chapter 3, we observed that the individual multilayer based device permits is capable of H_2 in the visible and near-IR part of the wavelength spectrum. From this we considered that it may be possible to include additional sensing channels along our fibre, provided the resonance conditions stimulated in each channel are greatly separated in the spectral domain.

In Chapter 4 we extended our model by including an additional multilayer sensing channel, as multichannel sensing functionality greatly improves the safe use of hydrogen energy. We discussed various multichannel sensing devices that appear throughout the literature. This led us to employ an optical fibre based multichannel device that operates under the principle of wavelength division multiplexing, by careful choice of the modulation layers in each channel. By ensuring a difference in thickness of the modulation layer thickness in each channel, the stimulation of two independent H_2 surface plasmon resonance conditions was observed. We determined the influence that the thickness of each multilayer component has on the performance of both channels. This was achieved by first determining the normalized output power through the fibre, and then measuring the performance of each configuration in terms of sensitivity, detection accuracy, and figure of merit. We determined approximate optimal metallic thicknesses for both sensing channels. We observed that a minimum difference in the modulation layer thicknesses of channel (1 & 2) is necessary such that the independent resonance dips can be observed. We designed a specific type of dual channel sensor, where one channel is expected to operate with a fast sensor response time of (4s to 4% H_2), thus,

providing an early warning indication of H_2 leakage, and the other channel operates with (267%) improvement in sensitivity, with relatively short response time (<15s to 4% H_2). To finish, we made preliminary investigations into the operation of an N-channel sensor, where (N=3, 4, 6).

Finally, we investigated the operation of a unique waveguide coupled optical fibre surface plasmon resonance H_2 sensor. The motivation for this was brought about by the discovery of additional resonance modes generated in Chapter 3 under certain conditions. We began by introducing the concept of leaky mode resonance, and discussing several types of configurations that permit the stimulation of surface plasmon and waveguide resonance. We proposed a specific kind of sensor (Ag/Ta_2O_5/Pd) embedded on a silica fibre core. We investigated the influence that the modulation layer thickness has on performance using both SiO_2 and Ta_2O_5. While both structures yield surface plasmon resonance conditions, the Ta_2O_5 based structures also stimulates additional resonance modes. We determined the output power through a series of configurations at three fixed angles of incidence that make up the operational angular range of our fibre. This allowed us to study the behaviour of particular modes as the metallic and modulation layer thicknesses varied. Using incident unpolarized light, we discovered that a large metallic layer thickness yields independent spectrally separated resonance conditions, while a small thickness permits the stimulation of a single deep resonance condition. Next, we determined the normalized output power through the fibre, using three different types of incident light; TM polarized, TE polarized, and unpolarized (TM+TE), for a range of metallic and modulation layer thicknesses. This allowed us to characterize each unpolarized resonance mode as originating from either TM or TE resonance contributions. Additionally, these figures allowed us to conclude that the single oscillation modes observed once the metallic thickness was low, are comprised of TM & TE resonance conditions. We modelled the electric field through a series of multilayer structures. By studying the field lineshape, we were able to characterize each resonance mode further as originating from the stimulation of SP, of leaky resonance modes. We plotted the resonance wavelengths of the surface plasmon, and TE0 resonance modes stimulated using TM & TE polarized light respectively, and observed that the resonance wavelength of the SPR and TE0 modes overlap within a very small metallic thickness range. In addition the deepest resonance conditions in the unpolarized output power were also demonstrated within the same very small metallic thickness range. We investigated the performance of various devices using

three incident sources of light, TM, TE, & unpolarized light. We demonstrated that, when using incident unpolarized light, the figure of merit is maximum in the configurations where the metallic thickness is within the aforementioned low thickness range. The highest observed figure of merit was determined using (d1=5nm) which corresponds to a (323.9%) improvement in the figure of merit compared to the highest figure of merit determined in this chapter using the previously determined, and widely referenced optimal thickness of (d1=50nm). The drastic improvement is attributed to the co-operation of the surface plasmon, and TE0 leaky resonance mode. To our knowledge, this is the first evidence of the stimulation of surface plasmon and waveguide mode resonance at the same resonance wavelength using a single OFSPR sensing structure. We also compared the operation of multiple resonance modes for H_2 sensing. Using a metallic thickness (d1=5nm) that permits the co-operation between (SPR + TE0) and the (TM0 + TE1), we show that the figure of merit in the combined (SPR + TE0) resonance mode is larger than the (TM0 + TE1). We also demonstrate that it is possible to simultaneously measure gaseous concentration using unpolarized light, at two different resonance wavelengths, using a single channel sensor.

Appendix A: Sample MATLAB Code

```
%-------------------------------------------------------------------------
% Main Model
%-------------------------------------------------------------------------
clear all
close all
ck = clock;
ck(4);
ck(5);
Start = [ck(4),ck(5)];
tic
format long
%-------------------------------------------------------------------------
changing_parameter_index = 1;
for changing_parameter = [1]; % [1,2,3]
d1_thickness_array = [50];
d2_thickness_array = [180];
d3_thickness_array = [3];
Y_fraction_array = [0.0];
NA_array = [0.22];
fD_array = [200e-6];
fL_array = [1e-2];
N=5;
fI_in = 1;
Num_Int_Points=106;
lambda_lower = 450;
lambda_upper = 2000;
lambda_step = 1;
    fL_index = 1;
for fL = fL_array;
    fD_index = 1;
for fD = fD_array
    NA_index = 1;
for NA = NA_array;
    Ag_thickness_index = 1;
for d1_thickness = d1_thickness_array*1e-9;     %(changing_parameter_index)
    Si_thickness_index = 1;
for d2_thickness = d2_thickness_array*1e-9;     %(changing_parameter_index)
    Pd_thickness_index = 1;
for d3_thickness = d3_thickness_array*1e-9;     %(changing_parameter_index)
    lambda_index=1;
for lambda = [lambda_lower:lambda_step:lambda_upper]*1e-9;
fA = pi*(fD/2)^2;
[n_SiO2_M_1965] = f_SiO2_M_1965(lambda);
n_core = n_SiO2_M_1965;
n_cladding =  sqrt(n_core^2 - NA^2);
theta_c = asind(n_cladding/n_core);
[abscissas, weights] = f_Gauss(Num_Int_Points);
abscissas=abscissas';
weights=weights';
Theta_Lower=theta_c;
Theta_Upper=90;
theta_array=((Theta_Upper-
Theta_Lower)/2)*abscissas+(Theta_Lower+Theta_Upper)/2;
[h1,h2] = f_hFunctions(lambda);
% Metals-----------------------------------------------------------------
[eps_BB_Pd] = f_BB_Pd(lambda);
eps_BB_PdH = h1*real(eps_BB_Pd)+h2*i*imag(eps_BB_Pd);
Pd = eps_BB_Pd;
```

```
PdH = eps_BB_PdH;
for Pd_permittivity = [Pd,PdH];
[eps_BB_Ag] = f_BB_Ag(lambda);
% Dielectrics-----------------------------------------------------------
[n_Si02_PY_2001] = f_Si02_PY_2001(lambda);
[eps_Ta2O5_Bright] = f_Ta2O5_Bright(lambda);
n_Ta2O5 = sqrt(eps_Ta2O5_Bright);
% Model-----------------------------------------------------------------
n(1) = n_core;
n(2) = sqrt(eps_BB_Ag);
n(3) = n_Ta2O5;
n(4) = sqrt(Pd_permittivity);
n(N) = 1+0i;
d(1) = 0;
d(2) = d1_thickness;
d(3) = d2_thickness;
d(4) = d3_thickness;
d(N) = 0;
for per = 1:N;
    EE(per)=real(n(per))^2-imag(n(per))^2 +i*(2*real(n(per))*imag(n(per)));
end
for ind_theta=1:Num_Int_Points;
    Ms=[1+0i 0+0i
      0+0i 1+0i];
    Mp=[1+0i 0+0i
      0+0i 1+0i];
theta_rad = theta_array(ind_theta).*pi/180;
for layer=2:N-1;
    beta_s = (2*pi/lambda)*d(layer)*sqrt(EE(layer)-
(n(1)^2*sin(theta_rad).^2));
    qs = sqrt(EE(layer)-(n(1)^2*sin(theta_rad).^2));
    beta_p = (2*pi/lambda)*d(layer)*sqrt(EE(layer)-
(n(1)^2*sin(theta_rad).^2));
    qp = sqrt(EE(layer)-(n(1)^2*sin(theta_rad).^2))/EE(layer);
m11s = cos(beta_s);
m12s = (-i/qs)*sin(beta_s);
m21s = (-i*qs)*sin(beta_s);
m22s = cos(beta_s);
Ms = Ms*[m11s m12s
          m21s m22s];
m11p = cos(beta_p);
m12p = (-i/qp).*sin(beta_p);
m21p = (-i*qp).*sin(beta_p);
m22p = cos(beta_p);
Mp = Mp*[m11p m12p
          m21p m22p];
end;
q1s=sqrt(EE(1)-(n(1)^2*sin(theta_rad)^2));
qNs=sqrt(EE(N)-(n(1)^2*sin(theta_rad)^2));
as = q1s*(Ms(1,1)+Ms(1,2)*qNs)-(Ms(2,1)+(Ms(2,2)*qNs));
bs = q1s*(Ms(1,1)+Ms(1,2)*qNs)+(Ms(2,1)+(Ms(2,2)*qNs));
rs=as/bs;
q1p=sqrt(EE(1)-(n(1)^2*sin(theta_rad).^2))/EE(1);
qNp=sqrt(EE(N)-(n(1)^2*sin(theta_rad).^2))/EE(N);
ap = q1p*(Mp(1,1)+Mp(1,2)*qNp)-(Mp(2,1)+(Mp(2,2)*qNp));
bp = q1p*(Mp(1,1)+Mp(1,2)*qNp)+(Mp(2,1)+(Mp(2,2)*qNp));
rp=ap/bp;
Nref = fL/(fD*tan(theta_rad));
Norm_Int=((Theta_Upper-Theta_Lower)/2)*sum(weights.*1);
% Calculation of Reflectance, for S & P vibrations-----------------------
if Pd_permittivity == Pd;
```

```
RS0(ind_theta) =(abs(rs))^2;
RP0(ind_theta) =(abs(rp))^2;
RSN_0(ind_theta)=power(rs*conj(rs),Nref);
RPN_0(ind_theta)=power(rp*conj(rp),Nref);
dP0(ind_theta) = (n_core^2)*(sin(theta_rad))*(cos(theta_rad))/((1-
((n_core^2)*(cos(theta_rad)^2)))^2);
end;
if Pd_permittivity == PdH;
RSh(ind_theta) =(abs(rs))^2;
RPh(ind_theta) =(abs(rp))^2;
RSN_h(ind_theta)=power(rs*conj(rs),Nref);
RPN_h(ind_theta)=power(rp*conj(rp),Nref);
dPh(ind_theta) = (n_core^2)*(sin(theta_rad))*(cos(theta_rad))/((1-
((n_core^2)*(cos(theta_rad)^2)))^2);
end
end                                                    % theta loop
% Calculation of Reflectance for S & P vibrations-------------------------
if Pd_permittivity == Pd;
Term_A0 = (RPN_0 + RSN_0).*dP0;
norP0_Term_A(lambda_index) = ((Theta_Upper-
Theta_Lower)/2)*sum(weights.*Term_A0);
Term_B0 = dP0;
norP0_Term_B(lambda_index) = ((Theta_Upper-
Theta_Lower)/2)*sum(weights.*Term_B0);
% Extra s- & p- light-----------------------------------------------------
Term_A0s = (RSN_0).*dP0;
Term_A0p = (RPN_0).*dP0;
norP0_Term_As(lambda_index) = ((Theta_Upper-
Theta_Lower)/2)*sum(weights.*Term_A0s);
norP0_Term_Ap(lambda_index) = ((Theta_Upper-
Theta_Lower)/2)*sum(weights.*Term_A0p);
end
%-------------------------------------------------------------------------
if Pd_permittivity == PdH;
Term_Ah = (RPN_h + RSN_h).*dPh;
norPh_Term_A(lambda_index) = ((Theta_Upper-
Theta_Lower)/2)*sum(weights.*Term_Ah);
Term_Bh = dPh;
norPh_Term_B(lambda_index) = ((Theta_Upper-
Theta_Lower)/2)*sum(weights.*Term_Bh);
% Extra - Mono s- and p- light--------------------------------------------
Term_Ahs = (RSN_h).*dPh;
Term_Ahp = (RPN_h).*dPh;
norPh_Term_As(lambda_index) = ((Theta_Upper-
Theta_Lower)/2)*sum(weights.*Term_Ahs);
norPh_Term_Ap(lambda_index) = ((Theta_Upper-
Theta_Lower)/2)*sum(weights.*Term_Ahp);
end
%-------------------------------------------------------------------------
end                                                    % Pd permittivity
loop
lambda_array(lambda_index) = lambda;
lambda_index=lambda_index+1;
end
P0 = 0.5*(norP0_Term_A./norP0_Term_B);
PH = 0.5*(norPh_Term_A./norPh_Term_B);
P0s = (norP0_Term_As./norP0_Term_B);
PHs = (norPh_Term_As./norPh_Term_B);
P0p = (norP0_Term_Ap./norP0_Term_B);
PHp = (norPh_Term_Ap./norPh_Term_B);
% Measuring Sensor Performance-------------------------------------------
```

```
[P0_max_position,P_lambda_max_0,P0_min_position,P_lambda_min_0,P10_0,P_a_le
ft_0,P_left_0x,P_left_0,P_left_position_0,P_lambda_left_0,P_a_right_0,P_rig
ht_0x,P_right_0,P_right_position_0,P_lambda_right_0,P_delta_lambda_sw_0] =
f_S0_P(P0,lambda_array);
[PH_max_position,P_lambda_max_H,PH_min_position,P_lambda_min_H,P1H_H,P_a_le
ft_H,P_left_Hx,P_left_H,P_left_position_H,P_lambda_left_H,P_a_right_H,P_rig
ht_Hx,P_right_H,P_right_position_H,P_lambda_right_H,P_delta_lambda_sw_H] =
f_SH_P(PH,lambda_array);
P_d_lambda_res_nm(changing_parameter_index) = (P_lambda_min_H -
P_lambda_min_0)*1e9;
P_delta_lambdaH_10(changing_parameter_index) = P_delta_lambda_sw_H*1e9;
P_lambda_min0(changing_parameter_index) = P_lambda_min_0*1e9;
P_min(changing_parameter_index) = min(P0);
P_lambda_minH(changing_parameter_index) = P_lambda_min_H*1e9;
P_minH(changing_parameter_index) = min(PH);
P_left_Ha(changing_parameter_index) = P_left_H;
P_right_Ha(changing_parameter_index) = P_right_H;
P_left_index = find(P_left_H == PH);
P_right_index = find(P_right_H == PH);
P_lambda_leftH(changing_parameter_index) = lambda_array(P_left_index)*1e9;
P_lambda_rightH(changing_parameter_index) =
lambda_array(P_right_index)*1e9;
P0_Ag_array(:,changing_parameter_index) = P0;
PH_Ag_array(:,changing_parameter_index) = PH;
d_lambda_res = P_lambda_minH - P_lambda_min0;
d_lambdaH_10 = P_lambda_rightH - P_lambda_leftH;
Sn = d_lambda_res./4;
DA = 1./d_lambdaH_10;
FOM = Sn./d_lambdaH_10;
% Save ------------------------------------------------------------------------
% P0_Ag(:,Ag_thickness_index) = P0;
% PH_Ag(:,Ag_thickness_index) = PH;
% P0_Si(:,Si_thickness_index) = P0;
% PH_Si(:,Si_thickness_index) = PH;
% P0_Pd(:,Pd_thickness_index) = P0;
% PH_Pd(:,Pd_thickness_index) = PH;
Sn_Pd(changing_parameter_index) = Sn;
DA_Pd(changing_parameter_index) = DA;
FOM_Pd(changing_parameter_index) = FOM;
P0_cp(:,changing_parameter_index) = P0;
PH_cp(:,changing_parameter_index) = PH;
%-------------------------------------------------------------------------------
Pd_thickness_index = Pd_thickness_index+1;
end
Si_thickness_index = Si_thickness_index+1;
end
Ag_thickness_index = Ag_thickness_index+1;
end
NA_index = NA_index+1;
end
fD_index = fD_index+1;
end
fL_index = fL_index+1;
end
changing_parameter_index = changing_parameter_index+1;
end
% Plot-------------------------------------------------------------------------
p0s= plot(lambda_array*1e9,P0s,'b');
hold all
phs = plot(lambda_array*1e9,PHs,'b:');
hold all
```

```
p0p= plot(lambda_array*1e9,P0p,'r');
hold all
php = plot(lambda_array*1e9,PHp,'r:');
hold all
p0= plot(lambda_array*1e9,P0,'k');
hold all
ph = plot(lambda_array*1e9,PH,'k:');
hold all
title([     'd1=', num2str(d1_thickness_array),'nm, ',...
            'd2=', num2str(d2_thickness_array),'nm ',...
            'd3=', num2str(d3_thickness_array),'nm ']);
xlabel('Wavelength (nm)')
ylabel('Normalized Power')
xlim([450,2000])
ylim([0,1])
legend([p0 p0p p0s], 'Unpolarized','TM','TE');
set(legend,'Location','Southeast');
figureHandle = gcf;
set(findall(figureHandle,'type','text'),'fontSize',8,'fontWeight','normal')
set(gca,'fontsize',8)
toc


%-------------------------------------------------------------------------
% Measure Performance - Dual Channel
%-------------------------------------------------------------------------
clear all
close all
format long
ck = clock;
ck(4);
ck(5);
Start = [ck(4),ck(5)]
tic
% loop
index=1;
for changingparameter = [10:0.1:90]
Ag_thickness = [50,changingparameter]*1e-9;     % channel paremeters (1,2)
SiO2_thickness = [100,300]*1e-9;                % channel paremeters (1,2)
Pd_thickness = [3,3]*1e-9;                      % channel paremeters (1,2)
lambda_step = 1;
lambda_upper = 2000;                % Note: Run twice(left, right)
lambda_lower = 450;
lambda_upperexcel = lambda_upper;
lambda_lowerexcel = lambda_lower;
% Initial Approximation-----------------------------------------------------
[lambdamin0,lambdaminh,lambdaleft0,lambdaright0,lambdalefth,lambdarighth] =
f_Fn1_DC(lambda_upper,lambda_lower,lambda_step,Ag_thickness,SiO2_thickness,
Pd_thickness);
% Need 6 more functions to determine each value
lambda_step_acc = 0.005;                % acc stepsize
plus_or_minus_lambda_range=2;
lambdamin0approx(index)=lambdamin0;             % Fn2
lambdaminhapprox(index)=lambdaminh;             % Fn3
lambdaleft0approx(index)=lambdaleft0*1e9;       % Fn4
lambdaright0approx(index)=lambdaright0*1e9;     % Fn5
lambdalefthapprox(index)=lambdalefth*1e9;       % Fn6
lambdarighthapprox(index)=lambdarighth*1e9;     % Fn7
%Find lambdamin0acc-------------------------------------------------------
lambda_upper = lambdamin0approx(index)+plus_or_minus_lambda_range;
lambda_lower = lambdamin0approx(index)-plus_or_minus_lambda_range;
```

```
[lambdamin0acc,Pmin0acc] =
f_Fn2_DC_lambdamin0(lambda_upper,lambda_lower,lambda_step_acc,Ag_thickness,
SiO2_thickness,Pd_thickness);
%Find lambdaminhacc-------------------------------------------------------
lambda_upper = lambdaminhapprox(index)+plus_or_minus_lambda_range;
lambda_lower = lambdaminhapprox(index)-plus_or_minus_lambda_range;
[lambdaminhacc,Pminhacc] =
f_Fn3_DC_lambdaminh(lambda_upper,lambda_lower,lambda_step_acc,Ag_thickness,
SiO2_thickness,Pd_thickness);
%Find lambdaleft0acc------------------------------------------------------
lambda_upper = lambdaleft0approx(index)+plus_or_minus_lambda_range;
lambda_lower = lambdaleft0approx(index)-plus_or_minus_lambda_range;
P0110acc = Pmin0acc*1.1;
[lambdaleft0acc,Pleft0acc] =
f_Fn4_DC_lambdaleft0(lambda_upper,lambda_lower,lambda_step_acc,Ag_thickness
,SiO2_thickness,Pd_thickness,P0110acc);
%Find lambdaright0acc-----------------------------------------------------
lambda_upper = lambdaright0approx(index)+plus_or_minus_lambda_range;
lambda_lower = lambdaright0approx(index)-plus_or_minus_lambda_range;
[lambdaright0acc,Pright0acc] =
f_Fn5_DC_lambdaright0(lambda_upper,lambda_lower,lambda_step_acc,Ag_thicknes
s,SiO2_thickness,Pd_thickness,P0110acc);
%Find lambdalefthacc------------------------------------------------------
lambda_upper = lambdalefthapprox(index)+plus_or_minus_lambda_range;
lambda_lower = lambdalefthapprox(index)-plus_or_minus_lambda_range;
Ph110acc = Pminhacc*1.1;
[lambdalefthacc,Plefthacc] =
f_Fn6_DC_lambdalefth(lambda_upper,lambda_lower,lambda_step_acc,Ag_thickness
,SiO2_thickness,Pd_thickness,Ph110acc);
%Find lambdarighthacc-----------------------------------------------------
lambda_upper = lambdarighthapprox(index)+plus_or_minus_lambda_range;
lambda_lower = lambdarighthapprox(index)-plus_or_minus_lambda_range;
[lambdarighthacc,Prighthacc] =
f_Fn7_DC_lambdarighth(lambda_upper,lambda_lower,lambda_step_acc,Ag_thicknes
s,SiO2_thickness,Pd_thickness,Ph110acc);
% Save--------------------------------------------------------------------
lambdamin0acci(index)=lambdamin0acc;
Pmin0acci(index)=Pmin0acc;
lambdaminhacci(index)=lambdaminhacc;
Pminhacci(index)=Pminhacc;
lambdaleft0acci(index)=lambdaleft0acc;
Pleft0acci(index)=Pleft0acc;
lambdaright0acci(index)=lambdaright0acc;
Pright0acci(index)=Pright0acc;
lambdalefthacci(index)=lambdalefthacc;
Plefthacci(index)=Plefthacc;
lambdarighthacci(index)=lambdarighthacc;
Prighthacci(index)=Prighthacc;
widthhi(index) = lambdarighthacci(index)-lambdalefthacci(index);
width0i(index) = lambdaright0acci(index)-lambdaleft0acci(index);
dlambdaresi(index) = lambdaminhacci(index)-lambdamin0acci(index);
Sni(index) = dlambdaresi(index)./4;
DAhi(index) = 1./widthhi(index);
FOMi(index) = Sni(index).*DAhi(index);
Ag_thickness1i(index)= Ag_thickness(1)*1e9;
Ag_thickness2i(index)= Ag_thickness(2)*1e9;
SiO2_thickness1i(index)= SiO2_thickness(1)*1e9;
SiO2_thickness2i(index)= SiO2_thickness(2)*1e9;
Pd_thickness1i(index)= Pd_thickness(1)*1e9;
Pd_thickness2i(index)= Pd_thickness(2)*1e9;
toc
```

```
index=index+1;
end
% Plot-----------------------------------------------------------------
ExcelFileName = ['Multilayer Raw Data7'];
ExcelSheet = ['d1ch2 right'];
xlswrite(ExcelFileName,Ag_thickness1i',ExcelSheet,'A3');
xlswrite(ExcelFileName,Ag_thickness2i',ExcelSheet,'B3');
xlswrite(ExcelFileName,SiO2_thickness1i',ExcelSheet,'C3');
xlswrite(ExcelFileName,SiO2_thickness2i',ExcelSheet,'D3');
xlswrite(ExcelFileName,Pd_thickness1i',ExcelSheet,'E3');
xlswrite(ExcelFileName,Pd_thickness2i',ExcelSheet,'F3');
xlswrite(ExcelFileName,Sni',ExcelSheet,'G3');
xlswrite(ExcelFileName,DAhi',ExcelSheet,'H3');
xlswrite(ExcelFileName,FOMi',ExcelSheet,'I3');
xlswrite(ExcelFileName,lambdamin0acci',ExcelSheet,'J3');
xlswrite(ExcelFileName,lambdaminhacci',ExcelSheet,'K3');
xlswrite(ExcelFileName,lambdaleft0acci',ExcelSheet,'L3');
xlswrite(ExcelFileName,lambdaright0acci',ExcelSheet,'M3');
xlswrite(ExcelFileName,lambdalefthacci',ExcelSheet,'N3');
xlswrite(ExcelFileName,lambdarighthacci',ExcelSheet,'O3');
xlswrite(ExcelFileName,lambda_lowerexcel',ExcelSheet,'P3');
xlswrite(ExcelFileName,lambda_upperexcel',ExcelSheet,'Q3')
xlswrite(ExcelFileName,Pmin0acci',ExcelSheet,'R3');
xlswrite(ExcelFileName,Pleft0acci',ExcelSheet,'S3');
xlswrite(ExcelFileName,Pright0acci',ExcelSheet,'T3');
xlswrite(ExcelFileName,Pminhacci',ExcelSheet,'U3');
xlswrite(ExcelFileName,Plefthacci',ExcelSheet,'V3');
xlswrite(ExcelFileName,Prighthacci',ExcelSheet,'W3');
toc

%-------------------------------------------------------------------------
% Optical Properties of Materials
%-------------------------------------------------------------------------
% Malitson 1965----------------------------------------------------------
function[n_SiO2_M_1965] = f_SiO2_M_1965(lambda)
N=3;
wavelength = lambda*1e6; % lambda in um
a(1) = 0.6961663;
a(2) = 0.4079426;
a(N) = 0.8974794;
b(1) = 0.0684043;
b(2) = 0.1162414;
b(N) = 9.896161;
for coeff = 1:N;
    x(coeff) = a(coeff)*wavelength^2/(wavelength^2-(b(coeff))^2);
end
n_SiO2_M_1965 = (1+x(1)+x(2)+x(3))^.5;

% Postava & Yamaguchi 2001-----------------------------------------------
function[n_SiO2_PY_2001] = f_SiO2_PY_2001(lambda)
wavelength = lambda*1e6;
a = 1.1336;
b = 9.261*1e-2;
x = a*(wavelength^2);
y = (wavelength^2)-(b^2);
n_SiO2_PY_2001 = sqrt(1+x/y);

% Ghatak and Thyagarajan 1998--------------------------------------------
function[n_SiO2_GT_1998] = f_SiO2_GT_1998(lambda)
N_SD_SiO2=3;
a(1) = 0.6961663;
```

```
a(2) = 0.4079426;
a(N_SD_SiO2) = 0.8974794;
b(1) =  0.004679148;
b(2) = 0.01351206;
b(N_SD_SiO2) = 97.93400;
for coeff = 1:N_SD_SiO2;
    x(coeff) = a(coeff)*(lambda*1e6)^2/((lambda*1e6)^2-b(coeff));
end
n_SiO2_GT_1998 = (1+x(1)+x(2)+x(3))^.5;

% Paek 1981----------------------------------------------------------------
function[n_SiO2_Paek_1981] = f_SiO2_Paek_1981(lambda)
wavelength = lambda*1e6;
c0 = 1.4508554;
c1 = -0.0031268;
c2 = -0.0000381;
c3 = 0.0030270;
c4 = -0.0000779;
c5 = 0.0000018;
L = 0.035;
t0 = c0;
t1 = c1*(wavelength^2);
t2 = c2*(wavelength^4);
t3 = c3/(wavelength^2-L);
t4 = c4/(wavelength^2-L)^2;
t5 = c5/(wavelength^2-L)^3;
n_SiO2_Paek_1981 = t0+t1+t2+t3+t4+t5;

% Perrotton 2011-----------------------------------------------------------
function[n_SiO2_Schott_2011] = f_SiO2_Schott_2011(lambda)
Wavelength=lambda*1e6
P(1)=1.45179;
P(2)=-0.00365;
P(3)=-0.00243;
P(4)=0.00012;
P(5)=-4.605e-6;
P(6)=9.635e-8;
n_SiO2_Schott_2011=P(1)+P(2)*Wavelength^2+P(3)*Wavelength^(-
2)+P(4)*Wavelength^(-4)+P(5)*Wavelength^(-6)+P(6)*Wavelength^(-8);

% Ishigure 1996------------------------------------------------------------
function[n_PMMA_Ishigure] = f_POF_PMMA_Ishigure(lambda)
N=3;
wavelength = lambda;
A(1) = 0.4663;
A(2) = 0.6965;
A(N) = 0.3223;
l(1) = 71.80*1e-9;
l(2) = 117.4*1e-9;
l(N) = 9237*1e-9;
for coeff = 1:N;
    x(coeff) = A(coeff)*wavelength^2/(wavelength^2-(l(coeff))^2);
end
n_PMMA_Ishigure = (1+x(1)+x(2)+x(3))^.5;

% Languy 2011--------------------------------------------------------------
function[n_PMMA2_Languy] = f_POF_PMMA2_Languy(lambda)
N=3;
wavelength = lambda*1e6;
B(1) = 4.841120*1e-1;
B(2) = 6.815579*1e-1;
```

```
B(N) = 1.028035*1e-2;
C(1) = 3.353637*1e-4;
C(2) = 1.096254*1e-2;
C(N) = 1.184708*1e-2;
for coeff = 1:N;
    x(coeff) = B(coeff)*wavelength^2/(wavelength^2-(C(coeff)));
end
n_PMMA2_Languy = (1+x(1)+x(2)+x(3))^.5;

% Dodge 1984----------------------------------------------------------------
function[n_SD_MgF2] = f_MgF2(lambda)
N=3;
wavelength = lambda*1e6;
a(1) = 0.48755108;
a(2) = 0.39875031;
a(N) = 2.3120353;
b(1) = 0.04338408;
b(2) = 0.09461442;
b(N) = 23.793604;
for coeff = 1:N;
    x(coeff) = a(coeff)*wavelength^2/(wavelength^2-(b(coeff))^2);
end
n_SD_MgF2 = (1+x(1)+x(2)+x(3))^.5;

% Bright 2013---------------------------------------------------------------
function[eps_Ta2O5_Bright] = f_Ta2O5_Bright(lambda)
lambda_cm = lambda*1e2;
lambda_um = lambda*1e6;
A = 2.06;
B = 0.025;
e_inf = (A + B/(lambda_um)^2)^2;
w_p0 = 6490;                          % in cm^-1
gamma_0 = 6.5e5;
w_test = [1/lambda_cm];
t2 = w_p0^2/(w_test^2-i*gamma_0*w_test);
w_j_array = [266, 500, 609, 672, 868, 3020];
w_pj_array = [1040, 573, 634, 408, 277, 373];
gamma_j_array = [188, 112, 88, 43, 113, 652];
final_j = 6;
for j = 1:final_j;
t3(j) = w_pj_array(j)^2 / (w_j_array(j)^2 - w_test^2 -
i*gamma_j_array(j)*w_test);
end
tt3 = t3(1)+t3(2)+t3(3)+t3(4)+t3(5)+t3(6);
eps_Ta2O5_Bright = e_inf - t2 + tt3;

% Sarika 2010---------------------------------------------------------------
function[n_Sarika_WO3] = f_Sarika_WO3(lambda)
lambda=lambda*1e6;     % um
n_Sarika_WO3 =  -107880*lambda^8 + 490800*lambda^7 - 965999*lambda^6 + ...
                1073738*lambda^5 -736739*lambda^4 + 319290*lambda^3 - ...
                85260*lambda^2 + 12804*lambda + -823;

% Bond 1965-----------------------------------------------------------------
function [n_ZnO_Bond] = f_ZnO_Bond(lambda)
lambda_um = lambda*1e6;
n_ZnO_Bond = (2.81418 + ((0.87968*lambda_um^2)/(lambda_um^2-0.3042^2)) -
(0.00711*lambda_um^2))^0.5;
```

```
% Sarika 2010 ------------------------------------------------------------
function[eps_DM_Sarika_ITO] = f_DM_Sarika_ITO(lambda)
lp_ITO = 5.6497e-7;
lc_ITO = 11.21076e-6;
eps_DM_Sarika_ITO =3.8-((lambda^2)/((lp_ITO^2)*(1+(i*lambda/lc_ITO))));

% DeVore 1951-------------------------------------------------------------
function[n_DeVore_TiO2] = f_DeVore_TiO2(lambda)
lambda=lambda*1e6;
n_DeVore_TiO2 = (5.913+(0.2441/(lambda^2-0.0843)))^0.5;

% Drude Model - Sharma 2008-----------------------------------------------
function[eps_DM_Ag] = f_DM_Ag(lambda)
Lambda_p=1.4541e-7;
Lambda_c=1.7614e-5;
c=2.99792458e8;
eps_DM_Ag=1-(lambda^2/(Lambda_p^2*(1+i*lambda/Lambda_c)));

% Lorentz Drude Model - Quinten 2001--------------------------------------
function[eps_LD_Y] = f_Y(lambda);
Xm = 1;
Sib = 9.63;
Wib = 2.9e15;
c = 3e8;
w = 2*pi*c/lambda;
Gammaib = 3e15;
wp = 5.2e15;
Gammafe = 1.5e14;
eps_LD_Y = 1+ Xm + Sib*Wib^2/((Wib^2) - (w^2) - i*w*Gammaib) - wp^2/(w^2 +
i*w*Gammafe);

% Brendel-Bormann 1992, Rakic 1992, Mathworks: Meierbachtol---------------
function[eps_BB_Pd] = f_BB_Pd(lambda)
lmin = 1e-7;
lmax = 1e-5;
dl = 5e-8;
N_BB = 1000;
l_input = lambda;
c = 2.997e8;
h = 6.626e-34;
hbar = h/(2*pi);
q = 1.602e-19;
i = complex(0,1);
wpmat = [9.01 9.03 10.83 14.98 18.51 10.75 15.92 9.72 9.59 7.29 13.22];
f0mat = [0.821 0.770 0.562 0.526 0.081 0.154 0.083 0.330 0.333 0.126
0.197];
GAMMA0mat = [0.049 0.050 0.030 0.047 0.035 0.048 0.022 9e-3 0.080 0.067
0.057];
mj = 8; %Choice of metal
if (mj == 1 || mj == 2)
    fmat = [0.05 0.133 0.051 0.467 4;0.054 0.05 0.312 0.719
1.648;zeros(9,5)];
    GAMMAmat = [0.189 0.067 0.019 0.117 0.052;0.074 0.035 0.083 0.125
0.179;zeros(9,5)];
    wmat = [2.025 5.185 4.343 9.809 18.56;0.218 2.885 4.069 6.137
27.97;zeros(9,5)];
    sigmamat = [1.894 0.665 0.189 1.17 0.516;0.742 0.349 0.83 1.246
1.795;zeros(9,5)];

else
```

```
    fmat = [zeros(1,4);zeros(1,4);0.076 0.081 0.324 0.726;0.213 0.06 0.182
0.014;...
          0.066 0.067 0.346 0.311;0.338 0.261 0.817 0.105;0.357 0.039 0.127
0.654;...
          0.769 0.093 0.309 0.409;0.186 0.665 0.551 2.214;0.427 0.218 0.513
2e-4;...
          6e-3 0.022 0.136 2.648];
    GAMMAmat = [zeros(1,4);zeros(1,4);0.056 0.047 0.113 0.172;0.312 0.315
1.587 0.172;...
              2.956 3.962 2.398 3.904;4.256 3.957 2.218 6.983;2.82 0.12
1.822 6.637;...
              2.343 0.497 2.022 0.119;0.498 1.851 2.604 2.891;1.877 0.1
0.615 4.109;...
              3.689 0.277 1.433 4.555];
    wmat = [zeros(1,4);zeros(1,4);0.416 2.849 4.819 8.136;0.163 1.561 1.827
4.495;...
          0.131 0.469 2.827 4.318;0.281 0.584 1.919 6.997;0.317 1.059 4.583
8.825;...
          0.066 0.502 2.432 5.987;0.782 1.317 3.189 8.236;1.459 2.661 0.805
19.86;...
          0.481 0.985 1.962 5.442];
    sigmamat = [zeros(1,4);zeros(1,4);0.562 0.469 1.131 1.719;0.013 0.042
0.256 1.735;...
              0.277 3.167 1.446 0.893;0.115 0.252 0.225 4.903;0.606 1.454
0.379 0.510;...
              0.694 0.027 1.167 1.331;0.031 0.096 0.766 1.146;0.463 0.506
0.799 2.854;...
              3.754 0.059 0.273 1.912];
end
f0 = f0mat(mj);
GAMMA0 = (q/hbar)*GAMMA0mat(mj);
wp = (q/hbar)*wpmat(mj);
f = fmat(mj,:);
GAMMA = (q/hbar).*GAMMAmat(mj,:);
w = (q/hbar).*wmat(mj,:);
sigma = (q/hbar).*sigmamat(mj,:);
OMEGA_P = sqrt(f0)*wp;
lambda = l_input;
omega = 2*pi*c./lambda;
epsf = 1 - OMEGA_P^2./(omega.*(omega + i*GAMMA0));
    a = (omega^2 + i*omega.*GAMMA).^(0.5);
    zplus = (a+w)./(sqrt(2).*sigma);
    zminus = (a-w)./(sqrt(2).*sigma);
    epsb =
(i*sqrt(pi).*f.*wp^2./(2*sqrt(2).*a.*sigma)).*(cef(zplus,N_BB)+cef(zminus,N
_BB));
    eps_BB_Pd = epsf + sum(epsb);

% A. Weideman----------------------------------------------------------------
function w = cef(z,N);
M = 2*N;
M2 = 2*M;
k = [-M+1:1:M-1]';
L = sqrt(N/sqrt(2));
theta = k*pi/M;
t = L*tan(theta/2);
f = exp(-t.^2).*(L^2+t.^2);
f = [0; f];
a = real(fft(fftshift(f)))/M2;
a = flipud(a(2:N+1));
Z = (L+i*z)./(L-i*z);
```

```
p = polyval(a,Z);
w = 2*p./(L-i*z).^2+(1/sqrt(pi))./(L-i*z);

% Locate Performance Values-------------------------------------------------
function[P0_max_position,P_lambda_max_0,P0_min_position,P_lambda_min_0,P10_
0,P_a_left_0,P_left_0x,P_left_0,P_left_position_0,P_lambda_left_0,P_a_right
_0,P_right_0x,P_right_0,P_right_position_0,P_lambda_right_0,P_delta_lambda_
sw_0] = f_S0_P(P0,lambda_array)
P0_max_position = find(P0==max(P0));
P_lambda_max_0 = lambda_array(P0_max_position);
P0_min_position = find(P0==min(P0));
P_lambda_min_0 = lambda_array(P0_min_position);
P10_0 = 1.1*min(P0);
for n = 1:P0_min_position
P_a_left_0(n) = P0(n);
end
[left index] = min(abs(P_a_left_0-P10_0));
P_left_0x = P_a_left_0(index);
P_left_position_0 = find(P_left_0x==P0);
P_left_0 = P0(P_left_position_0);
P_lambda_left_0 = lambda_array(P_left_position_0);
for n = P0_min_position:size(P0')
P_a_right_0(n) = P0(n);
end
[right index] = min(abs(P_a_right_0-P10_0));
P_right_0x = P_a_right_0(index);
P_right_position_0 = find(P_right_0x==P0);
P_right_0 = P0(P_right_position_0);
P_lambda_right_0= lambda_array(P_right_position_0);
P_delta_lambda_sw_0 = abs(P_lambda_right_0-P_lambda_left_0);

% Locate Performance Values v2----------------------------------------------
function[Pleft0,lambdaleft0,Pright0,lambdaright0,P0_max_position,P_lambda_m
ax_0,P0_min_position,P10_0,P_a_left_0,P_a_right_0] =
f_S0_New(P0,lambda_array)
P0_max_position = find(P0==max(P0));
P_lambda_max_0 = lambda_array(P0_max_position);
P0_min_position = find(P0==min(P0));
P_lambda_min_0 = lambda_array(P0_min_position);
P10_0 = 1.1*min(P0);
for n = 1:P0_min_position
P_a_left_0(n) = P0(n);
end
xx=n;
while P_a_left_0(xx)< P10_0
xx=xx-1;
Pleft = P_a_left_0(xx);
end
P_left_pos0 = find(Pleft==P0);
Pleft0 = P0(P_left_pos0);
lambdaleft0 = lambda_array(P_left_pos0
for n = P0_min_position:size(P0')
P_a_right_0(n) = P0(n);
end
aa=1;
while P_a_right_0(aa)< P10_0
aa=aa+1;
Pright = P_a_right_0(aa);
end
P_right_pos0 = find(Pright==P0);
Pright0 = P0(P_right_pos0);
```

```
lambdaright0 = lambda_array(P_right_pos0);

% Von Winckel-----------------------------------------------------------
function [x, w] = f_Gauss(n)
x = zeros(n,1);
w = x;
m = (n+1)/2;
for ii=1:m
    z = cos(pi*(ii-.25)/(n+.5));
    z1 = z+1;
while abs(z-z1)>eps
    p1 = 1;
    p2 = 0;
    for jj = 1:n
        p3 = p2;
        p2 = p1;
        p1 = ((2*jj-1)*z*p2-(jj-1)*p3)/jj;
    end
    pp = n*(z*p1-p2)/(z^2-1);
    z1 = z;
    z = z1-p1/pp;
end
    x(ii) = -z;
    x(n+1-ii) = z;
    w(ii) = 2/((1-z^2)*(pp^2));
    w(n+1-ii) = w(ii);
end

% Von Rottkay 1999------------------------------------------------------
function[h1,h2] = f_hFunctions(lambda)
lambda=lambda*1e9;
h1 = -4.678001583506010000000E-20*lambda^6 + 2.839032635764880000000E-
16*lambda^5 - 4.546618238505270000000E-13*lambda^4 -
4.351217028655810000000E-10*lambda^3 + 1.695113721892930000000E-06*lambda^2 -
7.732597951855180000000E-04*lambda + 0.416809043117607000000;
h2 = -7.466499492696110000000E-19*lambda^6 + 5.632545132351790000000E-
15*lambda^5 - 1.694782524035450000000E-11*lambda^4 +
2.557250012219920000000E-08*lambda^3 - 1.939946534238280000000E-05*lambda^2 +
6.192102885612940000000E-03*lambda + 0.279931576155566000000;

% Nanocomposite---------------------------------------------------------
del_array = [0.2];
del = del_array;
e_mod = n_SiO2_PY_2001^2;
e_Pd = Pd_permittivity;
e_eff = e_mod*((2*(1-del)*e_mod)+((1+2*del)*e_Pd))/(((2+del)*e_mod)+(1-
del)*e_Pd);
n(3) = sqrt(e_eff);

% 6 Channel Extension---------------------------------------------------
Ag_thickness = [50,50,50,50,50,50]*1e-9;
Pd_thickness = [3,3,3,3,3,3]*1e-9;
SiO2_thickness = [80,170,300,450,625,825]*1e-9;
ch_index = 1;
for channel_parameter = [1,2,3,4,5,6];
. . . . . .
d(2) = Ag_thickness(channel_parameter);
d(3) = SiO2_thickness(channel_parameter);
d(4) = Pd_thickness(channel_parameter);
. . . . . .
```

```
RSN_0ch(ch_index,:) = RSN_0;
RPN_0ch(ch_index,:) = RPN_0;
RSN_hch(ch_index,:) = RSN_h;
RPN_hch(ch_index,:) = RPN_h;
ch_index = ch_index+1;
end
. . . . . .
TA_0ch =
(RSN_0ch(1,:).*RSN_0ch(2,:).*RSN_0ch(3,:).*RSN_0ch(4,:).*RSN_0ch(5,:).*RSN_
0ch(6,:)) +
(RPN_0ch(1,:).*RPN_0ch(2,:).*RPN_0ch(3,:).*RPN_0ch(4,:).*RPN_0ch(5,:).*RPN_
0ch(6,:));
Term_A0ch= TA_0ch.*dP0;
norP0_Term_Ach(lambda_index) = ((Theta_Upper-
Theta_Lower)/2)*sum(weights.*Term_A0ch);
norP0_Term_Bch(lambda_index) = ((Theta_Upper-
Theta_Lower)/2)*sum(weights.*dP0);
TA_hch =
(RSN_hch(1,:).*RSN_hch(2,:).*RSN_hch(3,:).*RSN_hch(4,:).*RSN_hch(5,:).*RSN_
hch(6,:)) +
(RPN_hch(1,:).*RPN_hch(2,:).*RPN_hch(3,:).*RPN_hch(4,:).*RPN_hch(5,:).*RPN_
hch(6,:));
Term_Ahch= TA_hch.*dPh;
norPh_Term_Ach(lambda_index) = ((Theta_Upper-
Theta_Lower)/2)*sum(weights.*Term_Ahch);
norPh_Term_Bch(lambda_index) = ((Theta_Upper-
Theta_Lower)/2)*sum(weights.*dPh);
```

Publications

Downes, F. and C.M. Taylor (2015). Optical Fibre Surface Plasmon Resonance Sensor Based on a Palladium-Yttrium Alloy, Procedia Engineering, doi:10.1016/j.proeng.2015.08.738, (Downes and Taylor 2015).

Downes, F. and C.M. Taylor (2016). Theoretical investigation into the optimized design of a durable OFSPR hydrogen sensor based on a PdY alloy, SPIE Digital Library, doi:10.1117/12.2227128, (Downes and Taylor 2016).

Downes, F. and C.M. Taylor (2017). Theoretical investigation into the optimisation of an optical fibre surface plasmon resonance hydrogen sensor based on a PdY alloy, Measurement Science and Technology, doi:10.1088/1361-6501/28/1/015104, (F. Downes and C. M. Taylor 2017).

Downes, F. and C.M. Taylor (2017). Optimized design of a nanocomposite Ta2O5 and Pd multilayer OFSPR H2 sensor: a theoretical analysis, SPIE Digital Library, doi:10.1117/12.2252038, (Fionn Downes and Cian M. Taylor 2017).

Presentations

Environ: Dublin (2014), Sligo (2015), Limerick (2016).

Eurosensors: Freiburg (2015).

AECOM: Sligo (2015).

SPIE Photonics Europe: Brussels (2016).

Postgraduate Research Event: Sligo (2017).

SPIE Photonics West: San Francisco (2017).

Photonics Ireland: Galway (2017).

Additional Information

Best Student Paper Presentation Award at the biennial SPIE Photonics Europe conference (2016).

Postgraduate Society Chairperson (2015 & 2016).

Postgraduate Society Personality of the Year Award (2016).

IT Sligo Postgraduate Representative with Quality & Qualifications Ireland (2015).

Student Representative with Higher Educational Authority (2017).

Postgraduate Representative on the IT Sligo Research & Innovation Committee (2016).

References

A., L.H. (1881) *Wiedem. Ann*, 11, 70.

Abbas, A., Linman, M.J. and Cheng, Q. (2011a) 'New trends in instrumental design for surface plasmon resonance-based biosensors', *Biosensors and Bioelectronics*, 26(5), 1815-1824, available: http://dx.doi.org/http://dx.doi.org/10.1016/j.bios.2010.09.030.

Abbas, A., Linman, M.J. and Cheng, Q. (2011b) 'Sensitivity comparison of surface plasmon resonance and plasmon-waveguide resonance biosensors', *Sensors and Actuators B: Chemical*, 156(1), 169-175, available: http://dx.doi.org/https://doi.org/10.1016/j.snb.2011.04.008.

Ahn, J.H., Seong, T.Y., Kim, W.M., Lee, T.S., Kim, I. and Lee, K.-S. (2012) 'Fiber-optic waveguide coupled surface plasmon resonance sensor', *Optics Express*, 20(19), 21729-21738, available: http://dx.doi.org/10.1364/OE.20.021729.

Akowuah, E.K., Gorman, T., Haxha, S. and Oliver, J.V. (2010) 'Dual channel planar waveguide surface plasmon resonance biosensor for an aqueous environment', *Optics Express*, 18(24), 24412-24422, available: http://dx.doi.org/10.1364/OE.18.024412.

Al-Qazwini, Y., Noor, A.S.M., Yaacob, M.H., Harun, S.W. and Mahdi, M.A. (2015) 'Fabrication and Characterization of a Refractive Index Sensor Based on SPR in an Etched Plastic Optical Fiber', *Procedia Engineering*, 120, 969-974, available: http://dx.doi.org/http://dx.doi.org/10.1016/j.proeng.2015.08.829.

Alam, M.Z., Moreno, J., Aitchison, J.S. and Mojahedi, M. (2007) 'An integrated optic hydrogen sensor for fast detection of hydrogen', in *Optics East*, SPIE, 9.

Alam, M.Z., Moreno, J., Aitchison, J.S., Mojahedi, M. and Kazemi, A.A. (2008) 'Integrated multi-channel nano-engineered optical hydrogen and temperature sensor detection systems for launch vehicles', in *Optical Engineering + Applications*, SPIE, 7.

Alexiadou, M., Kandyla, M., Mousdis, G. and Kompitsas, M. (2017) 'Pulsed laser deposition of ZnO thin films decorated with Au and Pd nanoparticles with enhanced acetone sensing performance', *Applied Physics A*, 123(4), 262, available: http://dx.doi.org/10.1007/s00339-017-0900-y.

Ando, M. (2006) 'Recent advances in optochemical sensors for the detection of H2, O2, O3, CO, CO2 and H2O in air', *TrAC Trends in Analytical Chemistry*, 25(10), 937-948, available: http://dx.doi.org/https://doi.org/10.1016/j.trac.2006.06.009.

Ando, M., Chabicovsky, R. and Haruta, M. (2001) 'Optical hydrogen sensitivity of noble metal–tungsten oxide composite films prepared by sputtering deposition', *Sensors and Actuators B: Chemical*, 76(1), 13-17, available: http://dx.doi.org/https://doi.org/10.1016/S0925-4005(01)00561-5.

Ando, M., Kobayashi, T., Iijima, S. and Haruta, M. (1997) 'Optical recognition of CO and H2 by use of gas-sensitive Au-Co3O4 composite films', *Journal of Materials Chemistry*, 7(9), 1779-1783, available: http://dx.doi.org/10.1039/A700125H.

Armgarth, M. and Nylander, C. (1982) 'Blister Formation in Pd Gate MIS Hydrogen Sensors', *Electron Device Letters*, 3(12), 384-386.

Arnbak, J. (1969) 'Leaky waves on a dielectric rod', *Electronics Letters*, 5(3), 41-42, available: http://dx.doi.org/10.1049/el:19690027.

Bahrami, F., Maisonneuve, M., Meunier, M., Aitchison, J.S. and Mojahedi, M. (2013) 'An improved refractive index sensor based on genetic optimization of plasmon waveguide resonance', *Optics Express*, 21(18), 20863-20872, available: http://dx.doi.org/10.1364/OE.21.020863.

Baiad, M.D. and Kashyap, R. (2015) 'Concatenation of surface plasmon resonance sensors in a single optical fiber using tilted fiber Bragg gratings', *Optics Letters*, 40(1), 115-118, available: http://dx.doi.org/10.1364/OL.40.000115.

Barber, D.J. and Freestone, I.C. (1990) 'AN INVESTIGATION OF THE ORIGIN OF THE COLOUR OF THE LYCURGUS CUP BY ANALYTICAL TRANSMISSION ELECTRON MICROSCOPY', *Archaeometry*, 32(1), 33-45, available: http://dx.doi.org/10.1111/j.1475-4754.1990.tb01079.x.

BARONE, S. and INST., P.I.O.B.N.Y.M.R. (1956) *Leaky Wave Contributions to the Field of a Line Source Above a Dielectric Slab*, Defense Technical Information Center.

Benson, D.K., Tracy, C.E., Hishmeh, G.A., Ciszek, P.E., Lee, S.-H. and Haberman, D.P. (1999) 'Low-cost fiber optic hydrogen gas detector using guided-wave surface-plasmon resonance in chemochromic thin films', in 185-202.

Berger, C.E.H., Beumer, T.A.M., Kooyman, R.P.H. and Greve, J. (1998) 'Surface Plasmon Resonance Multisensing', *Analytical Chemistry*, 70(4), 703-706, available: http://dx.doi.org/10.1021/ac970929a.

Bevenot, X., Trouillet, A., Veillas, C., Gagnaire, H. and Clement, M. (2002) 'Surface plasmon resonance hydrogen sensor using an optical fibre', *Measurement Science & Technology*, 13(1), 118-124, available: http://dx.doi.org/10.1088/0957-0233/13/1/315.

Bodurov, I., Vlaeva, I., Yoveheva, T., Dragostinova, V. and Sainov, S. (2013) 'Surface properties of PMMA films with different molecular weights', *Bulgarian Chemical Communications*, 45, 77-80.

Boudiba, A., Roussel, P., Zhang, C., Olivier, M.-G., Snyders, R. and Debliquy, M. (2013) 'Sensing mechanism of hydrogen sensors based on palladium-loaded tungsten oxide (Pd–WO3)', *Sensors and Actuators B: Chemical*, 187, 84-93, available: http://dx.doi.org/https://doi.org/10.1016/j.snb.2012.09.063.

Brendel, R. and Bormann, D. (1992) 'An infrared dielectric function model for amorphous solids', *Journal of Applied Physics*, 71(1), 1-6, available: http://dx.doi.org/doi:http://dx.doi.org/10.1063/1.350737.

Bright, T.J., Watjen, J.I., Zhang, Z.M., Muratore, C., Voevodin, A.A., Koukis, D.I., Tanner, D.B. and Arenas, D.J. (2013) 'Infrared optical properties of amorphous and nanocrystalline Ta2O5 thin films', *Journal of Applied Physics*, 114(8), available: http://dx.doi.org/10.1063/1.4819325.

Butler, M.A. (1984) 'Optical fiber hydrogen sensor', *Applied Physics Letters*, 45(10), 1007-1009, available: http://dx.doi.org/doi:http://dx.doi.org/10.1063/1.95060.

Butler, M.A. (1991) 'FIBER OPTIC SENSOR FOR HYDROGEN CONCENTRATIONS NEAR THE EXPLOSIVE LIMIT', *Journal of the Electrochemical Society*, 138(9), L46-L47, available: http://dx.doi.org/10.1149/1.2086073.

Butler, M.A. (1994) 'MICROMIRROR OPTICAL-FIBER HYDROGEN SENSOR', *Sensors and Actuators B-Chemical*, 22(2), 155-163, available: http://dx.doi.org/10.1016/0925-4005(94)87015-2.

Buttner, W.J., Post, M.B., Burgess, R. and Rivkin, C. (2011) 'An overview of hydrogen safety sensors and requirements', *International Journal of Hydrogen Energy*, 36(3), 2462-2470, available: http://dx.doi.org/10.1016/j.ijhydene.2010.04.176.

Carter, L.W. (1950) *Elastomer reinforced with modified clay*.

Cassedy, E.S. and Cohn, M. (1961) 'On the Existence of Leaky Waves Due to a Line Source Above a Grounded Dielectric Slab', *IRE Transactions on Microwave Theory and Techniques*, 9(3), 243-247, available: http://dx.doi.org/10.1109/TMTT.1961.1125314.

Cennamo, N., Coelho, L., Santos, D.F., Baptista, J.M., Guerreiro, A., Jorge, P.A.S. and Zeni, L. (2015) 'Modal Filtering for Optimized Surface Plasmon Resonance Sensing in Multimode Plastic Optical Fibers', *Ieee Sensors Journal*, 15(11), 6306-6312, available: http://dx.doi.org/10.1109/jsen.2015.2450991.

Cennamo, N., Massarotti, D., Conte, L. and Zeni, L. (2011) 'Low Cost Sensors Based on SPR in a Plastic Optical Fiber for Biosensor Implementation', *Sensors*, 11(12), 11752-11760, available: http://dx.doi.org/10.3390/s111211752.

Chadwick, B. and Gal, M. (1993) 'Enhanced optical detection of hydrogen using the excitation of surface plasmons in palladium', *Applied Surface Science*, 68(1), 135-138, available: http://dx.doi.org/http://dx.doi.org/10.1016/0169-4332(93)90222-W.

Chadwick, B., Tann, J., Brungs, M. and Gal, M. (1994) 'A hydrogen sensor based on the optical generation of surface plasmons in a palladium alloy', *Sensors and Actuators B: Chemical*, 17(3), 215-220, available: http://dx.doi.org/http://dx.doi.org/10.1016/0925-4005(93)00875-Y.

Chen, C., Berini, P., Feng, D., Tanev, S. and Tzolov, V.P. (2000) 'Efficient and accurate numerical analysis of multilayer planar optical waveguides in lossy anisotropic media', *Optics Express*, 7(8), 260-272, available: http://dx.doi.org/10.1364/OE.7.000260.

Chen, X. and Jiang, K. (2010) 'Effect of aging on optical properties of bimetallic sensor chips', *Optics Express*, 18(2), 1105-1112.

Chen, Y., Zheng, R.S., Lu, Y.H., Wang, P. and Ming, H. (2011) 'Fiber-optic surface plasmon resonant sensor with low-index anti-oxidation coating', *Chinese Optics Letters*, 9(10), 4, available: http://dx.doi.org/10.3788/col201109.100605.

Chien, F.C. and Chen, S.J. (2004) 'A sensitivity comparison of optical biosensors based on four different surface plasmon resonance modes', *Biosensors and Bioelectronics*, 20(3), 633-642, available: http://dx.doi.org/https://doi.org/10.1016/j.bios.2004.03.014.

Chilwell, J. and Hodgkinson, I. (1984) 'Thin-films field-transfer matrix theory of planar multilayer waveguides and reflection from prism-loaded waveguides', *Journal of the Optical Society of America A*, 1(7), 742-753, available: http://dx.doi.org/10.1364/JOSAA.1.000742.

Choi, S.H., Kim, Y.L. and Byun, K.M. (2011) 'Graphene-on-silver substrates for sensitive surface plasmon resonance imaging biosensors', *Optics Express*, 19(2), 458-466, available: http://dx.doi.org/10.1364/oe.19.000458.

Choi, S.Y., Takahashi, K., Esashi, M. and Matsuo, T. (1986) 'Stabilization of MISFET Hydrogen Sensors', *Sensors and Actuators*, 9(4), 353-361, available: http://dx.doi.org/10.1016/0250-6874(86)80067-1.

Ciprian, D. and Hlubina, P. (2013a) 'Theoretical model of the influence of oxide overlayer thickness on the performance of a surface plasmon fibre-optic sensor', *Measurement Science & Technology*, 24(2), 1-10, available: http://dx.doi.org/10.1088/0957-0233/24/2/025105.

Ciprian, D. and Hlubina, P. (2013b) 'Theoretical model of the influence of oxide overlayer thickness on the performance of a surface plasmon fibre-optic sensor', *Measurement Science & Technology*, 24(2), 10, available: http://dx.doi.org/10.1088/0957-0233/24/2/025105.

Clausius, R. (1879) 'Die mechanistische Wa¨rmelehre II', *Vieweg, Brauschweig*.

Dai, J., Yang, M., Chen, Y., Cao, K., Liao, H. and Zhang, P. (2011) 'Side-polished fiber Bragg grating hydrogen sensor with WO3-Pd composite film as sensing materials', *Optics Express*, 19(7), 6141-6148.

Dai, J., Zhu, L., Wang, G., Xiang, F., Qin, Y., Wang, M. and Yang, M. (2017) 'Optical Fiber Grating Hydrogen Sensors: A Review', *Sensors*, 17(3), 577.

Do, A.-T.T., Giang, H.T., Do, T.T., Pham, N.Q. and Ho, G.T. (2014) 'Effects of palladium on the optical and hydrogen sensing characteristics of Pd-doped ZnO nanoparticles', *Beilstein Journal of Nanotechnology*, 5, 1261-1267, available: http://dx.doi.org/10.3762/bjnano.5.140.

Doremus, R.H. (1966) 'Optical Properties of Thin Metallic Films in Island Form', *Journal of Applied Physics*, 37(7), 2775-2781, available: http://dx.doi.org/10.1063/1.1782121.

Dostálek, J., Vaisocherová, H. and Homola, J. (2005) 'Multichannel surface plasmon resonance biosensor with wavelength division multiplexing', *Sensors and Actuators B: Chemical*, 108(1), 758-764, available: http://dx.doi.org/https://doi.org/10.1016/j.snb.2004.12.096.

Downes, F. and Taylor, C.M. (2015) 'Optical Fibre Surface Plasmon Resonance Sensor Based on a Palladium-Yttrium Alloy', *Procedia Engineering*, 120, 602-605, available: http://dx.doi.org/http://dx.doi.org/10.1016/j.proeng.2015.08.738.

Downes, F. and Taylor, C.M. (2016) 'Theoretical investigation into the optimized design of a durable OFSPR hydrogen sensor based on a PdY alloy', in 98860L-98860L-13.

Downes, F. and Taylor, C.M. (2017) 'Optimized design of a nanocomposite Ta2O5 and Pd multilayer OFSPR H2 sensor: a theoretical analysis', in 101000S-101000S-7.

Downes, F. and Taylor, C.M. (2017) 'Theoretical investigation into the optimisation of an optical fibre surface plasmon resonance hydrogen sensor based on a PdY alloy', *Measurement Science and Technology*, 28(1), 015104, available: http://dx.doi.org/10.1088/1361-6501/28/1/015104.

Drude, P. (1900a) 'Zur Elektronentheorie der Metalle', *Annalen der Physik*, 306(3), 566-613, available: http://dx.doi.org/10.1002/andp.19003060312.

Drude, P. (1900b) 'Zur Elektronentheorie der Metalle; II. Teil. Galvanomagnetische und thermomagnetische Effecte', *Annalen der Physik*, 308(11), 369-402, available: http://dx.doi.org/10.1002/andp.19003081102.

D'Amico, A., Palma, A. and Verona, E. (1982) 'Palladium-surface acoustic wave interaction for hydrogen detection', *Applied Physics Letters*, 41(3), 300-301, available: http://dx.doi.org/10.1063/1.93471.

Ehler, T.T. and Noe, L.J. (1995) 'Surface Plasmon Studies of Thin Silver/Gold Bimetallic Films', *Langmuir*, 11(10), 4177-4179, available: http://dx.doi.org/10.1021/la00010a088.

Fano, U. (1941) 'The Theory of Anomalous Diffraction Gratings and of Quasi-Stationary Waves on Metallic Surfaces (Sommerfeld's Waves)', *Journal of the Optical Society of America*, 31(3), 213-222, available: http://dx.doi.org/10.1364/JOSA.31.000213.

Faraday, M. (1857) 'X. The Bakerian Lecture. —Experimental relations of gold (and other metals) to light', *Philosophical Transactions of the Royal Society of London*, 147, 145-181, available: http://dx.doi.org/10.1098/rstl.1857.0011.

Fishbein, B.J., Watt, J.T. and Plummer, J.D. (1987) 'Time Resolved Annealing of Interface Traps in Polysilicon Gate Metal-Oxide-Silicon Capacitors', *Journal of The Electrochemical Society*, 134(3), 674-681, available: http://dx.doi.org/10.1149/1.2100530.

Gao, F. (2004) 'Clay/polymer composites: the story', *Materials Today*, 7(11), 50-55, available: http://dx.doi.org/https://doi.org/10.1016/S1369-7021(04)00509-7.

Garnett, J.C.M. (1904) 'Colours in Metal Glasses and in Metallic Films', *Proceedings of the Royal Society of London*, 73(488-496), 443-445.

Garnett, J.C.M. (1906) 'Colours in Metal Glasses, in Metallic Films, and in Metallic Solutions. II', *Philosophical Transactions of the Royal Society of London. Series A, Containing Papers of a Mathematical or Physical Character*, 205, 237-288.

Ghatak, A. and Thyagarajan, K. (1998) *An Introduction to Fiber Optics*, Cambridge: Cambridge University Press.

Golosovsky, M., Lirtsman, V., Yashunsky, V., Davidov, D. and Aroeti, B. (2009) 'Midinfrared surface-plasmon resonance: A novel biophysical tool for studying living cells', *Journal of Applied Physics*, 105(10), 102036, available: http://dx.doi.org/doi:http://dx.doi.org/10.1063/1.3116143.

Gordon Ii, J.G. and Swalen, J.D. (1977) 'The effect of thin organic films on the surface plasma resonance on gold', *Optics Communications*, 22(3), 374-376, available: http://dx.doi.org/http://dx.doi.org/10.1016/S0030-4018(97)90032-8.

Gotoh, K., Kawabata, K., Fujii, E., Morishige, K., Kinumoto, T., Miyazaki, Y. and Ishida, H. (2009) 'The use of graphite oxide to produce mesoporous carbon supporting Pt, Ru, or Pd nanoparticles', *Carbon*, 47(8), 2120-2124, available: http://dx.doi.org/https://doi.org/10.1016/j.carbon.2009.03.052.

Griessen, R., Huiberts, J.N., Kremers, M., vanGogh, A.T.M., Koeman, N.J., Dekker, J.P. and Notten, P.H.L. (1997) 'Yttrium and lanthanum hydride films with switchable optical properties', *Journal of Alloys and Compounds*, 253, 44-50, available: http://dx.doi.org/10.1016/s0925-8388(96)02891-5.

Grotewohl, H., Hake, B. and Deutsch, M. (2016) 'Intensity and phase sensitivities in metal/dielectric thin film systems exhibiting the coupling of surface plasmon and waveguide modes', *Applied Optics*, 55(30), 8564-8570, available: http://dx.doi.org/10.1364/AO.55.008564.

Gupta, B.D. and Sharma, A.K. (2005) 'Sensitivity evaluation of a multi-layered surface plasmon resonance-based fiber optic sensor: a theoretical study', *Sensors and Actuators B-Chemical*, 107(1), 40-46, available: http://dx.doi.org/10.1016/j.snb.2004.08.030.

Gwon, H.R. and Lee, S.H. (2010) 'Spectral and Angular Responses of Surface Plasmon Resonance Based on the Kretschmann Prism Configuration', *Materials Transactions*, 51(6), 1150-1155, available: http://dx.doi.org/10.2320/matertrans.M2010003.

Hall, D.B. and Yeh, C. (1973) 'Leaky waves in a heteroepitaxial film', *Journal of Applied Physics*, 44(5), 2271-2274, available: http://dx.doi.org/10.1063/1.1662549.

Hansen, W.N. (1968) 'Electric Fields Produced by the Propagation of Plane Coherent Electromagnetic Radiation in a Stratified Medium', *Journal of the Optical Society of America*, 58(3), 380-390, available: http://dx.doi.org/10.1364/JOSA.58.000380.

Haus, H. and Miller, D. (1986) 'Attenuation of cutoff modes and leaky modes of dielectric slab structures', *IEEE Journal of Quantum Electronics*, 22(2), 310-318, available: http://dx.doi.org/10.1109/JQE.1986.1072956.

Homola, J., Dostálek, J., Chen, S., Rasooly, A., Jiang, S. and Yee, S.S. (2002) 'Spectral surface plasmon resonance biosensor for detection of staphylococcal enterotoxin B in milk', *International Journal of Food Microbiology*, 75(1), 61-69, available: http://dx.doi.org/https://doi.org/10.1016/S0168-1605(02)00010-7.

Homola, J., Lu, H.B., Nenninger, G.G., Dostálek, J. and Yee, S.S. (2001) 'A novel multichannel surface plasmon resonance biosensor', *Sensors and Actuators B: Chemical*, 76(1), 403-410, available: http://dx.doi.org/https://doi.org/10.1016/S0925-4005(01)00648-7.

Hosoki, A., Nishiyama, M., Igawa, H., Seki, A., Choi, Y. and Watanabe, K. (2013) 'A surface plasmon resonance hydrogen sensor using Au/Ta2O5/Pd multi-layers on hetero-core optical fiber structures', *Sensors and Actuators B-Chemical*, 185, 53-58, available: http://dx.doi.org/10.1016/j.snb.2013.04.072.

Hosoki, A., Nishiyama, M., Igawa, H., Seki, A. and Watanabe, K. (2014) 'A hydrogen curing effect on surface plasmon resonance fiber optic hydrogen sensors using an annealed Au/Ta2O5/Pd multi-layers film', *Optics Express*, 22(15), 18556-18563, available: http://dx.doi.org/10.1364/oe.22.018556.

Hosoki, A., Nishiyama, M., Igawa, H. and Watanabe, K. (2016) 'Multipoint Hydrogen Sensing of Hetero-Core Fiber SPR Tip Sensors With Pseudorandom Noise Code Correlation Reflectometry', *IEEE Sensors Journal*, 16(8), 2447-2452, available: http://dx.doi.org/10.1109/JSEN.2016.2518701.

Huebert, T., Boon-Brett, L., Black, G. and Banach, U. (2011) 'Hydrogen sensors - A review', *Sensors and Actuators B-Chemical*, 157(2), 329-352, available: http://dx.doi.org/10.1016/j.snb.2011.04.070.

Hughes, R.C. and Schubert, W.K. (1992) 'Thin films of Pd/Ni alloys for detection of high hydrogen concentrations', *Journal of Applied Physics*, 71(1), 542-544, available: http://dx.doi.org/10.1063/1.350646.

Huiberts, J.N., Rector, J.H., Wijngaarden, R.J., Jetten, S., deGroot, D., Dam, B., Koeman, N.J., Griessen, R., Hjorvarsson, B., Olafsson, S. and Cho, Y.S. (1996) 'Synthesis of yttriumtrihydride films for ex-situ measurements', *Journal of Alloys and Compounds*, 239(2), 158-171, available: http://dx.doi.org/10.1016/0925-8388(96)02286-4.

Hübert, T., Boon-Brett, L., Black, G. and Banach, U. (2011) 'Hydrogen sensors–a review', *Sensors and Actuators B: Chemical*, 157(2), 329-352.

Ilchenko, S.G., Lymarenko, R.A. and Taranenko, V.B. (2017) 'Using Metal-Multilayer-Dielectric Structure to Increase Sensitivity of Surface Plasmon Resonance Sensor', *Nanoscale Res Lett*, 12(1), 295, available: http://dx.doi.org/10.1186/s11671-017-2073-1.

Imai, Y., Okuhara, Y., Noguchi, Y. and Takata, M. (2004) 'Optically readable hydrogen sensor using Pd/Y double-layered thin films', *Advances in Technology of Materials and Materials Processing Journal*, 6(1), 57-62.

Imai, Y., Okuhara, Y., Noguchi, Y. and Takata, M. (2006) 'Optically Readable Hydrogen Sensor Using Pd/Y Double-Layered Thin Films', *AZo Journal of Materials Online*, 2(ISSN 1833-122X), available: http://dx.doi.org/10.2240/azojomo0197.

Ishigure, T., Nihei, E. and Koike, Y. (1996a) 'Optimization of the refractive-index distribution of high-bandwidth GI polymer optical fiber based on both modal and material dispersions', *Polymer Journal*, 28(3), 272-275, available: http://dx.doi.org/10.1295/polymj.28.272.

Ishigure, T., Nihei, E. and Koike, Y. (1996b) 'Optimum refractive-index profile of the graded-index polymer optical fiber, toward gigabit data links', *Applied Optics*, 35(12), 2048-2053, available: http://dx.doi.org/10.1364/ao.35.002048.

Jha, R. and Sharma, A.K. (2009) 'Chalcogenide glass prism based SPR sensor with Ag-Au bimetallic nanoparticle alloy in infrared wavelength region', *Journal of Optics a-Pure and Applied Optics*, 11(4), available: http://dx.doi.org/10.1088/1464-4258/11/4/045502.

Jiang, Y.-X., Liu, B.-H., Zhu, X.-S., Tang, X.-L. and Shi, Y.-W. (2015) 'Long-range surface plasmon resonance sensor based on dielectric/silver coated hollow fiber with enhanced figure of merit', *Optics Letters*, 40(5), 744-747, available: http://dx.doi.org/10.1364/OL.40.000744.

Johnson, P.B. and Christy, R.W. (1972) 'Optical Constants of the Noble Metals', *Physical Review B*, 6(12), 4370-4379.

Jorgenson, R.C. and Yee, S.S. (1993) 'A fiber-optic chemical sensor based on surface plasmon resonance', *Sensors and Actuators B: Chemical*, 12(3), 213-220, available: http://dx.doi.org/http://dx.doi.org/10.1016/0925-4005(93)80021-3.

Kandyla, M., Chatzimanolis-Moustakas, C., Guziewicz, M. and Kompitsas, M. (2014) 'Nanocomposite NiO:Pd hydrogen sensors with sub-ppm detection limit and low operating temperature', *Materials Letters*, 119, 51-55, available: http://dx.doi.org/https://doi.org/10.1016/j.matlet.2013.12.104.

Kharadly, M.M.Z. and Jackson, W. (1953) 'The properties of artificial dielectrics comprising arrays of conducting elements', *Proceedings of the IEE - Part III: Radio and Communication Engineering*, 100(66), 199-212, available: http://dx.doi.org/10.1049/pi-3.1953.0042.

Kickelbick, G. (2006) 'Introduction to Hybrid Materials' in *Hybrid Materials* Wiley-VCH Verlag GmbH & Co. KGaA, 1-48.

Kim, C.C., Garland, J.W., Abad, H. and Raccah, P.M. (1992) 'MODELING THE OPTICAL DIELECTRIC FUNCTION OF SEMICONDUCTORS - EXTENSION OF THE CRITICAL-POINT PARABOLIC-BAND APPROXIMATION', *Physical Review B*, 45(20), 11749-11767, available: http://dx.doi.org/10.1103/PhysRevB.45.11749.

Kim, Y.-C., Peng, W., Banerji, S. and Booksh, K.S. (2005) 'Tapered fiber optic surface plasmon resonance sensor for analyses of vapor and liquid phases', *Optics Letters*, 30(17), 2218-2220, available: http://dx.doi.org/10.1364/OL.30.002218.

Kitamura, R., Pilon, L. and Jonasz, M. (2007) 'Optical constants of silica glass from extreme ultraviolet to far infrared at near room temperature', *Applied Optics*, 46(33), 8118-8133, available: http://dx.doi.org/10.1364/ao.46.008118.

Knapton, A.G. (1977) 'Palladium Alloys for Hydrogen Diffusion Membranes', *Platinum Metals Rev.*, **21**(2), 44.

Kracker, M., Worsch, C. and Rüssel, C. (2013) 'The effect of thermal annealing and hydrogen on the morphology and the optical properties of thin palladium layers', *Materials Letters*, 110, 114-116, available: http://dx.doi.org/https://doi.org/10.1016/j.matlet.2013.07.133.

Kracker, M., Worsch, C., Seeber, W. and Rüssel, C. (2014) 'Optical hydrogen sensing with modified Pd-layers: A kinetic study of roughened layers and dewetted nanoparticle films', *Sensors and Actuators B: Chemical*, 197, 95-103, available: http://dx.doi.org/https://doi.org/10.1016/j.snb.2014.02.063.

Krasnov, Y.S., Kolbasov, G.Y., Zaychenko, V.N. and Fomanyuk, S.S. (2008) 'Optical hydrogen sensor based on tungsten oxide film', in *2008 4th International Conference on Advanced Optoelectronics and Lasers*, Sept. 29 2008-Oct. 4 2008, 444-446, available: http://dx.doi.org/10.1109/CAOL.2008.4671909.

Krawczyk, S., Kamińska, A., Kozłowski, M., Radomska, J., Czerwosz, E. and Sobczak, K. (2014) 'Nanocomposite carbonaceous-palladium thin films for ammonia sensors', *Journal of Physics: Conference Series*, 564(1), 012004.

Kretschm.E and Raether, H. (1968) 'RADIATIVE DECAY OF NON RADIATIVE SURFACE PLASMONS EXCITED BY LIGHT', *Zeitschrift Fur Naturforschung Part a-Astrophysik Physik Und Physikalische Chemie*, A 23(12), 2135-&.

Kumar, P. and Malhotra, L.K. (2004) 'Palladium capped samarium thin films as potential hydrogen sensors', *Materials Chemistry and Physics*, 88(1), 106-109, available: http://dx.doi.org/10.1016/j.matchemphys.2004.06.038.

Lange, U., Hirsch, T., Mirsky, V.M. and Wolfbeis, O.S. (2011) 'Hydrogen sensor based on a graphene – palladium nanocomposite', *Electrochimica Acta*, 56(10), 3707-3712, available: http://dx.doi.org/https://doi.org/10.1016/j.electacta.2010.10.078.

Languy, F., Fleury, K., Lenaerts, C., Loicq, J., Regaert, D., Thibert, T. and Habraken, S. (2011) 'Flat Fresnel doublets made of PMMA and PC: combining low cost production and very high

concentration ratio for CPV', *Optics Express*, 19(10), A280-A294, available: http://dx.doi.org/10.1364/oe.19.00a280.

Lee, K.-S. and El-Sayed, M.A. (2006) 'Gold and Silver Nanoparticles in Sensing and Imaging: Sensitivity of Plasmon Response to Size, Shape, and Metal Composition', *The Journal of Physical Chemistry B*, 110(39), 19220-19225, available: http://dx.doi.org/10.1021/jp062536y.

Lewis, F.A. (1967) *The palladium hydrogen system*, London; New York: Academic Press.

Li, L., Liang, Y., Guang, J., Cui, W., Zhang, X., Masson, J.-F. and Peng, W. (2017) 'Dual Kretschmann and Otto configuration fiber surface plasmon resonance biosensor', *Optics Express*, 25(22), 26950-26957, available: http://dx.doi.org/10.1364/OE.25.026950.

Lin, K.Q., Lu, Y.H., Chen, J.X., Zheng, R.S., Wang, P. and Ming, H. (2008) 'Surface plasmon resonance hydrogen sensor based on metallic grating with high sensitivity', *Optics Express*, 16(23), 18599-18604, available: http://dx.doi.org/10.1364/oe.16.018599.

Liu, K., Xue, M., Jiang, J., Wang, T., Chang, P. and Liu, T. (2018) 'Theoretical modeling of a coupled plasmon waveguide resonance sensor based on multimode optical fiber', *Optics Communications*, 410, 552-558, available: http://dx.doi.org/https://doi.org/10.1016/j.optcom.2017.10.072.

Liu, Q., Liu, Y., Chen, S., Wang, F. and Peng, W. (2017) 'A Low-Cost and Portable Dual-Channel Fiber Optic Surface Plasmon Resonance System', *Sensors (Basel, Switzerland)*, 17(12), 2797, available: http://dx.doi.org/10.3390/s17122797.

Liu, Y., Chen, Y.-p., Song, H. and Zhang, G. (2012) 'Modeling analysis and experimental study on the optical fiber hydrogen sensor based on Pd-Y alloy thin film', *Review of Scientific Instruments*, 83(7), available: http://dx.doi.org/10.1063/1.4731725.

Liu, Y., Chen, Y.P., Song, H. and Zhang, G. (2012a) 'Hydrogen gas sensor based on palladium and yttrium alloy ultrathin film', *Review of Scientific Instruments*, 83(12), 6, available: http://dx.doi.org/10.1063/1.4770329.

Liu, Y., Chen, Y.P., Song, H. and Zhang, G. (2012b) 'Hydrogen gas sensor based on palladium and yttrium alloy ultrathin film', *Rev. Sci. Instrum*, 83(12), available: http://dx.doi.org/10.1063/1.4770329.

Liu, Y., Chen, Y.P., Song, H. and Zhang, G. (2012c) 'Modeling analysis and experimental study on the optical fiber hydrogen sensor based on Pd-Y alloy thin film', *Rev. Sci. Instrum*, 83(7), 1-5, available: http://dx.doi.org/10.1063/1.4731725.

Liu, Y., Chen, Y.P., Song, H. and Zhang, G. (2013) 'Characteristics of an Optical Fiber Hydrogen Gas Sensor Based on a Palladium and Yttrium Alloy Thin Film', *IEEE Sensors Journal*, 13(7), 2699-2704, available: http://dx.doi.org/10.1109/JSEN.2013.2258904.

Liu, Y. and Li, Y. (2016a) 'Enhanced sensitivity of transmission based optical fiber hydrogen sensor with multi-layer Pd-Y alloy thin film', *Sensors and Actuators B-Chemical*, 227, 178-184, available: http://dx.doi.org/10.1016/j.snb.2015.11.112.

Liu, Y. and Li, Y. (2016b) 'Enhanced sensitivity of transmission based optical fiber hydrogen sensor with multi-layer Pd–Y alloy thin film', *Sensors and Actuators B: Chemical*, 227, 178-184, available: http://dx.doi.org/http://dx.doi.org/10.1016/j.snb.2015.11.112.

Liu, Z., Wei, Y., Zhang, Y., Liu, C., Zhang, Y., Zhao, E., Yang, J. and Yuan, L. (2015) 'Compact distributed fiber SPR sensor based on TDM and WDM technology', *Optics Express*, 23(18), 24004-24012, available: http://dx.doi.org/10.1364/OE.23.024004.

Lorentz, H.A. (1905) 'The motion of electrons in metallic bodies I-III', *KNAW Proceedings*, 7, 438-453

Lorenz, L. (1869) *Vidensk. Selsk. Skrifter*, 8, 205.

Lu, M., Peng, W., Liu, Q., Liu, Y., Li, L., Liang, Y. and Masson, J.-F. (2017) 'Dual channel multilayer-coated surface plasmon resonance sensor for dual refractive index range measurements', *Optics Express*, 25(8), 8563-8570, available: http://dx.doi.org/10.1364/OE.25.008563.

Lundström, I., Shivaraman, S., Svensson, C. and Lundkvist, L. (1975) 'A hydrogen−sensitive MOS field−effect transistor', *Applied Physics Letters*, 26(2), 55-57, available: http://dx.doi.org/10.1063/1.88053.

Löfås, S., Malmqvist, M., Rönnberg, I., Stenberg, E., Liedberg, B. and Lundström, I. (1991) 'Bioanalysis with surface plasmon resonance', *Sensors and Actuators B: Chemical*, 5(1), 79-84, available: http://dx.doi.org/https://doi.org/10.1016/0925-4005(91)80224-8.

Mahajna, S., Neumann, M., Eyal, O. and Shalabney, A. (2016) 'Plasmon-Waveguide Resonances with Enhanced Figure of Merit and Their Potential for Anisotropic Biosensing in the Near Infrared Region', *Journal of Sensors*, 2016, 6, available: http://dx.doi.org/10.1155/2016/1898315.

Malitson, I.H. (1965) 'Interspecimen Comparison of the Refractive Index of Fused Silica', *Journal of the Optical Society of America*, 55(10), 1205-1208, available: http://dx.doi.org/10.1364/JOSA.55.001205.

Manchester, F.D., San-Martin, A. and Pitre, J.M. (1994) 'The H-Pd (hydrogen-palladium) System', *Journal of Phase Equilibria*, 15.

Mandelis, A. and Garcia, J.A. (1998) 'Pd/PVDF thin film hydrogen sensor based on laser-amplitude-modulated optical-transmittance: dependence on H-2 concentration and device physics', *Sensors and Actuators B-Chemical*, 49(3), 258-267, available: http://dx.doi.org/10.1016/s0925-4005(98)00137-3.

Marcuvitz, N. (1956) 'On field representations in terms of leaky modes or Eigenmodes', *IRE Transactions on Antennas and Propagation*, 4(3), 192-194, available: http://dx.doi.org/10.1109/TAP.1956.1144410.

Maxwell, J.C. (1873) 'A treatise on electricity and magnetism', *Oxford: Clarendon Press*, 1, 504.

McKenzie, D.R. and McPhedran, R.C. (1977) 'Exact modelling of cubic lattice permittivity and conductivity', *Nature*, 265, 128, available: http://dx.doi.org/10.1038/265128a0.

Meka D., O.V., Atre S. V., Prasad S. (2008) 'Palladium Polymer nanocomposite based Chemiresistive SO2 Sensor', *NSTI Nanotech conference proceedings article*, 1(ISBN 978-1-4200-8503-7).

Meredith, R.E. and Tobias, C.W. (1960) 'Resistance to Potential Flow through a Cubical Array of Spheres', *Journal of Applied Physics*, 31(7), 1270-1273, available: http://dx.doi.org/10.1063/1.1735816.

Mie, G. (1908) 'Beiträge zur Optik trüber Medien, speziell kolloidaler Metallösungen', *Annalen der Physik*, 330(3), 377-445, available: http://dx.doi.org/10.1002/andp.19083300302.

Minghong, Y., Zhi, L., Jixiang, D., Zhi, Y., Yi, Z. and Zhi, Z. (2013) 'Comparison of optical fiber Bragg grating hydrogen sensors with Pd-based thin films and sol–gel WO 3 coatings', *Measurement Science and Technology*, 24(9), 094009.

Monzón-Hernández, D., Luna-Moreno, D., Escobar, D.M. and Villatoro, J. (2010) 'Optical microfibers decorated with PdAu nanoparticles for fast hydrogen sensing', *Sensors and Actuators B: Chemical*, 151(1), 219-222, available: http://dx.doi.org/http://dx.doi.org/10.1016/j.snb.2010.09.018.

Morjan, M., Züchner, H. and Cammann, K. (2009) 'Contributions to a reliable hydrogen sensor based on surface plasmon surface resonance spectroscopy', *Surface Science*, 603(10–12), 1353-1359, available: http://dx.doi.org/http://dx.doi.org/10.1016/j.susc.2008.09.067.

Mossotti, O.F. (1850) 'Mem. della Soc.', *Scient. Modena*, 14, 49.

Mrstik, B.J., McMarr, P.J., Saks, N.S., Rendell, R.W. and Klein, R.B. (1993) 'Hydrogen permeability in thermally grown films of ${\mathrm{SiO}}_{2}$ on silicon substrates', *Physical Review B*, 47(7), 4115-4118.

Mubeen, S., Zhang, T., Yoo, B., Deshusses, M.A. and Myung, N.V. (2007) 'Palladium Nanoparticles Decorated Single-Walled Carbon Nanotube Hydrogen Sensor', *The Journal of Physical Chemistry C*, 111(17), 6321-6327, available: http://dx.doi.org/10.1021/jp067716m.

Nenninger, G.G., Clendenning, J.B., Furlong, C.E. and Yee, S.S. (1998) 'Reference-compensated biosensing using a dual-channel surface plasmon resonance sensor system based on a planar lightpipe configuration', *Sensors and Actuators B: Chemical*, 51(1), 38-45, available: http://dx.doi.org/https://doi.org/10.1016/S0925-4005(98)00218-4.

Noguez, C. (2007) 'Surface Plasmons on Metal Nanoparticles: The Influence of Shape and Physical Environment', *The Journal of Physical Chemistry C*, 111(10), 3806-3819, available: http://dx.doi.org/10.1021/jp066539m.

Noguez, C. and Román-Velázquez, C.E. (2004) 'Dispersive force between dissimilar materials: Geometrical effects', *Physical Review B*, 70(19), 195412.

Oates, T.W.H., Wormeester, H. and Arwin, H. (2011) 'Characterization of plasmonic effects in thin films and metamaterials using spectroscopic ellipsometry', *Progress in Surface Science*, 86(11-12), 328-376, available: http://dx.doi.org/10.1016/j.progsurf.2011.08.004.

Ohodnicki, J., Paul R., Baltrus, J.P. and Brown, T.D., ; U.S. Department of Energy, Washington, DC (United States) (2017) *Palladium and platinum-based nanoparticle functional sensor layers for selective H2 sensing*, 9,696,256; Other: 14/887,660 United States Other: 14/887,660 NETL English.

Ohodnicki, P.R., Baltrus, J.P. and Brown, T.D. (2015) 'Pd/SiO2 and AuPd/SiO2 nanocomposite-based optical fiber sensors for H-2 sensing applications', *Sensors and Actuators B-Chemical*, 214, 159-168, available: http://dx.doi.org/10.1016/j.snb.2015.02.076.

Ohodnicki, P.R., Buric, M.P., Brown, T.D., Matranga, C., Wang, C., Baltrus, J. and Andio, M. (2013) 'Plasmonic nanocomposite thin film enabled fiber optic sensors for simultaneous gas and temperature sensing at extreme temperatures', *Nanoscale*, 5(19), 9030-9039, available: http://dx.doi.org/10.1039/C3NR02891G.

Okamoto, T. and Yamaguchi, I. (1997) 'Absorption Measurement Using a Leaky Waveguide Mode', *Optical Review*, 4(3), 354-357, available: http://dx.doi.org/10.1007/s10043-997-0354-0.

Omidvar, A., Jaleh, B. and Nasrollahzadeh, M. (2017) 'Preparation of the GO/Pd nanocomposite and its application for the degradation of organic dyes in water', *Journal of Colloid and Interface Science*, 496, 44-50, available: http://dx.doi.org/https://doi.org/10.1016/j.jcis.2017.01.113.

Otto, A. (1968) 'EXCITATION OF NONRADIATIVE SURFACE PLASMA WAVES IN SILVER BY METHOD OF FRUSTRATED TOTAL REFLECTION', *Zeitschrift Fur Physik*, 216(4), 398-&, available: http://dx.doi.org/10.1007/bf01391532.

Otto, A. and Sohler, W. (1971) 'Modification of the total reflection modes in a dielectric film by one metal boundary', *Optics Communications*, 3(4), 254-258, available: http://dx.doi.org/https://doi.org/10.1016/0030-4018(71)90017-4.

O'Toole, P.I. and Hudson, T.S. (2011) 'New High-Density Packings of Similarly Sized Binary Spheres', *The Journal of Physical Chemistry C*, 115(39), 19037-19040, available: http://dx.doi.org/10.1021/jp206115p.

Paek, U.C., Peterson, G.E. and Carnevale, A. (1981) 'DISPERSIONLESS SINGLE-MODE LIGHTGUIDES WITH ALPHA-INDEX PROFILES', *Bell System Technical Journal*, 60(5), 583-598.

Palmisano, V., Weidner, E., Boon-Brett, L., Bonato, C., Harskamp, F., Moretto, P., Post, M.B., Burgess, R., Rivkin, C. and Buttner, W.J. (2015) 'Selectivity and resistance to poisons of commercial hydrogen sensors', *International Journal of Hydrogen Energy*, 40(35), 11740-11747, available: http://dx.doi.org/http://dx.doi.org/10.1016/j.ijhydene.2015.02.120.

Peng, W., Banerji, S., Kim, Y.-C. and Booksh, K.S. (2005) 'Investigation of dual-channel fiber-optic surface plasmon resonance sensing for biological applications', *Optics Letters*, 30(22), 2988-2990, available: http://dx.doi.org/10.1364/OL.30.002988.

Perrotton, C., Javahiraly, N., Slaman, M., Dam, B. and Meyrueis, P. (2011a) 'Fiber optic Surface Plasmon Resonance sensor based on wavelength modulation for hydrogen sensing', *Optics Express*, 19(S6), A1175-A1183.

Perrotton, C., Javahiraly, N., Slaman, M., Dam, B. and Meyrueis, P. (2011b) 'Fiber optic Surface Plasmon Resonance sensor based on wavelength modulation for hydrogen sensing', *Optics Express*, 19(23), A1175-A1183.

Perrotton, C., Slaman, M., Javahiraly, N., Schreuders, H., Dam, B. and Meyrueis, P. (2011c) 'Wavelength response of a surface plasmon resonance palladium-coated optical fiber sensor for hydrogen detection', *Optical Engineering*, 50(1), available: http://dx.doi.org/10.1117/1.3529432.

Perrotton, C., Westerwaal, R., Javahiraly, N., Slaman, M., Schreuders, H., Dam, B. and Meyrueis, P. (2013) 'A reliable, sensitive and fast optical fiber hydrogen sensor based on surface plasmon resonance', *Optics Express*, 21(1), 382-390.

Petryayeva, E. and Krull, U.J. (2011) 'Localized surface plasmon resonance: Nanostructures, bioassays and biosensing-A review', *Analytica Chimica Acta*, 706(1), 8-24, available: http://dx.doi.org/10.1016/j.aca.2011.08.020.

Pines, D. and Bohm, D. (1952) 'A Collective Description of Electron Interactions: II. Collective vs Individual Particle Aspects of the Interactions', *Physical Review*, 85(2), 338-353.

PM-Optics (2014) 'Refractive Index, Abbe Value and Dispersion Formula', available.

Postava, K. and Yamaguchi, T. (2001) 'Optical functions of low-k materials for interlayer dielectrics', *Journal of Applied Physics*, 89(4), 2189-2193, available: http://dx.doi.org/10.1063/1.1344214.

Powell, C.J. and Swan, J.B. (1960) 'Effect of Oxidation on the Characteristic Loss Spectra of Aluminum and Magnesium', *Physical Review*, 118(3), 640-643.

Quinten, M. (2011) *Optical Properties of Nanoparticle Systems*, WILEY-VHC.

Raether, H. (1986) *Surface Plasmons on Smooth and Rough Surfaces and on Gratings*, Springer Tracts in Modern Physics Volume 111 1988: springer.com.

Raether, H. (1988) 'SURFACE-PLASMONS ON SMOOTH AND ROUGH SURFACES AND ON GRATINGS', *Springer Tracts in Modern Physics*, 111, 1-133.

Rakic, A.D., Djurisic, A.B., Elazar, J.M. and Majewski, M.L. (1998) 'Optical properties of metallic films for vertical-cavity optoelectronic devices', *Applied Optics*, 37(22), 5271-5283, available: http://dx.doi.org/10.1364/ao.37.005271.

Rani, M., Shukla, S., Sharma, N.K. and Sajal, V. (2014) 'Theoretical study of nanocomposites based fiber optic SPR sensor', *Optics Communications*, 313, 303-314, available: http://dx.doi.org/10.1016/j.optcom.2013.10.048.

Rayleigh, L. (1892) 'LVI. On the influence of obstacles arranged in rectangular order upon the properties of a medium', *The London, Edinburgh, and Dublin Philosophical Magazine and Journal of Science*, 34(211), 481-502, available: http://dx.doi.org/10.1080/14786449208620364.

Rayleigh, L. (1907a) 'III. Note on the remarkable case of diffraction spectra described by Prof. Wood', *The London, Edinburgh, and Dublin Philosophical Magazine and Journal of Science*, 14(79), 60-65, available: http://dx.doi.org/10.1080/14786440709463661.

Rayleigh, L. (1907b) 'On the dynamical theory of gratings', *Proceedings of the Royal Society of London. Series A*, 79(532), 399-416, available: http://dx.doi.org/10.1098/rspa.1907.0051.

Refractiveindex.info (2015) 'Optical constants of BK7 N-BK7 (SCHOTT)', available.

Robert, B. (2011) 'Nanocomposites: a review of technology and applications', *Assembly Automation*, 31(2), 106-112, available: http://dx.doi.org/10.1108/01445151111117683.

Roy, R.K., Mandal, S.K. and Pal, A.K. (2003) 'Effect of interfacial alloying on the surface plasmon resonance of nanocrystalline Au-Ag multilayer thin films', *Eur. Phys. J. B*, 33(1), 109-114.

Runge, C. (1925) 'Zum Paschen-Backeffekt', *Annalen der Physik*, 381(2-3), 266-272, available: http://dx.doi.org/doi:10.1002/andp.19253810210.

Ryuichi, Takeyoshi and Akane, O. (1991) *Method for preparing a polyamide composite material*.

Salamon, Z., Macleod, H.A. and Tollin, G. (1997) 'Coupled plasmon-waveguide resonators: a new spectroscopic tool for probing proteolipid film structure and properties', *Biophysical Journal*, 73(5), 2791-2797, available: http://dx.doi.org/http://dx.doi.org/10.1016/S0006-3495(97)78308-5.

Salamon, Z. and Tollin, G. (2001) 'Optical Anisotropy in Lipid Bilayer Membranes: Coupled Plasmon-Waveguide Resonance Measurements of Molecular Orientation, Polarizability, and Shape', *Biophysical Journal*, 80(3), 1557-1567, available: http://dx.doi.org/https://doi.org/10.1016/S0006-3495(01)76128-0.

Sambles, J.R., Bradbery, G.W. and Yang, F.Z. (1991) 'OPTICAL-EXCITATION OF SURFACE-PLASMONS - AN INTRODUCTION', *Contemporary Physics*, 32(3), 173-183, available: http://dx.doi.org/10.1080/00107519108211048.

Sarika, S. and Gupta, B.D. (2010) 'Simulation of a surface plasmon resonance-based fiber-optic sensor for gas sensing in visible range using films of nanocomposites', *Measurement Science and Technology*, 21(11), 115202.

Savović, S. and Djordjevich, A. (2004) 'Influence of numerical aperture on mode coupling in step-index plastic optical fibers', *Applied Optics*, 43(29), 5542-5546, available: http://dx.doi.org/10.1364/AO.43.005542.

Sekimoto, S., Nakagawa, H., Okazaki, S., Fukuda, K., Asakura, S., Shigemori, T. and Takahashi, S. (2000) 'A fiber-optic evanescent-wave hydrogen gas sensor using palladium-supported tungsten oxide', *Sensors and Actuators B: Chemical*, 66(1–3), 142-145, available: http://dx.doi.org/http://dx.doi.org/10.1016/S0925-4005(00)00330-0.

Sekkat, D.V.N.a.S.H.a.Z. (2016) 'Extremely narrow resonances, giant sensitivity and field enhancement in low-loss waveguide sensors', *Journal of Optics*, 18(6), 065004.

Sellmeier (1871) 'Zur Erklärung der abnormen Farbenfolge im Spectrum einiger Substanzen', *Annalen der Physik*, 219(6), 272-282, available: http://dx.doi.org/10.1002/andp.18712190612.

Sengar, S.K., Mehta, B.R., Kulriya, P.K. and Khan, S.A. (2013) 'Enhanced hydrogenation and reduced lattice distortion in size selected Pd-Ag and Pd-Cu alloy nanoparticles', *Applied Physics Letters*, 103(17), available: http://dx.doi.org/10.1063/1.4826580.

Shah, K., Shukla, S., Sharma, N.K. and Sajal, V. (2016) 'Theoretical study of surface plasmon resonance based fiber optic sensor utilizing an additional layer of zinc oxide', *Optik - International Journal for Light and Electron Optics*, 127(14), 5743-5749, available: http://dx.doi.org/http://dx.doi.org/10.1016/j.ijleo.2016.04.016.

Shalabney, A. and Abdulhalim, I. (2010) 'Electromagnetic fields distribution in multilayer thin film structures and the origin of sensitivity enhancement in surface plasmon resonance sensors', *Sensors and Actuators a-Physical*, 159(1), 24-32, available: http://dx.doi.org/10.1016/j.sna.2010.02.005.

Shalabney, A. and Abdulhalim, I. (2011) 'Sensitivity-enhancement methods for surface plasmon sensors', *Laser & Photonics Reviews*, 5(4), 571-606, available: http://dx.doi.org/10.1002/lpor.201000009.

Shanak, H., Schmitt, H., Nowoczin, J. and Ziebert, C. (2004) 'Effect of Pt-catalyst on gasochromic WO3 films: optical, electrical and AFM investigations', *Solid State Ionics*, 171(1–2), 99-106, available: http://dx.doi.org/https://doi.org/10.1016/j.ssi.2004.04.001.

Sharma, A.K. and Gupta, B.D. (2004) 'Absorption-based fiber optic surface plasmon resonance sensor: a theoretical evaluation', *Sensors and Actuators B-Chemical*, 100(3), 423-431, available: http://dx.doi.org/10.1016/j.snb.2004.02.013.

Sharma, A.K. and Gupta, B.D. (2005) 'On the sensitivity and signal to noise ratio of a step-index fiber optic surface plasmon resonance sensor with bimetallic layers', *Optics Communications*, 245(1-6), 159-169, available: http://dx.doi.org/10.1016/j.optcom.2004.10.013.

Sharma, A.K. and Gupta, B.D. (2005) 'On the sensitivity and signal to noise ratio of a step-index fiber optic surface plasmon resonance sensor with bimetallic layers', *Optics Communications*, 245(1–6), 159-169, available: http://dx.doi.org/http://dx.doi.org/10.1016/j.optcom.2004.10.013.

Sharma, A.K. and Gupta, B.D. (2006) 'Fibre-optic sensor based on surface plasmon resonance with Ag-Au alloy nanoparticle films', *Nanotechnology*, 17(1), 124-131, available: http://dx.doi.org/10.1088/0957-4484/17/1/020.

Sharma, A.K. and Gupta, B.D. (2007) 'Metal–semiconductor nanocomposite layer based optical fibre surface plasmon resonance sensor', *Journal of Optics A: Pure and Applied Optics*, 9(2), 180.

Sharma, A.K., Jha, R. and Gupta, B.D. (2007) 'Fiber-optic sensors based on surface plasmon resonance: A comprehensive review', *Ieee Sensors Journal*, 7(7-8), 1118-1129, available: http://dx.doi.org/10.1109/jsen.2007.897946.

Sharma, A.K. and Mohr, G.J. (2008a) 'On the performance of surface plasmon resonance based fibre optic sensor with different bimetallic nanoparticle alloy combinations', *Journal of Physics D-Applied Physics*, 41(5), 7, available: http://dx.doi.org/10.1088/0022-3727/41/5/055106.

Sharma, A.K. and Mohr, G.J. (2008b) 'Theoretical understanding of an alternating dielectric multilayer-based fiber optic SPR sensor and its application to gas sensing', *New Journal of Physics*, 10, 12, available: http://dx.doi.org/10.1088/1367-2630/10/2/023039.

Sharma, B. and Kim, J.-S. (2017) 'Pd/Ag alloy as an application for hydrogen sensing', *International Journal of Hydrogen Energy*, 42(40), 25446-25452, available: http://dx.doi.org/https://doi.org/10.1016/j.ijhydene.2017.08.142.

Sharma, N.K. (2012) 'Performances of different metals in optical fibre-based surface plasmon resonance sensor', *Pramana-Journal of Physics*, 78(3), 417-427, available: http://dx.doi.org/10.1007/s12043-011-0245-6.

Shaver, P.J. (1967) 'ACTIVATED TUNGSTEN OXIDE GAS DETECTORS', *Applied Physics Letters*, 11(8), 255-257, available: http://dx.doi.org/10.1063/1.1755123.

Shim, J.Y., Lee, J.D., Jin, J.M., Cheong, H. and Lee, S.-H. (2009) 'Pd–Pt alloy as a catalyst in gasochromic thin films for hydrogen sensors', *Solar Energy Materials and Solar Cells*, 93(12), 2133-2137, available: http://dx.doi.org/https://doi.org/10.1016/j.solmat.2009.01.004.

Shrivastav, A.M. and Gupta, B.D. (2018) 'Ion-imprinted nanoparticles for the concurrent estimation of Pb(II) and Cu(II) ions over a two channel surface plasmon resonance-based fiber optic platform', in SPIE, 8.

Silva, S., Coelho, L., Frazao, O., Santos, J. and Malcata, F. (2012) 'A Review of Palladium-Based Fiber-Optic Sensors for Molecular Hydrogen Detection', *IEEE Sensors Journal*, 12(1), 93-102, available: http://dx.doi.org/10.1109/JSEN.2011.2138130.

Skivesen, N., Horvath, R., Thinggaard, S., Larsen, N.B. and Pedersen, H.C. (2007) 'Deep-probe metal-clad waveguide biosensors', *Biosensors and Bioelectronics*, 22(7), 1282-1288, available: http://dx.doi.org/https://doi.org/10.1016/j.bios.2006.05.025.

Slaman, M., Dam, B., Pasturel, M., Borsa, D.M., Schreuders, H., Rector, J.H. and Griessen, R. (2007) 'Fiber optic hydrogen detectors containing Mg-based metal hydrides', *Sensors and Actuators B: Chemical*, 123(1), 538-545, available: http://dx.doi.org/https://doi.org/10.1016/j.snb.2006.09.058.

Slaman, M., Dam, B., Schreuders, H. and Griessen, R. (2008) 'Optimization of Mg-based fiber optic hydrogen detectors by alloying the catalyst', *International Journal of Hydrogen Energy*, 33(3), 1084-1089, available: http://dx.doi.org/10.1016/j.ijhydene.2007.09.036.

Sommerfeld, A. (1909) 'Über die Ausbreitung der Wellen in der drahtlosen Telegraphie', *Annalen der Physik*, 333(4), 665-736, available: http://dx.doi.org/10.1002/andp.19093330402.

Sommerfeld, A. (1928) 'Zur Elektronentheorie der Metalle auf Grund der Fermischen Statistik', *Zeitschrift für Physik*, 47(1), 1-32, available: http://dx.doi.org/10.1007/bf01391052.

Song, H., Chen, Y.P., Zhang, G., Liu, Y., Huang, P.C., Zhao, H.W., Yang, M.H., Dai, J.X. and Li, Z. (2015) 'Optical fiber hydrogen sensor based on an annealing-stimulated Pd-Y thin film', *Sensors and Actuators B-Chemical*, 216, 11-16, available: http://dx.doi.org/10.1016/j.snb.2015.03.090.

Sta, I., Jlassi, M., Kandyla, M., Hajji, M., Koralli, P., Krout, F., Kompitsas, M. and Ezzaouia, H. (2016) 'Surface functionalization of sol–gel grown NiO thin films with palladium nanoparticles for hydrogen sensing', *International Journal of Hydrogen Energy*, 41(4), 3291-3298, available: http://dx.doi.org/https://doi.org/10.1016/j.ijhydene.2015.12.109.

Stern, E.A. and Ferrell, R.A. (1960) 'Surface Plasma Oscillations of a Degenerate Electron Gas', *Physical Review*, 120(1), 130-136.

Sundaram, R.S., Gómez-Navarro, C., Balasubramanian, K., Burghard, M. and Kern, K. (2008) 'Electrochemical Modification of Graphene', *Advanced Materials*, 20(16), 3050-3053, available: http://dx.doi.org/10.1002/adma.200800198.

Tabassum, R. and Gupta, B.D. (2015) 'Surface plasmon resonance-based fiber-optic hydrogen gas sensor utilizing palladium supported zinc oxide multilayers and their nanocomposite', *Applied Optics*, 54(5), 1032-1040, available: http://dx.doi.org/10.1364/ao.54.001032.

Tabassum, R. and Gupta, B.D. (2016a) 'Fiber optic hydrogen gas sensor utilizing surface plasmon resonance and native defects of zinc oxide by palladium', *Journal of Optics*, 18(1), available: http://dx.doi.org/10.1088/2040-8978/18/1/015004.

Tabassum, R. and Gupta, B.D. (2016b) 'SPR based fiber-optic sensor with enhanced electric field intensity and figure of merit using different single and bimetallic configurations', *Optics Communications*, 367, 23-34, available: http://dx.doi.org/http://dx.doi.org/10.1016/j.optcom.2016.01.014.

Tobiška, P., Hugon, O., Trouillet, A. and Gagnaire, H. (2001) 'An integrated optic hydrogen sensor based on SPR on palladium', *Sensors and Actuators B: Chemical*, 74(1–3), 168-172, available: http://dx.doi.org/http://dx.doi.org/10.1016/S0925-4005(00)00728-0.

Toki, K., Kusakabe, K., Odani, T., Kobuna, S. and Shimizu, Y. (1996) 'Deposition of SiO2 and Ta2O5 films by electron-beam-excited plasma ion plating', *Thin Solid Films*, 281, 401-403, available: http://dx.doi.org/http://dx.doi.org/10.1016/0040-6090(96)08691-9.

Tonks, L. and Langmuir, I. (1929) 'Oscillations in Ionized Gases', *Physical Review*, 33(2), 195-210.

Turbadar, T. (1959) 'Complete Absorption of Light by Thin Metal Films', *Proceedings of the Physical Society*, 73(1), 40.

Ung, T., Liz-Marzán, L.M. and Mulvaney, P. (2001) 'Optical Properties of Thin Films of Au@SiO2 Particles', *The Journal of Physical Chemistry B*, 105(17), 3441-3452, available: http://dx.doi.org/10.1021/jp003500n.

van Gogh, A.T.M., Nagengast, D.G., Kooij, E.S., Koeman, N.J., Rector, J.H., Griessen, R., Flipse, C.F.J. and Smeets, R. (2001) 'Structural, electrical, and optical properties of La1-zYzHx switchable mirrors', *Physical Review B*, 63(19), available: http://dx.doi.org/10.1103/PhysRevB.63.195105.

Vanotti, M., Blondeau-Patissier, V., Moutarlier, V. and Ballandras, S. (2015) 'Analysis of palladium and yttrium-palladium alloy layers used for hydrogen detection with SAW device', *Sensors and Actuators B-Chemical*, 217, 30-35, available: http://dx.doi.org/10.1016/j.snb.2015.02.049.

Vargas, W.E., Rojas, I., Azofeifa, D.E. and Clark, N. (2006) 'Optical and electrical properties of hydrided palladium thin films studied by an inversion approach from transmittance measurements', *Thin Solid Films*, 496(2), 189-196, available: http://dx.doi.org/10.1016/j.tsf.2005.08.346.

Verma, R. and Gupta, B.D. (2013) 'SPR based fiber optic two channel sensor in near infrared (NIR) region', *AIP Conference Proceedings*, 1536(1), 1316-1317, available: http://dx.doi.org/10.1063/1.4810727.

Verma, R. and Gupta, B.D. (2014a) 'A novel approach for simultaneous sensing of urea and glucose by SPR based optical fiber multianalyte sensor', *Analyst*, 139(6), 1449-1455, available: http://dx.doi.org/10.1039/C3AN01983G.

Verma, R. and Gupta, B.D. (2014b) 'SPR based three channels fiber optic sensor for aqueous environment', in *SPIE OPTO*, SPIE, 8.

Verma, R., Srivastava, S.K. and Gupta, B.D. (2012) 'Surface plasmon resonance based multi-channel and multi-analyte fiber optic sensor', in *Asia Pacific Optical Sensors Conference*, SPIE, 8.

von Rottkay, K., Rubin, M. and Duine, P.A. (1999) 'Refractive index changes of Pd-coated magnesium lanthanide switchable mirrors upon hydrogen insertion', *Journal of Applied Physics*, 85(1), 408-413, available: http://dx.doi.org/10.1063/1.369399.

Wait, J.R. (1967) 'Electromagnetic whispering gallery modes in a dielectric rod', *Radio Science*, 2(9), 1005-1017, available: http://dx.doi.org/10.1002/rds1967291005.

Wang, X., Tang, Y., Zhou, C. and Liao, B. (2013a) 'Design and optimization of the optical fiber surface plasmon resonance hydrogen sensor based on wavelength modulation', *Optics Communications*, 298, 88-94, available: http://dx.doi.org/10.1016/j.optcom.2013.01.054.

Wang, X., Tang, Y., Zhou, C. and Liao, B. (2013b) 'Theoretical investigation of a dual-channel optical fibre surface plasmon resonance hydrogen sensor based on wavelength modulation', *Measurement Science & Technology*, 24(6), available: http://dx.doi.org/10.1088/0957-0233/24/6/065102.

Wang, X.G., Tang, Y.K., Zhou, C.D. and Liao, B. (2013a) 'Design and optimization of the optical fiber surface plasmon resonance hydrogen sensor based on wavelength modulation', *Optics Communications*, 298, 88-94, available: http://dx.doi.org/10.1016/j.optcom.2013.01.054.

Wang, X.G., Tang, Y.K., Zhou, C.D. and Liao, B. (2013b) 'Theoretical investigation of a dual-channel optical fibre surface plasmon resonance hydrogen sensor based on wavelength modulation', *Measurement Science & Technology*, 24(6), 9, available: http://dx.doi.org/10.1088/0957-0233/24/6/065102.

Wang, Y., Liu, B., Xiao, S., Li, H., Wang, L., Cai, D., Wang, D., Liu, Y., Li, Q. and Wang, T. (2015) 'High performance and negative temperature coefficient of low temperature hydrogen gas sensors using palladium decorated tungsten oxide', *Journal of Materials Chemistry A*, 3(3), 1317-1324, available: http://dx.doi.org/10.1039/C4TA05229C.

Weaver, J.H. and Olson, C.G. (1977) 'OPTICAL-ABSORPTION OF HCP YTTRIUM', *Physical Review B*, 15(2), 590-594, available: http://dx.doi.org/10.1103/PhysRevB.15.590.

Wei, Y., Su, Y., Liu, C., Nie, X., Liu, Z., Zhang, Y. and Zhang, Y. (2017) 'Two-Channel SPR Sensor Combined Application of Polymer- and Vitreous-Clad Optic Fibers', *Sensors*, 17(12), 2862.

Wood, R.W. (1902) 'On a Remarkable Case of Uneven Distribution of Light in a Diffraction Grating Spectrum', *Proceedings of the Physical Society of London*, 18(1), 269.

Xu, C., Wang, X. and Zhu, J. (2008) 'Graphene−Metal Particle Nanocomposites', *The Journal of Physical Chemistry C*, 112(50), 19841-19845, available: http://dx.doi.org/10.1021/jp807989b.

Yang, M.H., Li, Z., Dai, J.X., Yang, Z., Zhang, Y. and Zhuang, Z. (2013) 'Comparison of optical fiber Bragg grating hydrogen sensors with Pd-based thin films and sol-gel WO3 coatings', *Measurement Science and Technology*, 24(9), available: http://dx.doi.org/10.1088/0957-0233/24/9/094009.

Yoshida, S., Yamaguchi, T. and Kinbara, A. (1971) 'Optical Properties of Aggregated Silver Films', *Journal of the Optical Society of America*, 61(1), 62-69, available: http://dx.doi.org/10.1364/JOSA.61.000062.

Yoshimura, K., Bao, S., Uchiyama, N., Matsumoto, H., Kanai, T., Nakabayashi, S. and Kanayama, H. (2008) 'New hydrogen sensor based on sputtered Mg–Ni alloy thin film', *Vacuum*, 83(3), 699-702, available: http://dx.doi.org/https://doi.org/10.1016/j.vacuum.2008.04.047.

Yu, C., Liu, L., Chen, X., Liu, Q. and Gong, Y. (2015) 'Fiber-Optic Fabry-Perot Hydrogen Sensor Coated With Pd-Y Film', *Photonic Sensors*, 5(2), 142-145, available: http://dx.doi.org/10.1007/s13320-015-0237-0.

Zenneck, J. (1907) 'Über die Fortpflanzung ebener elektromagnetischer Wellen längs einer ebenen Leiterfläche und ihre Beziehung zur drahtlosen Telegraphie', *Annalen der Physik*, 328(10), 846-866, available: http://dx.doi.org/10.1002/andp.19073281003.

Zhang, C., Boudiba, A., Navio, C., Bittencourt, C., Olivier, M.-G., Snyders, R. and Debliquy, M. (2011) 'Highly sensitive hydrogen sensors based on co-sputtered platinum-activated tungsten oxide films', *International Journal of Hydrogen Energy*, 36(1), 1107-1114, available: http://dx.doi.org/https://doi.org/10.1016/j.ijhydene.2010.10.011.

Zhang, P., Liu, L., He, Y., Ji, Y. and Ma, H. (2015) 'Self-Referenced Plasmon Waveguide Resonance Sensor Using Different Waveguide Modes', *Journal of Sensors*, 2015, 10, available: http://dx.doi.org/10.1155/2015/945908.

Zhang, Y.-n., Peng, H., Qian, X., Zhang, Y., An, G. and Zhao, Y. (2017) 'Recent advancements in optical fiber hydrogen sensors', *Sensors and Actuators B: Chemical*, 244, 393-416, available: http://dx.doi.org/https://doi.org/10.1016/j.snb.2017.01.004.

Zhao, Z., Carpenter, M.A., Xia, H. and Welch, D. (2006a) 'All-optical hydrogen sensor based on a high alloy content palladium thin film', *Sensors and Actuators B: Chemical*, 113(1), 532-538.

Zhao, Z., Carpenter, M.A., Xia, H. and Welch, D. (2006b) 'All-optical hydrogen sensor based on a high alloy content palladium thin film', *Sensors and Actuators B-Chemical*, 113(1), 532-538, available: http://dx.doi.org/10.1016/j.snb.2005.03.070.

Zhou, Y., Zhang, P., He, Y., Xu, Z., Liu, L., Ji, Y. and Ma, H. (2014) 'Plasmon waveguide resonance sensor using an Au–MgF2 structure', *Applied Optics*, 53(28), 6344-6350, available: http://dx.doi.org/10.1364/AO.53.006344.

Zou, J., Iyer, K.S. and Raston, C.L. (2012) 'Pd-sodium carboxymethyl cellulose nanocomposites display a morphology dependent response to hydrogen gas', *Green Chemistry*, 14(4), 906-908, available: http://dx.doi.org/10.1039/C2GC16456F.

Zourob, M., Mohr, S., Brown, B.J.T., Fielden, P.R., McDonnell, M. and Goddard, N.J. (2003) 'The development of a metal clad leaky waveguide sensor for the detection of particles', *Sensors and Actuators B: Chemical*, 90(1), 296-307, available: http://dx.doi.org/https://doi.org/10.1016/S0925-4005(03)00052-2.

Zucker, F.J. (1954) 'The Guiding and Radiationof Surface Waves', *PROC. Symp. on Modern Advances in Microowave Techniques, Polytechnic*, 4, 403-435.

Špačková, B., Piliarik, M., Kvasnička, P., Themistos, C., Rajarajan, M. and Homola, J. (2009) 'Novel concept of multi-channel fiber optic surface plasmon resonance sensor', *Sensors and Actuators B: Chemical*, 139(1), 199-203, available: http://dx.doi.org/https://doi.org/10.1016/j.snb.2008.12.020.